NAVAL POSTGRADUATE SCHOOL
Monterey, California

THESIS

B242133

THE DEVELOPMENT AND STRUCTURAL CHARACTERISTICS OF DEAN VORTICES IN A CURVED RECTANGULAR CHANNEL

by

Lawrence Richard Baun

September 1988

Thesis Advisor: Phillip M. Ligrani

Approved for public release; distribution is unlimited

T238690

:lassified
RITY CLASSIFICATION OF THIS PAGE

REPORT DOCUMENTATION PAGE

REPORT SECURITY CLASSIFICATION CLASSIFIED	1b RESTRICTIVE MARKINGS
SECURITY CLASSIFICATION AUTHORITY	3 DISTRIBUTION/AVAILABILITY OF REPORT Approved for public release; distribution is unlimited
DECLASSIFICATION/DOWNGRADING SCHEDULE	
ERFORMING ORGANIZATION REPORT NUMBER(S)	5 MONITORING ORGANIZATION REPORT NUMBER(S)
NAME OF PERFORMING ORGANIZATION VAL POSTGRADUATE HOOL	6b OFFICE SYMBOL (If applicable) 69
7a NAME OF MONITORING ORGANIZATION NAVAL POSTGRADUATE SCHOOL
ADDRESS (City, State, and ZIP Code) onterey, California 93943-5000	7b. ADDRESS (City, State, and ZIP Code) Monterey, California 93943-5000
NAME OF FUNDING/SPONSORING ORGANIZATION	8b. OFFICE SYMBOL (If applicable)
9. PROCUREMENT INSTRUMENT IDENTIFICATION NUMBER
ADDRESS (City, State, and ZIP Code)	10 SOURCE OF FUNDING NUMBERS PROGRAM ELEMENT NO. / PROJECT NO. / TASK NO / WORK UNIT ACCESSION NO

TITLE (Include Security Classification) THE DEVELOPMENT AND STRUCTURAL CHARACTERISTICS OF DEAN VORTICES IN A CURVED RECTANGULAR CHANNEL

PERSONAL AUTHOR(S) Baun, Lawrence R.

TYPE OF REPORT	13b TIME COVERED	14 DATE OF REPORT (Year, Month, Day)	15 PAGE COUNT
aster's Thesis	FROM _____ TO _____	1988, September	242

SUPPLEMENTARY NOTATION The views expressed in this thesis are those of the author nd do not reflect the official policy of the Department of Defense or the .S. Government.

COSATI CODES		
FIELD	GROUP	SUB-GROUP

18 SUBJECT TERMS (Continue on reverse if necessary and identify by block number)
Dean vortices; Dean number; Rectangular Curved Channel

ABSTRACT (Continue on reverse if necessary and identify by block number)
he development and structure of Dean vortices in a curved channel were easured and studied. A 40:1 aspect ratio channel with mild curvature was mployed. Circulation of mean streamwise vorticity, and maxima of treamwise, spanwise and radial components of vorticity increase as the ean number increases from 40 to 140. Mean vorticity components were etermined from measurements of the three components of mean velocity using miniature five hole pressure probe. Spectra obtained from a subminiature rossed-wire probe show principal and harmonic frequencies for Dean numbers reater than 165, when vorticies are twisting. Spectral peaks at other ean numbers provide evidence of oscillations also observed during flow isualization

) DISTRIBUTION/AVAILABILITY OF ABSTRACT ☒ UNCLASSIFIED/UNLIMITED ☐ SAME AS RPT ☐ DTIC USERS	21. ABSTRACT SECURITY CLASSIFICATION Unclassified
a. NAME OF RESPONSIBLE INDIVIDUAL hillip M. Ligrani	22b TELEPHONE (Include Area Code) (408) 646-3382 / 22c OFFICE SYMBOL 69Li

D FORM 1473, 84 MAR 83 APR edition may be used until exhausted. All other editions are obsolete

SECURITY CLASSIFICATION OF THIS PAGE

☆ U.S. Government Printing Office: 1986—606-24.

Unclassified

Approved for public release; distribution is unlimited

The Development and Structural Characteristics of Dean Vortices in a Curved Rectangular Channel

by

Lawrence Richard Baun
Lieutenant, United States Navy
B.S., Auburn University, 1979

Submitted in partial fulfillment of the
requirements for the degree of

MASTER OF SCIENCE IN MECHANICAL ENGINEERING

and

MECHANICAL ENGINEER

from the

NAVAL POSTGRADUATE SCHOOL
September 1988

ABSTRACT

The development and structure of Dean vortices in a curved channel were measured and studied. A 40:1 aspect ratio channel with mild curvature was employed. Circulation of mean streamwise vorticity, and maxima of streamwise, spanwise and radial components of vorticity increase as the Dean number increases from 40 to 140. Mean vorticity components were determined from measurements of the three components of mean velocity using a miniature five hole pressure probe. Spectra obtained from a subminiature crossed-wire probe show principal and harmonic frequencies for Dean numbers greater than 165, when vorticies are twisting. Spectral peaks at other Dean numbers provide evidence of oscillations also observed during flow visualization.

Thesis
B242923
C.1

TABLE OF CONTENTS

I. INTRODUCTION 1

A. BACKGROUND 1

B. OBJECTIVES 4

C. ORGANIZATION 4

II. CURVED CHANNEL 6

A. CHANNEL 6

B. DEAN NUMBER DETERMINATION 8

III. PRESSURE PROBE APPARATUS AND CALIBRATION 10

A. BACKGROUND 10

B. PROBE DESCRIPTION 11

C. EXPERIMENTAL DETAILS 13

1. Probe and Tubing 13

2. Transducers, Carrier Demodulators and Signal Processing 14

3. Computer and Software 17

D. PROBE CALIBRATION 18

1. Wind Tunnel 18

2. Calibration Sled 19

3. Calibration Procedure 19

E. CALIBRATION RESULTS 21

IV. MEASUREMENT CORRECTION PROCEDURES 24

A. SPATIAL RESOLUTION CORRECTION 24

B. INDUCED DOWNWASH VELOCITY CORRECTION 26

V. CURVED CHANNEL MEASUREMENT PROCEDURES AND QUALIFICATION 30

A. MEASUREMENT PROCEDURES AND APPARATUS 30

1. Traversing Mechanism 30

2. Measurement Procedure 31

3. Data Reduction 33

B. CHANNEL QUALIFICATION TESTS 35

C. FIVE HOLE PROBE QUALIFICATION 36

D. SPATIAL RESOLUTION AND DOWNWASH VELOCITY CORRECTION APPLICATIONS 37

VI. POWER SPECTRA APPARATUS AND PROCEDURES 39

A. PROBES AND MEASUREMENT CHAIN 39

1. Hot-Wire Probes 39

2. Signal Measurement 41

B. SIGNAL PROCESSING AND ANALYSIS 42

1. High Speed Digital Acquisition and Analysis 43

2. Real Time Signal Analysis 44

VII. FLOW VISUALIZATION APPARATUS AND PROCEDURES 45

A. SMOKE GENERATOR 45

B. CAMERA AND LIGHTING 46

1. Radial-Spanwise Plane Photographs 46

2. Concave Surface Exterior Photographs 47

VIII. RESULTS 48

A. PREVIOUS STUDIES 49

B. SURVEYS OF MEAN VELOCITY AND MEAN VORTICITY COMPONENTS 50

1. Total Pressure and Streamwise Velocity Distributions 51

a. De=49 - De=64 52

b. De=64 - De=86 52

c. De=95 - De=137 53

d. De=137 - De=201 53

2. Velocity Perturbation Measurements 53

3. Mean Vorticity Distributions 55

a. Streamwise Vorticity 55

b. Radial Vorticity 58

c. Spanwise Vorticity 59

4. Detailed Pressure and Vorticity Measurements 60

a. De=77.9 61

b. De=102.2 61

c. De=119.0 61

d. De=131.6 62

C. SPECTRA OF HOT-WIRE SIGNAL MEASUREMENTS 62

1. De=40 - De=144 63

2. De=120 - De=160 64

3. De=165 - De=200 65

D. FLOW VISUALIZATION 66
1. Radial-Spanwise Plane 67
2. Exterior View - Concave Surface 68
IX. SUMMARY AND CONCLUSIONS 69
APPENDIX A. FIGURES 71
APPENDIX B. UNCERTAINTY ANALYSIS 202
APPENDIX C. SOFTWARE DIRECTORY 207
LIST OF REFERENCES 218
INITIAL DISTRIBUTION LIST 221

LIST OF FIGURES

Page

Figure 1. Curved Channel Geometry 72

Figure 2. Schematic of One Dean Vortex Pair 72

Figure 3. Schematic of Test Facility 73

Figure 4. Test Facilty (Side View) 74

Figure 5. Schematic of Support Block 75

Figure 6. Five Hole Pressure Probe Geometry 76

Figure 7. Five Hole Pressure Probe 77

Figure 8. Five Hole Pressure Probe, 100 μm 78
Between Scale Markings

Figure 9. Pressure Probe Calibration sled 79

Figure 10. Cp Yaw vs. Yaw, 1.9 m/s 80

Figure 11. Cp Pitch vs. Pitch, 1.9 m/s 80

Figure 12. Cp Total vs. Pitch, 1.9 m/s 81

Figure 13. Cp Total-Static vs. Pitch, 1.9 m/s 81

Figure 14. Cp Static vs. Pitch, 1.9 m/s 82

Figure 15. Cp Yaw vs. Yaw, 1.1 m/s 83

Figure 16. Cp Yaw vs. Yaw, 1.9 m/s 83

Figure 17. Cp Yaw vs. Yaw, 2.9 m/s 84

Figure 18. Cp Yaw vs. Yaw, 5.0 m/s 84

Figure 19. Successive Positions of the Five Hole 85
Pressure Probe and Probe Parts, Looking
Downstream

Figure 20. Curved Channel Traversing Mechanism, ...86
Transducers, Probe and Probe Mount

Figure 21. Total Pressure Distribution 87
a) Miniature Kiel Probe, De=54
b) Five-hole Probe, De=49

Figure 22. Streamwise Velocity Profiles Plotted 88
Against CCPF, De=36.6

Figure 23. a) Streamwise Velocity Contours, De=100 89
b) Secondary Velocity Vectors, No
Corrections, De=100

Figure 24. Secondary Velocity Vectors, De=100 90
a) Spatial Resolution Correction Only
b) Spatial Resolution and Downwash Velocity
Correction

Figure 25. Hot-wire Probe Mounting 91

Figure 26. a) Hot-wire Measurement Setup 92
b) Oscilliscope, Bridge and Filter Amplifier

Figure 27. Radial-Spanwise Plane Flow Visualization 93

Figure 28. Radial-Spanwise Plane Flow Visualization, ...94
115 Degree Streamwise Location

Figure 29. Total Pressure Contours, ...95
De=49.3 to De=95.5..95

Figure 30. Total Pressure Contours, ...96
De=86.2 to De=137.0

Figure 31. Total Pressure Contours, ...97
De=126.3 to De=201.8

Figure 32. Total Pressure Differentials, Maximum and ...98
Minimum

Figure 33. Streamwise Velocity Contours, ...99
De=49.3 to De=95.5

Figure 34. Streamwise Velocity Contours, ...100
De=86.2 to De=137.0

Figure 35. Streamwise Velocity Contours, ...101
De=126.3 to De=201.8

Figure 36. Velocity Perturbation Contours, ...102
De=49.3 to De=95.5

Figure 37. Velocity Perturbation Contours, ...103
De=86.2 to De=137.0

Figure 38. Velocity Perturbation Contours, ...104
De=126.3 to De=201.8

Figure 39. Streamwise Vorticity Contours, ...105
De=53.2 to De=100.3

Figure 40. Streamwise Vorticity Contours, ...106
De=100.3 to De=146.1

Figure 41. Peak Streamwise Vorticity vs. Dean #, ...107
Left Vortex Pair

Figure 42. Peak Streamwise Vorticity vs. Dean #, ...108
Middle Vortex Pair

Figure 43. Peak Streamwise Vorticity vs. Dean #, ...109
Right Vortex Pair

Figure 44. Peak Streamwise Vorticity vs. Dean #, ...110
Total Measured Area

Figure 45. Vortex Circulation vs. Dean #, ...111
Left Vortex Pair

Figure 46. Vortex Circulation, vs. Dean #, ...112
Middle Vortex Pair

Figure 47. Vortex Circulation, vs. Dean #, ...113
Right Vortex Pair

Figure 48. Vortex Circulation, vs. Dean #, ...114
Average Vortex Pair

Figure 49. Radial Vorticity Contours, ...115
De=36.6 to De=86.2

Figure 50. Radial Vorticity Contours, ...116
De=86.2 to De=137.0

Figure 51. Radial Vorticity Contours, ...117
De=137.0 to De=230.7

Figure 52. Peak Radial Vorticity vs. Dean #, ...118
Left Vortex Pair

Figure 53. Peak Radial Vorticity vs. Dean #, ...119
Middle Vortex Pair

Figure 54. Peak Radial Vorticity vs. Dean #, ...120
Right Vortex Pair

Figure 55. Peak Radial Vorticity vs. Dean #, ...121
Total Measured Area

Figure 56. Spanwise Vorticity Contours, ...122
De=36.6 to De=86.2

Figure 57. Spanwise Vorticity Contours, ...123
De=86.2 to De=137.0

Figure 58. Spanwise Vorticity Contours, ...124
De=137.0 to De=230.7

Figure 59. Peak Spanwise Vorticity vs. Dean #, ...125
Left Vortex Pair

Figure 60. Peak Spanwise Vorticity vs. Dean #, ...126
Middle Vortex Pair

Figure 61. Peak Spanwise Vorticity vs. Dean #, ...127
Right Vortex Pair

Figure 62. Peak Spanwise Vorticity vs. Dean #, ...128
Total Measured Area

Figure 63. De=77.9, a) Secondary Flow Vectors 129
b) Streamwise Vorticity Contours

Figure 64. De=77.9, a) Total Pressure Contours 130
b) Streamwise Velocity Contours

Figure 65. De=77.9, a) Radial Vorticity Contours 131
b) Spanwise Vorticity Contours

Figure 66. De=102.2, a) Secondary Flow Vectors 132
b) Streamwise Vorticity Contours

Figure 67. De=102.2, a) Total Pressure Contours 133
b) Streamwise Velocity Contours

Figure 68. De=102.2, a) Radial Vorticity Contours 134
b) Spanwise Vorticity Contours

Figure 69. De=119.0, a) Secondary Flow Vectors 135
b) Streamwise Vorticity Contours

Figure 70. De=119.0, a) Total Pressure Contours 136
b) Streamwise Velocity Contours

Figure 71. De=119.0, a) Radial Vorticity Contours 137
b) Spanwise Vorticity Contours

Figure 72. De=131.6, a) Secondary Flow Vectors 138
b) Streamwise Vorticity Contours

Figure 73. De=131.6, a) Total Pressure Contours 139
b) Streamwise Velocity Contours

Figure 74. De=131.6, a) Radial Vorticity Contours 140
b) Spanwise Vorticity Contours

Figure 75. De=40, Subminiature Hot-wire Spectra, ...141
Real Time Analysis

Figure 76. De=40, a) Subminiature Hot-wire 142
Spectra, Digital Analysis
b) Sample Time Trace

Figure 77. De=60, Subminiature Hot-wire Spectra, ...143
Real Time Analysis

Figure 78. De=60, a) Subminiature Hot-wire Spectra, ...144
Digital Analysis
b) Sample Time Trace

Figure 79. De=69, Subminiature Hot-wire Spectra, ...145
Real Time Analysis

Figure 80. De=78, Subminiature Hot-wire Spectra, ...146
Real Time Analysis

Figure 81. De=80, Subminiature Hot-wire Spectra, ...147
Real Time Analysis

Figure 82. De=80, a) Subminiature Hot-wire Spectra, ...148
Digital Analysis
b) Sample Time Trace

Figure 83. De=90, a) Subminiature Hot-wire Spectra, ...149
Digital Analysis
b) Sample Time Trace

Figure 84. De=95, Subminiature Hot-wire Spectra, ...150
Real Time Analysis

Figure 85. De=100, Subminiature Hot-wire Spectra, ...151
Real Time Analysis

Figure 86. De=100, a) Subminiature Hot-wire spectra, ..152
Digital Analysis
b) Sample Time Trace

Figure 87. De=110, Subminiature Hot-wire Spectra, ...153
Real Time Analysis

Figure 88. De=110, a) Subminiature Hot-wire Spectra, ..154
Digital Analysis
b) Sample Time Trace

Figure 89. De= 114, Subminiature Hot-wire Spectra, ...155
Real Time Analysis

Figure 90. De= 120, Subminiature Hot-wire Spectra, ...156
Real Time Analysis

Figure 91. De=120, a) Subminiature Hot-wire Spectra, ..157
Digital Analysis
b) Sample Time Trace

Figure 92. De=126, Subminiature Hot-wire Spectra, ...158
Real Time Analysis

Figure 93. De=130, Subminiature Hot-wire Spectra, ...159
Real Time Analysis

Figure 94. De=130, a) Subminiature Hot-wire Spectra, ..160
Digital Analysis
b) Sample Time Trace

Figure 95. De=134, Subminiature Hot-wire Spectra, ...161
Real Time Analysis

Figure 96. De=140, Subminiature Hot-wire Spectra, ...162
Real Time Analysis

Figure 97. De=140, a) Subminiature Hot-wire Spectra, ..163
Digital Analysis
b) Sample Time Trace

Figure 98. De=150, Subminiature Hot-wire Spectra, ...164
Real Time Analysis

Figure 99. De= 150, a) Subminiature Hot-wire 165
Spectra Digital Analysis
b) Sample Time Trace

Figure 100. De=150, Subminiature Hot-wire Spectra, ...166
Real Time Analysis

Figure 101. De=160, a) Subminiature Hot-wire Spectra, ..167
Digital Analysis
b) Sample Time Trace

Figure 102. De=132, a) Conventional Hot-wire Spectra, ..168
Digital Analysis
b) Sample Time Trace

Figure 103. De=140, Subminiature Hot-wire Spectra, ...169
Real Time Analysis

Figure 104. De=140, a) Subminiature Hot-wire Spectra, ..170
Digital Analysis
b) Sample Time Trace

Figure 105. De=140, a) Conventional Hot-wire Spectra, ..171
Digital Analysis
b) Sample Time Trace

Figure 106. De=152, a) Conventional Hot-wire Spectra, ..172
Digital Analysis
b) Sample Time Trace

Figure 107. De=153, a) Subminiature Hot-wire Spectra, ..173
Digital Analysis
b) Sample Time Trace

Figure 108. De=157, a) Subminiature Hot-wire Spectra, ..174
Digital Analysis
b) Sample Time Trace

Figure 109. De=160, a) Subminiature Hot-wire Spectra, ..175
Digital Analysis
b) Sample Time Trace

Figure 110. De=165, a) Conventional Hot-wire Spectra, ..176
Digital Analysis
b) Sample Time Trace

Figure 111. De=168, a) Conventional Hot-wire Spectra, ..177
Digital Analysis
b) Sample Time Trace

Figure 112. De=170, Subminiature Hot-wire Spectra, ...178
Real Time Analysis

Figure 113. De=175, a) Conventional Hot-wire Spectra, ..179
Digital Analysis
b) Sample Time Trace

Figure 114. De=180, a) Conventional Hot-wire Spectra, ..180
Real Time Analysis
b) Sample Time Trace

Figure 115. De=180, a) Conventional Hot-wire Spectra, ..181
Digital Analysis
b) Sample Time Trace

Figure 116. De=184, Subminiature Hot-wire Spectra, ...182
Real Time Analysis

Figure 117. De=190, a) Subminiature Hot-wire Spectra, ..183
Digital Analysis
b) Sample Time Trace

Figure 118. De=190, a) Conventional Hot-wire Spectra, ..184
Digital Analysis
b) Sample Time Trace

Figure 119. De=190, Subminiature Hot-wire Spectra, ...185
Real Time Analysis

Figure 120. De=200, a) Conventional Hot-wire Spectra, ..186
Digital Analysis
b) Sample Time Trace

Figure 121. Radial-Spanwise Plane Flow Visualization ...187
a) De=51.9, b) De=64.4,
c) De=95.4, d) De=107.7

Figure 122. Concave Surface Flow Visualization, ...188
De=88.5, 50°-80°

Figure 123. Concave Surface Flow Visualization, ...189
De=97.0, 50°-80°

Figure 124. Concave Surface Flow Visualization, ...190
De=106.6, 50°-80°

Figure 125. Concave Surface Flow Visualization, ...191
De=125.4, 50°-80°

Figure 126. Concave Surface Flow Visualization, ...192
De=145.2, 50°-80°

Figure 127. Concave Surface Flow Visualization, ...193
De=165.6, 50°-80°

Figure 128. Concave Surface Flow Visualization, ...194
De=54.2, 80°-110°

Figure 129. Concave Surface Flow Visualization, ...195
De=64.5, 80°-110°

Figure 130. Concave Surface Flow Visualization, ...196
De=74.8, 80°-110°

Figure 131. Concave Surface Flow Visualization, ...197
De=86.1, 80°-110°

Figure 132. Concave Surface Flow Visualization, ...198
De=94.5, 80°-110°

Figure 133. Concave Surface Flow Visualization, ...199
De=104.8, 80°-110°

Figure 134. Concave Surface Flow Visualization, ...200
De=142.8, 80°-110°

Figure 135. Uncertainty Analysis Flow Chart 201

LIST OF SYMBOLS

a	Spanwise Wavenumber
a'	Diameter of Pressure Probe Tip, used for Downwash Velocity Correction
A_{ch}	Cross Sectional Area of Curved Channel
A_{or}	Cross Sectional Area of Orifice
A_p	Cross Sectional Area of Outlet Pipe
$\bar{C}$	Average Transducer Calibration Coefficient
CCPF	Curved Channel Poiseuille Flow
C_{pp}	Probe Calibration Coefficient, Pitch
C_{ps}	Probe Calibration Coefficient, Static Pressure
C_{pt}	Probe Calibration Coefficient, Total Pressure
C_{pts}	Probe Calibration Coefficient, Total-Static Pressure
C_{py}	Probe Calibration Coefficient, Yaw
d	Channel Height = ro - ri
De	Dean Number = $(\bar{U}d/\nu) * \sqrt{d/r_i}$
De_{cr}	Critical Dean Number = 35.92
d_p	Outlet Pipe Diameter
$\bar{E}$	Average Transducer Voltage Reading
K	Flow Coefficient
K_p	Slope of Probe Calibration Pitch Coefficient Curve
K_{ts}	Slope of Probe Calibration Total-Static Coefficient Curve

K_y	Slope of Probe Calibration Yaw Coefficient Curve
$\dot{m}$	Mass Flow RAte
P_{amb}	Ambient Pressure
P_1	Pressure Measured at Five Hole Port One
P_2	Pressure Measured at Five Hole Port Two
P_3	Pressure Measured at Five Hole Port Three
P_4	Pressure Measured at Five Hole Port Four
P_5	Pressure Measured at Five Hole Port Five
$\bar{P}$	Average Pressure (P2+P3+P4+P5)/4
$P_{manometer}$	Manometer Pressure Reading
P_{mean}	Average Differential Pressure Measured
P_t	Total Pressure
P_s	Static Pressure
Re_{ch}	Channel Reynolds Number = $\bar{U}d/\nu$
Re_p	Pipe Reynolds Number = $\bar{U}d_p/\nu$
Re_{probe}	Probe Tip Reynolds Number = $\bar{U}a'/\nu$
r_i	Inside Radius of Channel Curvature
r_o	Outside Radius of Channel Curvature
U	Total Velocity
$\bar{U}$	Mean Velocity
U_θ	Streamwise Velocity, also Ux
U_r	Radial Velocity, also Uy
U_x	Streamwise Velocity, also Uθ
U_y	Radial Velocity, also Ur

U_z	Spanwise Velocity
Y	Expansion Coefficient
Y/d	Normalized Radial Direction
z/d	Normalized Spanwise Direction
Γ_x	Streamwise Circulation
Δ	Coefficient used for Determining Downwash Velocity Correction
ΔP_{or}	Orifice Pressure Drop
δ	Uncertainty Estimate
λ	Spanwise Spacing of Vortex Pairs
ν	Kinematic Viscosity
ρ	Density
θ	Streamwise Location from Start of Curvature
$\omega\theta$	Mean Streamwise Vorticity, also ω_x
ω_r	Mean Radial Vorticity, also ω_y
ω_x	Mean Streamwise Vorticity, also ω_θ
ω_y	Mean Radial Vorticity, also ω_r
ω_z	Mean Spanwise Vorticity

ACKNOWLEDGMENT

I would like to express my heartfelt appreciation to all those who made this work possible. In particular, my thesis advisor, Professor Ligrani was always able to provide guidance and keep things in perspective. The Mechanical Engineering shop personnel, specifically Tom McCord, Tom Christian, Charles Crow and Jim Schofield were always willing to respond to "short-fuzed" requirements and provide excellent craftmanship. Dr. Bart Singer's work in developing software and measurement techniques for this study was invaluable. Finally, to Lisa and Evan, who provided love, patience and encouragement to see me through this work, to you I am forever grateful.

I. INTRODUCTION

A. BACKGROUND

Flow in a curved channel with mild curvature and a 40 to 1 aspect ratio was studied. Results are presented for channel Reynolds numbers, $\bar{U}d/\nu$, less than 1600. In particular, the structure of Dean vortices and their development as Reynolds numbers increases was investigated. The presence of Dean vortices in curved channel flow has an important influence on flow structure, heat transfer characteristics and eventually, transition to turbulent flow.

Centrifugal forces imposed by concave curvature of streamlines cause curved channel flow to be non-azimuthal. As curvature is imposed, centrifugal forces are greater on the faster moving fluid particles near the center of the channel than near the concave or convex surfaces. The centrifugal instability causes the faster moving fluid to displace fluid near the concave wall. The particles near the concave surface are then forced in the spanwise direction and then toward the center of the channel. This centrifugal instability results in spanwise periodic pairs of counter-rotating vortices (Figures 1, 2) [Ref. 1].

While significant experimental and analytic research has been accomplished on flows between concentric cylinders and over concave surfaces, little work has been done to study flow in curved channels. The first analytical study of curved channel flow was by W.R. Dean [Ref. 2] in 1928. He found that, for a narrow gapped channel ($r_i/r_o \sim 1$), flow is unstable to small disturbances when the value of $\bar{U}d/\nu\sqrt{d/r_i}$ is greater than 35.92. The parameter $Re_{ch}\sqrt{d/r_i}$ is now known as the Dean number, De. Reid [Ref. 3] and Hammerlin [Ref. 4] verified Dean's findings in additional analytic work and further defined a neutral stability curve which divides stable and unstable flow regimes.

The first published experimental work done on high aspect ratio curved channel flow is by Kelleher et al. [Ref. 5]. These experiments show that, by traversing a hot-wire in a spanwise direction at several different radii, the secondary flow in the channel is periodic and undergoes a phase change as the probe is moved from the concave to the convex side of the channel. The range of Dean numbers for this experiment and accompanying flow visualization is 79 to 113.

Using the same channel as in this study, Siedband [Ref. 6] and Niver [Ref. 7] used flow visualization to study Dean vortex structure and development. Siedband used a smoke wire at a Dean number range of 167-461 and at one streamwise location. Niver photographed Dean vortices

using smoke at several different streamwise locations and a Dean number range of 40-220. The same 40 to 1 aspect ratio and radius ratio of 0.979 were employed in these studies as was used by Kelleher et al. [Ref. 5].

Finlay et al. [Ref.1, 8] used the three-dimensional, incompressible Navier-Stokes equations to numerically simulate curved channel flow with a geometry also similar to the Kelleher experiment. These simulations determined that the axisymmetric Dean vortices develop at least two different types of streamwise travelling waves. At a Dean number of 63.8 undulating Dean vortex flow consists of developing vortices and long streamwise wave lengths. At Dean numbers of 78.5 and 98.2, twisting Dean vortex flow is evident. This is characterized by a much shorter streamwise wave length and higher unsteadiness. Ligrani and Niver [Ref. 9] supported Finlay's findings and concluded, through flow visualization, that Dean vortices develop such that they increase in radial height as the Dean number changes from 40 to 100. In this range, the vortices show some spanwise and radial unsteadiness but are generally symmetric. Above a Dean number of about 100, vortices start to twist and are non-symmetric. Spanwise and radial oscillations become more pronounced and vortex flow becomes more unsteady. In all cases, the state of the vortex pairs is dependent upon the streamwise location as well as the flow rate.

B. OBJECTIVES

The objectives of this thesis are;

1. To measure the three mean velocity components of Dean vortices over a range of Dean numbers from 40 to 220.

2. Using the results from objective 1, determine the three components of mean vorticity over the same Dean number range.

3. To measure the frequencies of different unsteady events through the use of spectra of subminiature and conventional hot-wire voltage fluctuations.

4. To investigate flow characteristics using flow visualization techniques.

5. To compare qualitative and quantitative results with those given by Ligrani and Niver [Ref. 9], Kelleher et al. [Ref. 5] and Finlay et al. [Ref. 1, 8].

C. ORGANIZATION

Subsequent to this introduction, Chapter 2 discusses the curved channel facility used in this study. Chapter 3 explains, in detail, the five hole pressure probe used in the experiments to include its calibration. Chapter 4 describes spatial resolution and downwash velocity corrections developed and adapted for five hole probe measurements. Chapter 5 shows the results of channel and probe qualification tests including qualification of pressure and velocity corrections. Chapter 6 describes subminiature and conventional hot-wire probe measurement equipment and procedures. Chapter 7 describes flow visualization equipment and techniques. Chapter 8 presents

the results of this study and comparison with previous studies. Chapter 9 gives a summary and conclusions.

II. CURVED CHANNEL

A. CHANNEL

Details on the design and construction of the Naval Postgraduate School Curved Channel Research Facility can be found in Siedband [Ref. 6], Niver [Ref. 7:pp. 10-13] and Ligrani and Niver [Ref. 9]. A schematic [Ref. 7] and a photograph [Ref. 6] are shown in Figures 3 and 4. For completeness, a discussion on the channel and recent modifications are provided below.

The channel is an open circuit suction facility designed for low speed transition studies. The inlet section consists of an aluminum honeycomb and three screens which reduce the spatial non-uniformities in the flow. The inlet is followed by a 20:1 contraction ratio nozzle. Flow is accelerated through the nozzle into a 2.44 m long straight duct. This entry length allows for fully developed channel flow entering the curved section for all Dean numbers studied. The flow then enters a curved test section with a convex wall radius of 59.69 cm and concave wall radius of 60.96 cm. After the flow completes a 180 degree turn it enters another 2.44 m straight duct and goes through another honeycomb, screens and a diffuser into an outlet plenum.

A 5.08 cm diameter pipe connects the outlet plenum to a second plenum which is kept at a low pressure by a 1/3 horsepower blower. A globe valve for flow throttling and an orifice plate for mass flow measurement are located in the connecting pipe. The upper and lower walls of the channel are made of seamless sheets of polycarbonate (Lexan). The side walls, longitudinal supports and cross beam supports maintain a cross section of 1.27 cm by 50.8 cm within ± 0.015 cm for channel depth, and ± 0.05 cm for the channel width. [Ref. 10]

In order to isolate the channel from the blower and laboratory floor vibrations, rubber mounts were added between the inlet section and the plenum and their respective frames. Rubber vibration mounts were also used to mount the blower and blower frame.

A slot was cut in the curved section of the channel to allow pressure measurements. The slot is 0.32 cm wide and 7.62 cm long and is located in the convex wall of the channel. It is aligned in the spanwise direction 5.08 cm off of the centerline of the channel at the 120 degree streamwise location. Since cutting the slot at this location caused stress relief in the convex wall, care was taken to construct a support block which could eliminate any non-uniformities in the channel wall and provide an air tight seal through which a pressure probe could be inserted. A Lexan support block, (15.24 cm x 6.35 m x 2.22 cm) was

fabricated for this purpose. While the support block was being epoxied to the convex wall, the wall in the vicinity of the slot was pulled inward, toward the center of the curvature radius. This eliminated any bowing of the convex wall around the slot area. Foam strips were adhered to brass inserts which were placed just inside the slot. The brass inserts and compressed foam were positioned so that a probe could be inserted into the channel and move freely in the spanwise and radial directions without any air leakage. A schematic of the Lexan support block and the foam sealing device is shown in Figure 5.

B. DEAN NUMBER DETERMINATION

The mass flow rate and Dean number were calculated by measuring the pressure drop across the 1.5 inch ASME orifice. The orifice pressure drop is measured using a Celesco model LCVR differential pressure transducer and a Celesco DC10D carrier demodulator. The signal is collected and processed using a Hewlett-Packard (HP) 3498A extender, HP3497A data acquisition system and a HP300 model 9836S computer. Additional details on the transducers, DAS and computer are found in the next chapter.

Once the pressure drop is determined, a first guess at the Dean number is made by interpolating pressure drop vs. Dean number data from Niver [Ref. 7:p. 33]. Density is

calculated using ambient temperature and pressure readings and the perfect gas relationship. The expansion coefficient, Y, is calculated from Holman and Gajda [Ref. 11]. Using the first guess Dean number to give an initial mass flow rate, the pipe Reynolds number, Re_p is calculated as follows;

$$Re_p = \dot{m} d_p / \rho \nu A_p$$

The flow coefficient, K, is then interpolated from the ASME Tables [Ref. 12]. Mass flow rate is updated using the equation;

$$\dot{m} = K A_{or} Y \sqrt{2 \rho \Delta P_{or}}$$

This procedure is continued iteratively until the mass flow rate converges to within one percent of the previous value. Finally, the Dean number is calculated using;

$$De = (\dot{m} / \rho A_{ch}) \times (d/\nu) \times \sqrt{d/r_i}$$

III. PRESSURE PROBE APPARATUS AND CALIBRATION

A detailed investigation on the fabrication, use and calibration of five hole pressure probes is presented by Ligrani et al. [Ref. 10]. To provide a complete explanation of experimental apparatus and methods used for this thesis, portions of that article are presented in this chapter.

A. BACKGROUND

In the present investigation, a miniature five hole pressure probe having a probe tip diameter of 1.22 mm was developed to meet requirements of spatial resolution and minimal flow blockage. The probe was developed to measure three components of mean velocity at individual locations within the curved channel. In the working section of the channel, the cross-section is 12.7 mm x 508.0 mm. With this limited access for instrumentation, insertion and use of any existing type of triple-sensor hot-wire probe was not considered. The large measuring volumes and high cost of laser-doppler velocimetry systems made them an impractical alternative.

Procedures for the calibration and application of ordinary-sized five hole pressure probes are described by Treaster and Yocum [Ref. 13]. Here, calibration coefficients for the yaw angle, pitch angle, and total

pressure are independent of Reynolds number based on probe tip diameters for Reynolds numbers ranging from 2000 to 7000. The static pressure coefficient shows small Reynolds number dependence which, if unaccounted for, results in errors in magnitudes of measured velocity. Five hole probes similar in size to the ones used by Treaster and Yocum are used extensively throughout the fluid dynamics community and many results obtained from such probes are available in the literature. Treaster and Houtz [Ref. 14] describe the fabrication and calibration of miniature five hole pressure probes with tip diameters ranging from 1.07 mm to 1.68 mm. Calibration coefficients are defined in the same manner as given by Treaster and Yocum and also show similar dependence on Reynolds number and wall proximity. In a companion paper, Welz [Ref. 15] describes a double interpolation procedure to obtain velocity direction and magnitude from calibration data and measured pressures.

B. PROBE DESCRIPTION

Two schematics and a photograph of the miniature five hole pressure probe are shown in Figures 6, 7 and 8 respectively. The diameter of the probe tip is 1.22 mm, where the central tube is surrounded by four other tubes, where the end of each is tapered at a 45 degree angle with respect to the mouth of the central tube. Each of the five hole tubes is made from stainless steel hypodermic tubing

with inner and outer diameters of .203 mm and .406 mm, respectively. The probe was constructed by first spot welding together these five tubes. The five were then bent in a 90 degree turn with a radius of 1.52 mm to avoid any tube crimping. Silver solder was then used to join the five tubes together continuously along their length. Finally, the portions of the probe tip were tapered to appropriate angles using a surface grinder. This approach is different from the one described by Treaster and Houtz wherein probe tips are ground and sanded into appropriate shapes after solder is used to completely encase all tubes.

Figure 6 shows that the present probe tip extends 5.08 mm (4 tip diameters) beyond the bend in the stem to minimize the effects of stem flow blockage at the measuring location. Similarly, the tip is 22.9 mm (19 tip diameters) from the 9.53 mm diameter cylinder. Within this cylinder, each tube is connected to a 1.60 mm diameter tube using a small manifold for each tube connection. The mounting cylinder was sized for easy handling and mounting. On top of the cylinder is a second set of manifolds with five male connectors for attachment to 6.35 mm outer diameter/4.67 mm inner diameter polyflow tubing.

The miniature five hole probe was designed to minimize the adverse effects of flow blockage and spatial resolution when used for measurements in the curved channel. When in

place for measurements at the centerline of the channel, the mounting cylinder is not exposed to the flow, and the probe produces 4.8 percent blockage over a 12.7 mm x 12.7 mm area. The tip is conical rather than a prism type to minimize near-flow blockage effects which are particularly severe for prism type probes.

C. EXPERIMENTAL DETAILS

1. Probe and Tubing

The tubing used to connect the probe to transducers influences the pressure detected at the transducer. In particular, low amplitude pressure oscillations may result when there is a large volume of air in the tubes relative to that in the probe. With zero differential pressure applied across the transducer, these oscillations have peak to peak pressure amplitudes about .0003 cm of water. The period of oscillation is approximately one minute. These variations are believed to result due to compressibility of the gas and the constriction provided to the air as it passes through the .20 mm inner diameter holes in the probe tip from the larger diameter tubing. The motion of the air and the constriction result in pressure waves which seem to initiate from small disturbances to the tubing. As the volume of air in the tubes increases, the pressure detected at the transducer becomes more unsteady and longer decay times are required before the measurement reaches a steady state.

Ordinarily, to overcome such effects, tubing is fixed in place so that it may experience minimal vibration. Another alternative, used in the present study, is to minimize the volume of air in tubes. Flexible plastic tubing with 3.16 mm outer diameter and 2.66 mm inner diameter (commercially known as 1/8 inch Polyflow), less than 20 cm long, is employed for this purpose along with plastic adapters to connect the tubes to the male connections of the probe manifold. For differential pressures less than 0.2 cm of water, the pressure unsteadiness is then reduced considerably.

2. Transducers, Carrier Demodulators and Signal Processing

Two different sets of transducers are used to convert pressure to an electrical signal. For differential pressures less than .25 cm of water, Validyne model DP103-06 variable reluctance differential transducers are employed. For higher pressures, Celesco model LCVR variable reluctance transducers are used. A separate transducer is used to measure pressure relative to the atmosphere for each port of the five hole probe.

The five Validyne transducers each have a full scale range of .25 cm of water differential pressure, and are used to measure pressures as low as .013 cm of water or five percent of the full scale range. These devices are quite sensitive, requiring extra care as they are used,

particularly as tubing from the probe is connected or disconnected. This is done very slowly while monitoring transducer output to avoid pressure overload. Each transducer is supported in a vertical position by a plexiglass mount slightly above the probe. This mount minimizes gravitational effects, vibration and orients transducers to minimize the influence of magnetic fields from two nearby stepping motors. Shielded cables connect the transducers to Celesco CD10D carrier demodulator units. The shields extend to the transducer cases to provide a ground connection to the demodulators and significantly reduce electronic noise. Further reductions are achieved by mounting the demodulators on a thick metal plate to further isolate them from the stepping motors. The carrier demodulator units are essentially AC bridge circuits which produce a DC voltage output proportional to the pressure signal from the transducers.

The signal to noise ratio of the Validyne transducer/carrier demodulator system ranges from 100 to 5000. The amount of temperature drift for zero differential pressure is typically less than .01 volts over an eight hour period. This drift was recorded to be as high as about .1 volt, but only for one transducer. This is still quite low considering that the maximum voltage produced from a demodulator is 10 volts. Demodulators are adjusted to

maximize output voltage in order to minimize the adverse effects of zero drift and to maximize the signal to noise ratio.

The Celesco model LCVR variable reluctance differential pressure transducers are supported by the short tubes extending from the mouth of the probe. The full scale range of each transducer is 2 cm of water. Celesco carrier demodulators are again employed to convert electrical output to DC voltage. When compared to the Validyne transducers, Celesco devices have higher noise levels and for differential pressures less than .2 cm of water, more significant calibration non-linearities.

Each transducer/demodulator system is calibrated by first adjusting the zero so that the output with no applied pressure is less than .01 volts. This small offset voltage is determined from the average of 50 samples taken by the data acquisition system, recorded and then accounted for in subsequent signal processing. Next, a constant pressure, close to the value expected during measurement, is applied simultaneously to the unused orifice of the transducer and a Meriam Model 40GD10 WM 1.27 cm horizontal manometer, which can be read to an accuracy of 0.005 cm of water. A calibration coefficient is then determined to be the ratio of the manometer pressure and the difference between the average voltage and offset voltage. This procedure is repeated three times to give three calibration coefficients

which are then averaged to reduce experimental uncertainty. A typical value for Celesco transducers is 0.15 cm of water differential pressure per volt. Calibration coefficients for Validyne transducers are typically about .015 cm of water per volt.

3. Computer and Software

Each transducer/demodulator system is connected to a Hewlett-Packard (HP) 3498A extender which is controlled by a HP3497A data acquisition/control unit. The HP3497A is equipped with analog multiplexing and a digital voltmeter with 1μV sensitivity. The 3497A is controlled by a HP Series 300, Model 9836S computer, which also processes the data. The HP9836S is equipped with a MC68000, 8MHz 16/32-bit processor, dual 5½ inch floppy disk drives, and a memory of 1M bytes.

When data is acquisitioned from the probe, voltage samples are recorded sequentially from the five channels until 50 samples have accumulated for each channel. The mean and standard deviation are subsequently calculated for each channel. 100 additional samples are then recorded for each channel provided each is within three standard deviations of the current mean value. The overall sampling rate is about 5Hz.

D. PROBE CALIBRATION

1. Wind Tunnel

The wind tunnel used for probe calibration is located in the laboratories of the Department of Mechanical Engineering of the Naval Postgraduate School. It is an open circuit blower tunnel which provides uniform flow at the nozzle exit with a free stream turbulence intensity of approximately 0.1 percent at 30 m/s. Air enters the fan inlet from the surrounding air through a coarse filter. A 1.6 mm clearance between the fan and diffuser isolates vibrations from the fan to the wind tunnel body. The diffuser contains a second fine filter to remove small particles from the air as well as four baffle vanes to reduce noise and minimize the likelihood of flow separations. This diffuser is then followed by a header containing a honeycomb and three screens to reduce spatial nonuniformities. A 16:1 contraction ratio nozzle leads to the 3.05 m long, 0.610 m wide test section. The height of the top wall is adjustable. For this work, a zero pressure gradient is maintained to within 0.013 cm of water differential pressure along the length of the test section. The exit of the tunnel vents to the laboratory.

2. Calibration Sled

To set probe angles during calibration, the probe is positioned in a manually operated traversing unit manufactured by United Sensor and Control Corp. The unit has been modified to include a protractor to facilitate positioning the probe to an accuracy of 0.5 degrees over a range of yaw angles from -40 degrees to +40 degrees. The traversing device is mounted on a horizontal sled which fits on top of the wind tunnel side walls. The mounting sled can be rotated through a range of pitch angles from -45 to +45 degrees to an accuracy of 0.5 degrees. The pressure transducers rotate with the probe and are sensitive to the direction of gravity and thus the pitch angle. To account for diaphragm deflection from gravity as the transducers are rotated, a constant multiplied by the sine of the pitch angle is added to the pressure signal.

Figure 9 shows a photograph of the calibration sled mounted on the top of the wind tunnel with probe, traversing device, protractor and transducers.

3. Calibration Procedure

The probe is calibrated in the uniform free stream of the wind tunnel. The right handed coordinate system shown in Figure 6 is used. Positive yaw angles exist when the pressure at port two is greater than that at port three; pitch is considered positive when the pressure at port four is greater than that at port five.

The probe is first aligned in the wind tunnel. Zero yaw is defined to be that angle where the pressures at ports two and three are equal. The calibration sled is constructed so that at zero pitch angle, the probe mounting cylinder is vertical within 0.5 degrees. Here, the difference in the pressures at ports four and five produces a nonzero pitch coefficient, which is also used for zero pitch when measurements are made.

To obtain calibration data, the probe is manually fixed at a known yaw angle and then rotated through the pitch plane. Similar procedures are employed by Treaster and Yocum [Ref. 13] and Treaster and Houtz [Ref. 14]. A total of 25 angle combinations are used, five pitch angles at five different yaw angles. In addition to the pressures at the probe's five holes, the total and static pressures are required. The total pressure is measured with a Kiel-type total pressure probe; the static pressure is measured at the same streamwise position with a pressure tap in the side wall of the tunnel. To account for small changes in the free stream velocity, the static and total pressures are updated periodically. Typically, they vary less than 0.0005 cm of water during a three hour calibration session.

For each probe position during calibration, yaw, pitch, total, and total minus static pressure coefficients are calculated using;

$$C_{py} = (P_2 - P_3)/(P_1 - \bar{P})$$

$$C_{pp} = (P_4 - P_5)/(P_1 - \bar{P})$$

$$C_{pt} = (P_t - \bar{P})/(P_1 - \bar{P})$$

and

$$C_{pts} = (P_t - P_s)/(P_1 - \bar{P})$$

respectively. C_{pp} and C_{py} have the same form as the coefficients employed by Treaster and Yocum [Ref. 13]. New expressions for C_{pt} and C_{pts} are used to produce coefficients which do not approach zero as the yaw angle and pitch angle approach zero.

E. CALIBRATION RESULTS

Calibration coefficients are presented in Figures 10-14 for a mean speed of 1.9 m/s, which corresponds to a Reynolds number based on probe tip diameter Re_{probe} of 86. C_{py} in Figure 10 increases with yaw angle and is close to zero at zero yaw angle. Some slight dependence on pitch angle is evident. C_{pp} variation with yaw and pitch in Figure 11 shows similar behavior, except it is about equal to -.15 at zero pitch angle for all values of the yaw angle tested. In Figures 12-14 C_{pt}, C_{pts} and C_{ps} show significant dependence on yaw angle at a given pitch angle. Here,

$C_{ps} = P_1 - P_s/P_1 - \bar{P}$. The C_{pt} and C_{pts} curves are somewhat non-symmetric about zero pitch angle indicating a slightly non-symmetric probe tip.

The dependence of the yaw coefficient on probe Reynolds number is illustrated by results presented in Figures 15-18. These results correspond to mean speeds ranging from 1.1 to 5.0 m/s and Reynolds numbers ranging from 86 to 391. Except for some differences for Re~86 due to scatter resulting from measurements of extremely low pressure levels, the yaw coefficient calibration curves are repeatable with minimal scatter and are independent of Reynolds number. This includes the value of C_{py} at zero yaw angle and zero pitch angle. Other coefficients show similar behavior, in contrast to the results of Treaster and Yocum wherein the static pressure coefficient shows significant Re_{probe} dependence. The forms of the presently used coefficients were chosen to avoid this problem.

Calibration results and data reduction procedures were checked by placing the probe in the wind tunnel at known yaw and pitch angles and then determining these angles using the measurement procedures. At a mean speed of 2.7 m/s, both measured angles were generally within .3 degrees of preset angles. Differences of about .5 degrees occurred only when the yaw angle was greater than 15 degrees.

Based on a 95 percent confidence level, the uncertainties of C_{py} and C_{pp} are both estimated to be about $\pm$ .02. The uncertainty of C_{pts} is typically $\pm$.04. The uncertainties of the slopes of the yaw and pitch calibration curves are approximately $\pm$ 4.4 percent. A sample uncertainty analysis is given in Appendix B.

IV. MEASUREMENT CORRECTION PROCEDURES

Adjustments must be made to account for pressure and velocity gradients measured in a three-dimensional flow field. Two of the most important adjustments result from spatial resolution and induced downwash velocity corrections. Ligrani et al. [Ref. 16] present a detailed account of the literature reviewed and methods used to employ the corrections used in this study. The results of this study are presented in this chapter as they apply to curved channel measurements.

A. SPATIAL RESOLUTION CORRECTION

Accounting for spatial resolution of multi-hole pressure probes is necessary since different pressure ports are at different locations. The simplest accounting corrects pressures so that all appear to be measured at the same physical location. For five hole probes, if this common point is chosen to be the location of the central hole, then four pressures require adjustment.

Figure 19 illustrates how the spatial resolution scheme is applied. Here, locations of the five pressure ports are shown as the probe is moved to different z locations at a constant value of y. For this case, to simplify discussion, corrections are applied only to ports two and three. In

most real applications, the scheme is also used simultaneously for ports four and five, provided probe data are available for at least three locations in different planes normal to the wall. Spanwise gradients in total pressure appear as differences in pressures measured at ports two and three. Thus, for the situation of Figure 19, pressures from ports one, four and five are not affected by spanwise gradients. Only P_2 and P_3 require adjustment.

The correction is implemented after pressures from each of the five holes are recorded at measurement locations k=1, 2, 3, ... n. As a first step, cubic spline curves are fit to pressures measured at port two for probe positions k=1, 2, 3 ... n. The exact spanwise position of this port is used and not the location of the center hole. In Figure 19, these locations of P_2 measurement are $z_k + d$, where d is the distance between the center hole (port one) and the center position of each adjacent hole. A similar procedure is used for P_3 measured from port three, except that its locations are $z_k - d$. One smooth curve is constructed for each port, each of which is then used to calculate the value of P_2 and P_3 at the location of port one. In Figure 19, these pressures are designated $P_{2,k}$ and $P_{3,k}$, and evaluated at locations z_k and fully corrected to account for finite spatial resolution. They may then be used to calculate the yaw coefficient for determination of the yaw angle at location z_k. If pressures from ports 4 and 5 had been

corrected to give $P_{4,k}$ and $P_{5,k}$, then these pressures could then be used to calculate pitch coefficients for pitch angle determination at z_k.

With this approach there are no adjustable coefficients. Required are y and z locations of port one and d, the distance between port one and the center of the other probe pressure ports. For the custom-made miniature probe, d = .041 cm. The scheme assumes that pressures vary smoothly without significant discontinuities between pressure port locations and measurement locations. At the end points of any traverse, satisfactory results may be obtained by extrapolation. For optimal accuracy, in the present study, endpoints are discarded after interpolation for their neighbors is completed.

This scheme is physically more realistic than others which employ streamwise velocity gradients as a basis to account for spatial resolution. Finite spatial resolution is caused by variations of pressure, and thus, pressures must be corrected and not velocities or velocity gradients.

B. INDUCED DOWNWASH VELOCITY CORRECTION

The downwash velocity is part of induced secondary flow which occurs as a result of the blockage of blunt bodies within transverse gradients of mean streamwise velocity. Young and Maas [Ref. 17] show that velocities measured in

boundary layers using flat-faced pitot probes correspond to positions farther from the wall than where the measurements are actually made. Livesey [Ref. 18] obtains similar results for flat-faced probes, but finds that apparent streamline displacement depends strongly on probe shape. Lighthill [Ref. 19] describes a theoretical model for flow around a sphere in a uniform velocity gradient. He finds that the displacement of the stagnation streamline is caused by downwash velocity near the sphere with flow from regions of high streamwise velocity to regions of lower streamwise velocity. He also confirms earlier work showing that downwash velocity can be quite significant and depends strongly on the shape of the probe. For multiple hole probes that are used to determine flow direction as well as speed, the induced downwash velocity, if uncorrected, causes larger errors than displacement of the stagnation streamline.

After pressures and pressure coefficients are corrected for effects of finite spatial resolution, the velocity distribution is determined as described in Chapter 5. With this velocity field in the computer memory, adjustment for downwash velocity effects can proceed.

The present correction for induced downwash velocity is based on the work of Lighthill [Ref. 19]. He shows that $D/(a'dU/ds)$ is of the order of one near a sphere. Here, a' is the sphere radius, and D is the induced downwash velocity

in the s direction, which is normal to the direction of U. dU/ds is the gradient of the U component of velocity with respect to the s-direction. For probe tips, downwash velocities in the normal and spanwise directions may be estimated using;

$$D_y = \frac{dU_x}{dy} a'E_y \qquad \text{and} \qquad D_z = \frac{dU_x}{dz} a'E_z$$

where a' is the probe tip radius and dimensionless quantities E_y and E_z are coefficients which depend on probe geometry. These may be different from each other, especially for non-axisymmetric probe tips. In the present study, however, these two coefficients for the normal and spanwise directions are assumed to be the same and equal to E. Normal and spanwise velocity components U_y and U_z corrected for the effects of downwash velocity are then given by;

$$U_y = U_{yu} + \frac{dU_x}{dy} \Delta \qquad \text{and} \qquad U_z = U_{zu} + \frac{dU_x}{dz} \Delta$$

where $\Delta = a'E$. In the above two equations, U_{yu} and U_{zu} represent velocities uncorrected for the downwash effect. dU_x/dy and dU_x/dz are determined by fitting U_x with cubic spline curves in the y and z directions. The cubic splines are differentiated analytically and the values of the derivatives at every measurement point are then calculated.

In the present application, the final velocity components are corrected by numerically fitting the cubic splines and differentiating them. The corrected velocities are stored to be used for later plotting and vorticity computations.

V. CURVED CHANNEL MEASUREMENT AND QUALIFICATION

This chapter describes measurement procedures and channel qualification tests which are presented by Ligrani et al. [Ref. 10, 17]. Portions of these articles are presented here as they apply to this study.

A. MEASUREMENT PROCEDURES AND APPARATUS

1. Traversing Mechanism

When measurements are made in the channel, the probe is oriented using a mount attached to a travelling block which is part of an automated two-dimensional traversing mechanism. The set-up is shown in Figure 20. The travelling block moves in the spanwise and radial directions. These parts are driven by 20-thread per inch drive screws and guided by ground steel, case-hardened support shafts. The drive screws are rotated by Superior Electric type M092-FD310 stepping motors. These motors are controlled by a MITAS Motion Controller, which directs the movement of the probe according to instructions from the HP9836S computer by means of an RS232C data interface.

The mount used to orient the probe is also evident in Figure 20. This mount consists of two collars. The first may be rotated relative to the radially mounted travelling block to allow the pitch angle of the probe to be set relative to the channel flow. A second collar is attached to the probe by means of a set screw, which allows the yaw angle of the probe to be adjusted. Changes to the yaw angle as small as ±.1 degrees and to the pitch angle as small as ±.5 degrees are possible with this mechanism.

2. Measurement Procedure

The probe is positioned and aligned before measurements are made. The probe is first inserted into the channel at a spanwise location 5.08 cm from the centerline so that part just touches the concave wall. Then it is visually aligned with the flow and subsequently moved to the channel centerline using the MITAS controller. Small adjustments to the probe yaw angle and pitch angle are now made using the probe mount to obtain a zero yaw coefficient and a small pitch coefficient. A bulk flow velocity of 0.3 m/s is used for alignment since flow here is in the streamwise direction and minimal secondary flows are present. The low speed also means that the pressure differences between the ports are small, hence there is some scatter in the pitch and yaw coefficients. The final orientation of the probe gives a yaw coefficient of 0.0 ±0.01 and a pitch coefficient of -.60 ± .01. This is

equivalent to +4.5 degrees offset accounting for the pitch coefficient of -.15 obtained during calibration alignment. More accurate pitch alignment forces the probe against the edge of the slot, hence the pitch offset is corrected during data reduction. No offset is applied or needed for the yaw angle.

In a typical spanwise/radial plane traverse, the probe moves in the radial direction from the concave wall to the convex wall as measurements are made. To begin measurements at a new spanwise location, the probe first moves 0.254 cm in the spanwise direction, then in the reverse span direction 0.127 cm, and finally toward the convex wall until it is .254 cm away. A new radial measuring traverse then begins. This procedure is used for positioning to reduce the adverse effects of backlash and give repeatable data regardless of the direction of spanwise probe motion.

When measurements are made at a particular location, 150 samples of each pressure are averaged. This is done by sampling pressure signals from probe ports in sequence so that a longer averaging time is provided for each channel, thereby minimizing the influence of short duration unsteadiness in the channel. For each probe location, about two minutes of acquisition and processing time is required. A traverse over an entire plane requires about

eight hours. The entire process is computer controlled and generally performed at night when there is minimal unsteadiness at the channel inlet resulting from laboratory disturbances.

3. Data Reduction

Measure pressures from each probe port are stored by the computer until an experiment is completed. These data are then corrected to account for the effect of finite spatial resolution using procedures described in Chapter 4.

The next step is to determine the values of C_{py} and C_{pp} for each location using measured pressures. A four step procedure is used to determine the yaw angle and the pitch angle. First, a preliminary pitch angle p′ is calculated using;

$$p' = 9.8\ (C_{pp} + 0.15) - p_{off}$$

This equation provides a reasonable fit to pitch angle calibration data such as that shown in Figure 11 for a mean velocity of 1.9 m/sec. Here, p_{off}=4.5 degrees, the pitch angle offset resulting from the probe mount. Referring to yaw angle calibration data in Figure 10, the second step requires the determiniation of a preliminary yaw angle y′ by interpolation using p′ and the measured value of C_{py}. In the third step, pitch angle is determined using the measured value of C_{pp} and y′, again interpolating from results such as the ones presented in Figure 11. The final pitch angle p is then determined by subtracting p_{off}. In the

fourth step, the final yaw angle y is determined from C_{py} and p by interpolating results such as those in Figure 10.

Now that the yaw angle and pitch angle are known, C_{pts} is computed using a double linear interpolation procedure. A plot of C_{pts} versus yaw angle and pitch angle at a mean speed of 1.9 m/s is shown in Figure 13. Knowing C_{pts}, the total velocity magnitude U is determined using;

$$U = (2\ C_{pts}\ (P_1 - \bar{P})/\rho)^{\frac{1}{2}}$$

where ρ is the fluid density. This approach gives less uncertainty for U than one which employs two separate coefficients for the total pressure and static pressure (i.e. Treaster and Yocum, [Ref. 14]). The total pressure relative to atmospheric pressure P_{amb} at each measurement location then follows using;

$$P_{amb} - P_t = (P_{amb} - \bar{P}) - C_{pt}\ (P_1 - \bar{P})$$

C_{pt} is obtained using a double linear interpolation scheme from results such as the ones given in Figure 12. A coefficient for static pressure C_{ps} is not used for data reduction. The three velocity components are subsequently given by;

$$U_\theta = U \cos(\text{yaw}) \cos(\text{pitch})$$

$$U_r = U \sin(\text{yaw})$$

$$U_z = U \cos(\text{yaw}) \sin(\text{pitch})$$

In the final phase of data reduction, corrections are made to account for the downwash velocity correction as described in Chapter 4.

B. CHANNEL QUALIFICATION TESTS

In order to qualify the performance of the curved channel, a number of tests were conducted. Many of these tests are explained in detail by Ligrani and Niver [Ref. 9] and are summarized here.

Turbulence intensity levels were measured at the nozzle exit using a horizontal hot-wire probe. The probe was mounted normal to the flow direction and operated in the constant temperature mode. At a Dean number of 290 (local mean velocity of 3.4 m/sec) a turbulence intensity of 0.0006 was measured. At a Dean number of 450 (local mean velocity of 5.2 m/sec) a turbulence intensity of 0.001 was measured.

A miniature Kiel probe was used to ensure that the geometry of the channel at the measurement slot was uniform. The Kiel probe provides an accurate measure of total pressure when flow vectors are misaligned as much as 40 degrees from the probe tip. The diameters of the shield and pressure port of this probe are 1.59 mm and 0.4 mm. The same traversing mechanism and procedure is used for Kiel probe measurements as was described for the five hole probe. The Celesco 2 cm transducer was used to obtain measurements with the Kiel probe. Results of total pressure measurements relative to ambient pressure for a Dean number of 54 are shown in Figure 21a.

Several different tests were made to determine the effects of perturbations on the flow field. Blockages of as high as 50 percent of the inlet nozzle did not appear to disturb the measurements taken at the 120 degree location or cause flow visualization results at any point in the curved section to be different. The effect of slight non-symmetries or discontinuities were checked by temporarily deforming the convex and concave walls of the channel or placing a strip of tape near the nozzle exit. No changes to the flow were noted for Dean numbers less than 200. It was found that leaks of any size, particularly upstream of, and near the location of measurement points would have a significant effect on measured results. Unsteadiness forced on the flow by moving objects or laboratory personnel around the nozzle entrance also had an effect on measured results. To minimize the effect of unsteadiness on experiments, they were run at night when there was little activity in the laboratory spaces.

C. FIVE-HOLE PROBE QUALIFICATION

In order to qualify the behavior of the miniature five hole pressure probe, the total pressure distribution was measured and compared with measurements from the miniature Kiel probe. Total pressure measurements for a Dean number of 49 are shown in Figure 21b. Comparison with the Kiel probe measurement (Figure 21a) shows excellent agreement

providing evidence of accurate five hole probe alignment and measurement procedures. Comparison is made at this Dean number since minimal secondary flows are present and because gradients of mean streamwise velocity are very small in the spanwise direction. For the data presented in Figure 21a, 40 spanwise locations and 8 vertical ones are used with a resolution of 0.127 cm. The measurement area begins 0.127 cm from the concave wall, 5.08 cm from the channel centerline and extends to 0.254 cm from the convex wall, 10.16 cm from the channel centerline.

D. SPATIAL RESOLUTION AND DOWNWASH VELOCITY CORRECTION APPLICATIONS

Figure 22 shows measurements of streamwise velocity after corrections are applied, plotted at three radial traverse locations and compared to Curved Channel Poiseuille Flow (CCPF) profiles. Equations for CCPF are given by Finlay et al., [Ref. 1]. The measurements were taken at a Dean number of 36 and are generally in excellent agreement with the CCPF profile for this Dean number. Small differences may be attributed to scatter caused by the extreme difficulty in measuring the low pressure levels associated with these velocities.

Another example of the application of pressure and velocity corrections is now presented. At a Dean number of 100, secondary flow velocities are reasonably steady and

spanwise periodic. The velocity field thus has pressure gradient in both spanwise and radial directions.

Figure 23a shows contours of streamwise velocity. This distribution depends only weakly on the corrections. Figure 23b shows secondary velocity vectors when no corrections are made. Velocity vectors point away from regions of high streamwise velocity to lower speed regions. Such behavior is present for radial and spanwise components and is physically unrealistic, especially near surfaces. Figure 24a shows secondary flow vectors from the same flow after the pressures are corrected only for spatial resolution. These vectors are substantially different from those in Figure 23b, even though vectors near walls still point away from the regions of high streamwise velocity. The largest vector in Figure 23b is .14 m/s, whereas the largest vector in Figure 24a is .10 m/s. In Figure 24b, both spatial resolution and downwash corrections are applied. Here, the value of Δ employed in the induced downwash velocity corrections is .025 cm or .4a'. Velocity vectors follow expected behavior. Well defined vortices are evident and vectors show no consistent tendency to point into walls or away from regions of high streamwise velocity. Secondary flow vectors indicate upwash from the concave to the convex surfaces over the same areas where streamwise velocity deficits are present in Figure 23a.

VI. POWER SPECTRA APPARATUS AND PROCEDURES

Spectra of voltage fluctuations from hot-wire anemometers which resulted from velocity fluctuations at the hot-wire probe tip are now presented. Measurements were made by inserting a subminiature or conventional horizontal hot-wire into the curved channel at the 110 degree streamwise location. These hot-wire probes were mounted through a plug in the channel side wall and aligned so that wires were sensitive to streamwise and spanwise flow components in the case of the horizontal wire, or to all three flow components in the case of the subminiature crossed-wire probe. The hot-wires were mounted on the centerline between the concave and convex walls so that the wires were 9.60 or 9.92 cm from the channel side wall. Flow visualization has shown that this is an adequate distance to avoid side wall effects. A photograph of the horizontal wire probe mounting is shown in Figure 25.

A. PROBES AND MEASUREMENT CHAIN

1. Hot-Wire Probes

The primary device used for spectral measurements was the subminiature crossed-wire probe. This was chosen to take advantage of the excellent spatial resolution associated with this type probe. This hot-wire was

manufactured at NASA Ames Research Center using fabrication techniques discussed in Westphal et al. [Ref. 20] and Ligrani and Bradshaw [Ref. 21]. The crossed-wire probe is manufactured of 90% platinum / 10% rhodium wire with a nominal diameter of 0.625 microns and a length of about 200 microns.

The horizontal hot-wire probe used is a DANTEC type 55P05. This probe is fabricated of platinum plated tungsten and has a diameter and wire length of 5 microns and 1.25 mm respectively. The horizontal wire was used to determine velocity fluctuations averaged over a much wider portion of the channel depth than the subminiature wire and, in some cases, resulted in slightly different spectra than from the subminiature wire.

Checks were made to assure that no vortex shedding from hot-wires existed to affect power spectra. H. Schlichting [Ref. 22, pp. 28-32] presents a relationship between the Strouhal number and Reynolds number. Knowing the Reynolds number, one can determine the frequency of vortex shedding off of the wire, if it exists. Even when the diameter of the large wire and the maximum velocity measured are considered, the wire diameter Reynolds number for the present study is less than one, which indicates that there is no vortex shedding off of the hot-wire filaments. As an additional check, vortex shedding off of the prongs supporting the wire filament was investigated. For the

large hot-wire the maximum Reynolds number attained is 4.9. Based on these calculations, it was determined that there is no vortex shedding off of the prongs.

2. Signal Measurement

The continuous signal from either hot-wire was sent to a DANTEC 55M10 CTA Standard Bridge via a five meter coaxial cable. The bridge was operated in the constant temperature mode. The subminiature hot-wire sensor has much higher resistance than a standard hot-wire. Due to this, the DANTEC bridge was modified by adding a 2000 ohm metal-foil resistor at the location of the .09 ohm setting resistor. Recalibration of the bridge against an ohmmeter indicated that 98.90 ohms should be added to the bridge reading when the decade controller was switched to the .09 ohm position. Adjustment of cable impedence was accomplished by setting the cable compensator to the 5 m position. For subminiature hot-wire measurements, the bridge gain was set at "1". For the conventional horizontal wire the bridge gain was set at "2". Subminiature wire and conventional wire sensors were used at an overheat ratio of 1.2 and 1.5 respectively.

A DANTEC 56N20 Signal Conditioner was employed to filter and amplify the hot-wire signal. The HF filter was set to 0.1 Hz in all cases to remove the DC signal. To prevent aliasing, the LF filter was set at 100 or 300 Hz, depending on the frequency range being investigated. Gain

settings were maximized depending on the type of wire and flow rate. Typically, a gain of 100 was used with the subminiature wire at all flow conditions. A gain of 500 was used with the conventional wire at Dean numbers less than 120. Above this flow rate a gain of 100 was used.

Output from the DANTEC Signal Conditioner was sent simultaneously to signal processor equipment and a PRECISION model 1476A 10KHz oscilliscope. The oscilliscope was used to help determine the frequency ranges that should be investigated.

For the 1.25 mm wire, the time response of the sensor-bridge combination was adjusted by using the square wave test function of the bridge. Using an overheat ratio of 1.5, a response time of 12.5 μsec was achieved. Photographs of the probe measurement chain equipment are shown in Figures 26a and 26b.

B. SIGNAL PROCESSING AND ANALYSIS

Two different methods were used to obtain spectra of signals from the hot wire sensor. The first of these was a Hewlett-Packard high speed data acquisition system with accompanying Fast Fourier Transform software. The second method employed was a Scientific Atlanta real time signal analyzer. The two methods were used simultaneously to check software and to identify spectral variations from digital and electronic noise.

1. High Speed Digital Acquisition and Analysis

A HP6944A Multiprogrammer mainframe unit was used for digital processing of the hot-wire time domain signal. This utilizes a four channel HP69755A FET high speed data acquisition card in conjunction with a HP69750A scanner control card. Each channel has a maximum sampling rate of 25 KHz. One channel operation is used for our purposes. A HP69759A 500 KHz, 12 bit analog to digital converter digitizes and passes data via HP14717A buffered ADC cable and HP69791A 64K RAM to the HP9836S computer. Data is gathered and sent to the computer as blocks of 2048 integer data points. A complete sampling of data consists of sixteen blocks of data. The acquisition of data, including acquisition rate, is controlled by the computer using parameters input by the user. The digitized time signal is stored on floppy disk for analysis at a later time.

The time domain signal is transformed to frequency domain using a Fast Fourier Transform routine adapted from Brigham [Ref. 23]. The transform and acquisition software were written in BASIC 4.0 by Dr. B.A. Singer. The FFT reads and processes each of the sixteen blocks data separately and ensemble averages the sixteen blocks. The Hanning Window weighting parameter is used to treat the side lobes for each block of data. Before plotting, the amplitude of the signal is converted to normalized power as ($Volts^2/Hz$) so that the

integral of the power over the frequency range is one. The digital processing equipment and transform were tested using a DYNASCAN model 3010 Function Generator.

2. Real Time Signal Analysis

For real time analysis of the hot-wire signal, a Scientific Atlanta (Spectral Dynamics Division) SD380Z Signal Analyzer was used. The SD380Z is a four channel, microprocessor based signal analyzer. The analyzer was used in the spectrum mode of display with the trigger set for "free run". This allows data acquisition at the maximum rate depending on the frequency resolution used. For the 800 line frequency resolution used, this equates to a sample size of 2048 bits of data sampled at 10 KHz. The Hanning Window FFT weighting parameter was chosen so that both methods of signal analysis could be compared. Similarly, data was plotted as $Volts^2/Hz$ vs. Hz. Blocks of transformed data were ensemble averaged over the maximum of 999 ensembles. A HP7470 plotter was used with an IEEE 488 interface to plot the spectra display. The advantage to using this signal analyzer is that it allows for much faster processing and display of spectral plots which allows a large number of frequency ranges to be investigated in a short time. Data is presented in Chapter 8 using both real time signal analysis and the HP/DAS-FFT system. It is evident from the plots (Figures 75-120), that the systems produce nearly identical results.

VII. FLOW VISUALIZATION APPARATUS AND PROCEDURES

Flow visualization photographs were obtained to illustrate the qualitative behavior of Dean vortices. Both the radial-spanwise plane and the exterior of the channel (viewed from the outer, or concave side) were observed and photographed. Equipment and methods used are presented below.

A. SMOKE GENERATOR

Rather than using the wood-burning generator used by Niver [Ref. 7], a commercial fog/smoke generator was employed. This device was selected because it is safer, more compact and more convenient than the wood burning smoke generator. The commercial generator is a ROSCO model 1500 Fog and Smoke Machine, which uses ROSCO Fog/Smoke Fluid, a mix of glycols of low molecular weight. The fluid is drawn into the smoke generator, heated to near its vaporization point and atomized by forcing the fluid through an orifice. The smoke is then pumped into an inlet plenum and injected into the entrance of the channel through 1.27 cm inside diameter tubes. The smoke plenum was designed to provide laminar jets of smoke at the entrance of the curved channel.

The best method for using the smoke generator for flow visualization was to inject a puff of smoke into the channel entrance and then turn the smoke generator off. After a period of time a steady stream of smoke could be viewed at the location to be photographed. Generally, pictures could be taken over about a ten second period. The amount of smoke injected into the channel was increased as the Dean number was increased.

B. CAMERA AND LIGHTING

1. Radial-Spanwise Plane Photographs

Radial-spanwise plane photographs were taken using generally the same equipment and procedures as described by Niver [Ref. 7] and Ligrani and Niver [Ref. 9]. Here, Kodak T-Max 400 film was used. The Nikon F3 camera body and 55 mm, f2.8 lens were used with a Nikon MD-4 motor drive and a Nikon MT-2 intervalometer. Best results were obtained with an aperature setting of f4.0, a shutter speed of 60, and an ASA of 1600. All photographs were taken in sequence with the intervalometer set for a pulse time of 0.1 seconds, an interval time of 0.1 seconds and in the repeat mode. The total time between photographs is 0.2 seconds. A schematic of the setup used for photographs of illuminated radial-spanwise planes is shown in Figure 27 [Ref. 7].

2. Concave Surface Exterior Photographs

Photographs were taken from the outside of the concave surface at locations encompassing the 50-80 degrees, 80-110 degrees, and 110-140 degrees streamwise positions. The photographs were also taken in sequence using the same intervalometer settings as mentioned above. Color Trans lighting was used instead of an automatic flash for surface illumination. The best results were obtained using Kodak T-Max 400 film and ASA set at 1600. The aperature and shutter speed were adjusted manually for different lighting conditions. Typical settings were f4.0 and a shutter speed of 30.

Photographs were taken as the camera viewed one-half of the channel width, after adjusting the camera and lighting. After a photograph sequence was taken at one Dean number, the Dean number was increased and a pause of at least sixty seconds was taken in order to allow any disturbances from the flow rate adjustment to decay. After a range of Dean numbers was photographed at one streamwise location, the camera and lighting system were repositioned to the next downstream location and the photograph sequence was repeated.

VIII. RESULTS

This chapter presents measured mean velocities, mean vorticity distributions, power spectra and photographs of flow visualization. All results from this study were obtained for Dean numbers from 40 to 230. The three mean velocity components and the three components of mean vorticity were determined from pressure measurements. All of these pressure measurements were taken 120 degrees from the start of curvature in a radial-spanwise plane 5.08 cm to 10.16 cm off the channel centerline. Spectra of velocity fluctuations were obtained at the channel centerline using a subminiature crossed hot-wire probe 110 degrees from the start of curvature at locations 9.60 and 9.92 cm from the side wall of the channel. Flow visualization photographs were obtained at the same spanwise-radial plane as the pressure measurements and also with the camera viewing the concave surface of the channel from the channel exterior.

This chapter is subdivided into four sections. Part A contains a review of previous studies of flow in channels with a geometry similar to ours. Part B presents results of five hole pressure probe measurements. Part C presents the results of hot-wire measurements of velocity fluctuations. Part D presents flow visualization photographs taken for this study.

A. PREVIOUS STUDIES

A previous investigation of high aspect ration (40:1) curved channel flow with a radius ratio of .979 was made by Kelleher et al. [Ref. 5]. These authors measured variations of velocity with spanwise direction using a hot-wire at Dean numbers from 79 to 113 at a location 135 degrees from the start of curvature. Results for different radial positions showed significant variations of velocity providing evidence of spanwise periodic vortices.

Finlay et al. [Refs. 1, 8] developed computational simulations of curved channel flow by means of three-dimensional integrations of the incompressible Navier-Stokes equations. To this author's knowledge, this is the only previously published work which includes a detailed description of the structural characteristics of Dean vortices. Results from Finlay's work indicate that instabilities in curved channel flow sometimes cause Dean vortices to develop with different types of superimposed travelling waves. Undulating Dean vortex flow is found above a critical Dean number of 35.92, but is not fully developed for streamwise distances less than one circumference. Due to this, and the fact that travelling waves associated with undulating Dean vortex flow have long streamwise wavelengths, undulating Dean vortex flow is difficult to detect experimentally. As Dean number increases, a second type of instability causes twisting Dean

vortex flow. Travelling waves associated with twisting Dean vortex flow have a much shorter wavelengths than undulating Dean vortex flow. Twisting Dean vortices are non-symmetric and fully developed for $De > 2.5\ De_{cr}$ and streamwise distances less than π radians. [Ref. 1]

Ligrani and Niver [Ref. 9] describe results from a flow visualization study of curved channel flow. These experiments were conducted in the same channel as the present study. Figure 28 shows a series of photographs taken by these authors at the 115 degree streamwise location where the concave surface is on the bottom and the convex surface is at the top of each photograph. The left hand side of the photographs is 10.16 cm from the channel centerline. The width of the area in the photograph spans 5.08 cm. Flow upwash regions (from concave to convex wall) are seen as narrow "stems" of mushroom shaped smoke patterns. The broad "petals" on either side of the upwash region contain fluid which is being forced outward and away from the convex wall. The first photo shows the initial development of a flow instability at De=53. From De=73 to De=100 mushroom shaped smoke patterns evidence pairs of vortices which increase in radial height with Dean number. These vortices are also considered to be symmetric which means that the two vortices in each pair are similar. Some non-symmetry is evident at De=90 which may be caused by partially developed undulating Dean vortex flow or a

transient disturbance passing through the channel. At De=123 the vortex pairs become non-symmetric. The vortices also appear to twist in the spanwise and radial directions. This "rocking" motion, characteristic of twisting Dean vortex flow, is more noticeable as flow rate increases. Eventually, for Dean numbers greater than 192, the mushroom shaped patterns evidencing vortex pairs are not recognizable. Significant Dean vortex patterns are also seen as streamwise location changes.

B. SURVEYS OF MEAN VELOCITY AND MEAN VORTICITY COMPONENTS

Each contour plots found in Figures 29 through 58 are taken from an 8 by 40 grid of data points spaced .0127 cm apart. The Y/d axis in these plots is opposite in direction to the R axis previously defined (Figure 1). The Y/d axis and the Z/d axis are normalized by the channel height, d, so that Y/d = 0 represents the concave surface and Y/d = 1 represents the convex surface. Z/d is measured with respect to the channel centerline.

1. Total Pressure and Streamwise Velocity Distributions

Total pressure measurements normalized by P_{mean} are given in Figures 29-31 for De=36-201, where P_{mean} is an average of the maximum and minimum pressure differentials measured. A graph of these maximum and minimum pressures measured at each Dean number is presented in Figure 32. This figure shows that the range of total pressures measured

increases nearly linearly with respect to Dean number. Streamwise velocity measurements in Figures 33-35 are normalized by $\overline{U}$, where $\overline{U}$ is the same mean velocity used to calculate the Dean number.

a. De=49 - De=64

Figures 29 and 33 show results for De=49 - 64. Here, a spatially uniform, undisturbed flow is evident at the lower De. As flow rate increases, areas of low pressure and low streamwise velocity develop near the concave wall. Flow visualization photographs taken at this same location [Ref. 9] show a uniform layer of smoke which develops a "wavy" appearance along the concave surface as Dean number increases.

b. De=64 - De=86

Figures 29 and 33 show pressure and velocity variations as the flow rate changes. Here, the areas of low pressure and velocity nearly extend to the full channel height. Gradients of pressure and velocity appear to be more spanwise periodic at De=73.48 and 86.24 than at De=64.49. For Dean numbers in this range, Ligrani and Niver indicate the presence of spanwise periodic, mushroom shaped smoke patterns. These are symmetric vortices and are not all the same height. The low pressure/low streamwise velocity regions correspond to secondary flow upwash regions from the concave to the convex wall.

c. De=95 - De=137

For the Dean number range from De=95.52 to 137.0, Figures 30 and 34 show low pressure, low velocity areas which are not spanwise periodic. Flow visualization for the same conditions (Figure 28) shows that mushroom shaped smoke patterns are full height relative to the channel depth. These pairs of vortices are non-symmetric and have a slight unsteady "rocking" motion.

d. De=137 - De=201

Figures 31 and 35 show that as Dean number increases, time-averaged measurements of pressure and velocity indicate that the flow is spanwise uniform. Simulations [Ref. 1] and flow visualization [Ref. 9] indicate that vortices are still present for these Dean numbers but are much more unsteady, especially in the spanwise direction, than at lower Dean numbers. Because of the amplitude and period of this unsteadiness, time-averaged results show gradients only in the radial direction.

2. Velocity Perturbation Measurements

Curved Channel Poiseuille Flow (CCPF) is present when flow in the curved channel is two-dimensional and laminar, without secondary flows. This type of flow exists for Dean numbers less than 35.92. CCPF profiles differ from straight channel Poiseuille flow velocity profile in that the maximum velocity is shifted slightly closer to the concave wall. Figures 36 through 38 show plots of the

difference between measured streamwise velocity and mean velocity from the CCPF solution. The CCPF solution for streamwise velocity, U(CCPF), is obtained by determining the mass flow rate (and $\bar{U}$) from measured data and matching this $\bar{U}$ to the CCPF velocity profile. The data is plotted here, using U_θ - U(CCPF) normalized by $\bar{U}$. This illustrates perturbations to CCPF caused by time-averaged secondary flows.

Figure 36 shows that at De=49.27, the measured flow is nearly spanwise uniform. As flow rate increases to De=53.2 and De=57.5, perturbations in the form of streamwise velocity deficits and surpluses are evident. Locations of velocity deficits match locations of the low pressure/velocity upwash regions shown in Figures 29-35.

The radial position of the peak velocity deficit at De=53.2 (Figure 36) is $Y/d \simeq 0.3$. The U_θ - U(CCPF) results from simulations [Ref. 1:pp. 17-18] at De=44.18 show that the radial position of the peak deficit is at Y/d=0.25. As Dean number increases, our data shows that this radial position of the peak velocity deficit moves toward the convex wall. At De=137.0 the peak velocity deficit is centered at $Y/d \simeq 0.5$.

At Dean numbers greater than 137.0 (Figure 38) contours of velocity deficits and surplus magnitudes become more spanwise uniform. This is consistent with the spanwise

uniformity seen in the pressure and velocity data previously presented for the same Dean numbers.

3. Mean Vorticity Distributions

Streamwise, radial and spanwise components of mean vorticity were determined from distributions of the three mean velocity components. Figures 39 through 62 present results from these vorticity calculations. Vorticity values at each point are obtained by numerically differentiating velocity values with respect to radial or spanwise distance. Streamwise vorticity, ω_θ, radial vorticity, ω_r, and spanwise vorticity, ω_z are given by;

$$\omega_\theta = \frac{\partial u_z}{\partial r} - \frac{\partial u_r}{\partial z}, \quad \omega r = \frac{\partial u_\theta}{\partial z}$$

and

$$\omega_z = \frac{\partial u_\theta}{\partial r}$$

respectively. Since measurements were taken in a single radial-spanwise plane, velocity changes with respect to streamwise distance were not included and assumed to be small. In the vorticity contour plots of this section, areas of negative vorticity are shown as dashed lines and areas of positive vorticity are shown as solid lines.

a. Streamwise Vorticity

Streamwise vorticity contour plots are shown in Figures 39 and 40. At the lower Dean numbers (53.2-64.49), there are no distinct patterns of positive or negative

vorticity. Pressure/velocity measurement contour plots (Figures 29-35) for Dean numbers between 53.2 and 64.5 show disturbances to the flow that appear as spanwise non-periodic low pressure/velocity areas near the concave surface. As mentioned, flow visualization for these conditions shows a wavy smoke layer developing along the concave wall.

Figures 39 and 40 show that, as the flow rate increases, areas of positive and negative vorticity are present as represented by circular-shaped contour lines. From De=95.52 to De=126.3 these vorticity regions are seen as concentric circles with higher magnitudes of vorticity closer to the center of the circles. At this same Dean number range, Figures 30 and 34 show that areas of low pressure/velocity extend across the depth of the channel. If vorticity and pressure/velocity plots are compared at each Dean number, it can be seen that the areas of positive and negative vorticity lie on either side of the low pressure/velocity regions.

Figure 40 shows that, as the Dean number increases to De=137.0, peak magnitudes of vorticity decrease. At De=141.6 and De=146.1, the data shows little or no evidence of streamwise vorticity. Here, time-averaged pressure and velocity distributions are spanwise uniform due to unsteadiness in the flow.

To further evaluate the effect of flow rate on mean streamwise vorticity measurements, magnitudes of peak vorticity are plotted against Dean number. These plots are shown in Figures 41-44. Here, a vortex pair is considered to be the portion of an ω_x contour plot with a negative vorticity area just to the left of an area of positive vorticity. Typically, three vortex pairs, which will be referred to as the left, middle and right pairs, are evident in each contour plot. Peak vorticity is then defined as the average of the absolute values of peak positive and negative vorticity. The left and right vortex pairs (Figures 41 and 43) show little, if any relationship between peak vorticity and Dean number. Figure 42 shows that, for the middle vortex pair, peak vorticity values increase as flow rate increases for $40 < De < 130$. Thus, the strengths of the vortices appear to vary across the measurement plane. Figure 44 shows the average for all three vortex pairs wherein peak vorticity increases slightly with Dean number. In all four plots, peak vorticity values decrease above De=126.3 due to time-averaging and significant unsteadiness in the flow.

Vortex circulation, Γ_x, is plotted as a function of Dean number in Figures 45-48. Streamwise circulation is calculated by summing streamwise vorticity values over an area of positive or negative vorticity and multiplying this sum by $(.0127\ cm)^2$, where .0127 cm is the spacing of the

data. The value of Γ_x plotted is the average of the absolute values of positive and negative circulation. In general, circulation appears to increase with Dean number up to De=126.3. Above this Dean number circulation values decrease. Figure 48 shows that, when circulation is averaged over the entire measured area, it increases with Dean number up to De=126.3, after which the time-averaged measurements then decrease with Dean number.

b. Radial Vorticity

Figures 49 through 51 show contours of radial vorticity over the spanwise-radial plane of measurements. Since the U_θ component of mean velocity is measured with better accuracy than other components, radial vorticity measurements are more accurate than streamwise vorticity measurements. As a result, adjacent positive and negative radial vorticity contours provide particularly clear indications of Dean vortices. According to Finlay et al. [Ref. 1:pp. 62-63], the locations of radial vorticity maxima and minima might also identify locations of shear layer instabilities.

Figures 49 through 51 show undisturbed flow up to De=57.5. At De=57.5 relatively low-level radial vorticity magnitudes are present on the right hand side of the contour plot. As Dean number increases up to 137.0, radial vorticity for each vortex pair increases. At Dean

numbers greater than 137.0, no time-averaged radial vorticity is evident due to unsteadiness in the flow.

Figures 52-55 show peak radial vorticity values plotted against Dean number. Similar to streamwise peak vorticity values, measurements for the left, middle and right vortex pairs are plotted separately. Peak radial vorticity magnitudes for the entire measured are plotted in Figure 55. Here, as before, peak vorticity is defined as the average of the absolute values of peak positive and negative vorticity. In contrast to peak streamwise vorticity data, peak radial vorticity increases with Dean number at about the same rate for all three vortex pairs for Dean number up to 126.

c. Spanwise Vorticity

Figures 56 through 58 show the development of spanwise vorticity over the range of Dean numbers where measurements were made. Vorticity contours at De=36.6 - De=53.2 are spanwise uniform. At higher Dean numbers, negative vorticity contours move closer to the convex surface at the locations of vortex upwash. Between these upwash areas, positive vorticity contours move closer to the concave wall. These vorticity contours clearly indicate that the location of maximum streamwise velocity is close to the convex surface at vortex upwash locations. The time-averaged vorticity measurements taken above De=141.6

indicate a spanwise uniform flow. This is consistent with the high Dean number measurements previously discussed.

Figures 59 through 62 show the changes in peak spanwise vorticity magnitudes with Dean number. As with the other vorticity components, the three vortex pairs are evaluated separately and together. Peak positive and negative vorticity magnitudes are plotted separately for each vortex pair. Peak negative vorticity values increase with Dean number at a faster rate than peak positive vorticity. Above De=126.3, peak positive vorticity values continue to increase with Dean number while peak negative vorticity values decrease.

4. Detailed Pressure and Vorticity Measurements

Figures 63 through 74 show detailed plots of secondary flow vectors, mean vorticity components, total pressure differentials and streamwise velocity. The maximum secondary flow vector size is shown in the bottom left hand corner of the vector plots. Axes of the plots are normalized as previously described. This data was obtained by traversing the five hole pressure probe using the same methods as for the larger area plots but with thirteen radial positions and thirty spanwise positions. The spacing between the data points is .076 cm in both radial and spanwise directions.

a. De=77.9

Secondary flow vectors at this Dean number (Figure 63a) do not show a distinct pattern of secondary flow except for the upwash region near the center of the plot. Vorticity, $P_{total} - P_{ambient}$, and streamwise velocity data (Figures 63b-65) are similar in quality to previously presented plots of data taken at De=73.5 and De=86.2.

b. De=102.2

Secondary flow vectors (Figure 66a) show three secondary flow upwash regions from concave to convex surfaces. Figures 67a,b show that the low pressure/low velocity region near the center of the plots coincides with an upwash region. Vorticity plots (Figures 68a,b) indicate that the vortex pair is symmetric with respect to the upwash region.

c. De=119.0

Secondary flow vectors shown in Figure 69a clearly show a vortex pair. Streamwise vorticity contours plotted in Figure 69b show that these vortices lie on either side of the upwash region. Total pressure and streamwise velocity contours (Figure 70) show that the low pressure/ velocity region extends from the concave to convex walls. Radial and spanwise vorticity plots (Figure 71) indicate that this vortex pair is slightly non-symmetric with respect

d. De=131.6

These plots (Figures 72-74) show upwash regions from two vortex pairs. From the secondary flow vectors, it to the flow upwash. This data agrees with flow visualization taken at De=123 (Figure 28) which shows smoke patterns leaning to one side.
is evident that upwash velocity is much greater than downwash velocity. Total pressure, velocity and vorticity plots all indicate that the flow disturbance on the right side of the measured area is less intense than the disturbance on the left side.

C. SPECTRA OF HOT-WIRE SIGNAL MEASUREMENTS

To obtain information on the nature of unsteadiness in Dean vortex flow, hot-wire voltage fluctuations resulting from velocity fluctuations were analyzed. Spectra obtained from Fourier transforms of time-domain signals indicate the frequencies of different modes of oscillations in the flow. Measurements were taken over the Dean number range of 40 to 200 using both the subminiature crossed-wire probe and a conventional horizontal-wire probe. Measurement techniques are described in Chapter 6.

Oscillations or unsteadiness in the flow contribute to energy levels seen in spectral plots. If the flow measured is steady, no spectral energy will be apparent. Flow oscillations at a specific frequency will result in a relatively sharp spectral peak at that frequency and

harmonics at multiples of that frequency. If vortices oscillate over a range of frequencies, relatively broad spectral peaks and their harmonics will be evident.

The effect of background electronic noise was evaluated by collecting data with no flow in the channel. Results indicate the presence of sharp spectral peaks with principals and harmonics of 60 Hz. This background noise is the result of signals picked up from the power supply and signal processing equipment. These spectral peaks are generally four to five orders of magnitude less than spectral peak amplitudes with flow.

In order to select frequency ranges of interest for different flow conditions, a frequency range of 0-1000 Hz was first examined at all flow conditions. From this initial investigation, it was determined that two frequency ranges should be used at different flow rates. For Dean numbers from 40 to 114, the 0-40 Hz range was used. For Dean numbers from 120 to 160, both the 0-40 Hz and 0-300 Hz frequency ranges were employed. At Dean numbers from 165 to 200, the 0-300 Hz range was studied.

1. De=40 - De=114

Spectra and time traces for Dean numbers ranging from 40 to 114 are presented in Figures 75-89. From De=40 to De=80, the highest energy level is measured at 2 Hz. Additional broad spectral peaks are seen at 8 Hz, 14 Hz, and two pairs at 18-22 Hz and 28-32 Hz. Sharp spectral peaks

seen in the digital spectral plots at 20 and 40 Hz are attributed to digital processing "noise". These same sharp peaks are not seen in the real-time spectral plots. Because so many events seem to be contributing to spectral energy, it is impossible to indicate which peaks are due to principal oscillations and which peaks are harmonics. Ligrani and Niver [Ref. 9] observed both radial and spanwise vortex oscillations in this flow range. The vortices they observed generally do not span the full height of the channel and vary in height when compared to one another.

Above De=80, Figures 83-89 show that an additional spectral peak appears at about 12 Hz. The amplitude of this peak increases as Dean number increases up to De=114. Ligrani and Niver have shown that in this same flow range, Dean vortices are nearly full channel height and appear to be relatively steady.

2. De=120 - De=160

Figures 90-101 present spectra and time traces for De=120 to De=160 at 0-40 Hz. As flow rate increases, the spectral peak that was seen at 12 Hz has decreased in amplitude. At De=130, the 28-32 Hz pair of spectral peaks has also decreased in amplitude. A single broad peak at 30 Hz is now evident. At De=140 to De=160 there are no spectral peaks which stand out relative to background energy levels. Subminiature and conventional-sized hot-wires yield similar results for this frequency range.

Figures 102-109 present spectra and time traces for De=120 to De=160 at 0-300 Hz. Relatively sharp, narrow spectral peaks seen at 60, 120, 180 and 240 Hz are due to background electronic noise. In this frequency range, subminiature and conventional hot-wire sensors yield different results. This difference is evident in Figures 104-105 and Figures 106-107, which show spectra taken at De=140 and De=152/153 respectively. Spectra taken when the conventional wire is employed show broad spectral peaks not evident when the subminiature wire is employed. These differences may be due to flow interference or disturbances caused by the larger sensor. The differences might also be due to the fact that the larger wire senses velocity fluctuations over a larger area of the flow.

Flow visualization observations at this Dean number range [Ref. 9] indicate that Dean vortices are nearly full channel height and begin to develop a "rocking" motion. Finlay, et al. [Ref. 1, 8] describe this flow phenomena as twisting Dean vortex flow.

3. De=165 - De=200

Figures 110-120 present spectra and time traces for De=165 to De=200. Hot-wire spectra in the De=165 to 200 range were taken from both subminiature and conventional-sized sensors, and both sensors give similar results. At De=165 to De=175, Figures 110-113 show broad principal and harmonic spectral peaks at about 60 and 120 Hz. At De=180

(Figures 114-115) a second harmonic is evident at about 180 Hz. These principals and harmonics are believed to result from twisting Dean vortex flow.

Figures 116-120 show that, as the Dean number increases above De=184, the principal and harmonics previously seen decrease in amplitude. At De=200 no spectral peaks are evident.

Flow visualization observations [Ref. 9] indicate that vortex pairs are twisting and are non-symmetric for this Dean number range. Temporal power spectra from simulations of fully developed twisting Dean vortex flow [Ref. 1:pp. 50-51] show principal and harmonics spaced about 60 Hz apart.

D. FLOW VISUALIZATION

Flow visualization photographs are presented in Figures 121 through 134. All photographs for a particular Dean number and location were taken in sequence 0.2 seconds apart. For the radial-spanwise plane photographs, the top of each photo represents the convex wall and the bottom the concave wall. The right side is 5.08 cm off the channel centerline. For the exterior view photographs, the left side of the photos represent the channel centerline and the right side is the channel side-wall. Streamwise distance increases from top to bottom of each exterior view photograph.

1. Radial-Spanwise Plane

Figure 121 presents four photograph sequences taken in the radial-spanwise plane. The white smoke was injected close to the bottom of the channel inlet and remains along the bottom of the 2.44 m straight section as it enters the test section. In the curved section, the smoke remains along the convex surface until it is disturbed. Because of this method of injecting smoke, flow disturbances originating along the convex surface contain much denser smoke than disturbances originating near the concave surface [Ref.9:p. 13].

Figure 121a presents a sequence of five photographs taken at De=51.9. These photographs show a disturbance of the flow along the concave surface. This wavy smoke layer is neither spanwise periodic or steady. The disturbances appear to move in both the spanwise and radial directions.

Figure 121b presents a sequence of four photographs taken at De=64.4. These photographs show mushroom-shaped smoke patterns which oscillate in the radial and spanwise directions. The smoke patterns are, in addition, not all the same height.

Figure 121c presents a sequence of four photographs taken at De=95.4. Here, the mushroom-shaped patterns are spanwise periodic and relatively stable. When individual

smoke patterns are distorted, they all appear to lean or distort in the same spanwise direction.

Figure 121d presents a sequence of three photographs taken at De=107.7. Here, the mushroom-shaped smoke patterns indicate vortices that are nearly full channel height. Distortion in the smoke patterns indicates unsteadiness in the flow, possibly due to a transient disturbance.

2. Exterior View - Concave Surface

Figures 122 through 134 present photographs of a portion of the exterior concave surface of the channel. These photographs are shown in the sequence they were taken, clockwise from upper left. The secondary flow evident in these photographs appears as tubes of smoke. These tubes of smoke surround vortex pairs which are relatively void of smoke [Ref. 9:pp. 22-23]. These photographs do not show clear evidence of any type of travelling wave superimposed on the flow. It is evident however, that the tubes of smoke are not always spanwise periodic. In many sequences, an apparent merging or splitting of vortex pairs is seen, probably as a result of vortex pair destruction and creation. Shortly after this activity, the vortex pairs tend to retain their "normal" spanwise spacing.

IX. SUMMARY AND CONCLUSIONS

The development and structural characteristics of Dean vortices in a curved channel were measured and evaluated. Methods employed for experiments include the use of a miniature five hole pressure probe, a subminiature crossed hot-wire probe and flow visualization photography.

The five hole pressure probe was developed specifically for use in the curved channel. Its qualification included calibration in a wind tunnel and the development of spatial resolution and induced downwash velocity correction schemes. Pressure measurements were used to determine the three mean velocity components of Dean vortex flow. From these, the three components of mean vorticity were also determined.

Pressure measurements show that, at low Dean numbers, spanwise non-periodic disturbances develop near the concave surface of the channel. Above De=57.5, vortices were measured and vorticity levels calculated. It was determined that vortex pairs tend to become spanwise non-periodic as Dean numbers increases above De=95. Levels of vorticity increase as Dean number increases, until steady vortices caused by twisting Dean vortex flow are present. Because the length scales of the spanwise unsteadiness are greater than spanwise vortex spacing for De > 140, pressure measurements show gradients only in the radial direction.

Hence, at these Dean numbers pressure measurements do not resolve local spatial variations due to twisting Dean vortex flow.

Velocity fluctuations caused by unsteadiness in Dean vortex flow were measured with a subminiature crossed-wire hot-wire as well as with a conventional horizontal hot-wire. Spectral analysis of these fluctuations indicate that, at relatively low Dean numbers (De=40 - De=114), several low frequency modes of vortex oscillation are present. For De < 90-100 these are associated with partially developed Dean vortex flow. As Dean number increases greater than 160, spectra show a principal peak and harmonic peaks, evidencing the presence of twisting Dean vortices. These measurements above De=160 compare favorably with the results of simulations conducted using similar flow conditions.

Dean vortex flow was observed using flow visualization techniques. The characteristics of pairs of Dean vortices appears to be strongly affected by the local small disturbances which initiate vortex development. When smoke patterns are viewed from the outside of the concave surface, they appear as tubes of smoke, each of which surrounds a vortex pair. Because of new development and destruction of vortex pairs, these occasionally appear to merge and split. Before and after such activity, a specific spanwise spacing seems to be maintained.

APPENDIX A

FIGURES

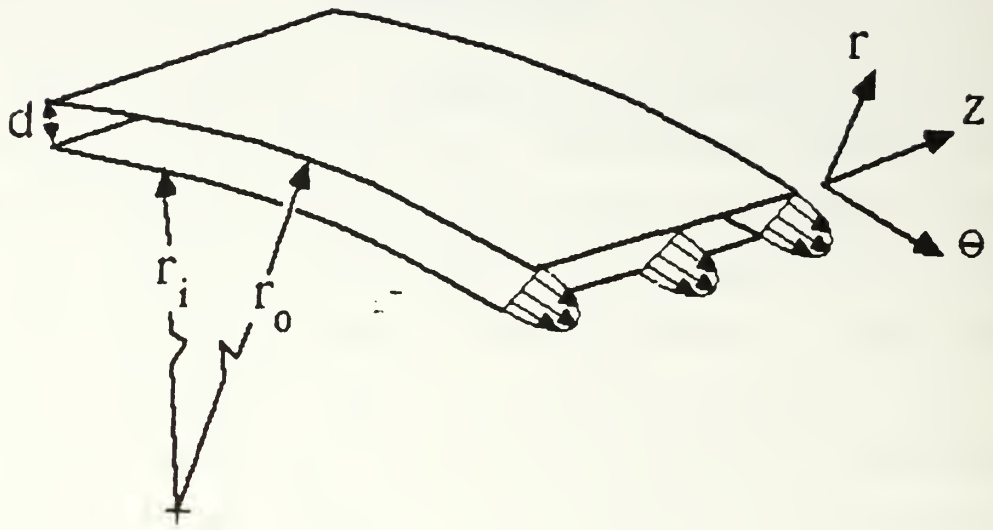

Figure 1. Curved Channel Geometry

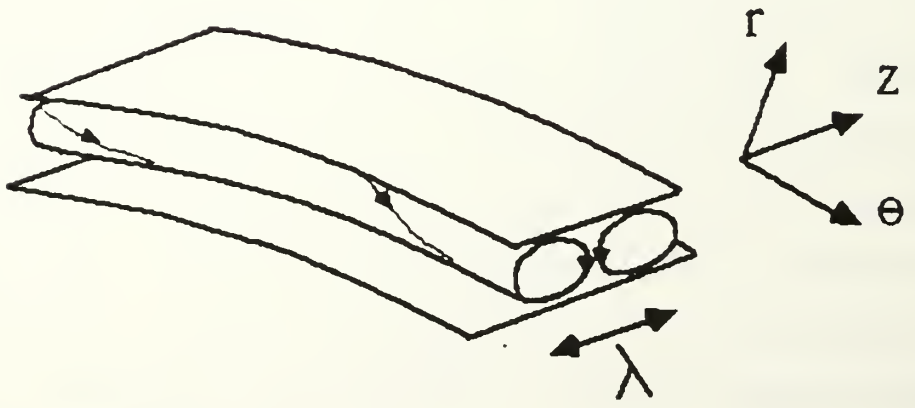

Figure 2. Schematic of One Dean Vortex Pair

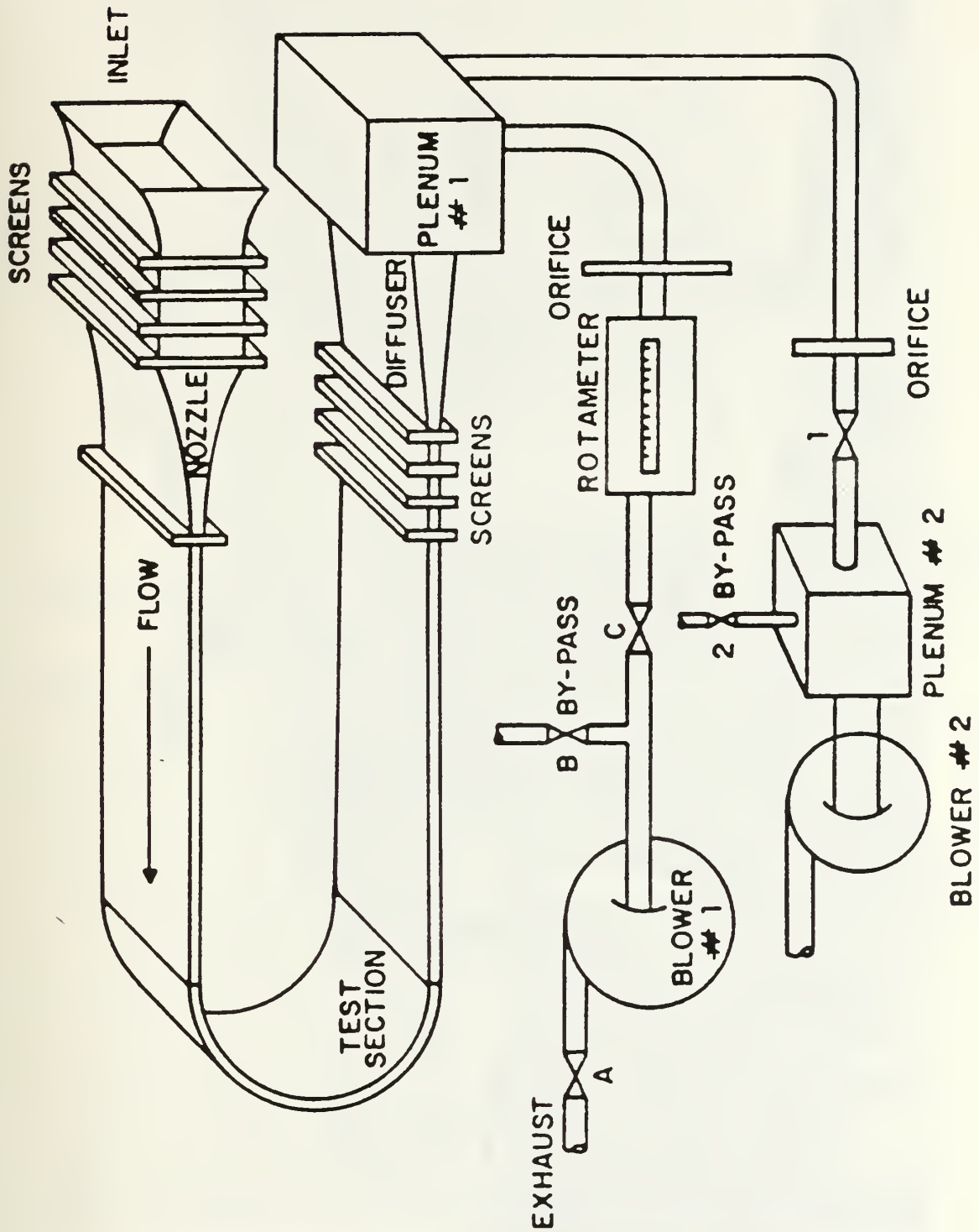

Figure 3. Schematic of Test Facility

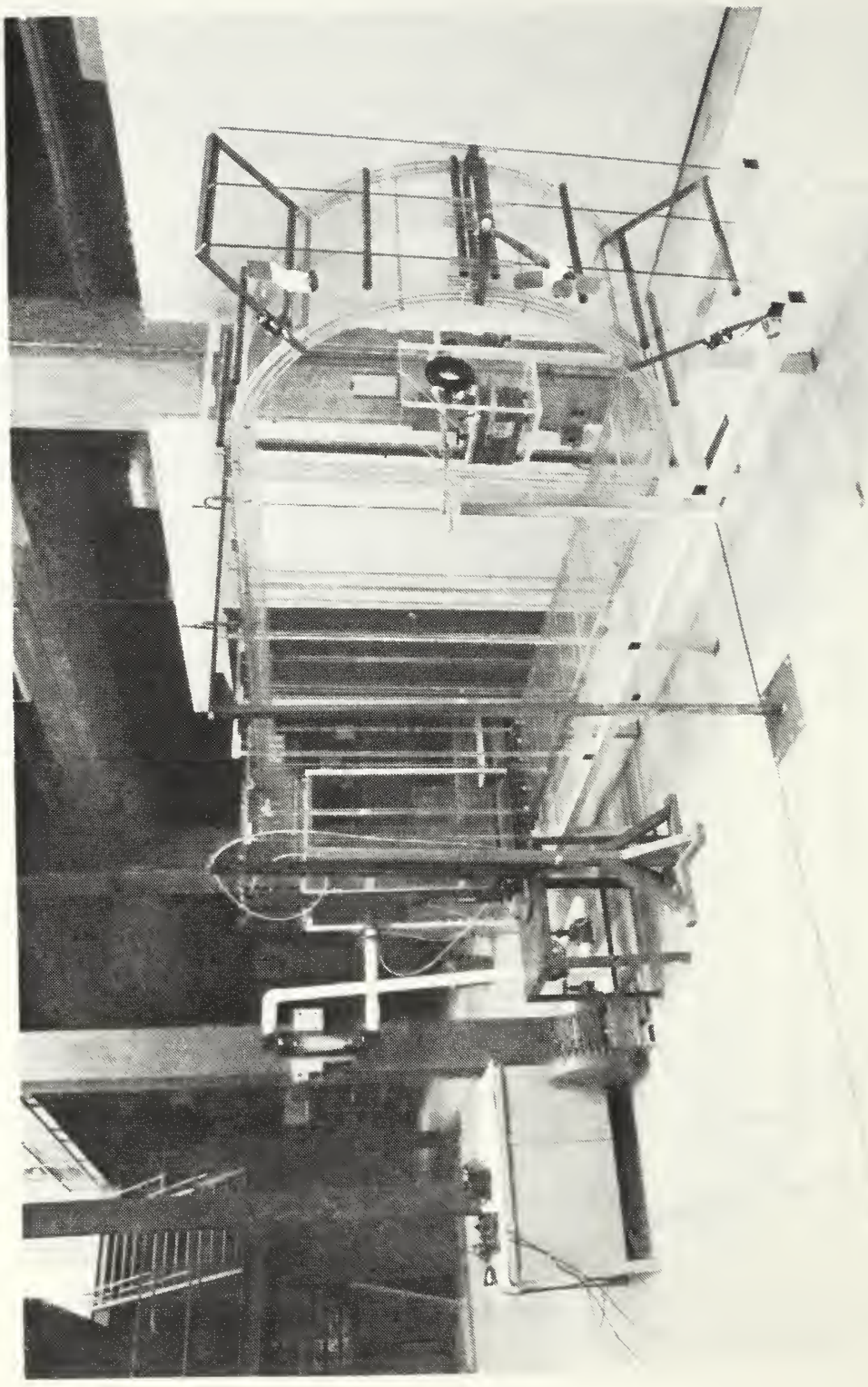

Figure 4. Test Facility (Side View)

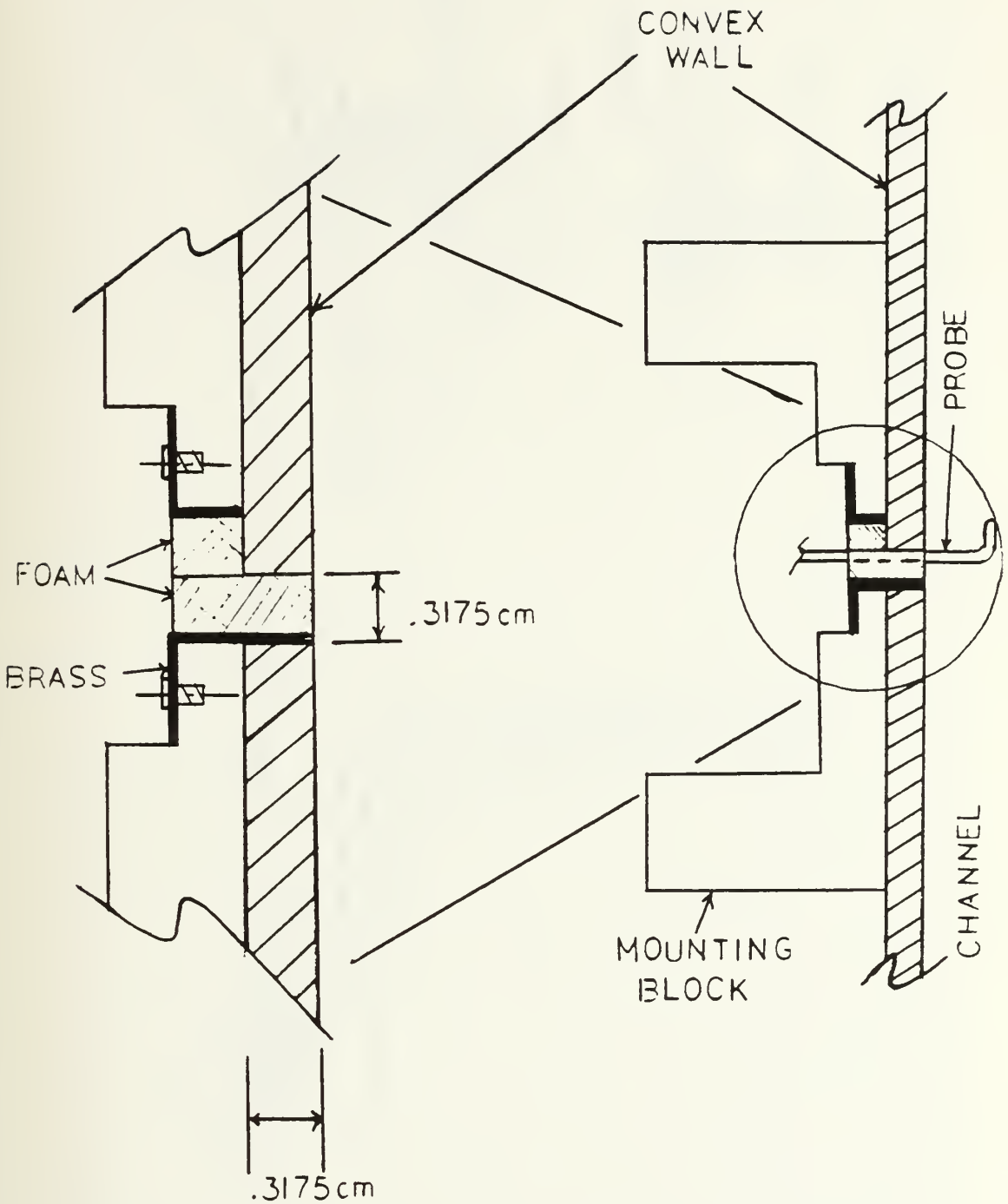

Figure 5. Schematic of Support Block

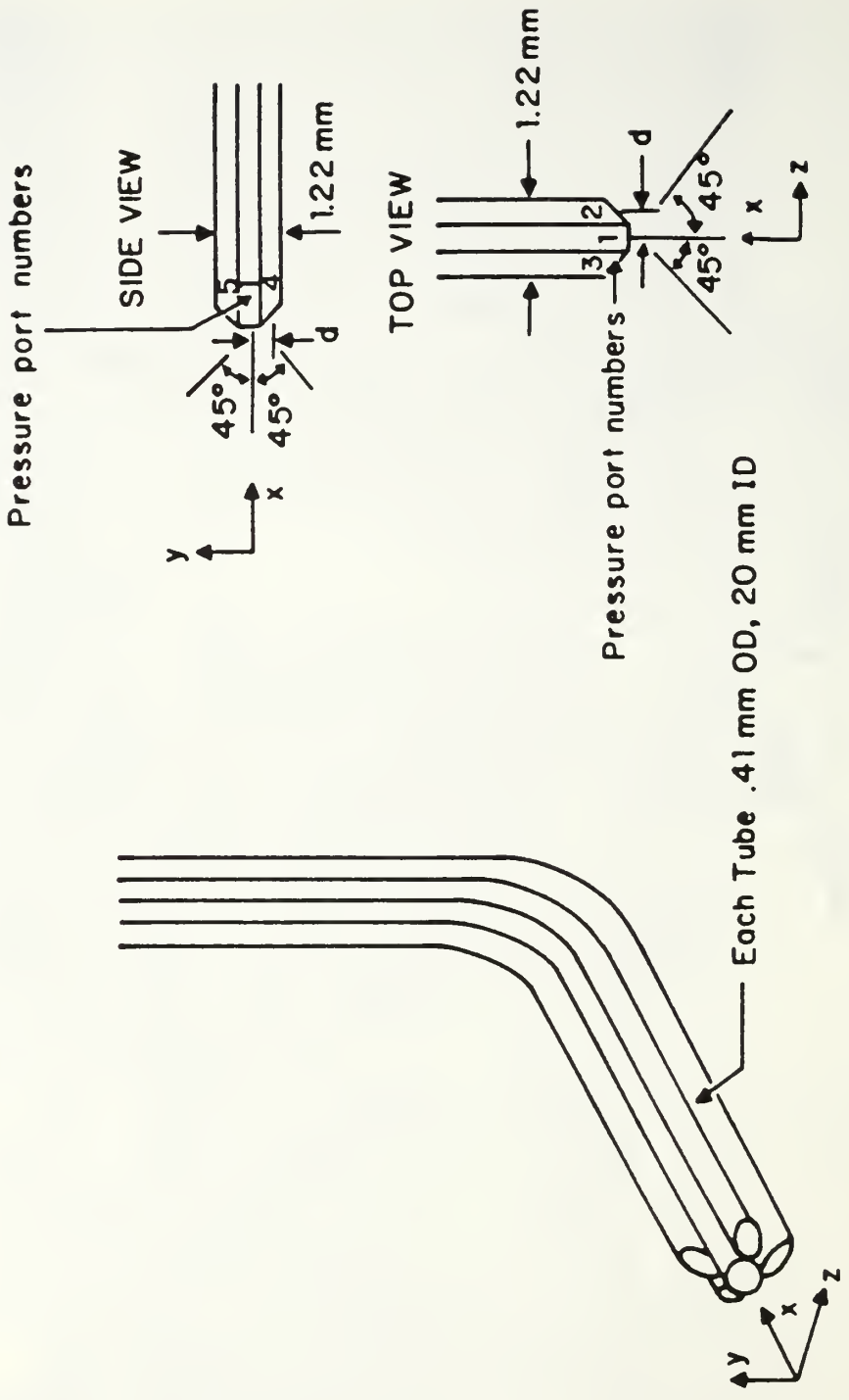

Figure 6. Five Hole Pressure Probe Geometry

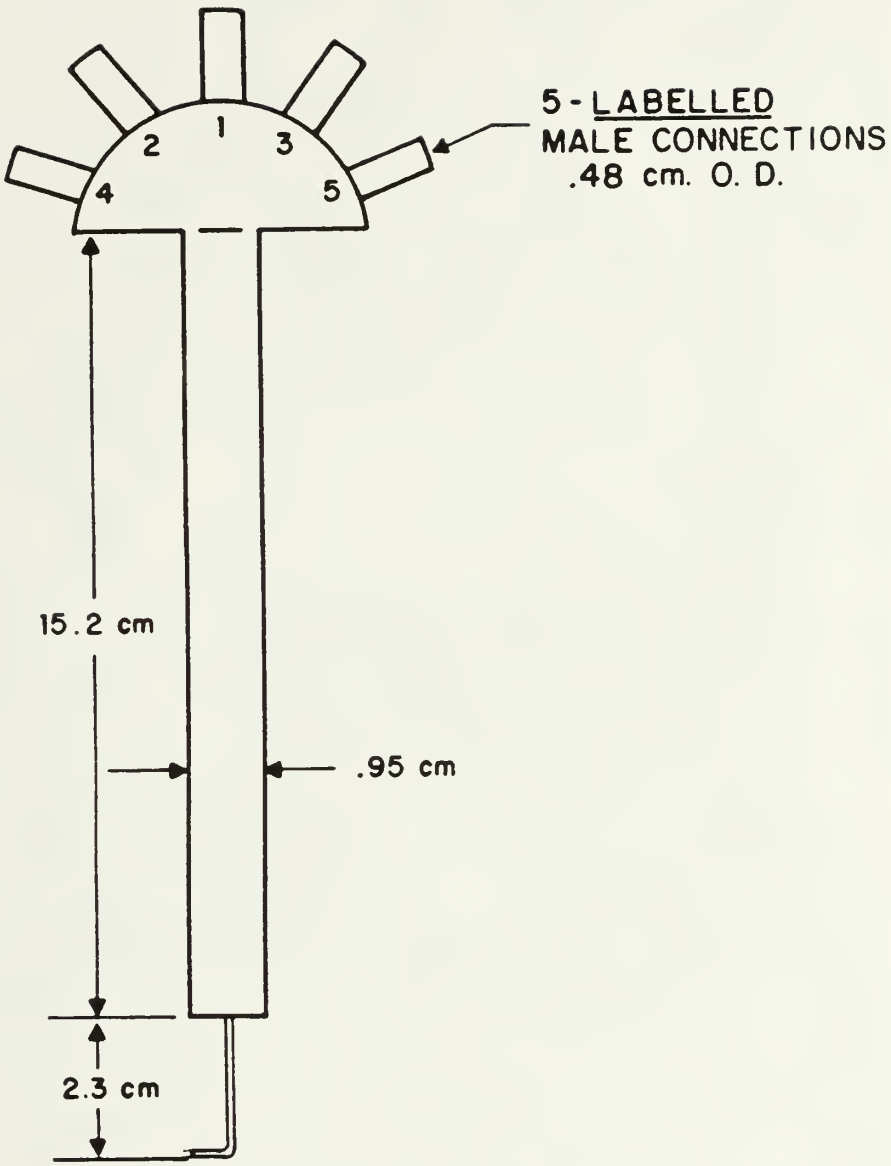

Figure 7. Five Hole Pressure Probe

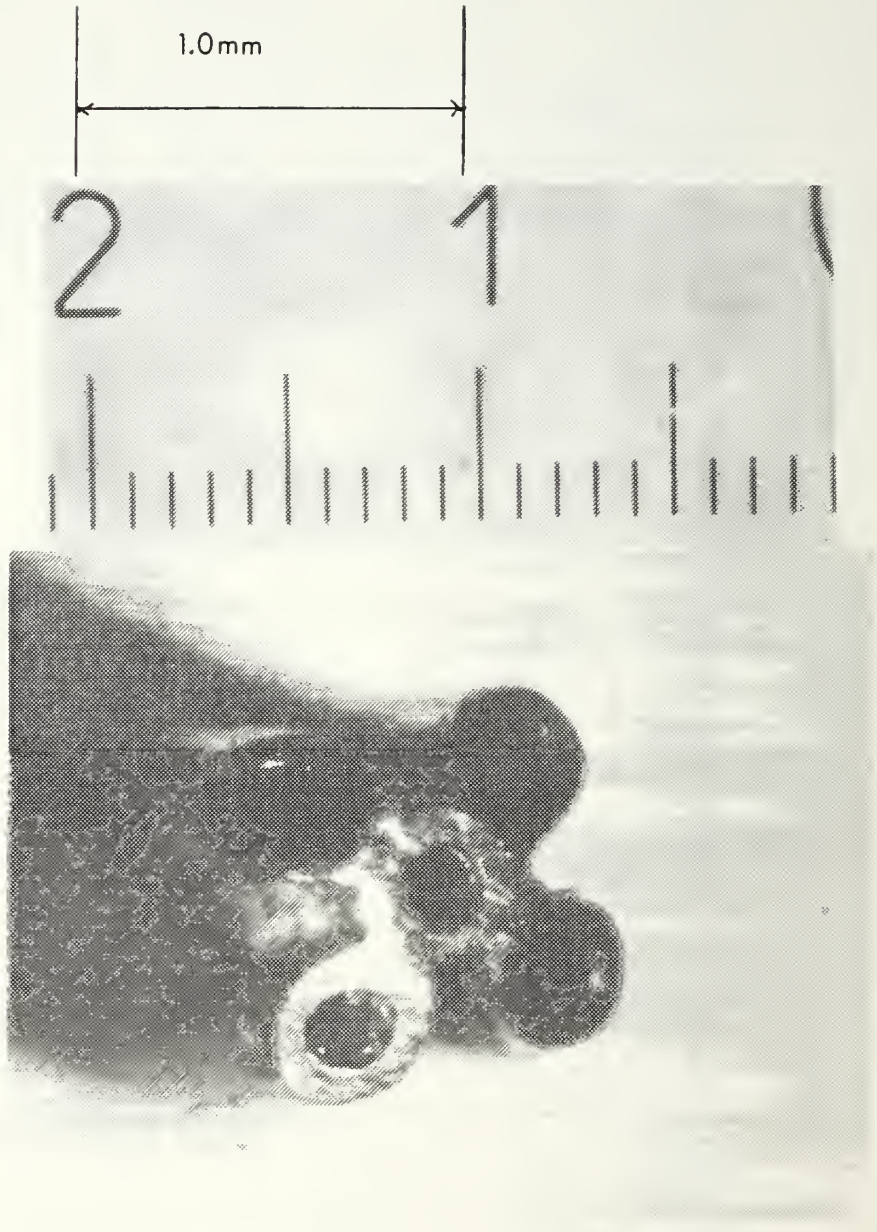

Figure 8. Five Hole Pressure Probe
100μm Between Scale Markings

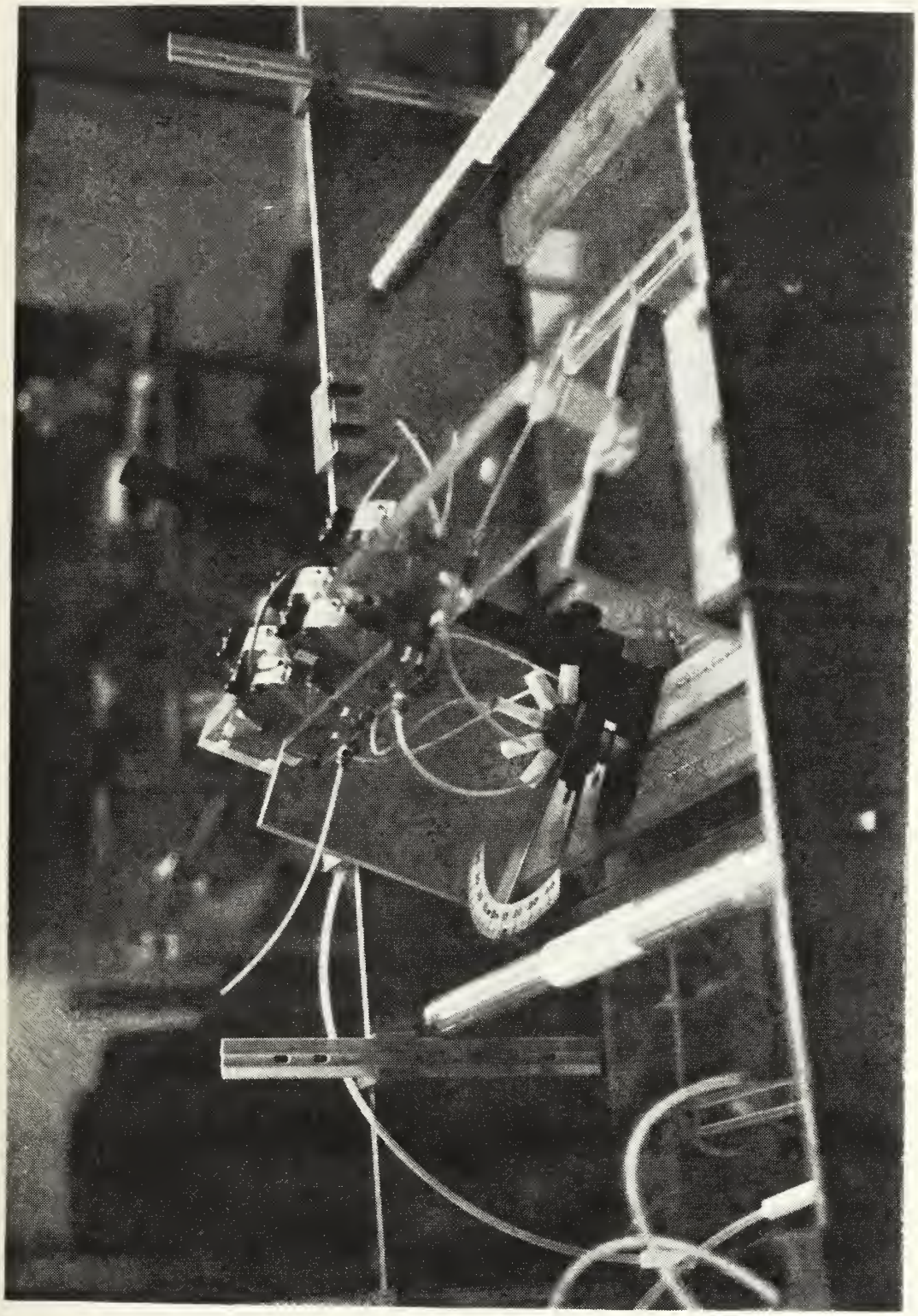

Figure 9. Pressure Probe Calibration Sled

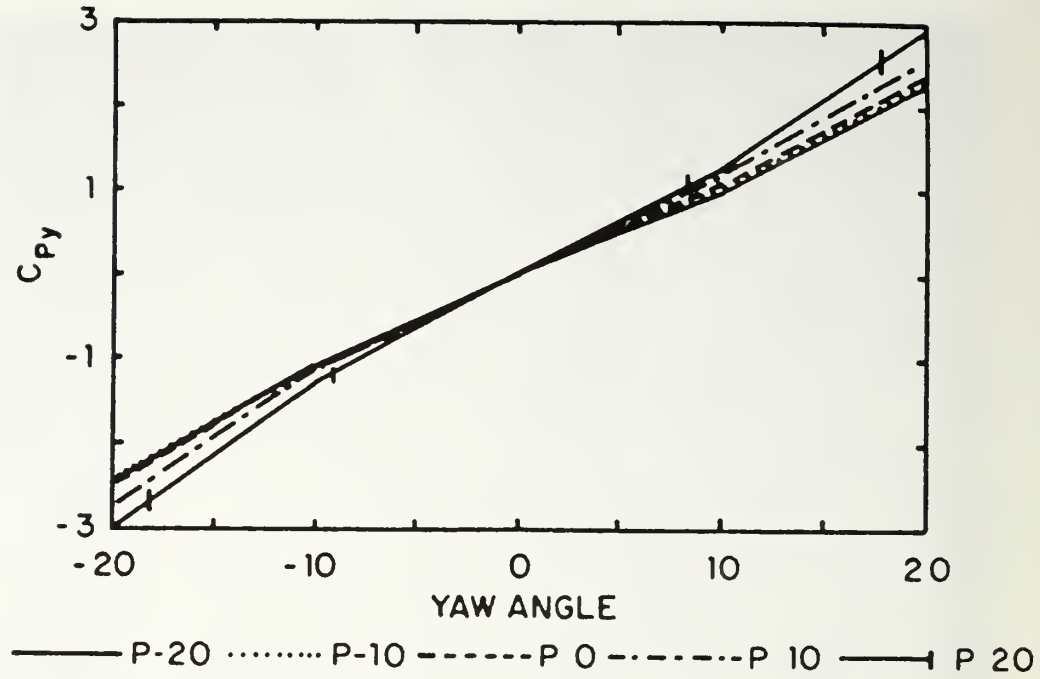

Figure 10. C_p Yaw vs. Yaw, 1.9 m/s

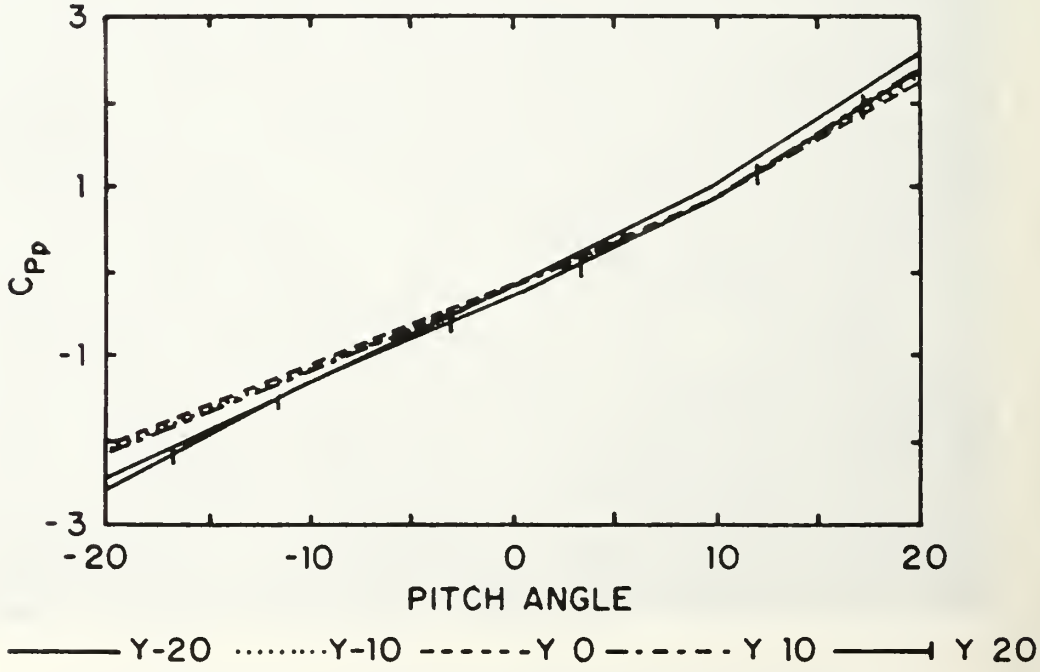

Figure 11. C_p Pitch vs. Pitch, 1.9 m/s

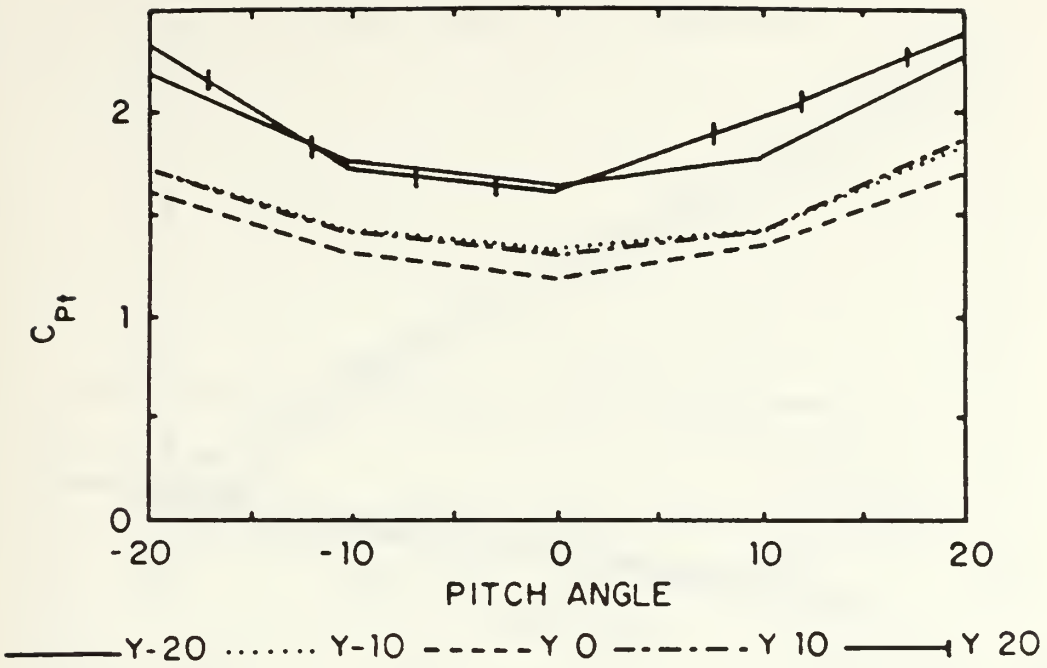

Figure 12. C_p Total vs. Pitch, 1.9 m/s

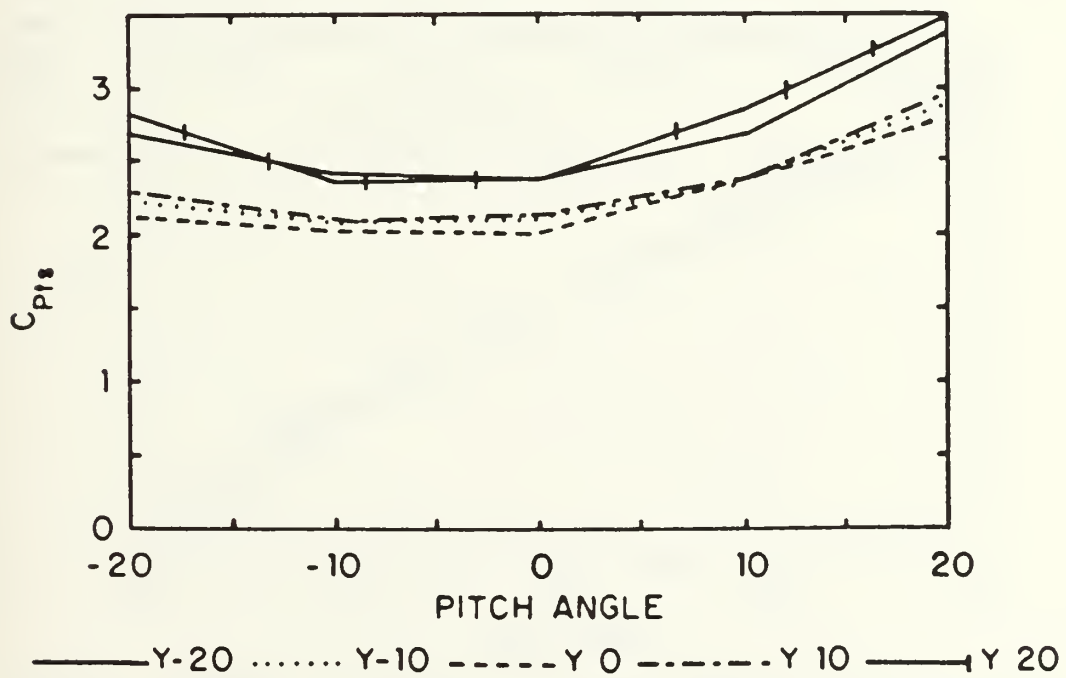

Figure 13. C_p Total-Static vs. Pitch, 1.9 m/s

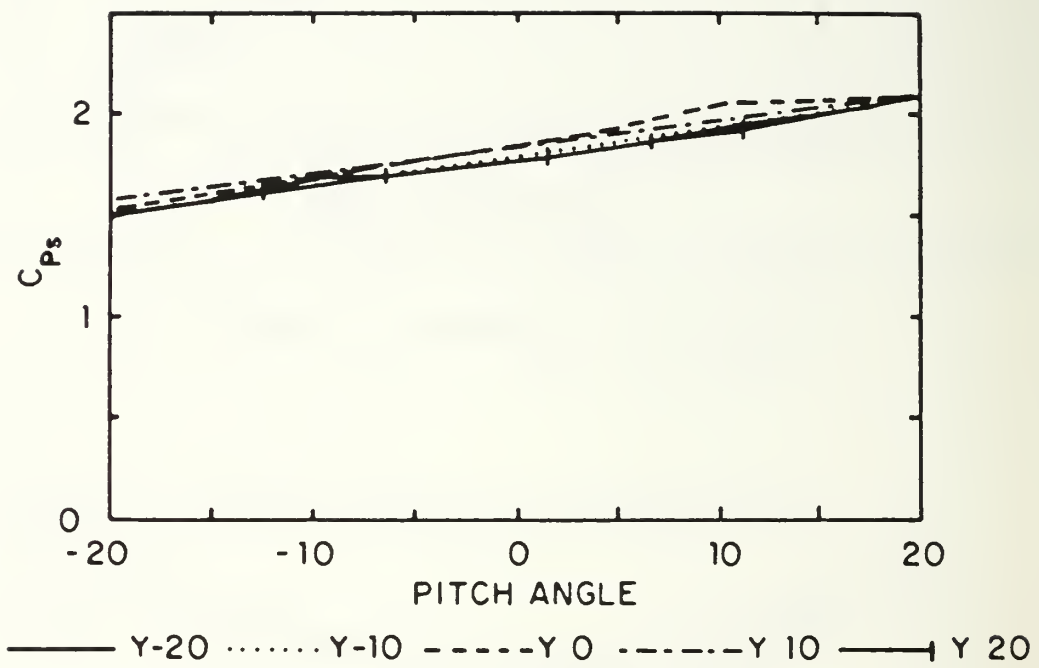

Figure 14. C_p Static vs. Pitch, 1.9 m/s

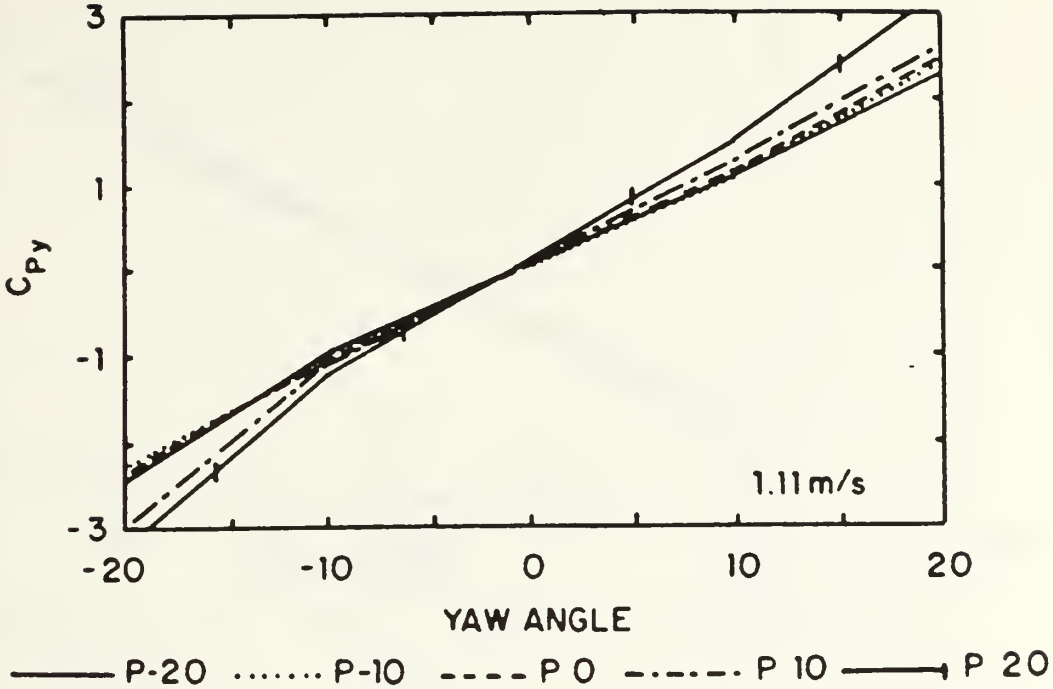

Figure 15. C_p Yaw vs. Yaw, 1.1 m/s

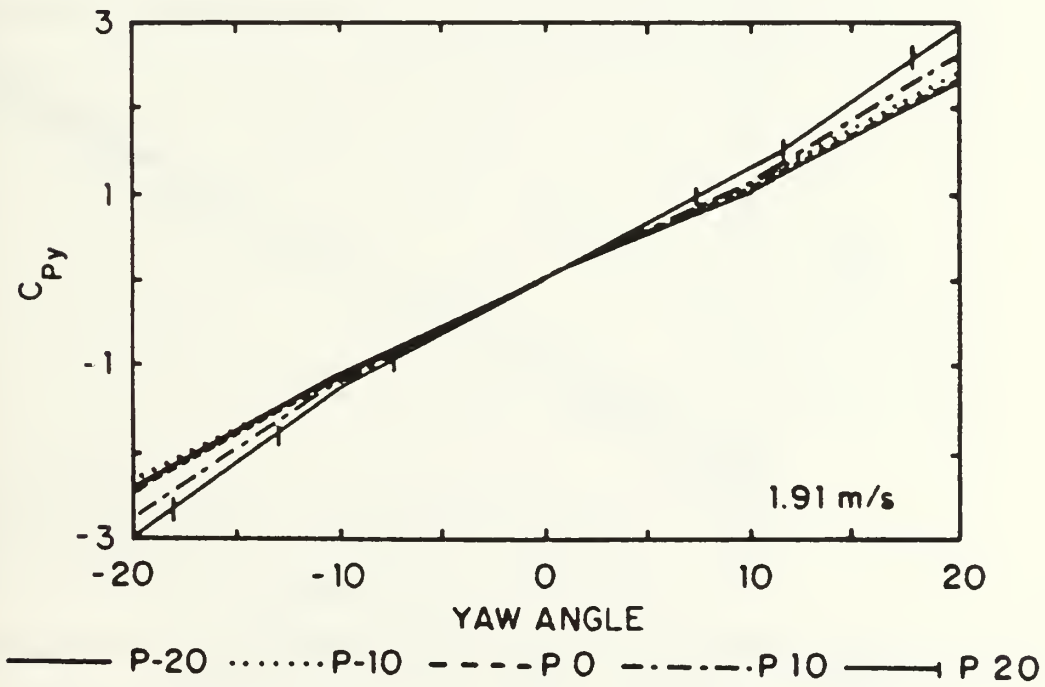

Figure 16. C_p Yaw vs. Yaw, 1.9 m/s

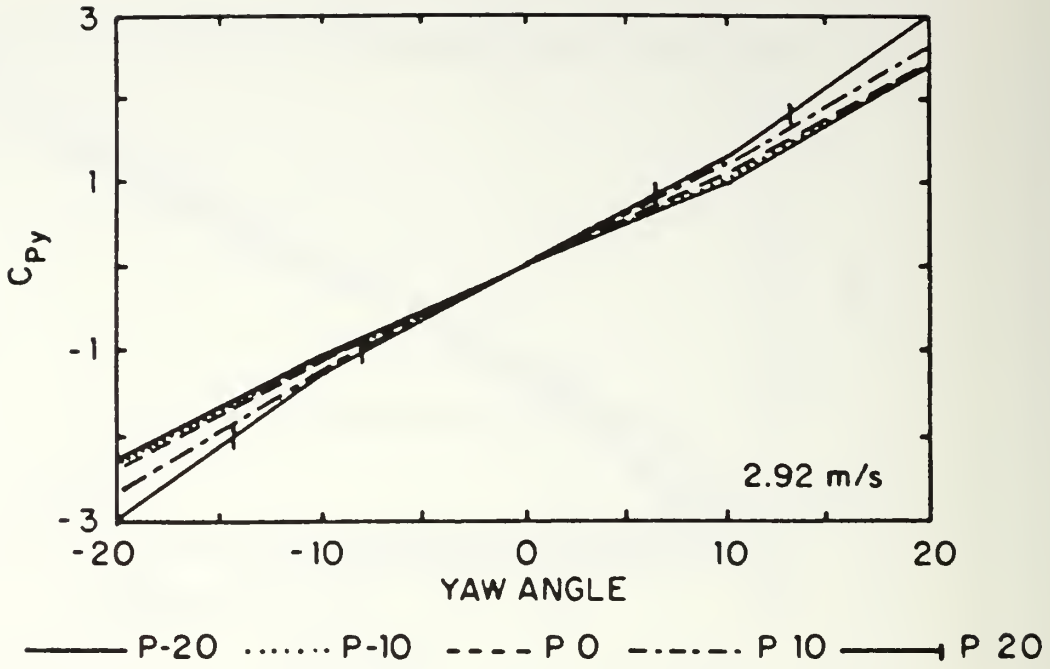

Figure 17. C_p Yaw vs. Yaw, 2.9 m/s

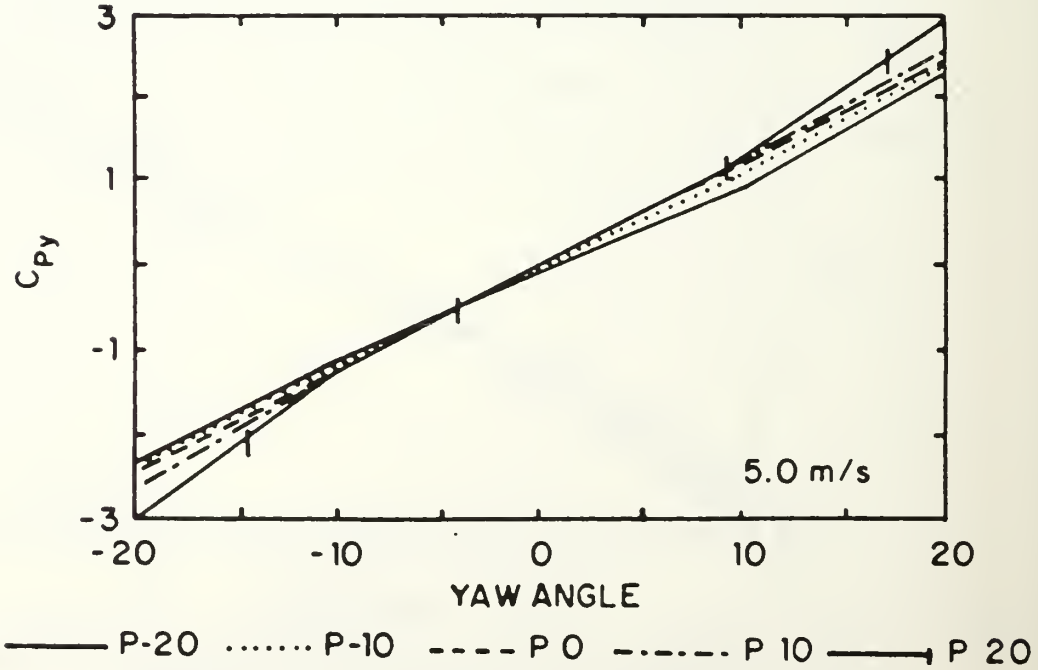

Figure 18. C_p Yaw vs. Yaw, 5.0 m/s

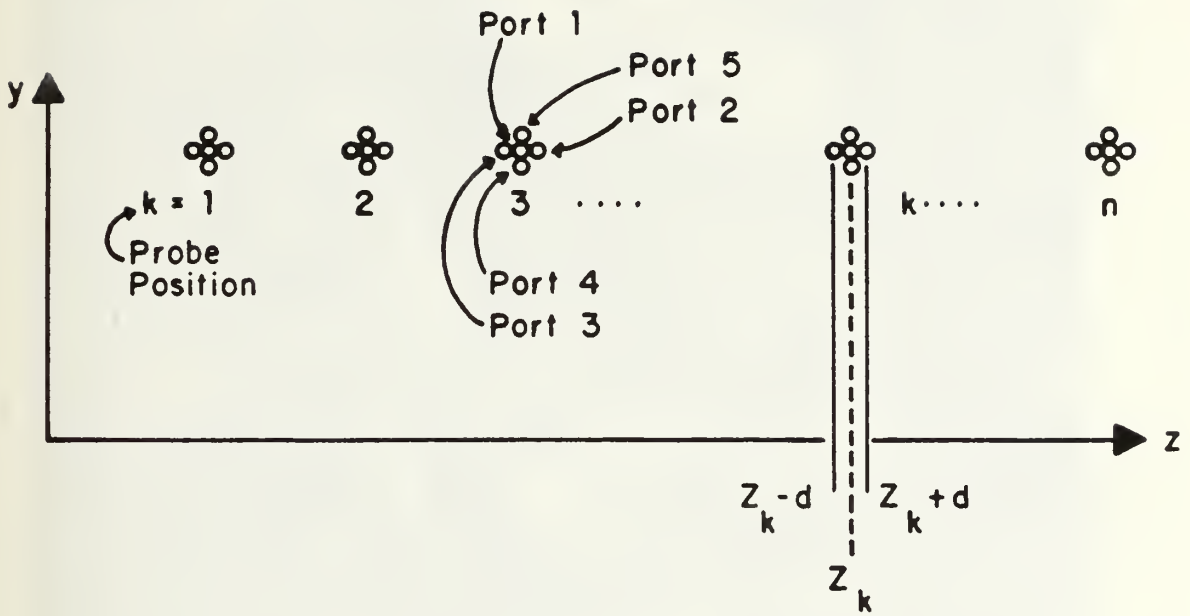

Figure 19. Successive Positions of the Five Hole Pressure Probe and Probe Ports, Looking Downstream

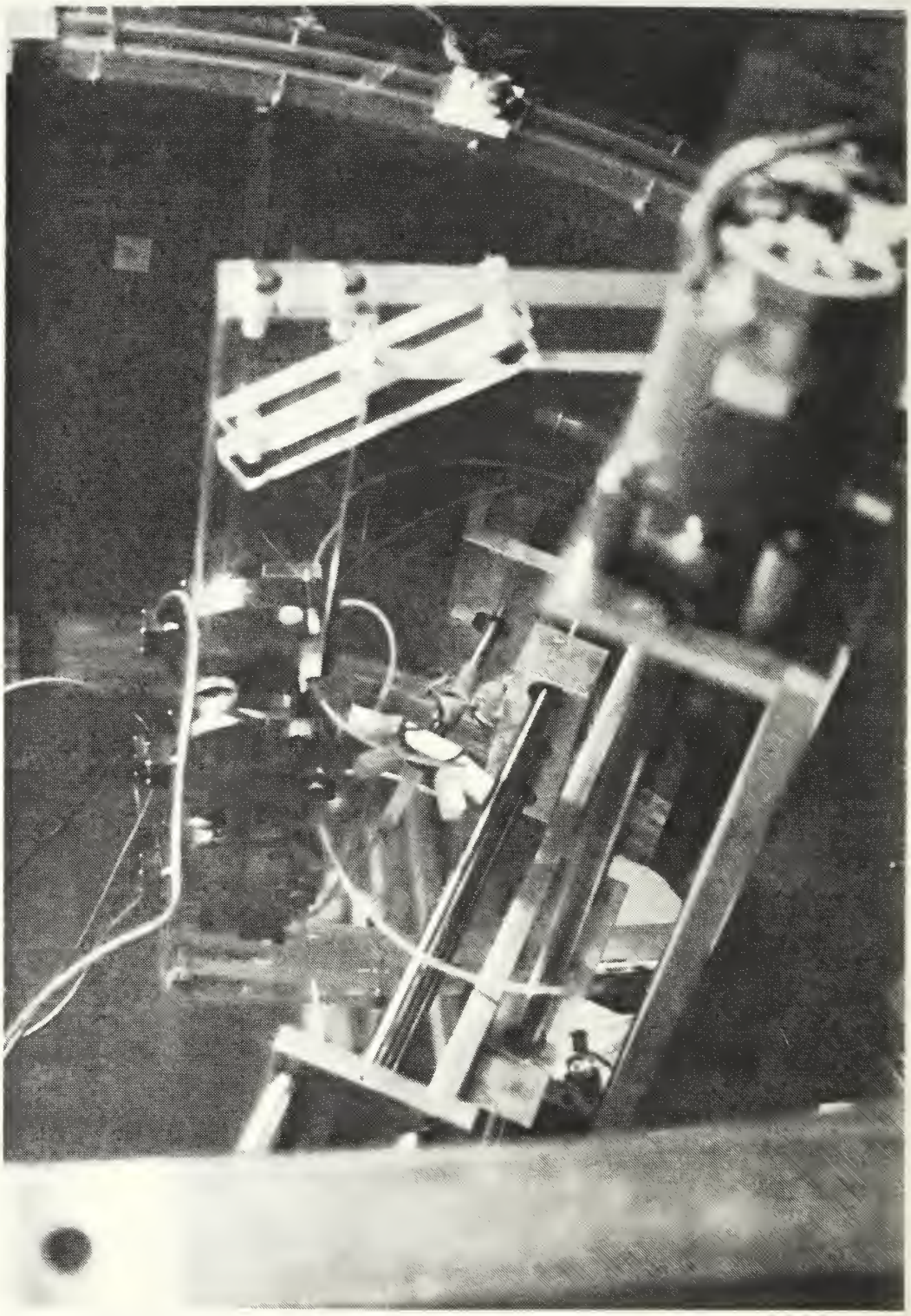

Figure 20. Curved Channel Traversing Mechanism, Transducers, Probe and Probe Mount

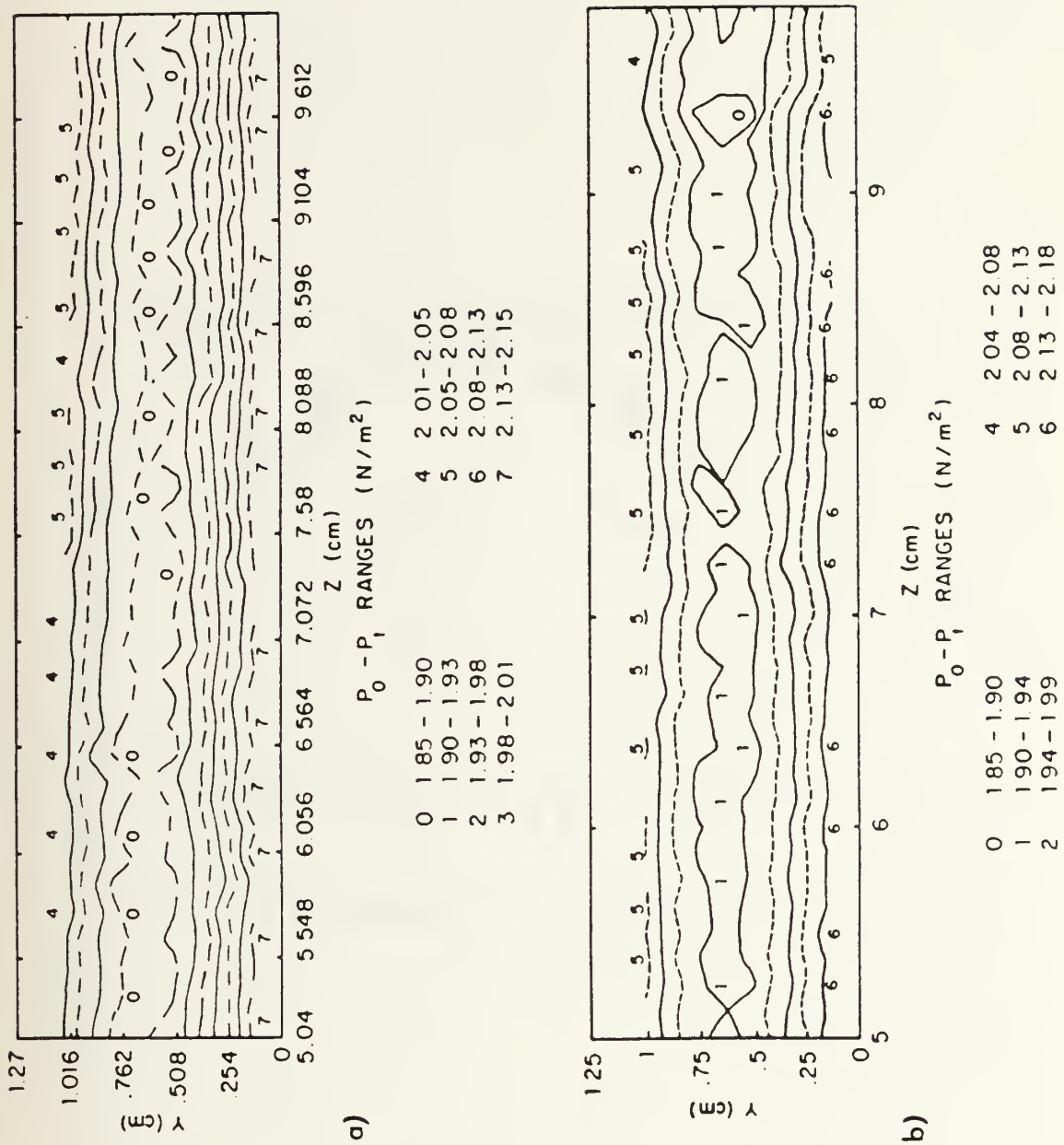

Figure 21. Total Pressure Distribution
a) Miniature Kiel Probe, De=54
b) Five Hole Probe, De=49

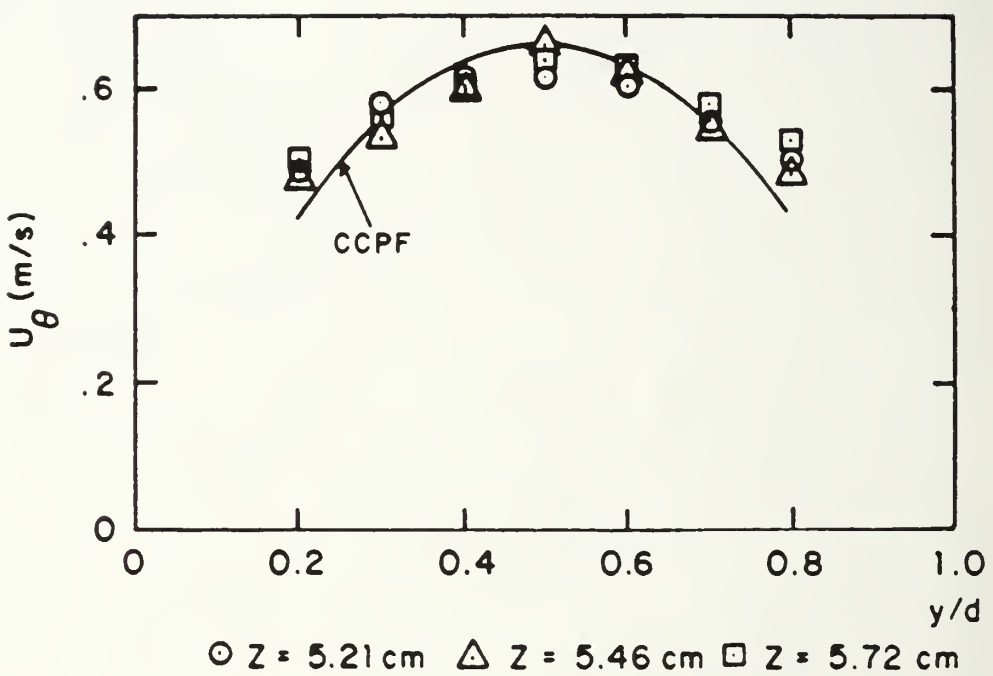

Figure 22. Streamwise Velocity Profiles Plotted Against CCPF, De=36.6

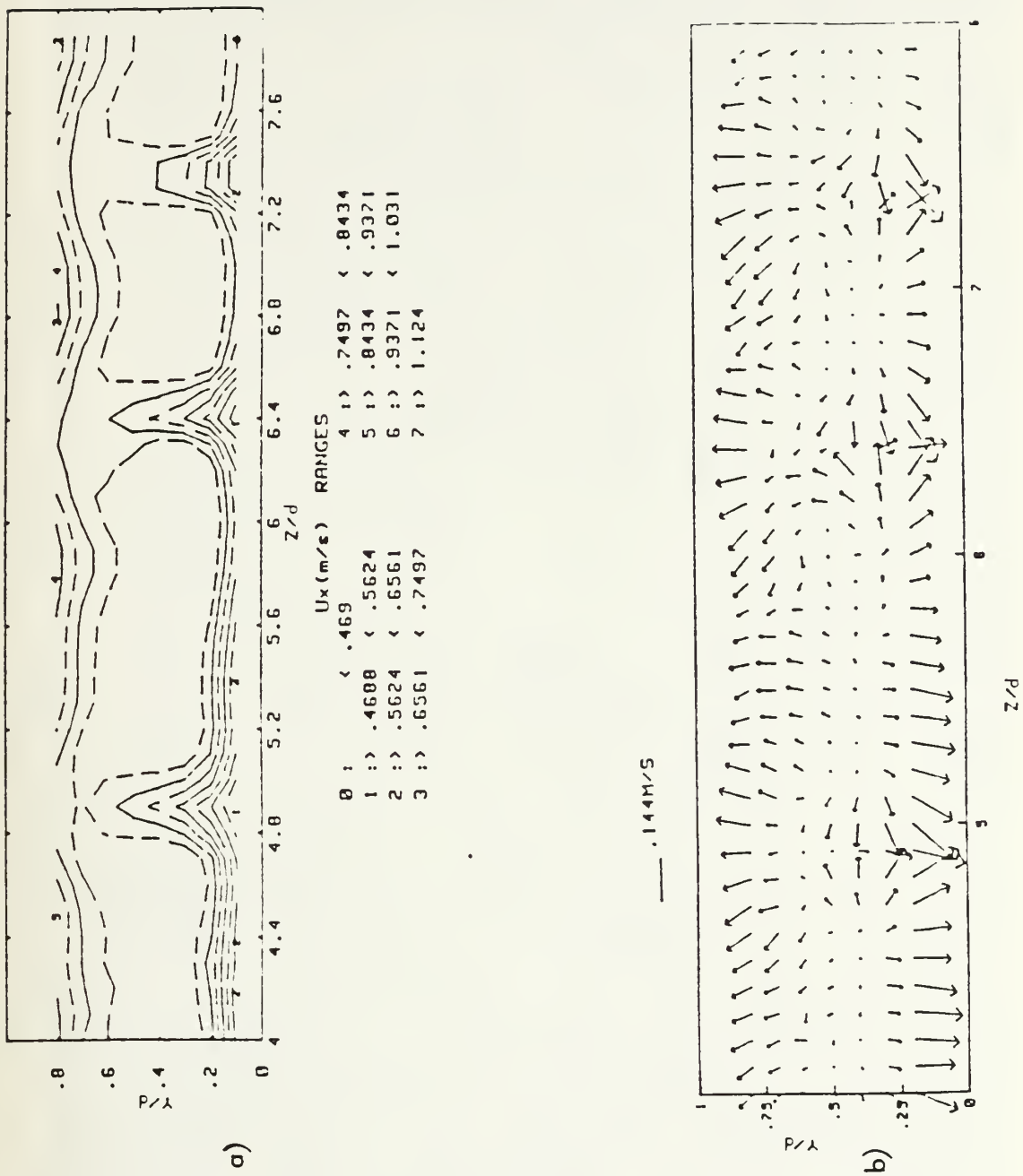

Figure 23. a) Streamwise Velocity Contours, De=100
b) Secondary Velocity Vectors, No Corrections, De=100

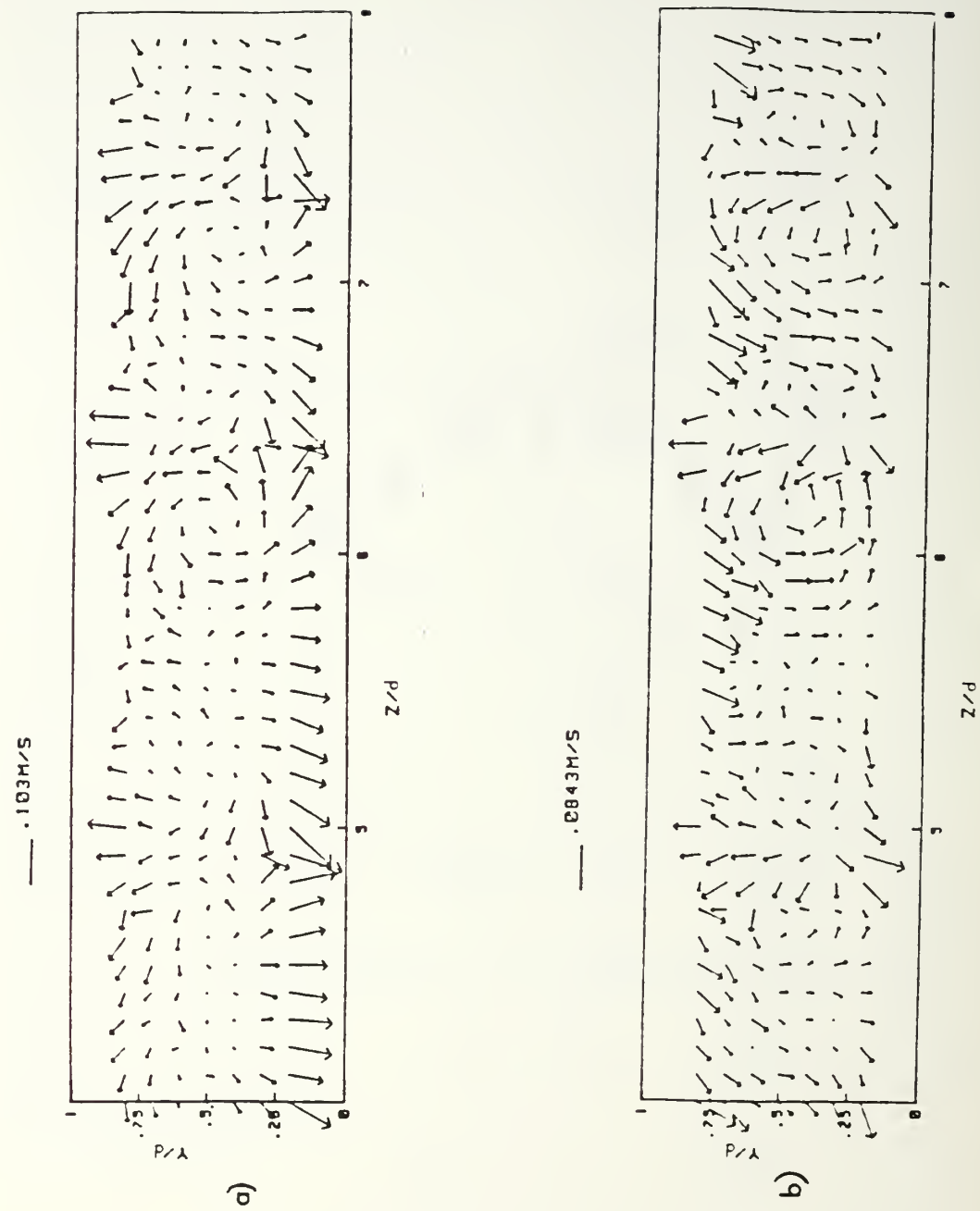

Figure 24. Secondary Velocity Vectors, De=100
a) Spatial Resolution Correction Only
b) Spatial Resolution and Downwash Velocity Correction

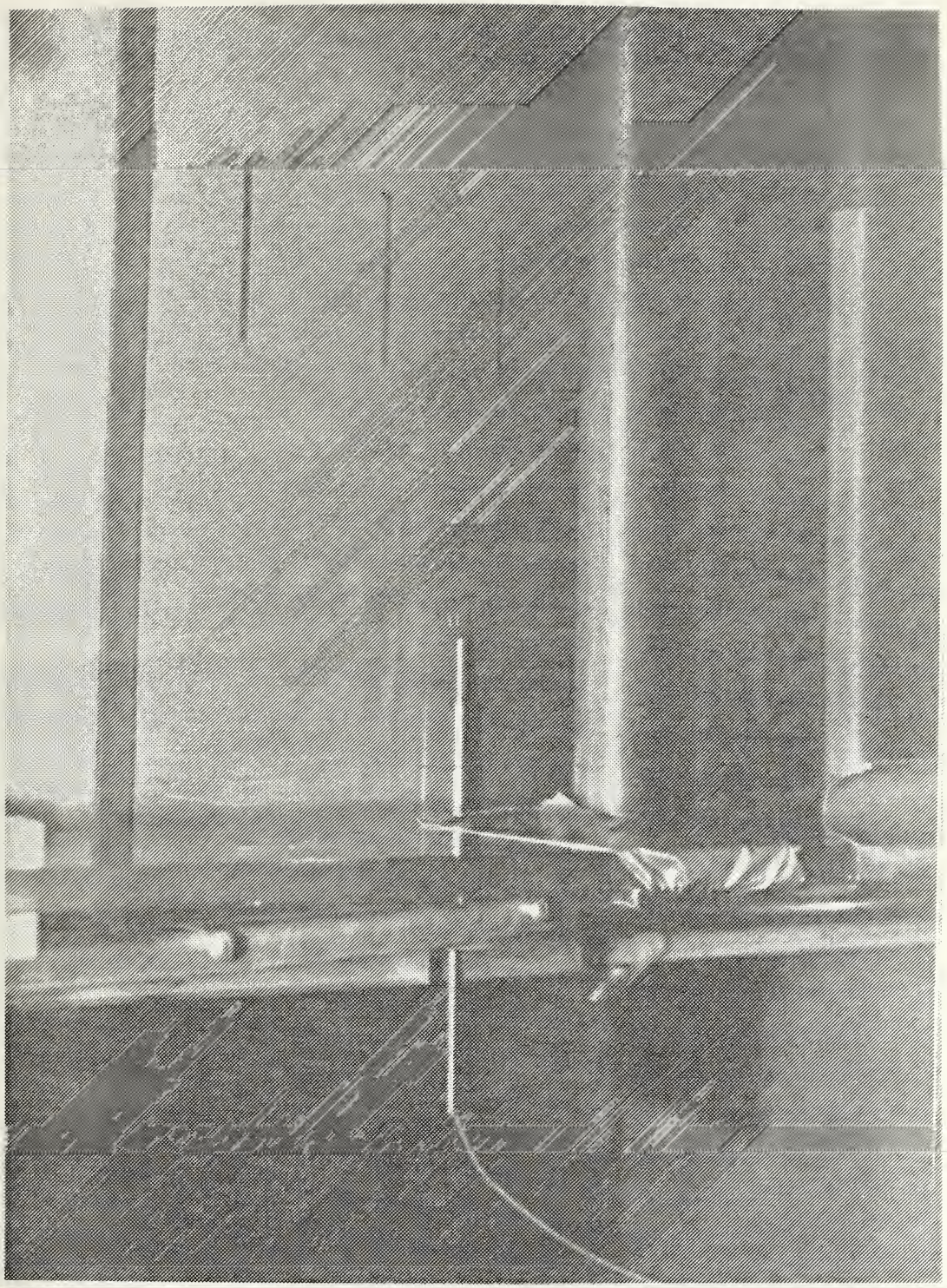

Figure 25. Hot-wire Probe Mounting

a)

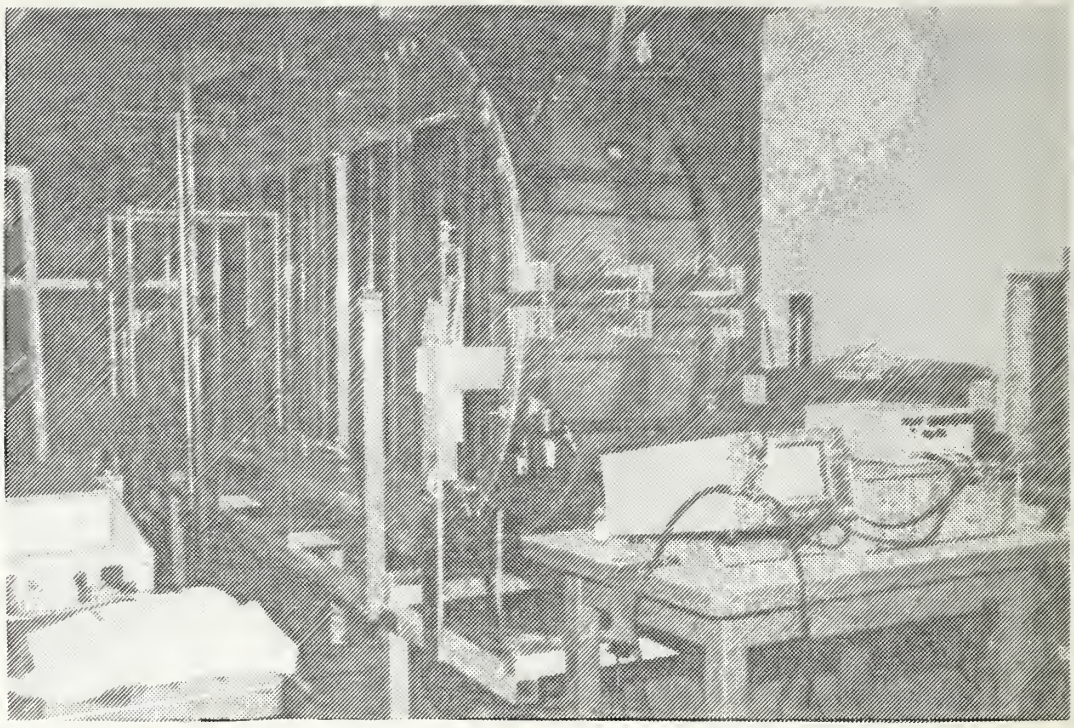

b)

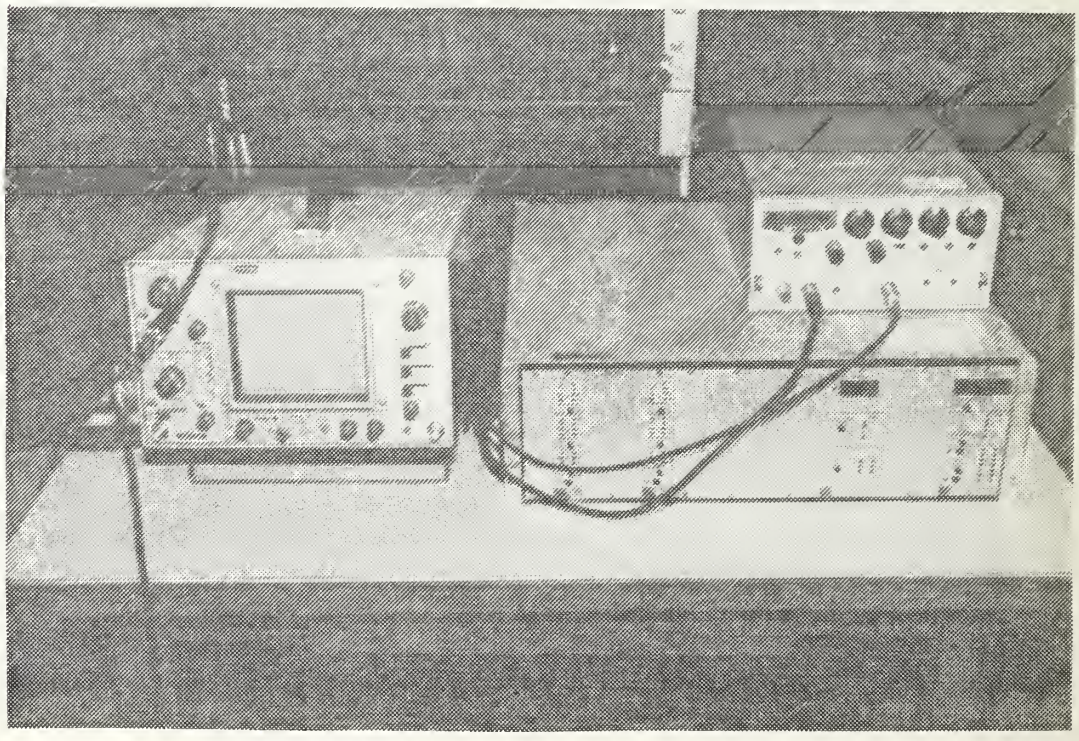

Figure 26. a) Hot-wire Measurement Setup
b) Oscilliscope, Bridge and Filter Amplifier

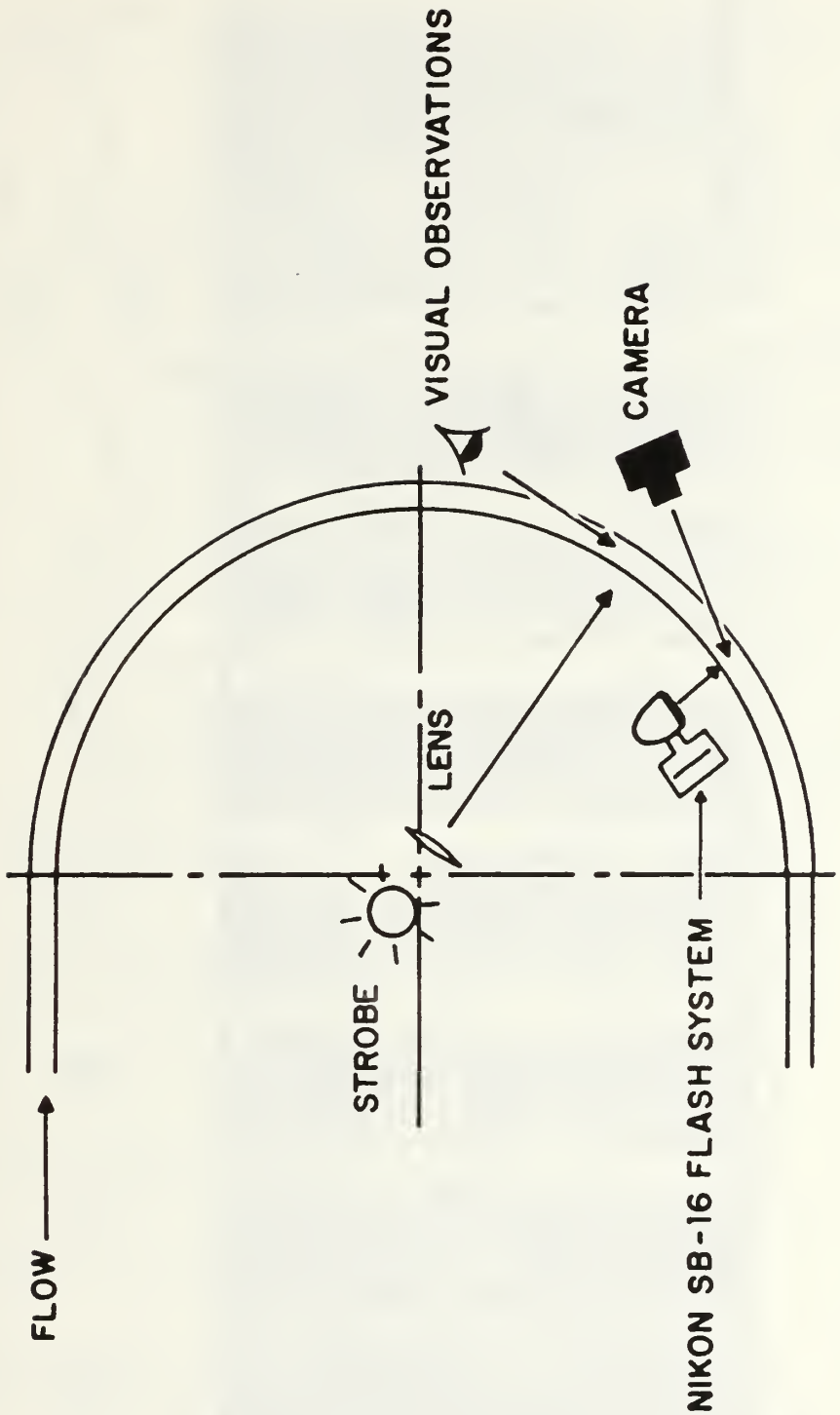

Figure 27. Radial-Spanwise Plane Flow Visualization

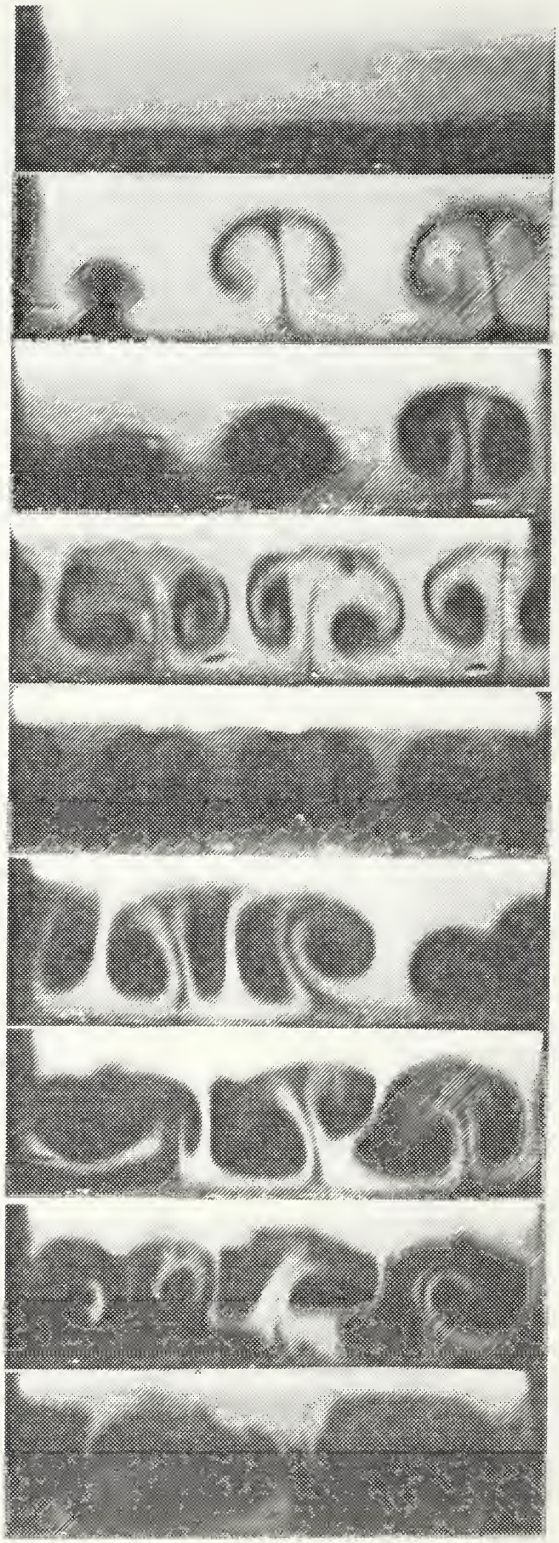

Figure 28. Radial-Spanwise Plane Flow Visualization, 115 Degree Streamwise Location

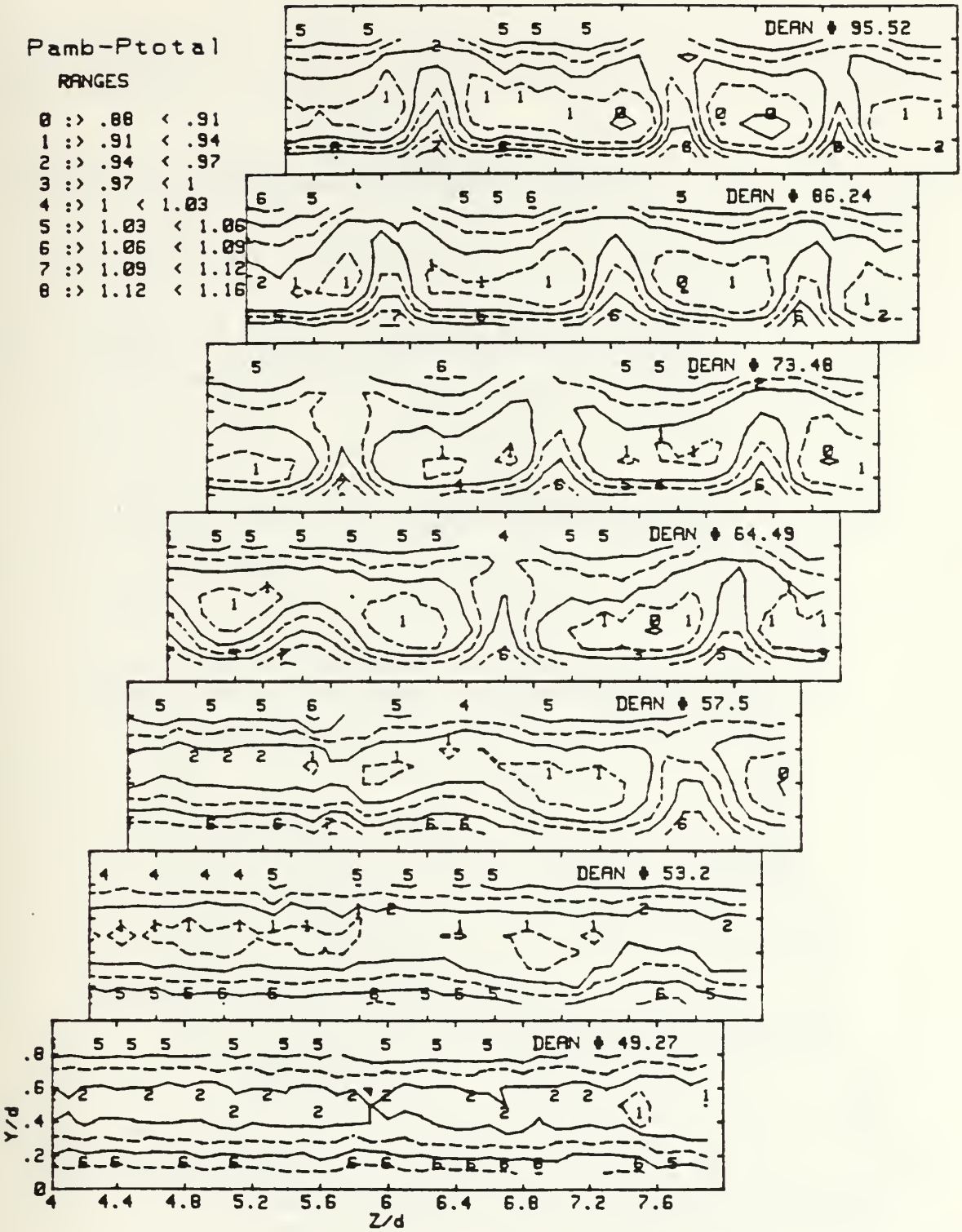

Figure 29. Total Pressure Contours, De=49.3 to De=95.5

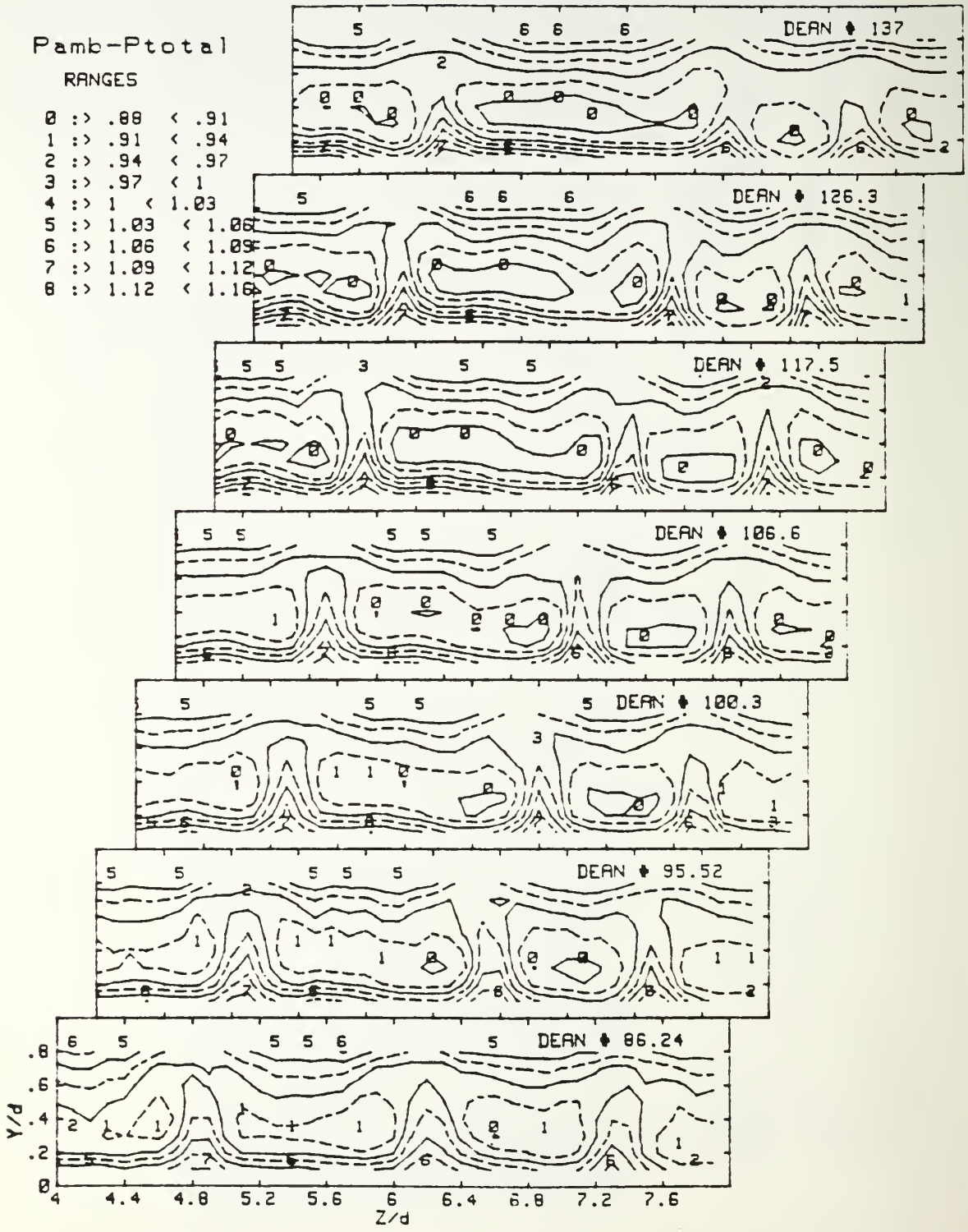

Figure 30. Total Pressure Contours, De=86.2 to De=137.0

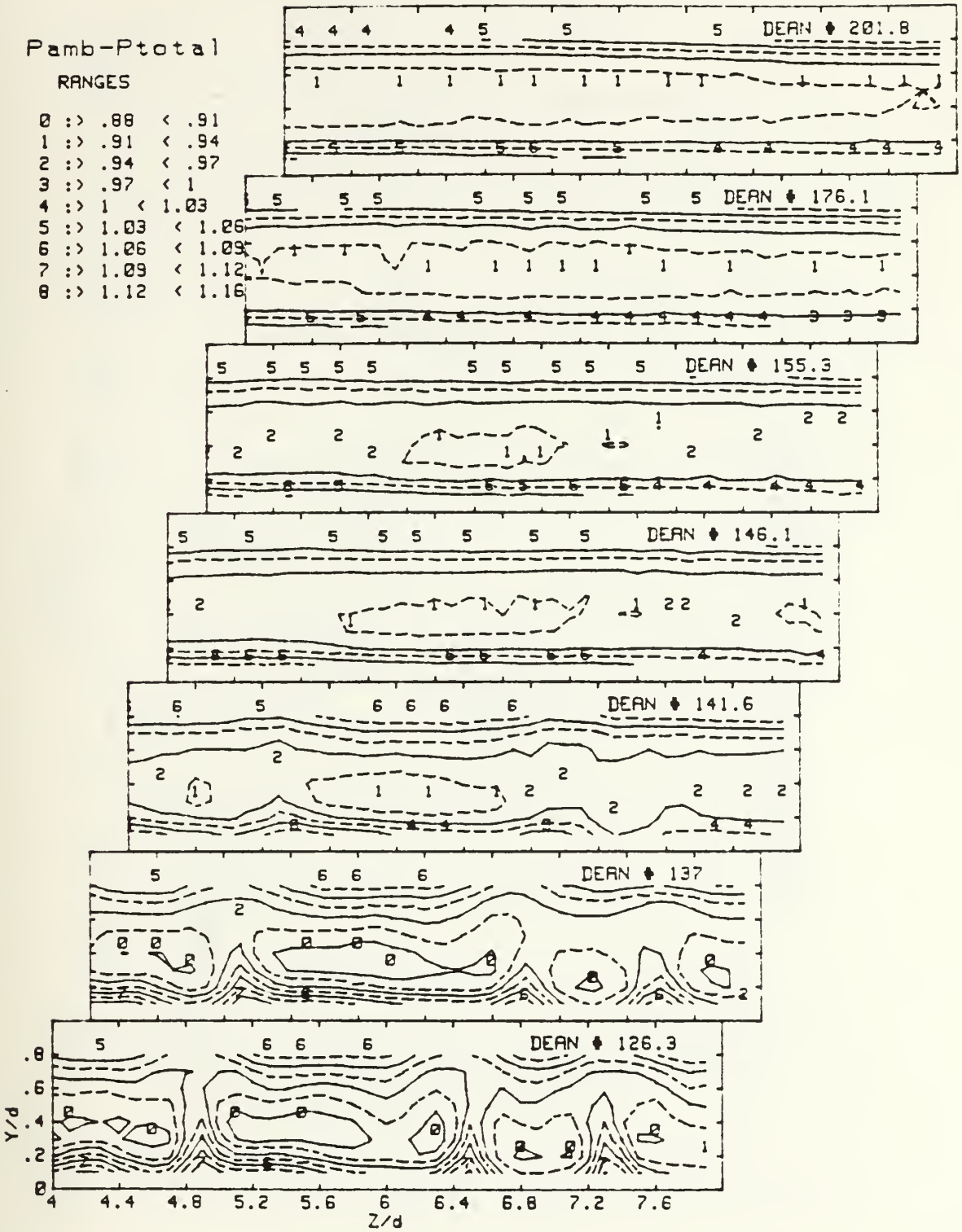

Figure 31. Total Pressure Contours, De=126.3 to De=201.8

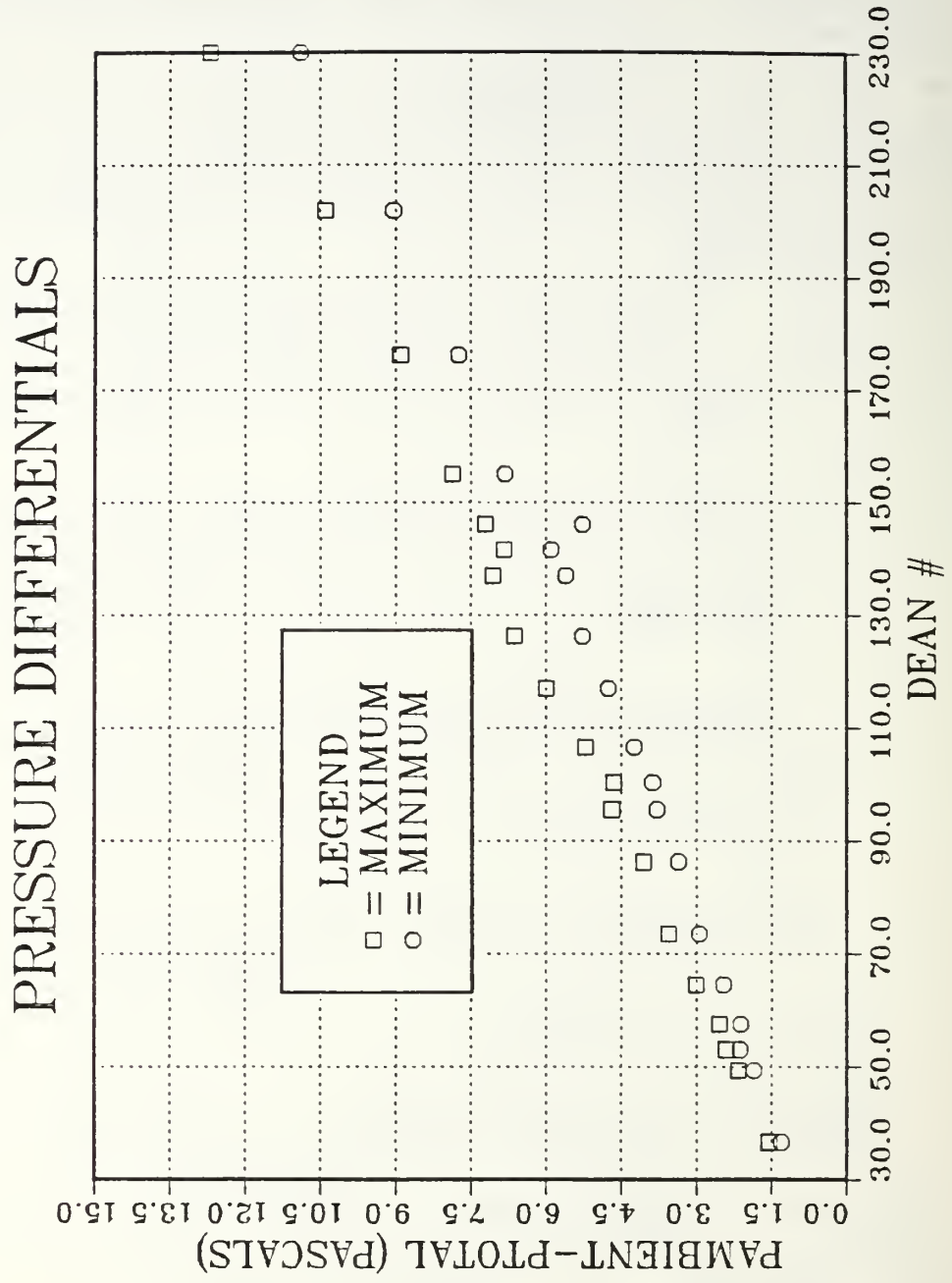

Figure 32. Total Pressure Differentials, Maximum and Minimum

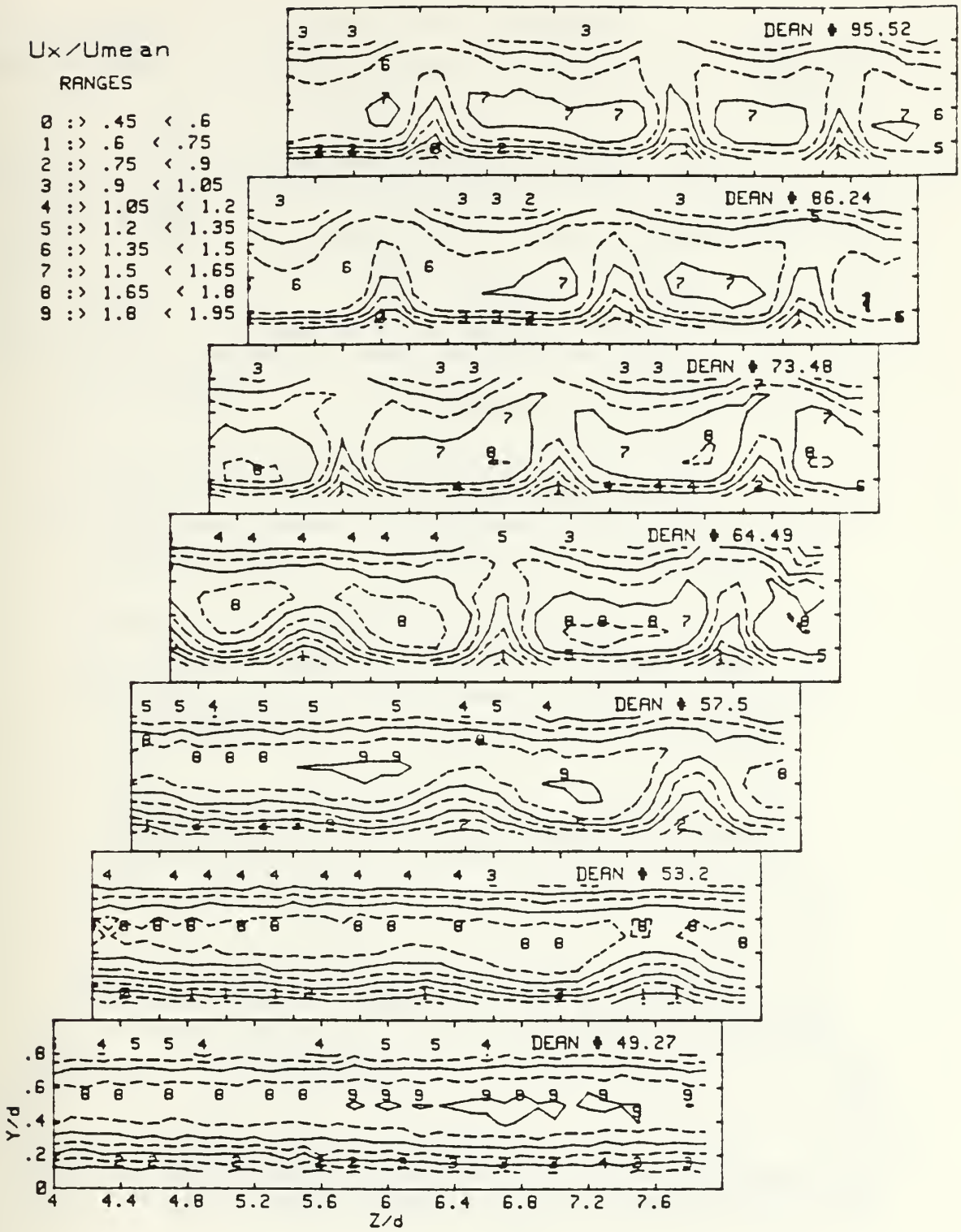

Figure 33. Streamwise Velocity Contours, De=49.3 to De=95.5

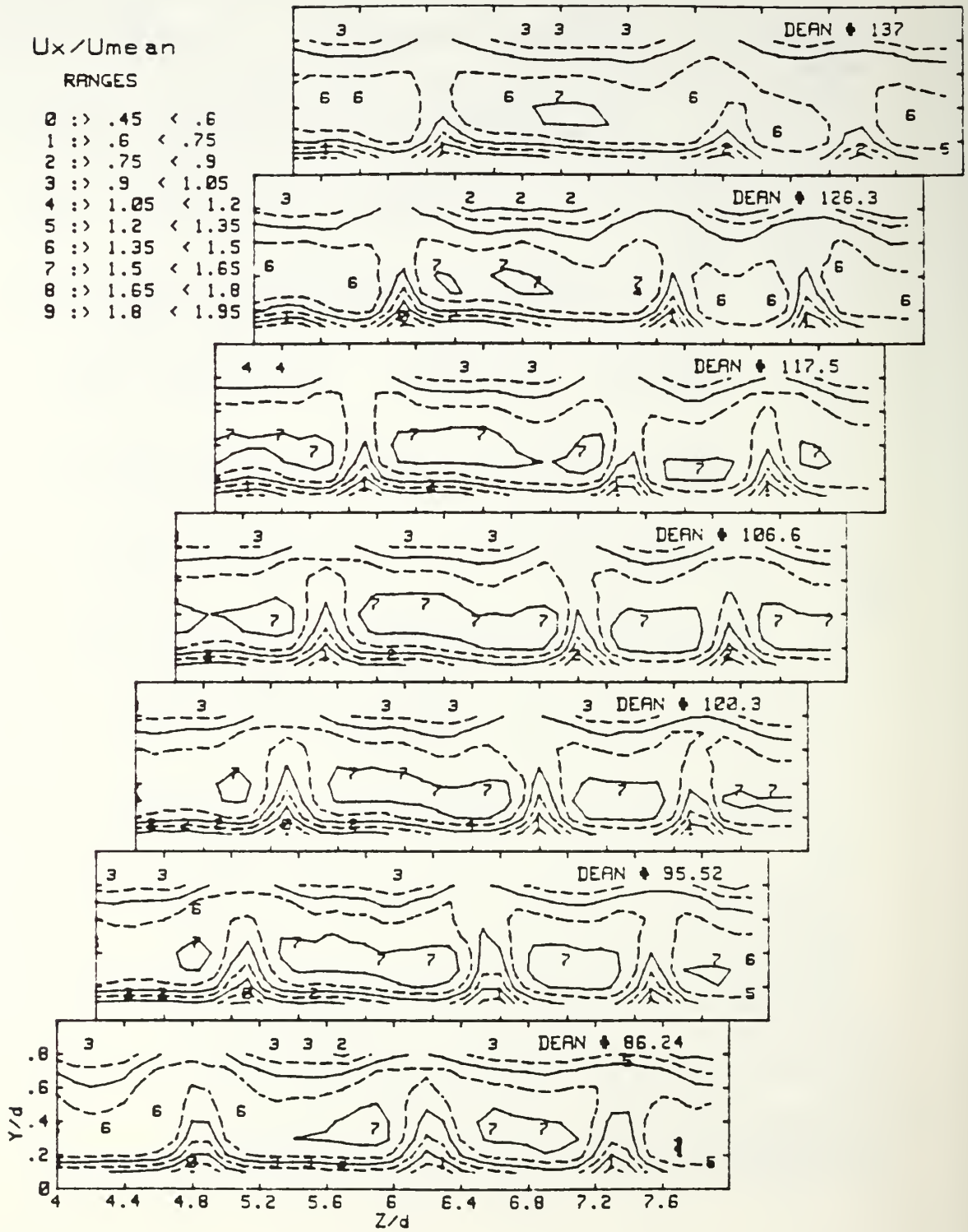

Figure 34. Streamwise Velocity Contours, De=86.2 to De=137.0

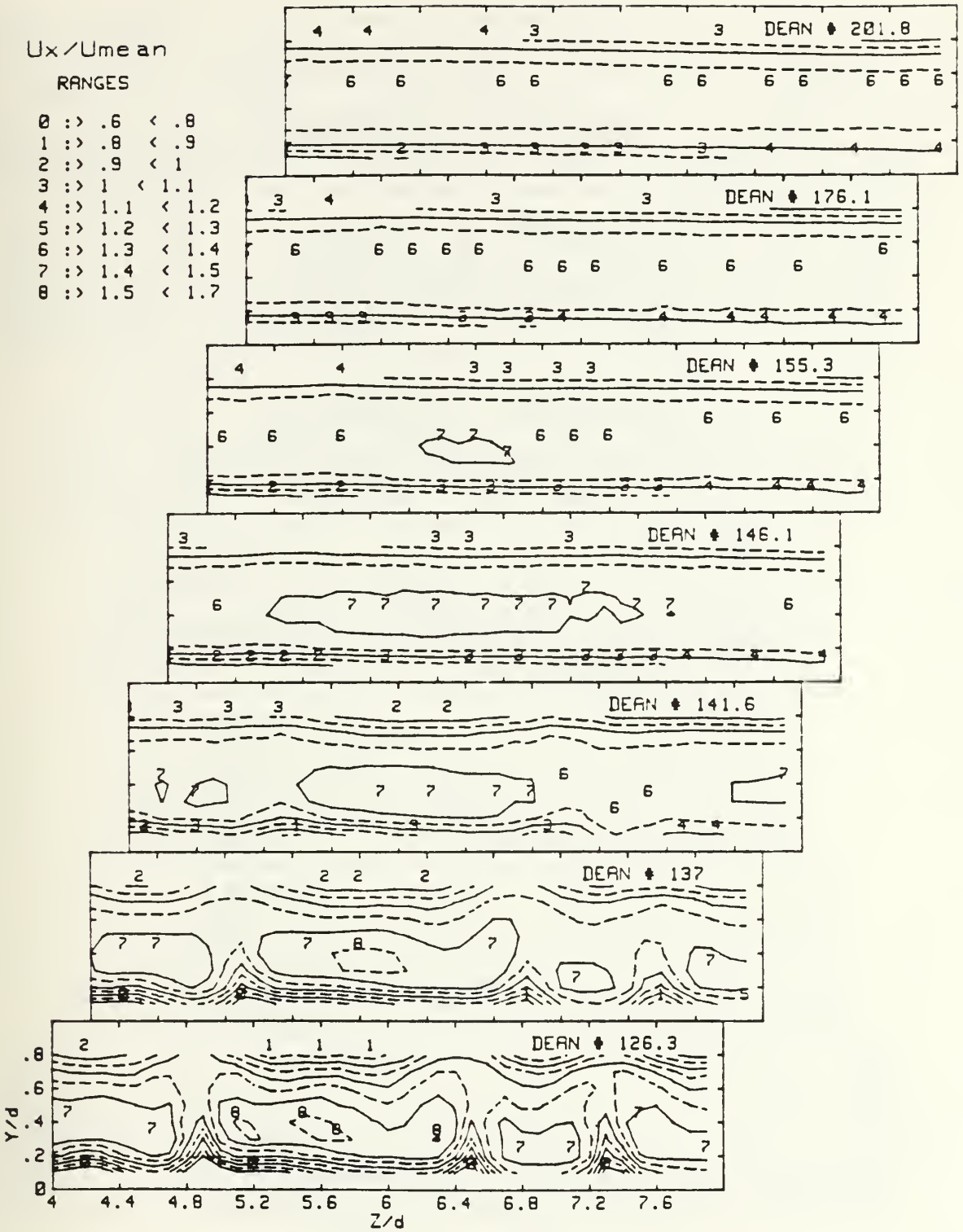

Figure 35. Streamwise Velocity Contours, De=126.3 to De=201.8

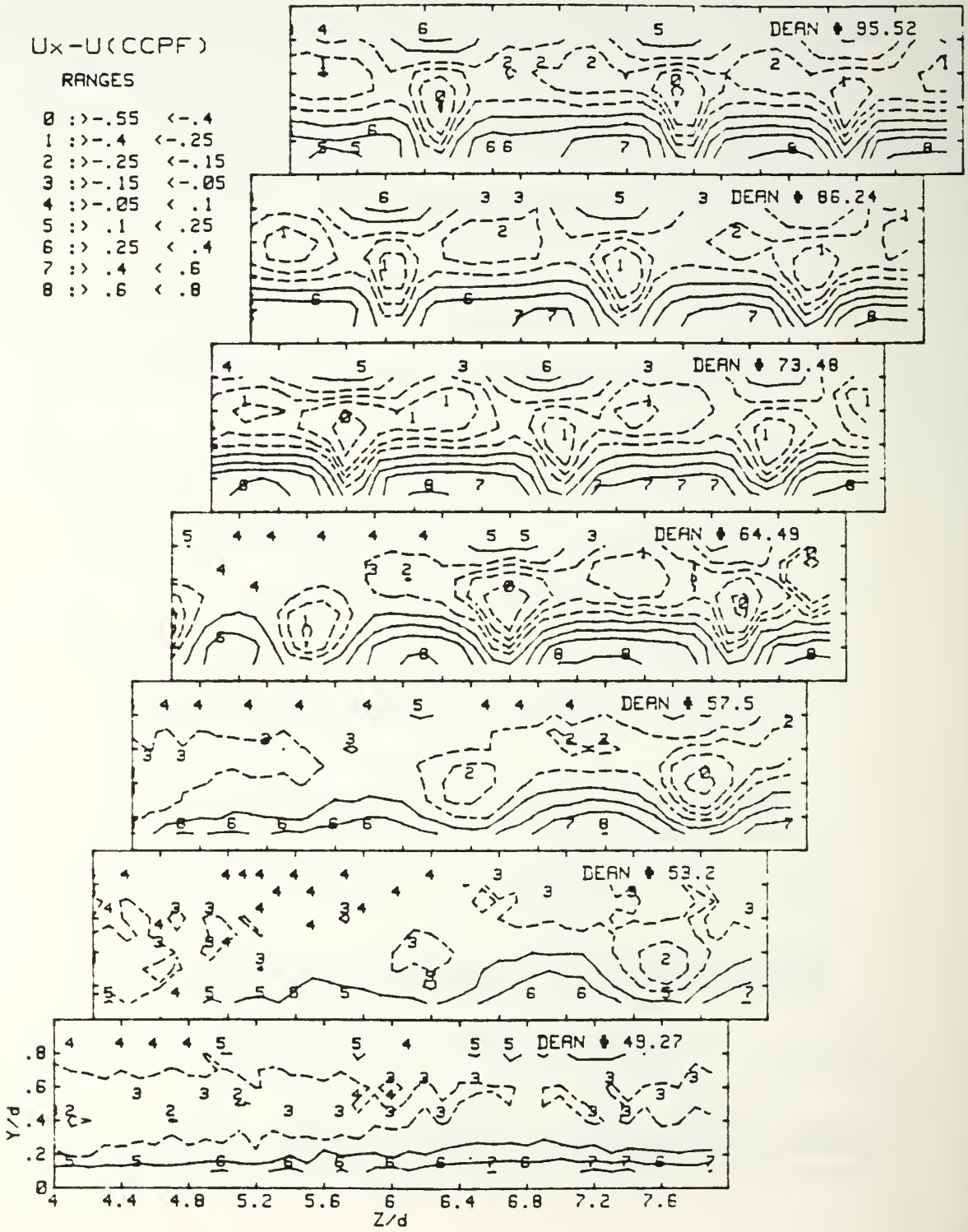

Figure 36. Velocity Perturbation Contours, De=49.3 to De=95.5

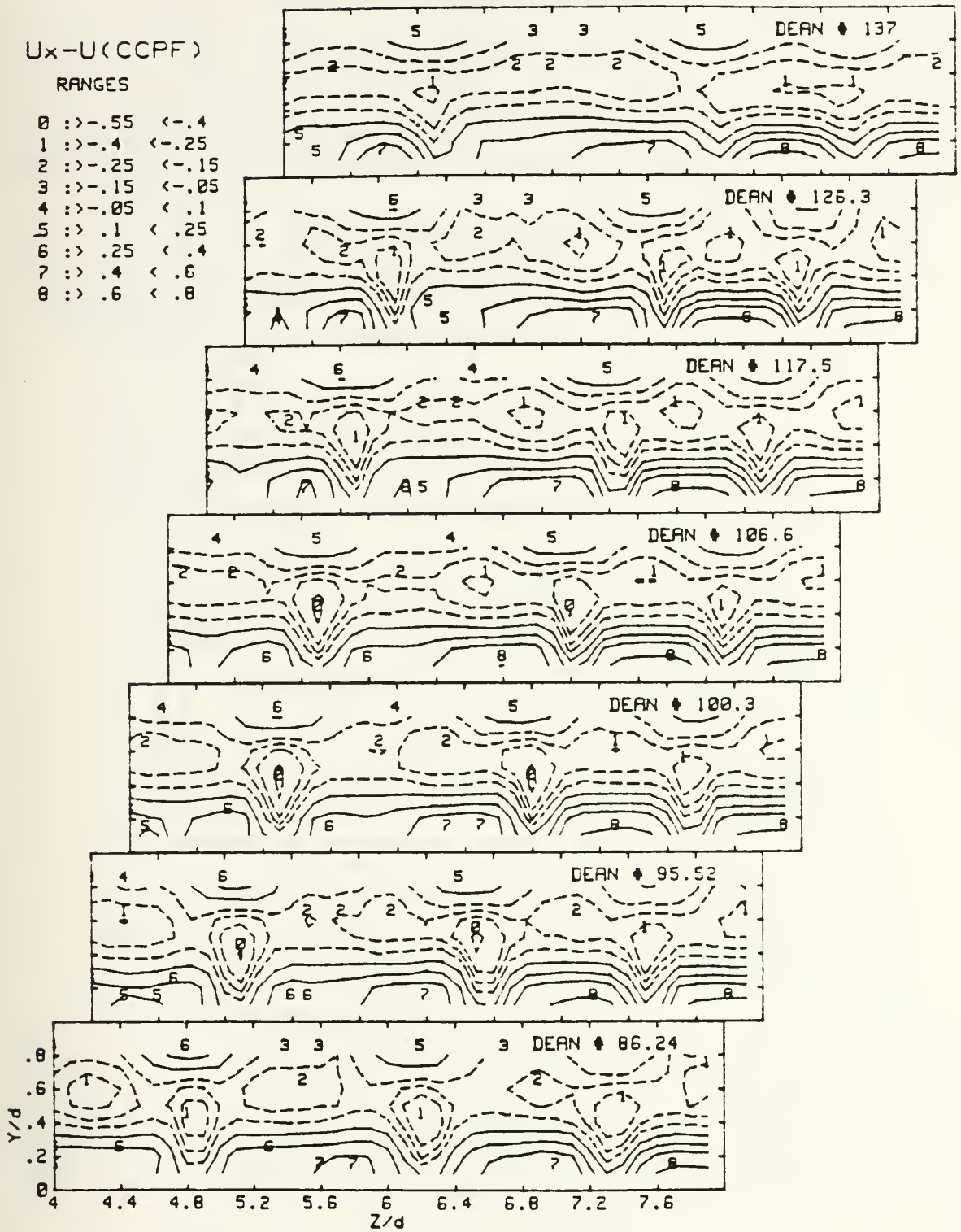

Figure 37. Velocity Perturbation Contours, De=86.2 to De=137.0

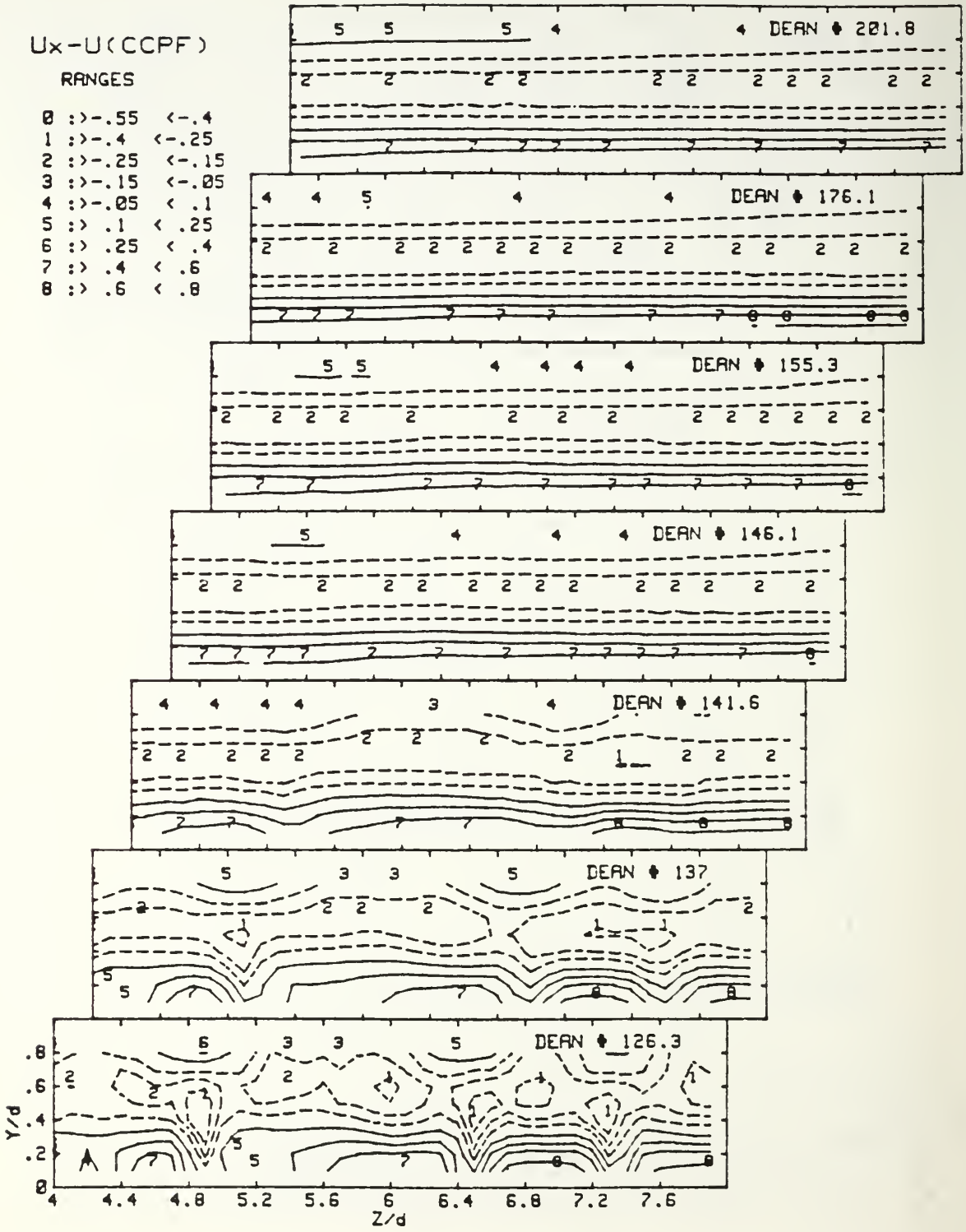

Figure 38. Velocity Perturbation Contours, De=126.3 to De=201.8

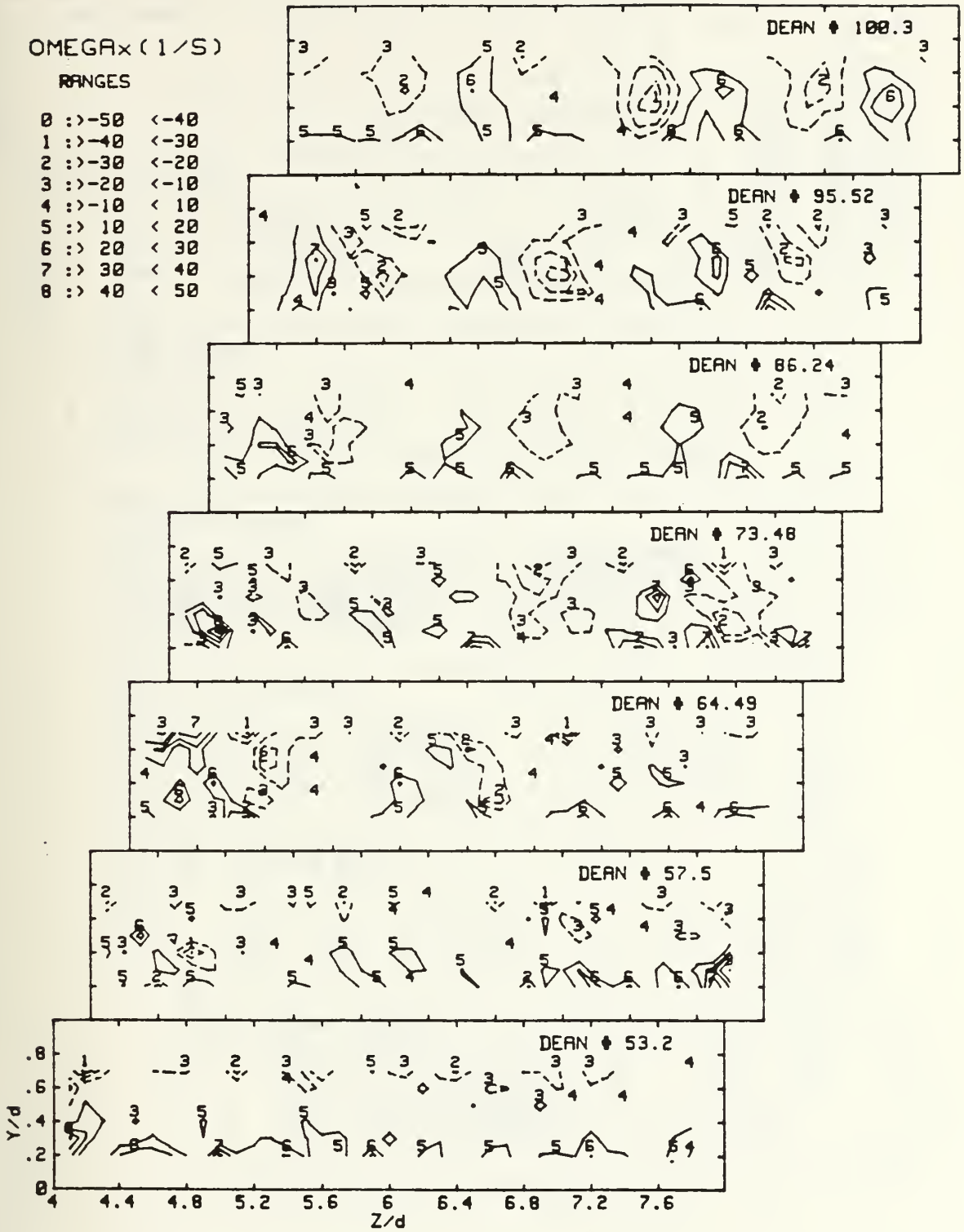

Figure 39. Streamwise Vorticity Contours, De=53.2 to De=100.3

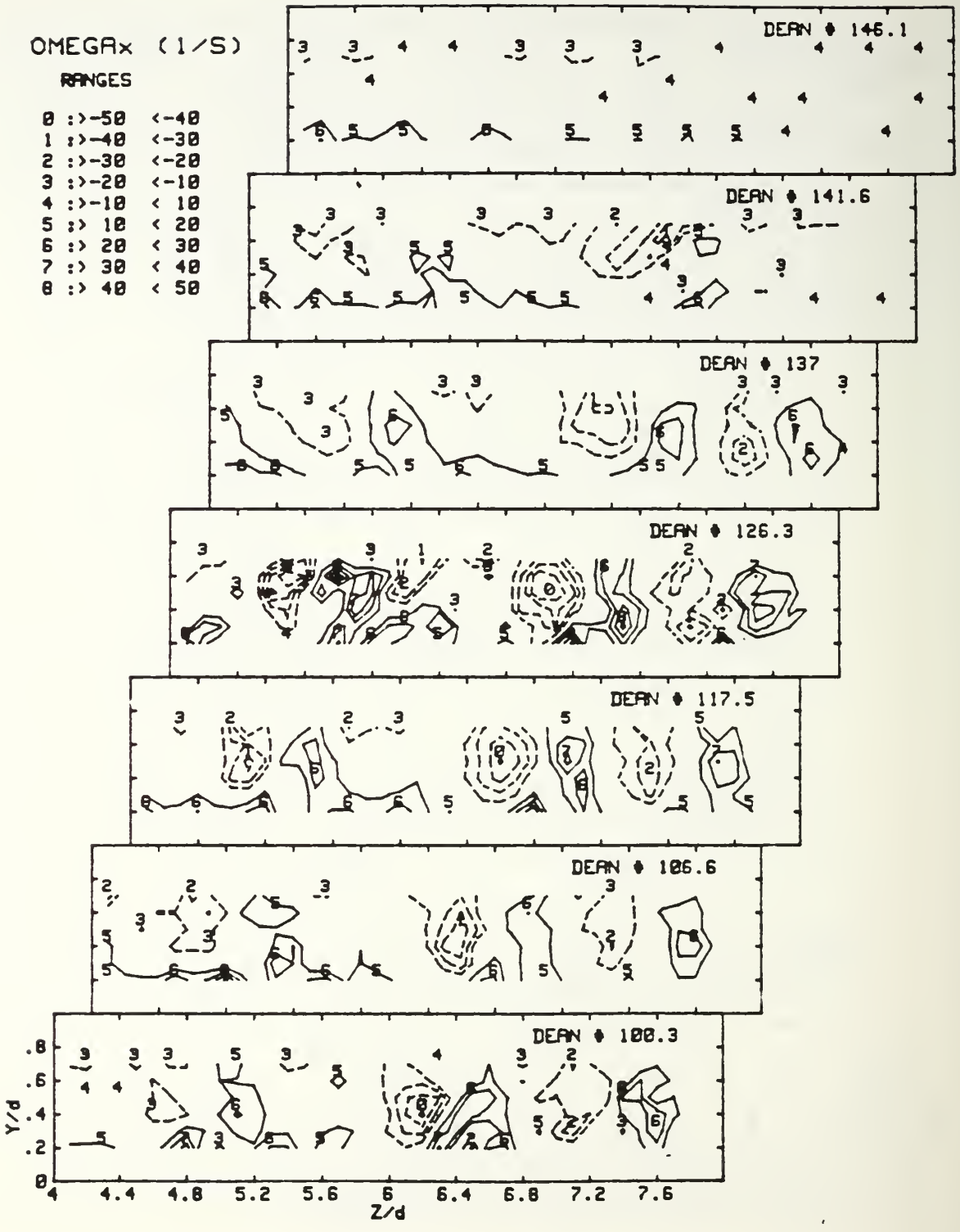

Figure 40. Streamwise Vorticity Contours, De=100.3 to De=146.1

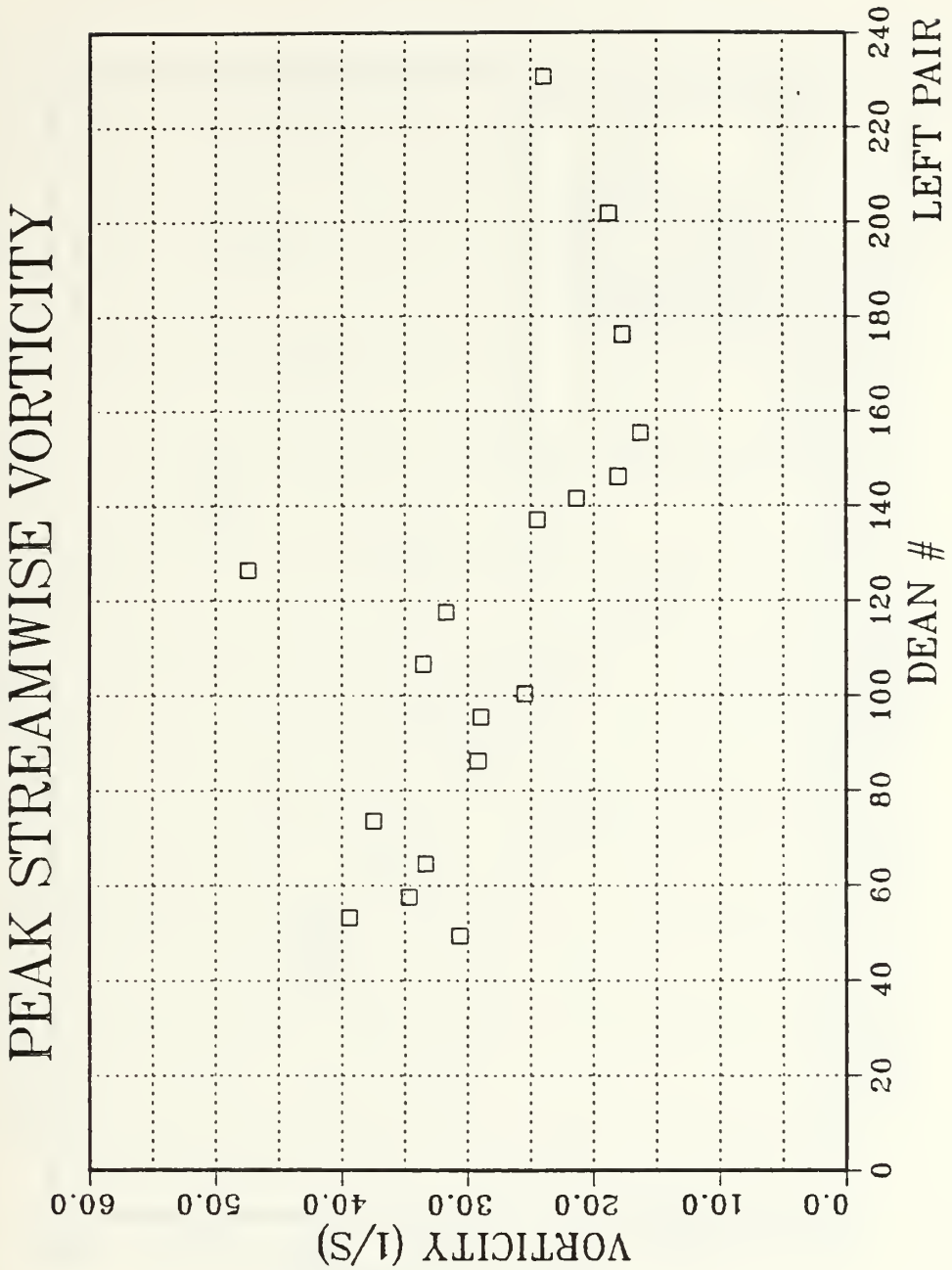

Figure 41. Peak Streamwise Vorticity vs. Dean #, Left Vortex Pair

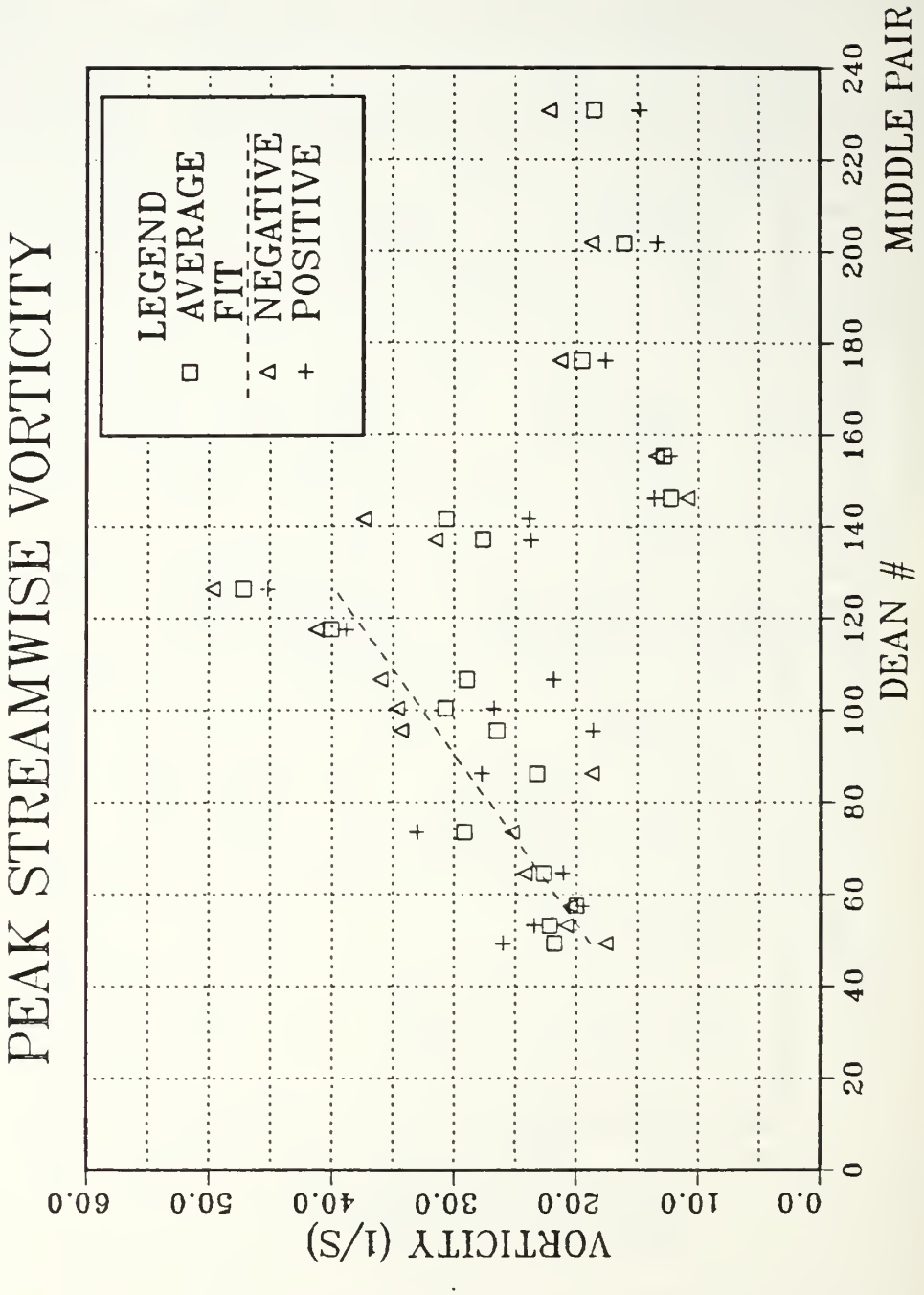

Figure 42. Peak Streamwise Vorticity vs. Dean #, Middle Vortex Pair

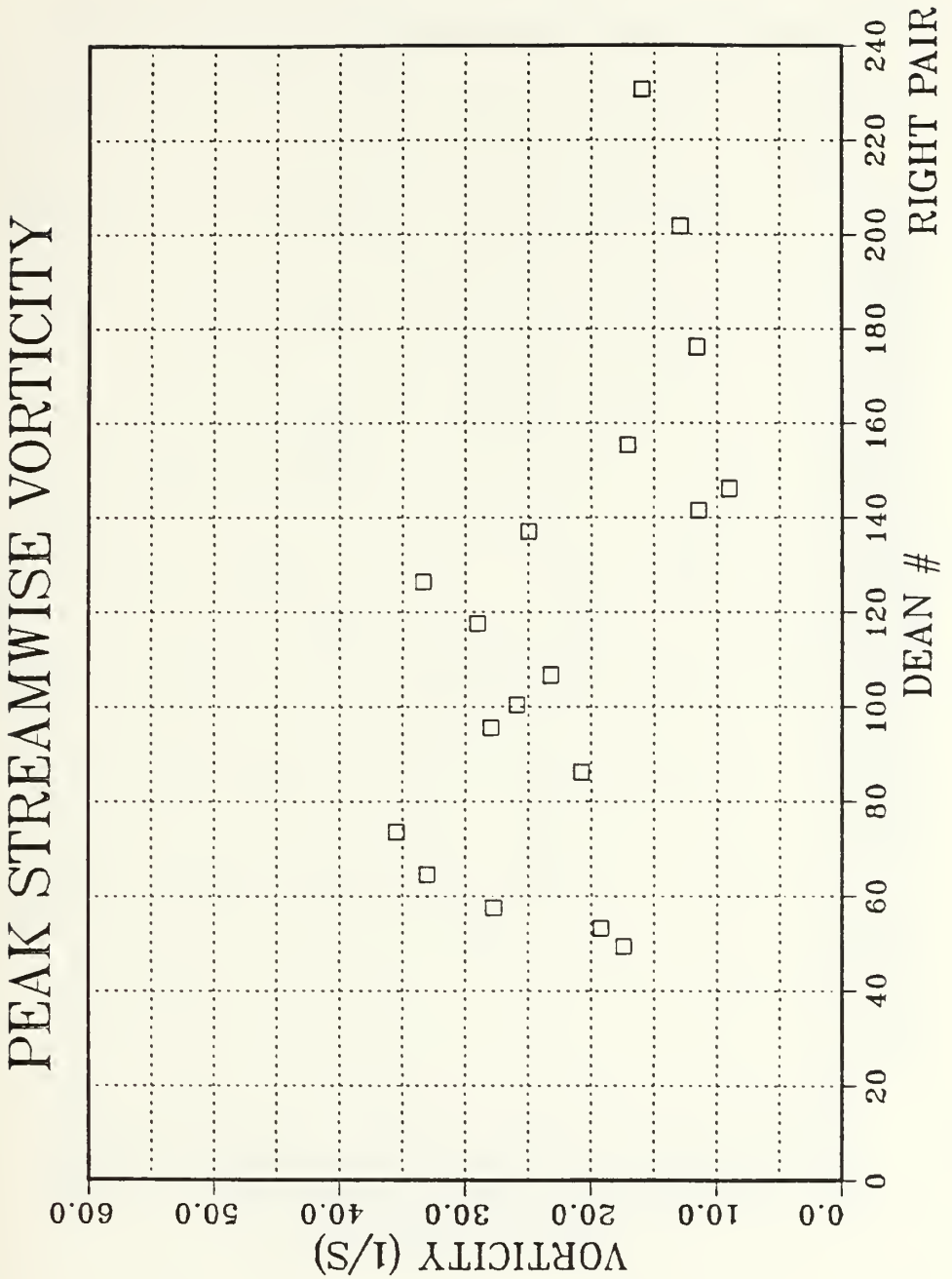

Figure 43. Peak Streamwise Vorticity vs. Dean #, Right Vortex Pair

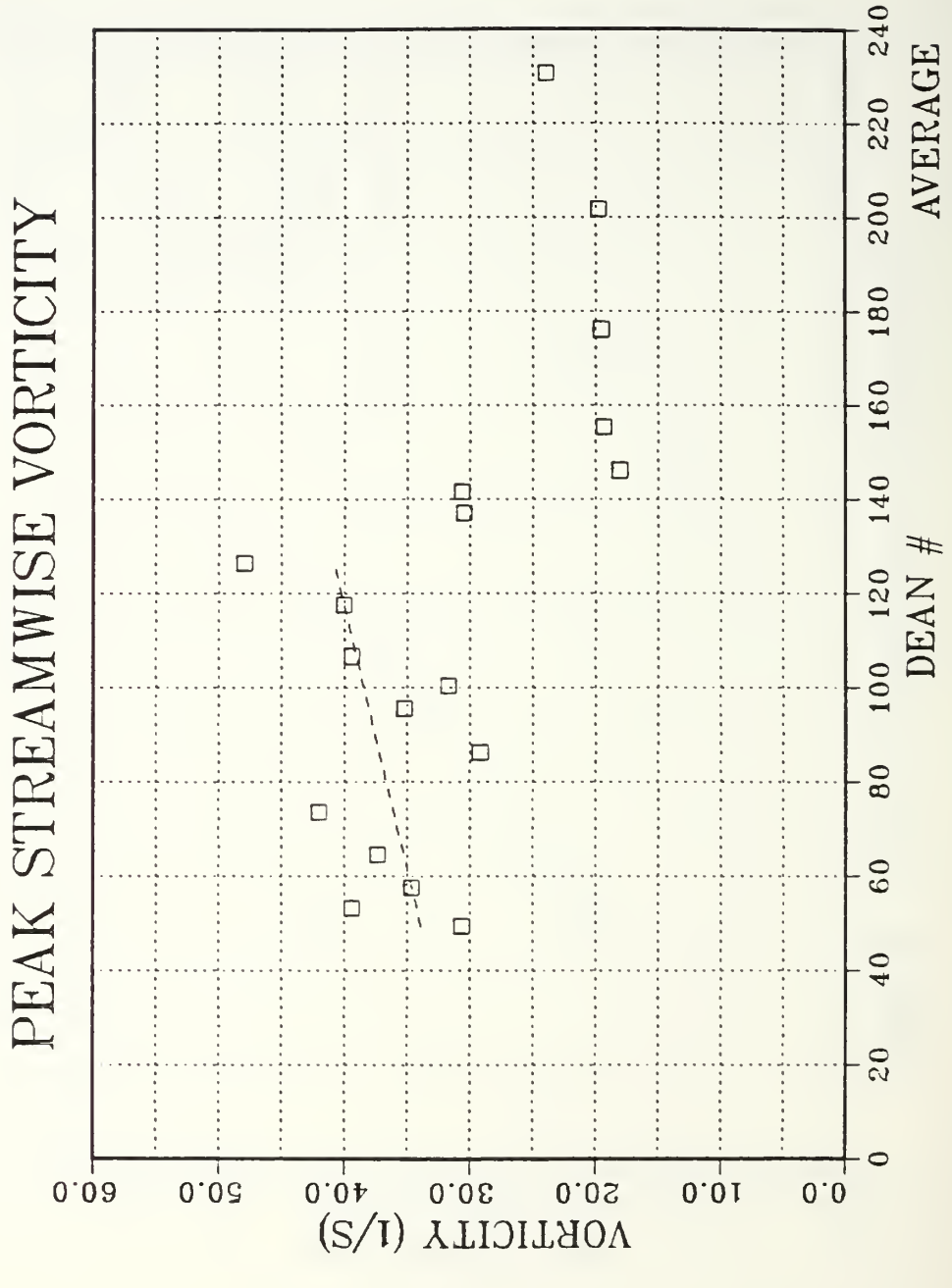

Figure 44. Peak Streamwise Vorticity vs. Dean #, Total Measured Area

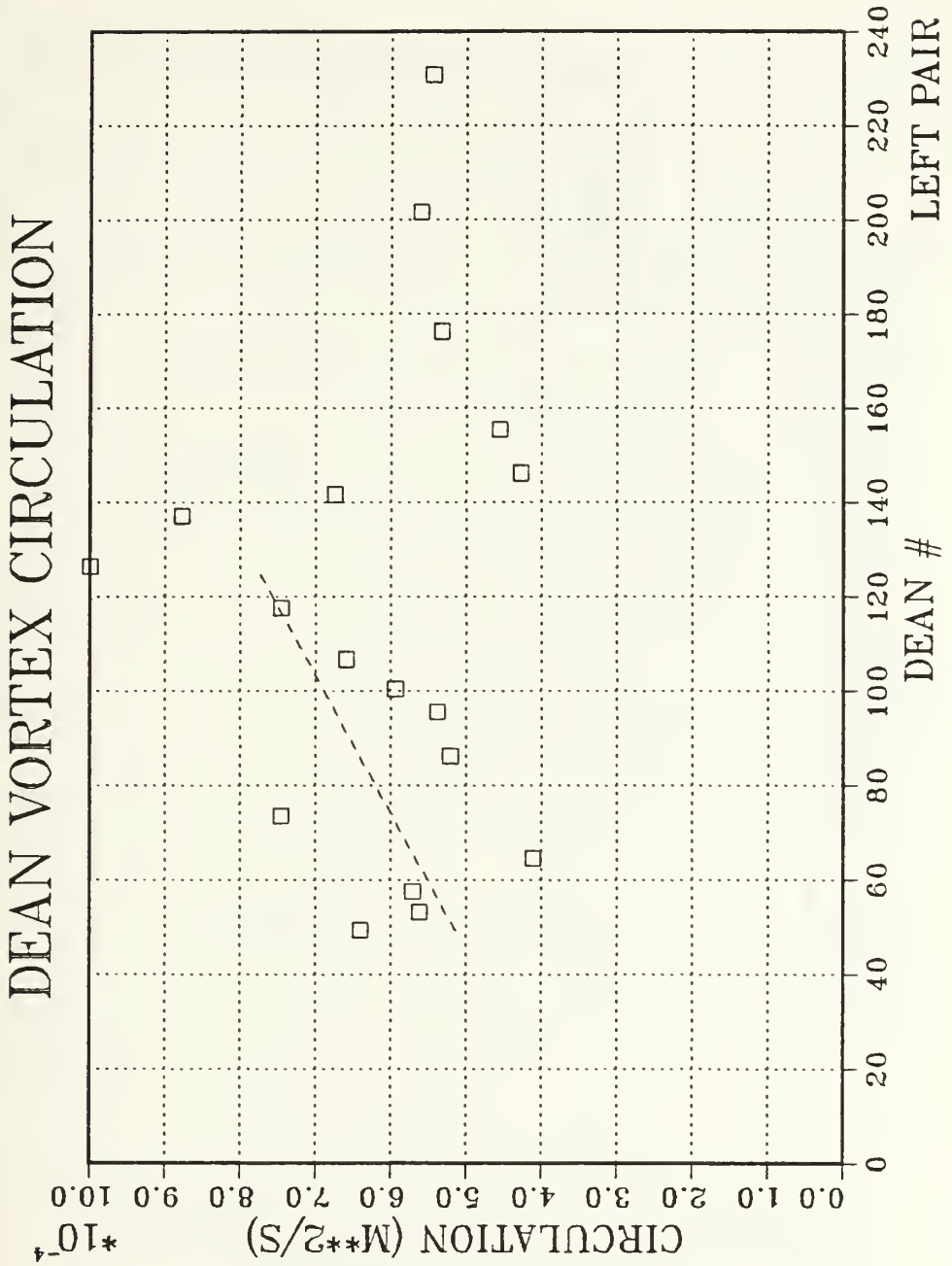

Figure 45. Vortex Circulation vs. Dean #, Left Vortex Pair

Figure 46. Vortex Circulation vs. Dean #, Middle Vortex Pair

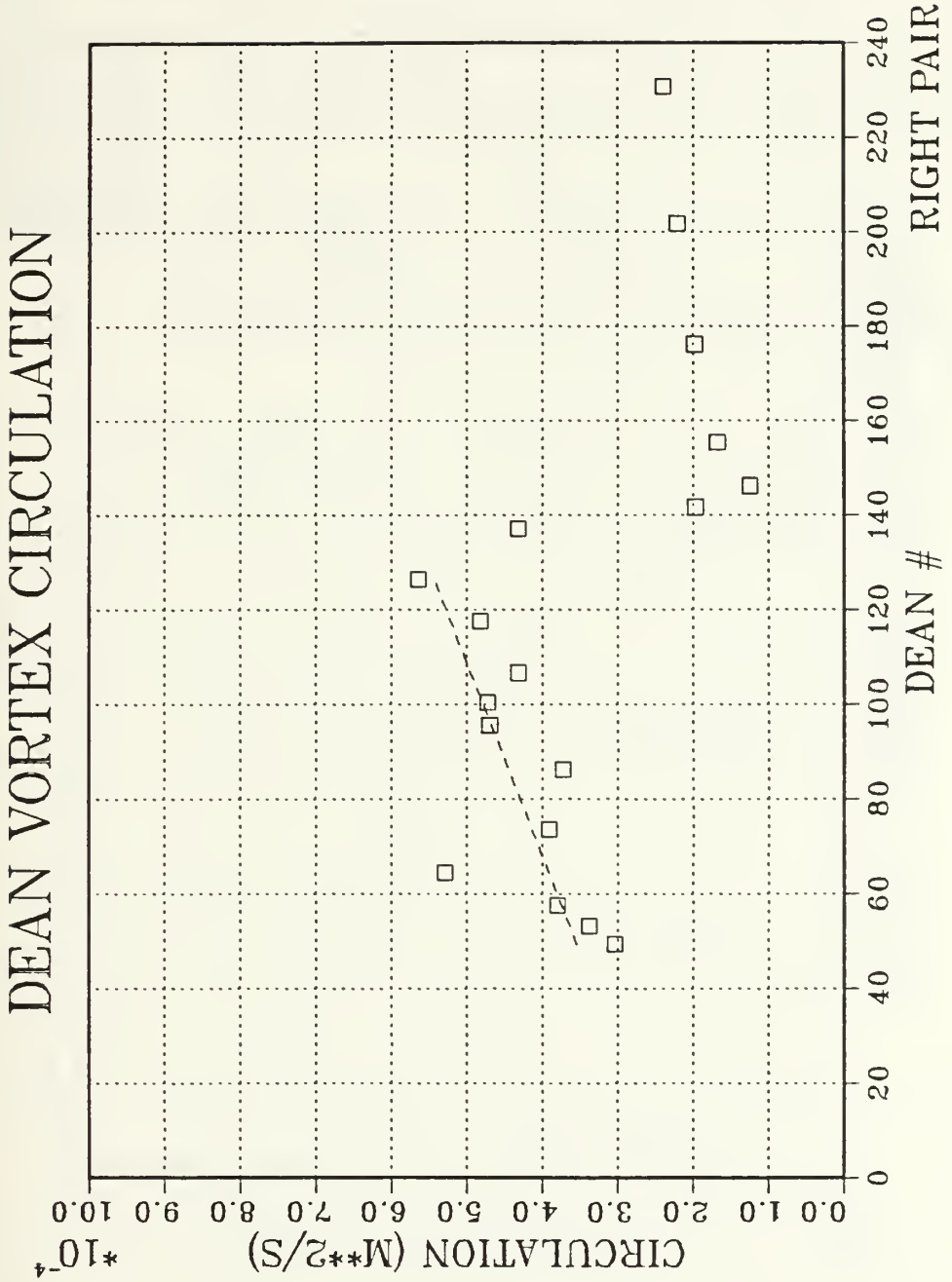

Figure 47. Vortex Circulation vs. Dean #, Right Vortex Pair

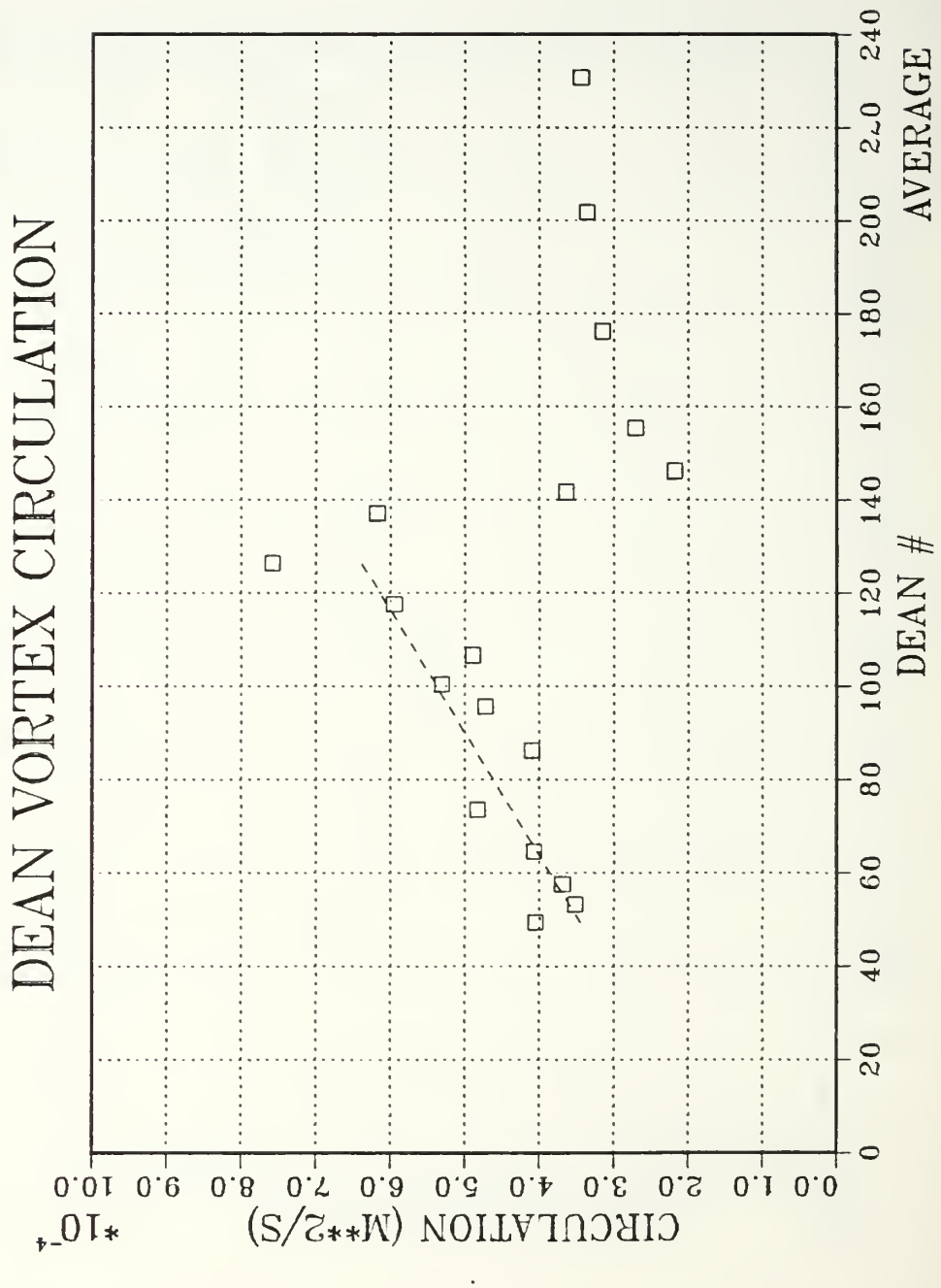

Figure 48. Vortex Circulation vs. Dean #, Average Vortex Pair

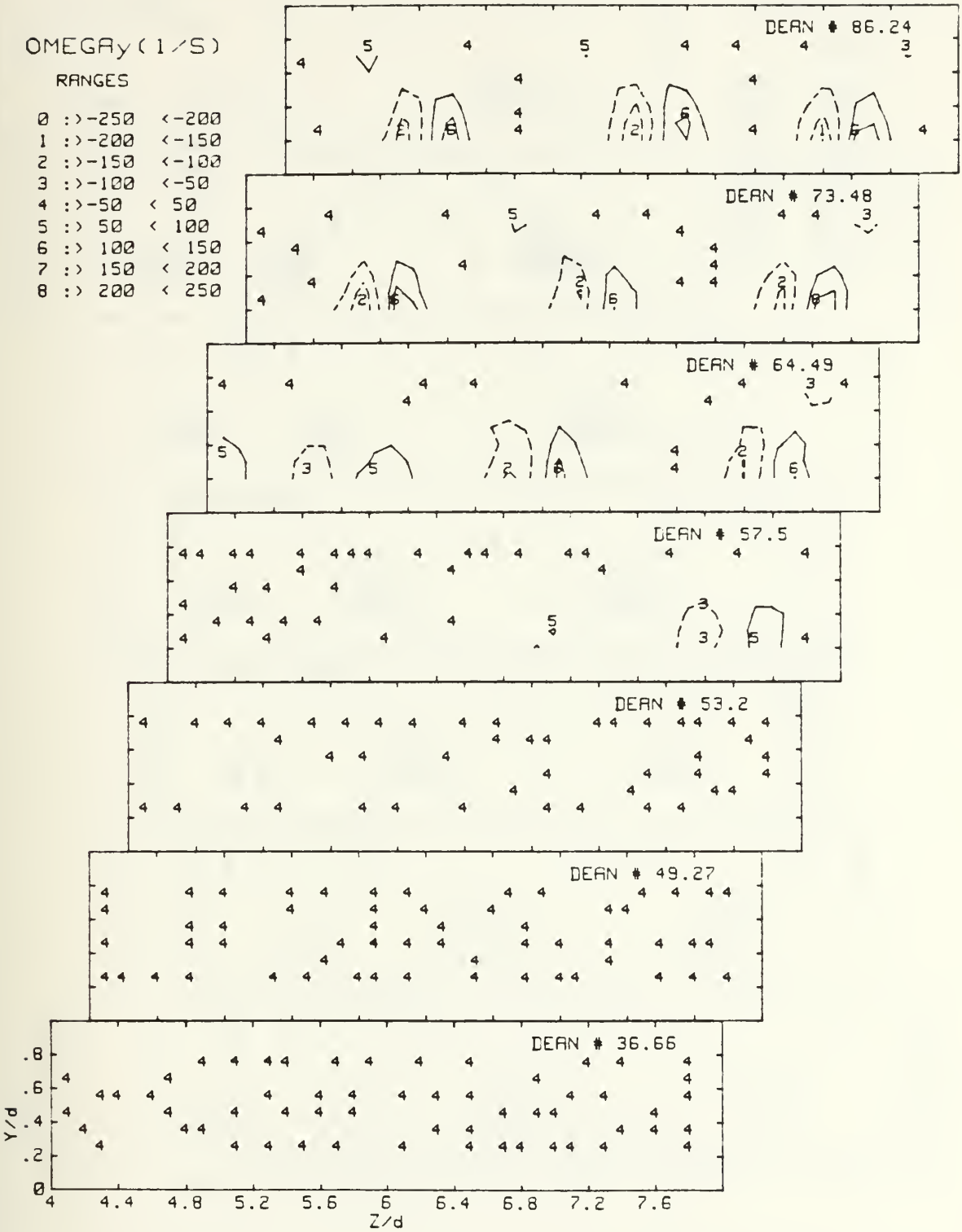

Figure 49. Radial Vorticity Contours, De=36.6 to De=86.2

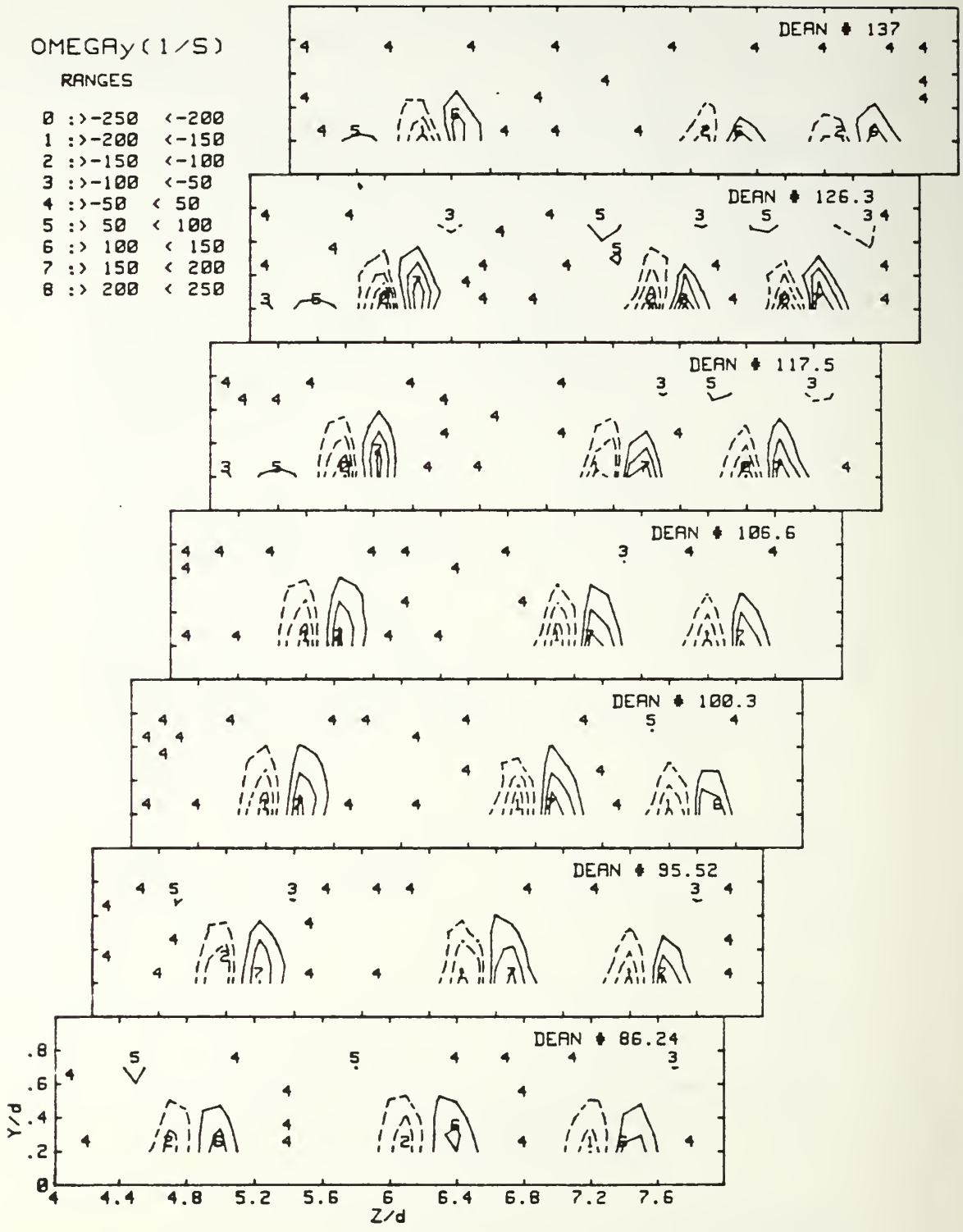

Figure 50. Radial Vorticity Contours, De=86.2 to De=137.0

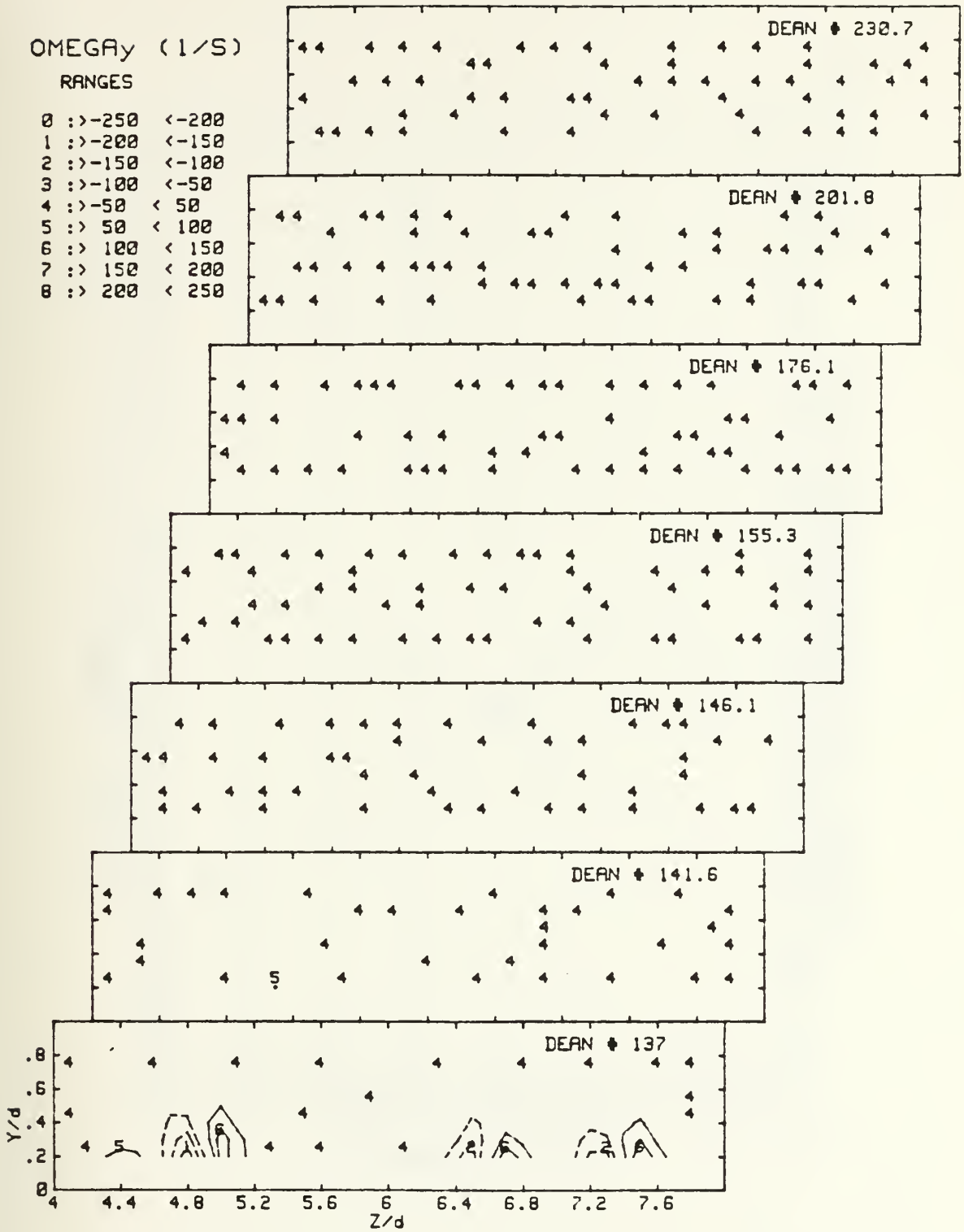

Figure 51. Radial Vorticity Contours, De=137.0 to De=230.7

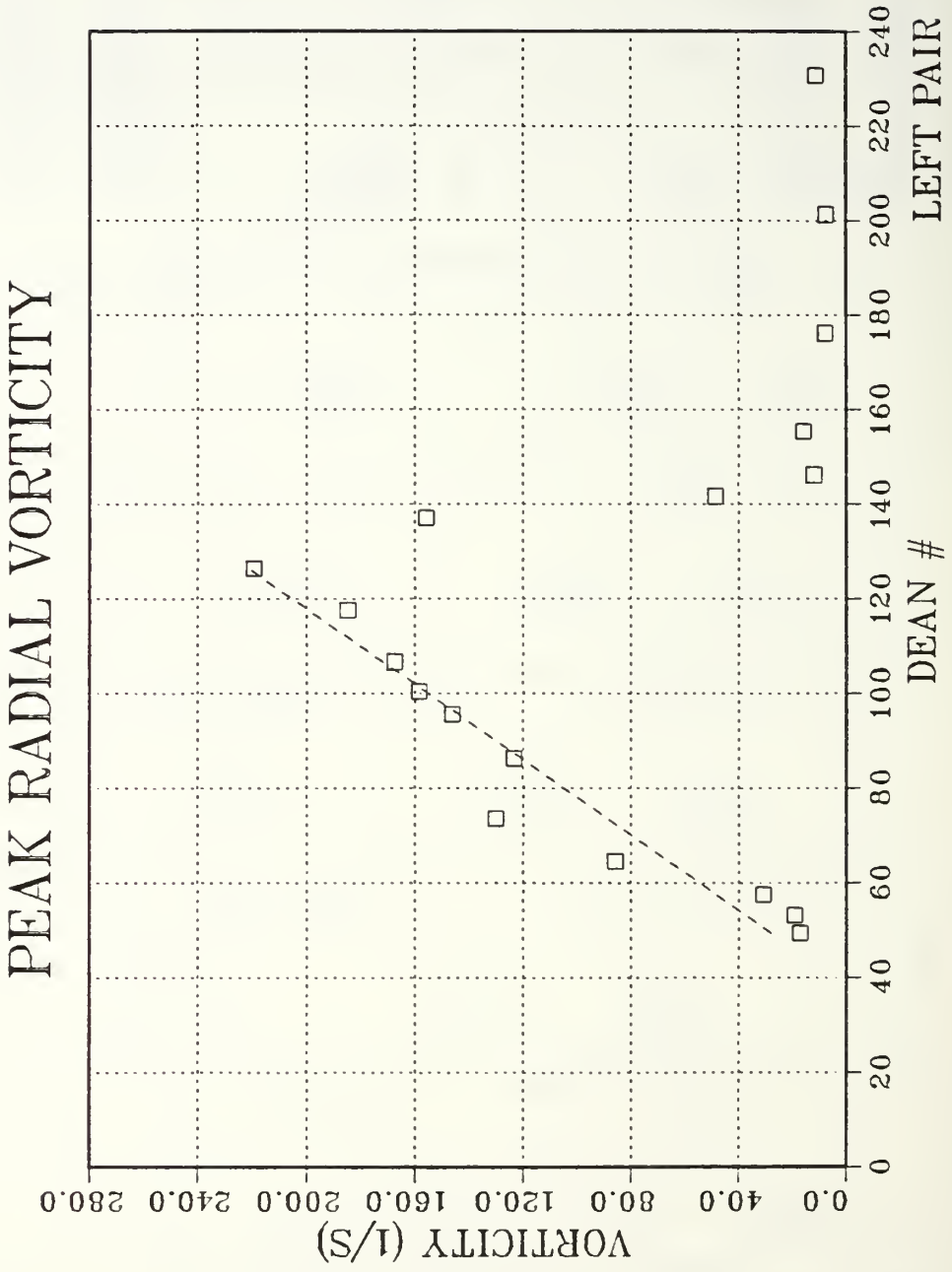

Figure 52. Peak Radial Vorticity vs. Dean #, Left Vortex Pair

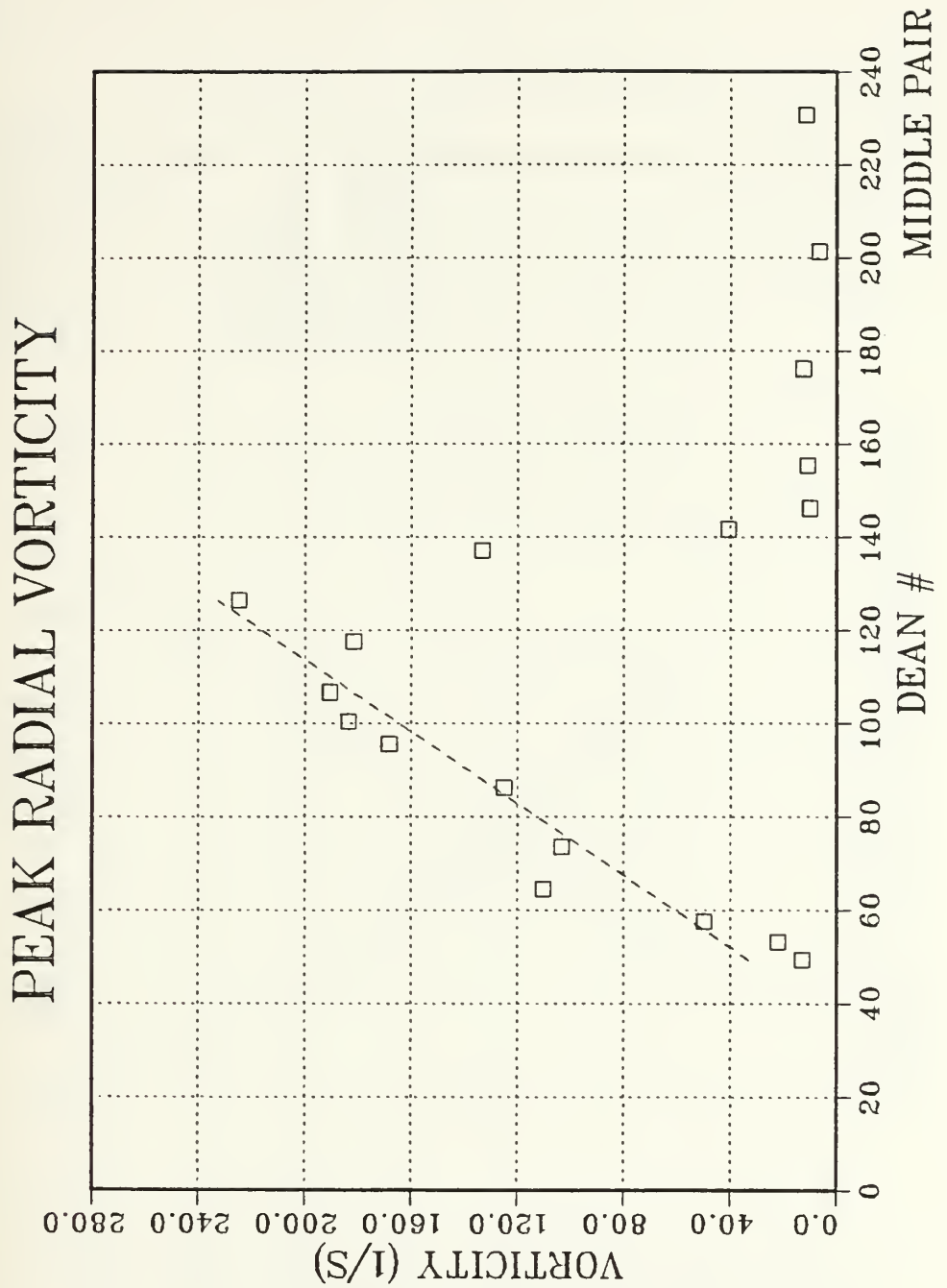

Figure 53. Peak Radial Vorticity vs. Dean #, Middle Vortex Pair

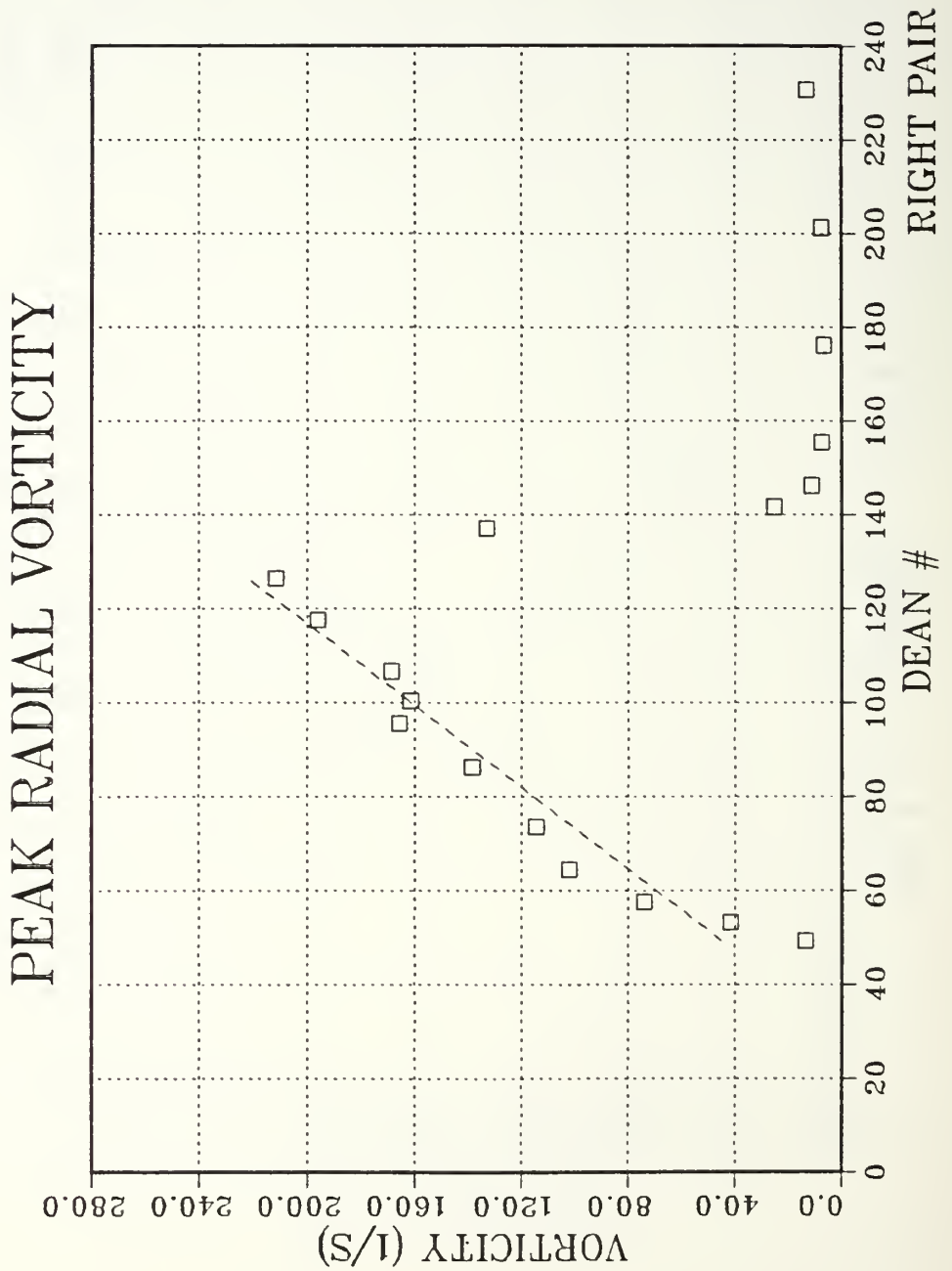

Figure 54. Peak Radial Vorticity vs. Dean #, Right Vortex Pair

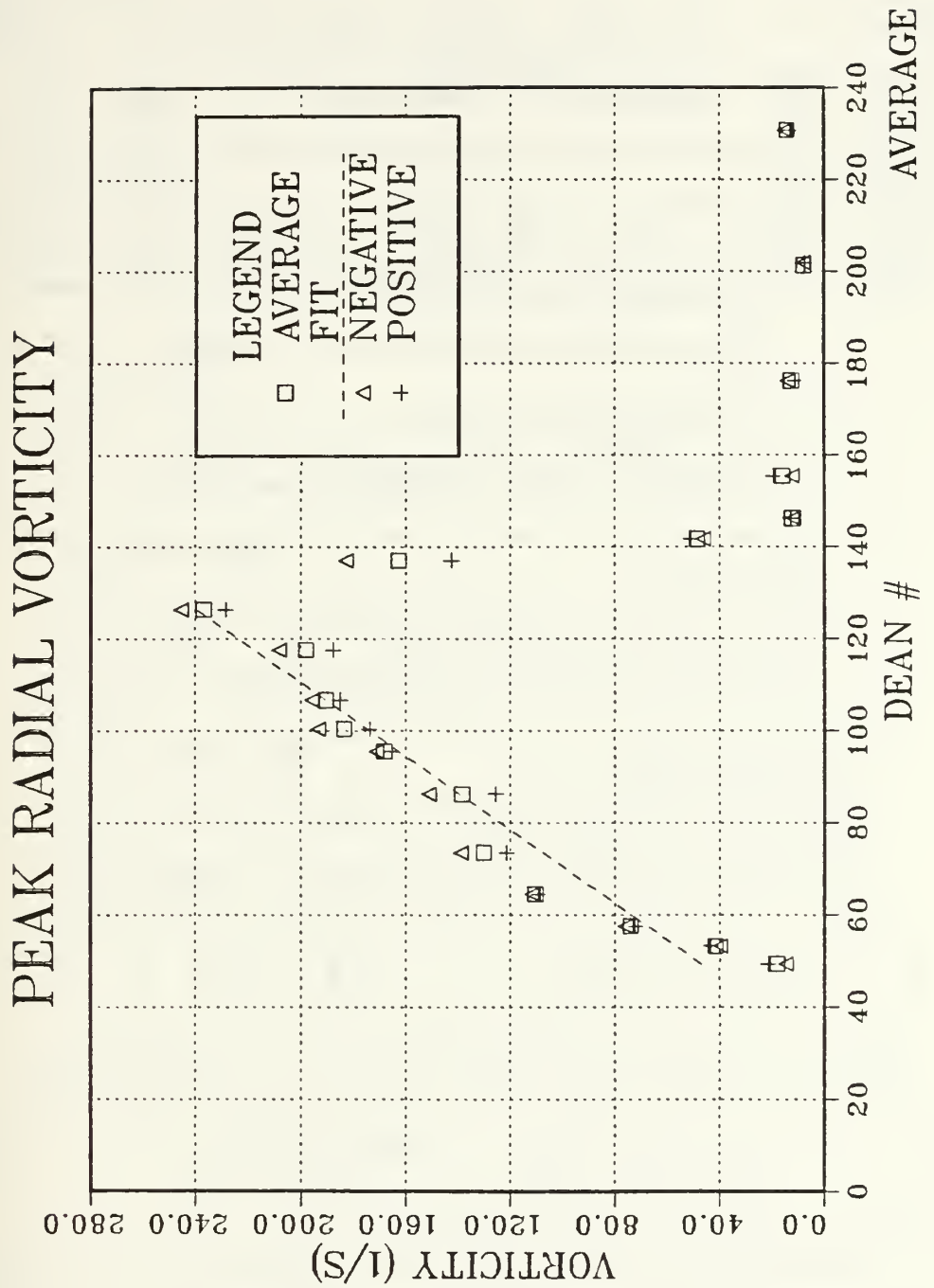

Figure 55. Peak Radial Vorticity vs. Dean #, Total Measured Area

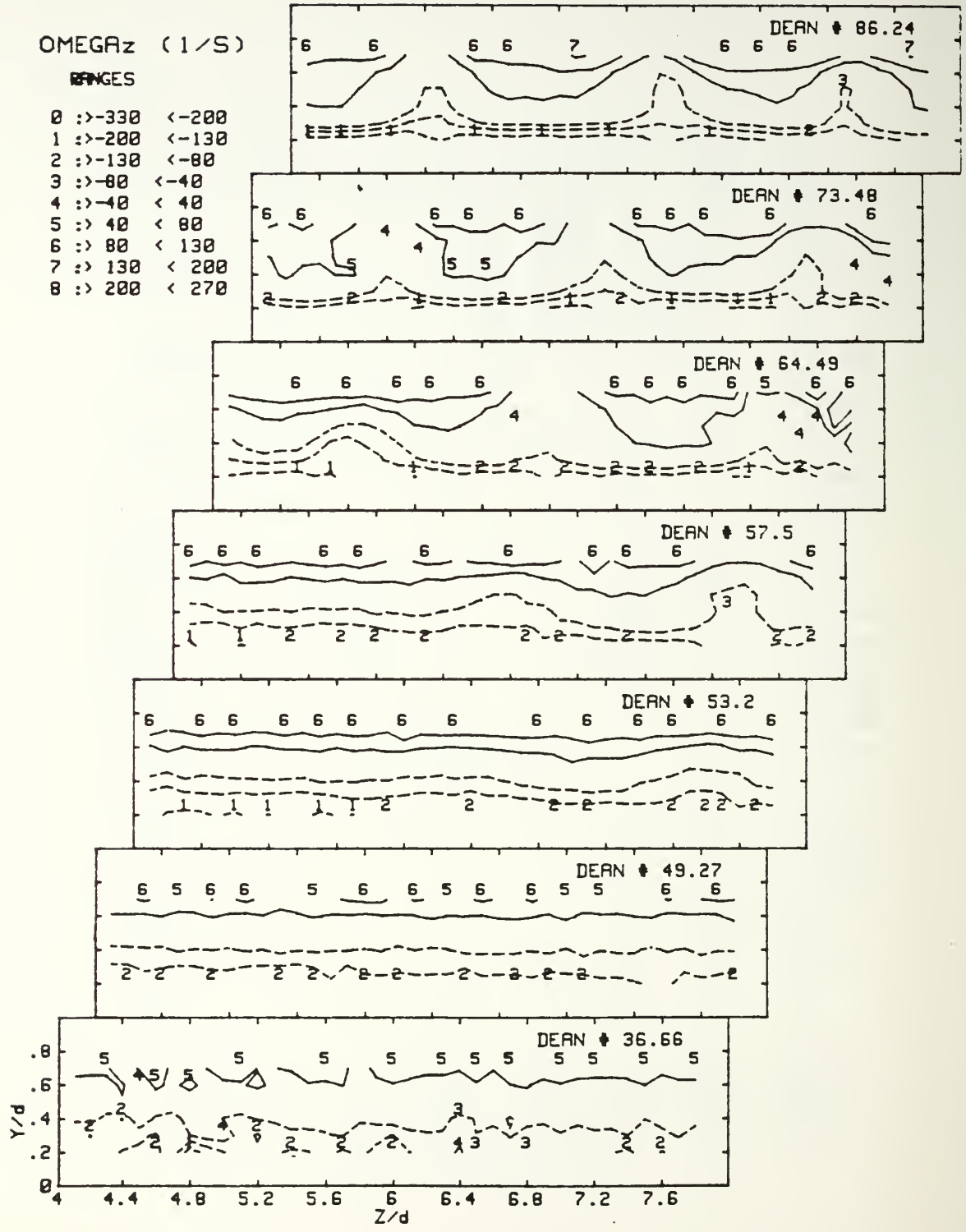

Figure 56. Spanwise Vorticity Contours, De=36.6 to De=86.2

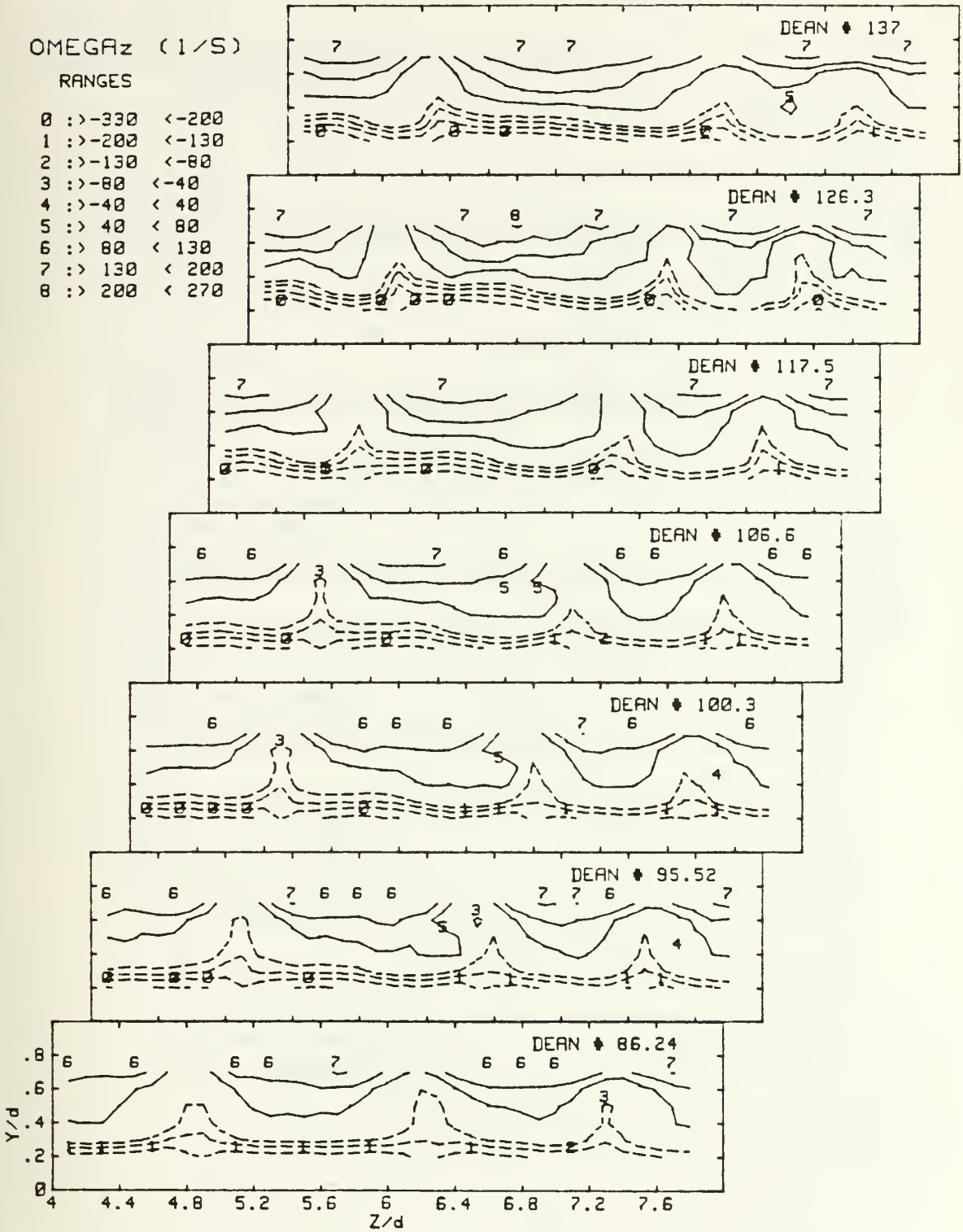

Figure 57. Spanwise Vorticity Contours, De=86.2 to De=137.0

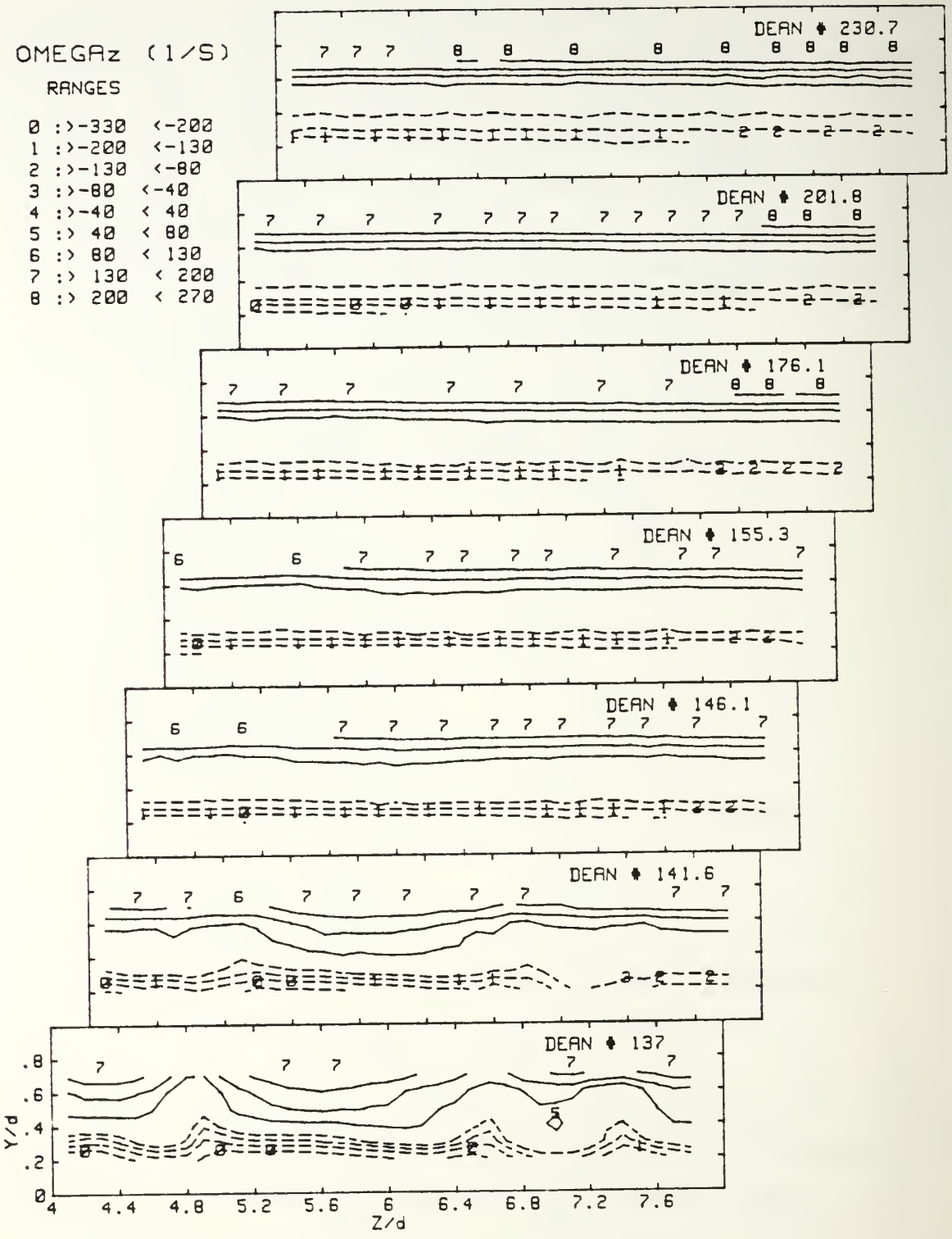

Figure 58. Spanwise Vorticity Contours, De=137.0 to De=230.7

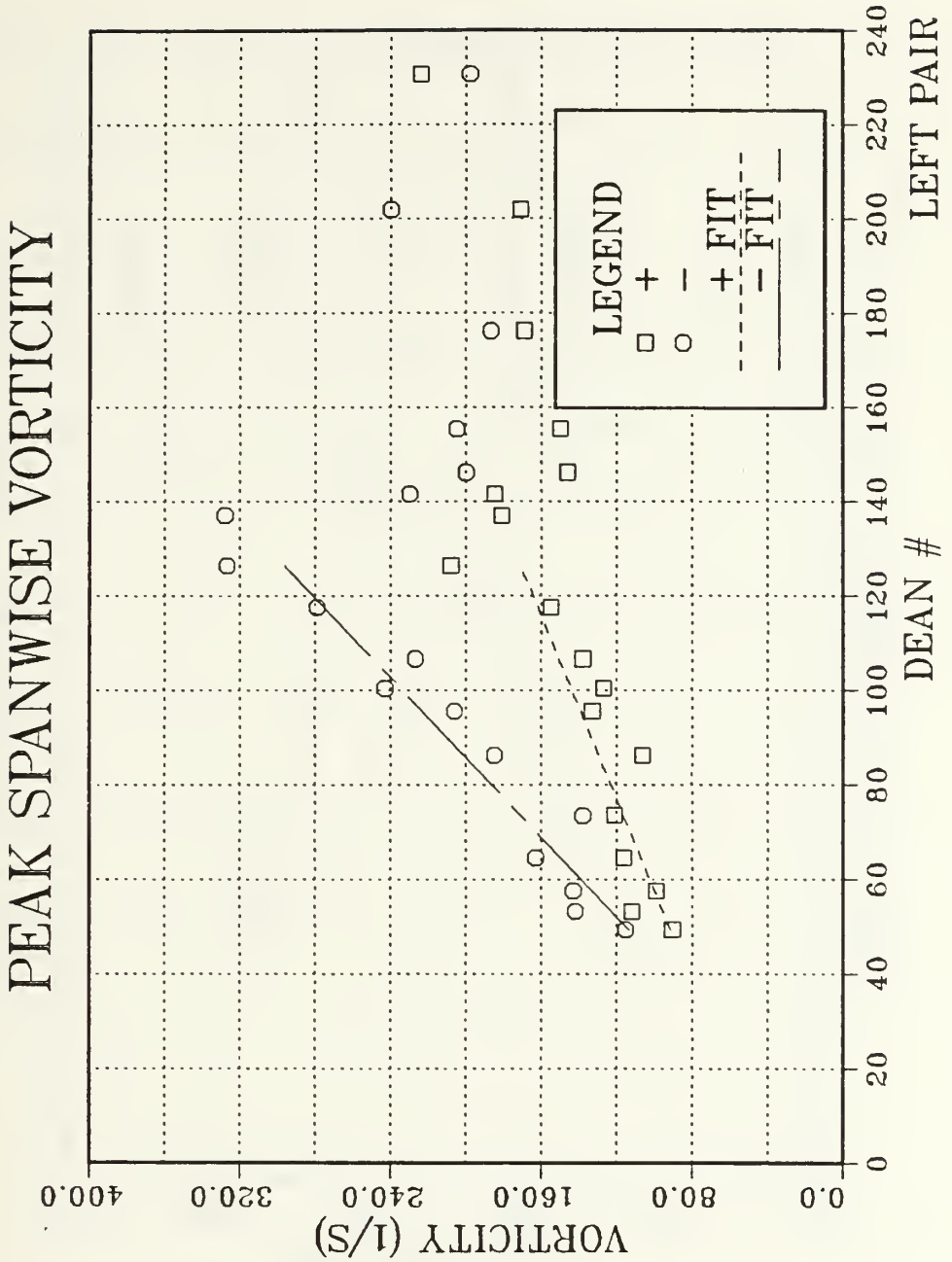

Figure 59. Peak Spanwise Vorticity vs. Dean #, Left Vortex Pair

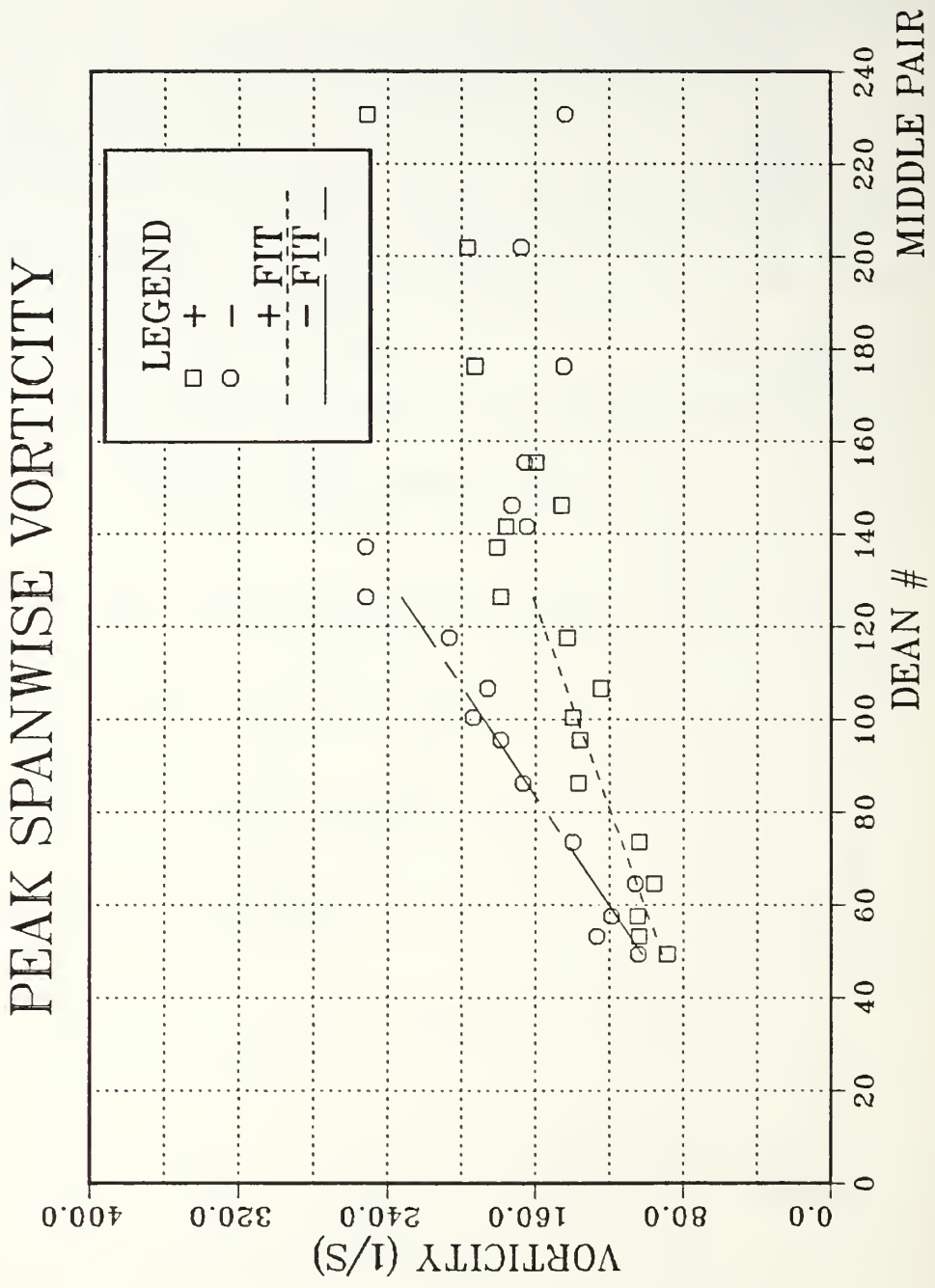

Figure 60. Peak Spanwise Vorticity vs. Dean #, Middle Vortex Pair

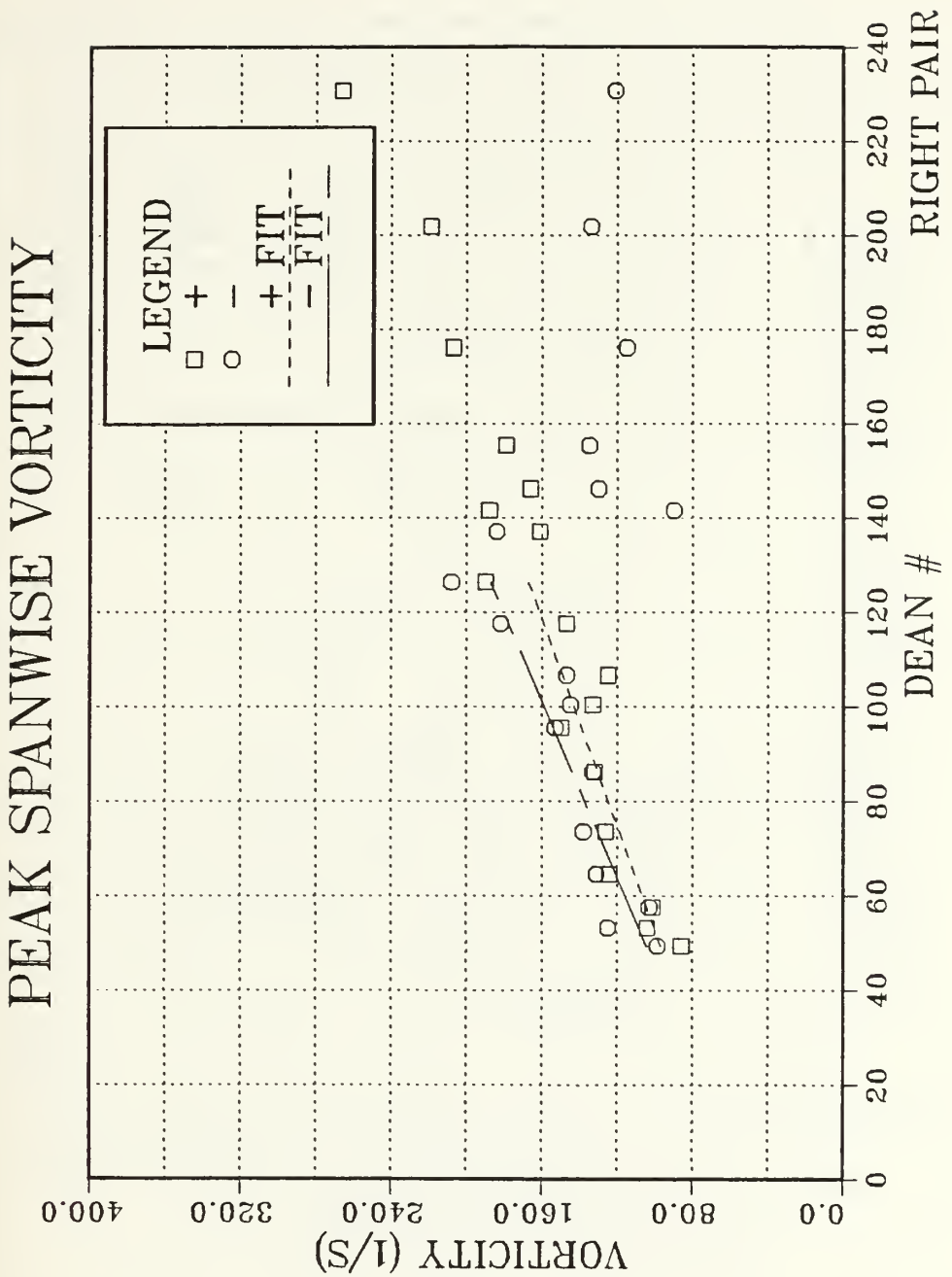

Figure 61. Peak Spanwise Vorticity vs. Dean #, Right Vortex Pair

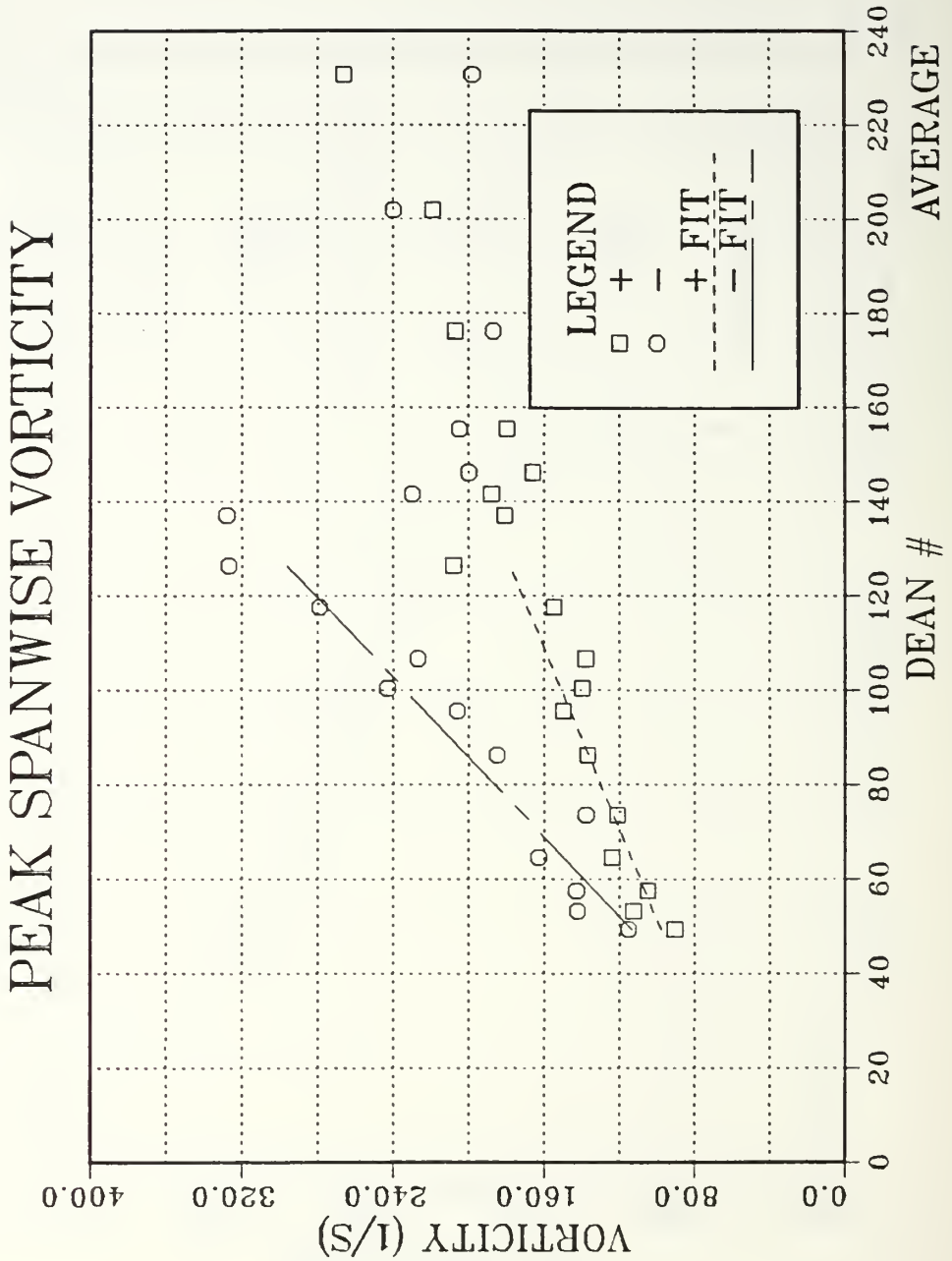

Figure 62. Peak Spanwise Vorticity vs. Dean #, Total Measured Area

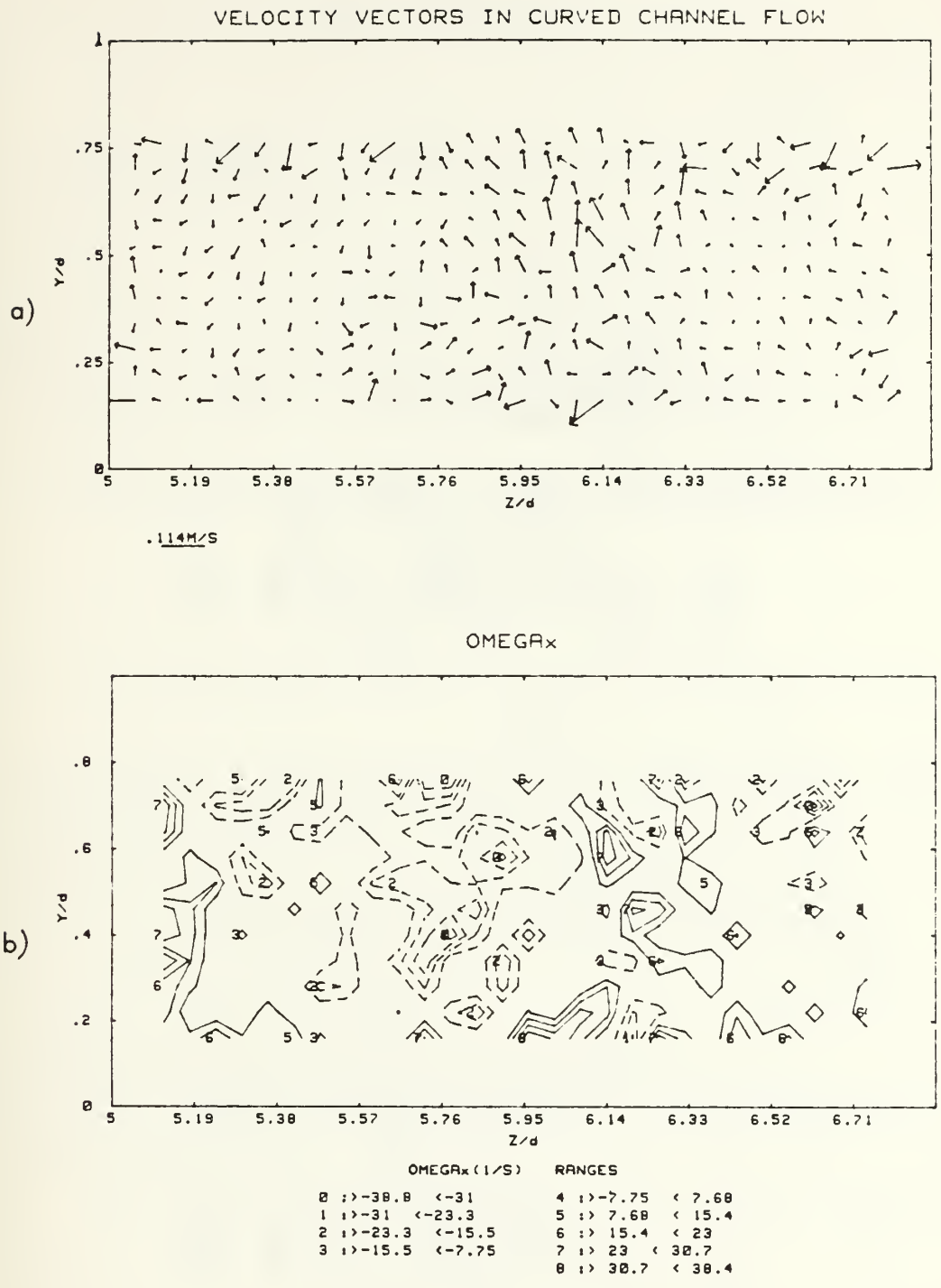

Figure 63. De=77.9, a) Secondary Flow Vectors
b) Streamwise Vorticity Contours

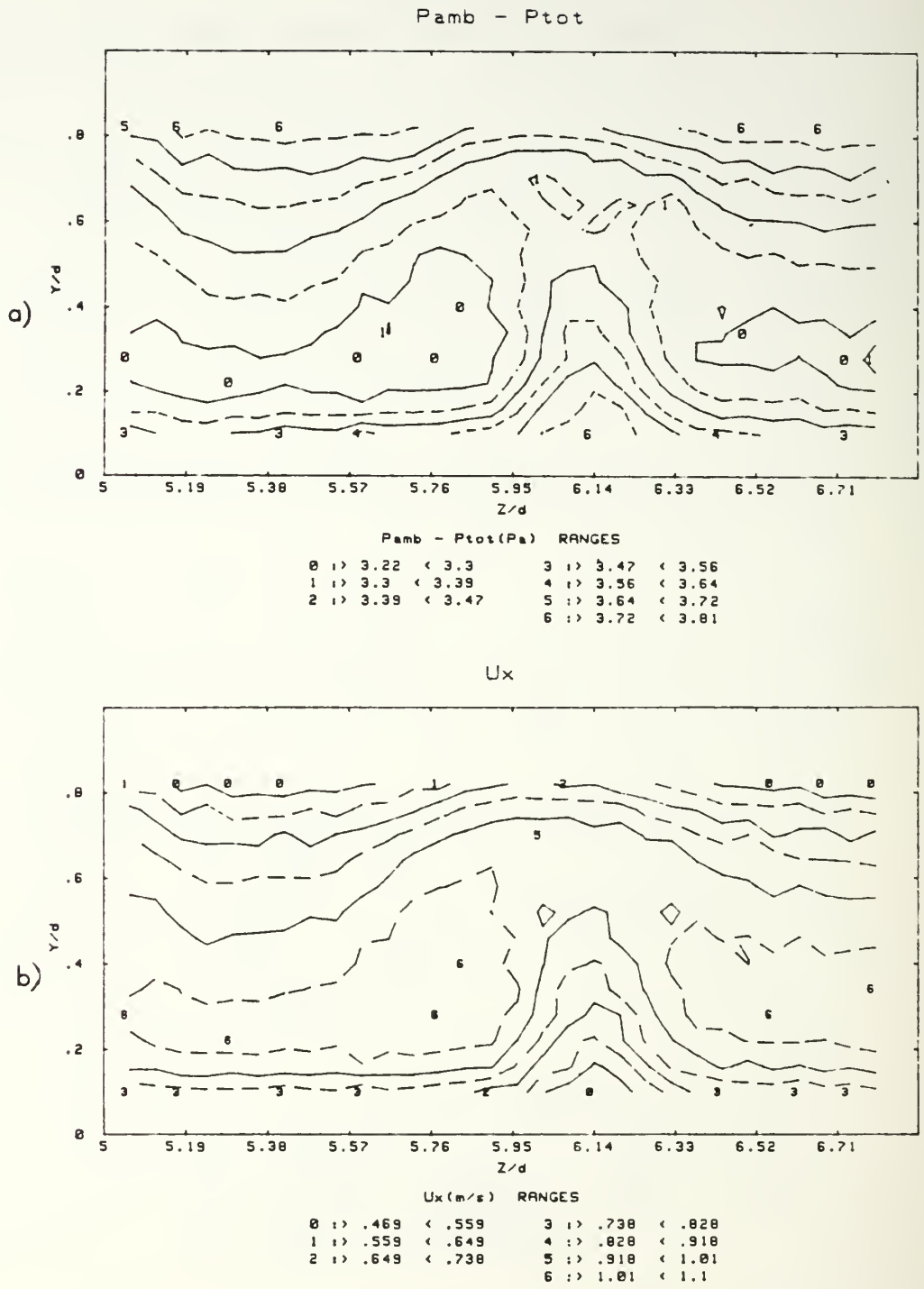

Figure 64. De=77.9, a) Total Pressure Contours
b) Streamwise Velocity Contours

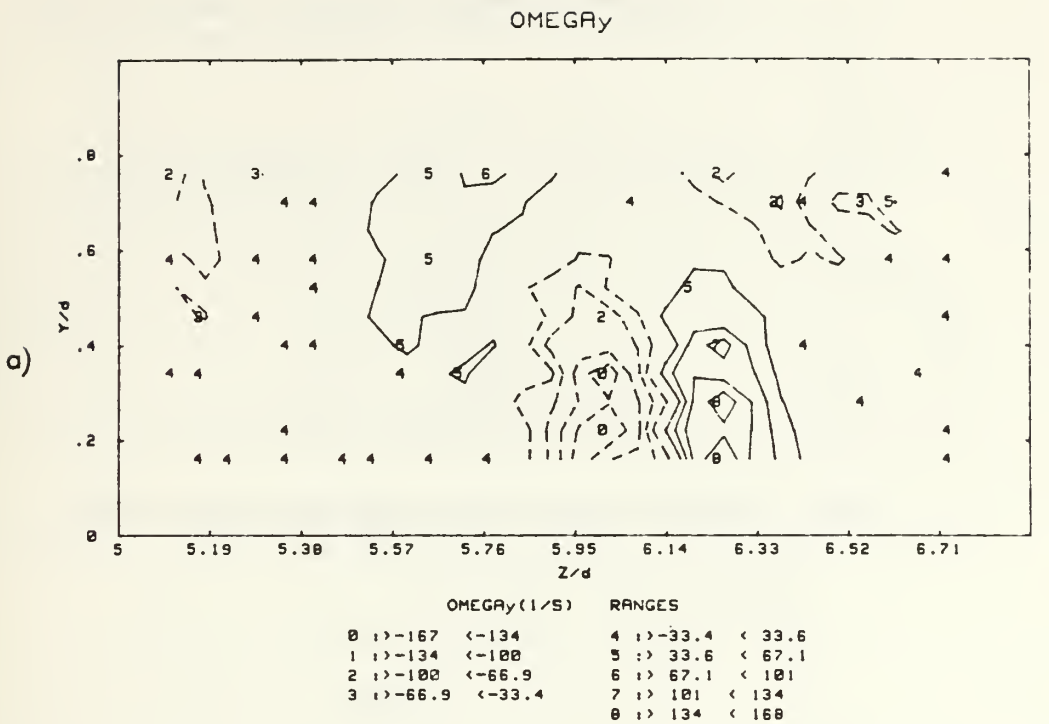

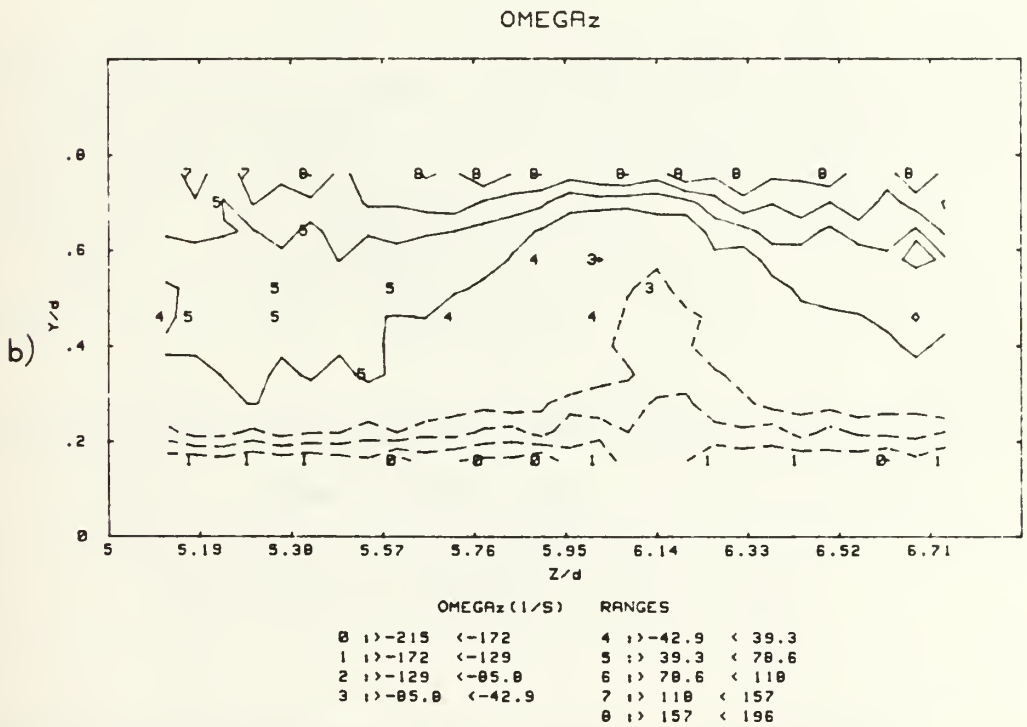

Figure 65. De=77.9, a) Radial Vorticity Contours
b) Spanwise Vorticity Contours

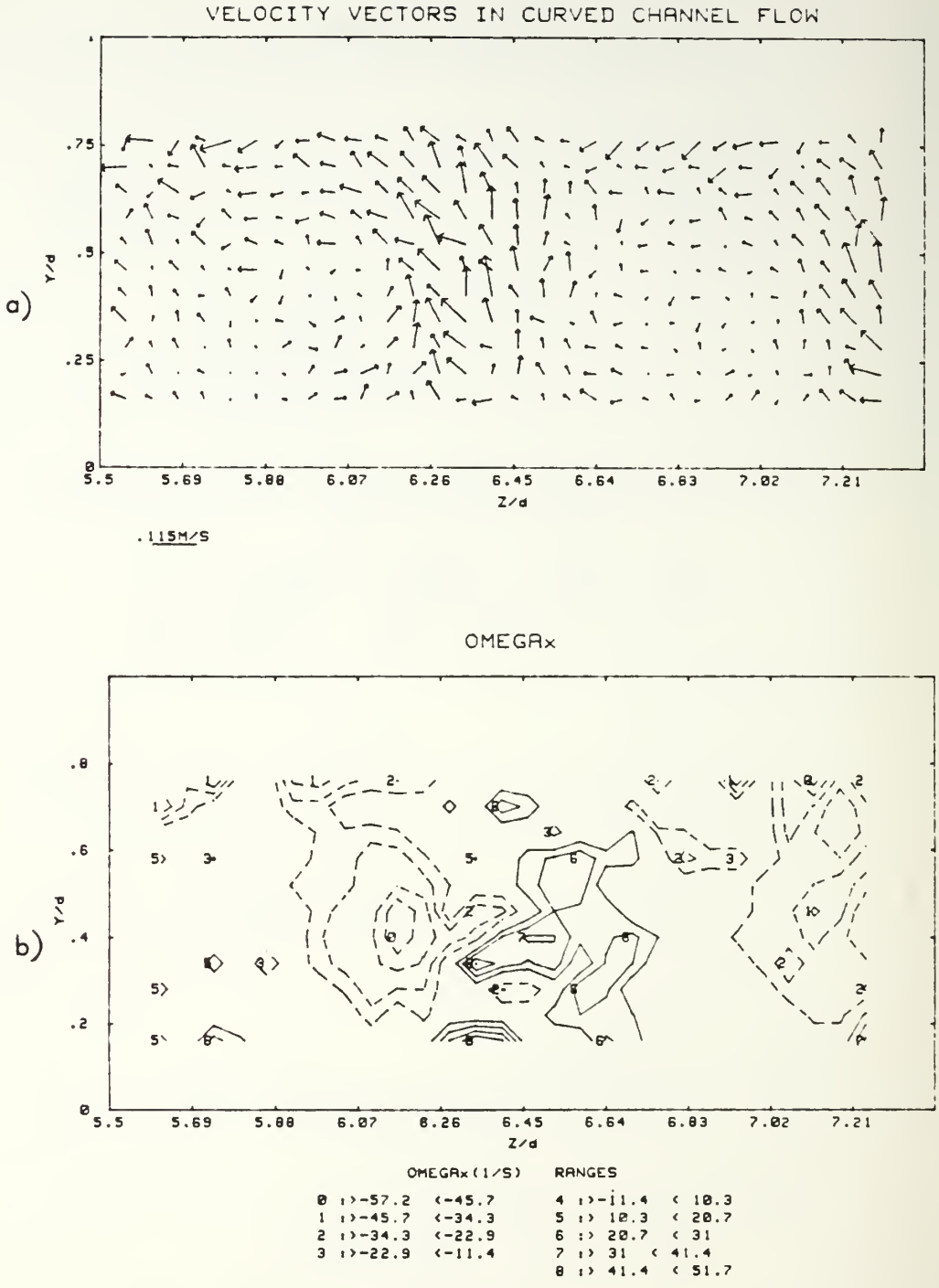

Figure 66. De=102.2, a) Secondary Flow Vectors
b) Streamwise Vorticity Contours

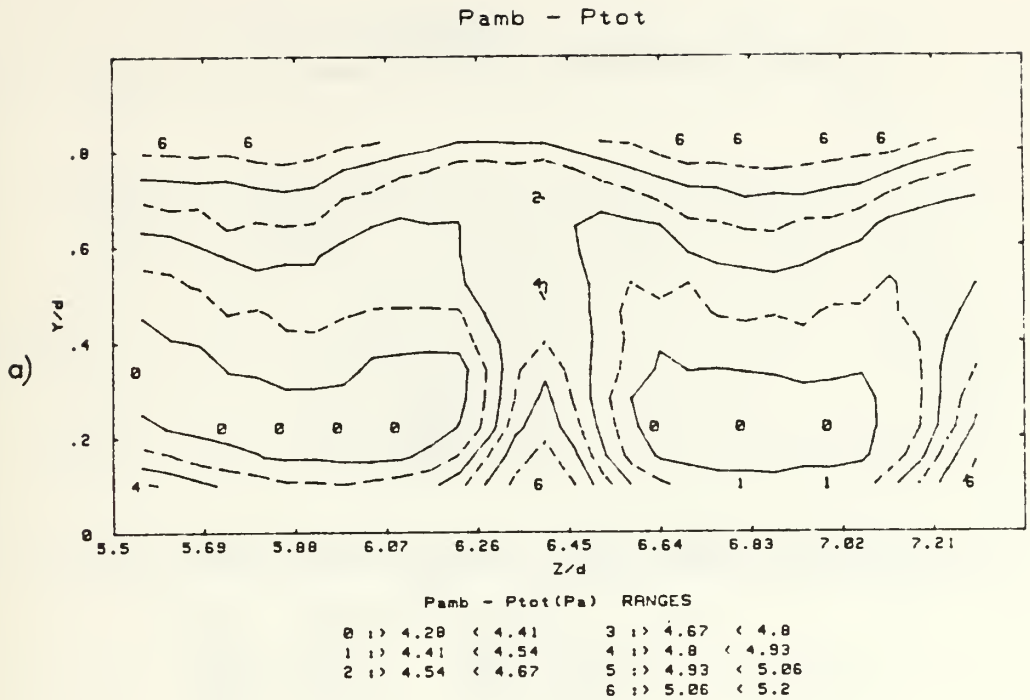

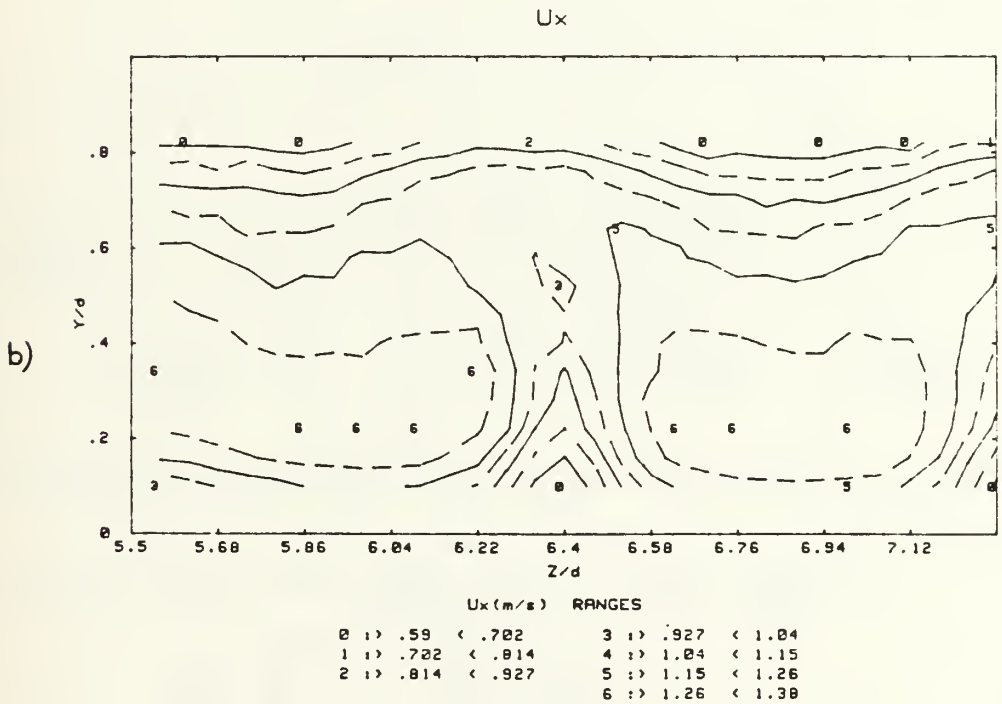

Figure 67. De=102.2, a) Total Pressure Contours
b) Streamwise Velocity Contours

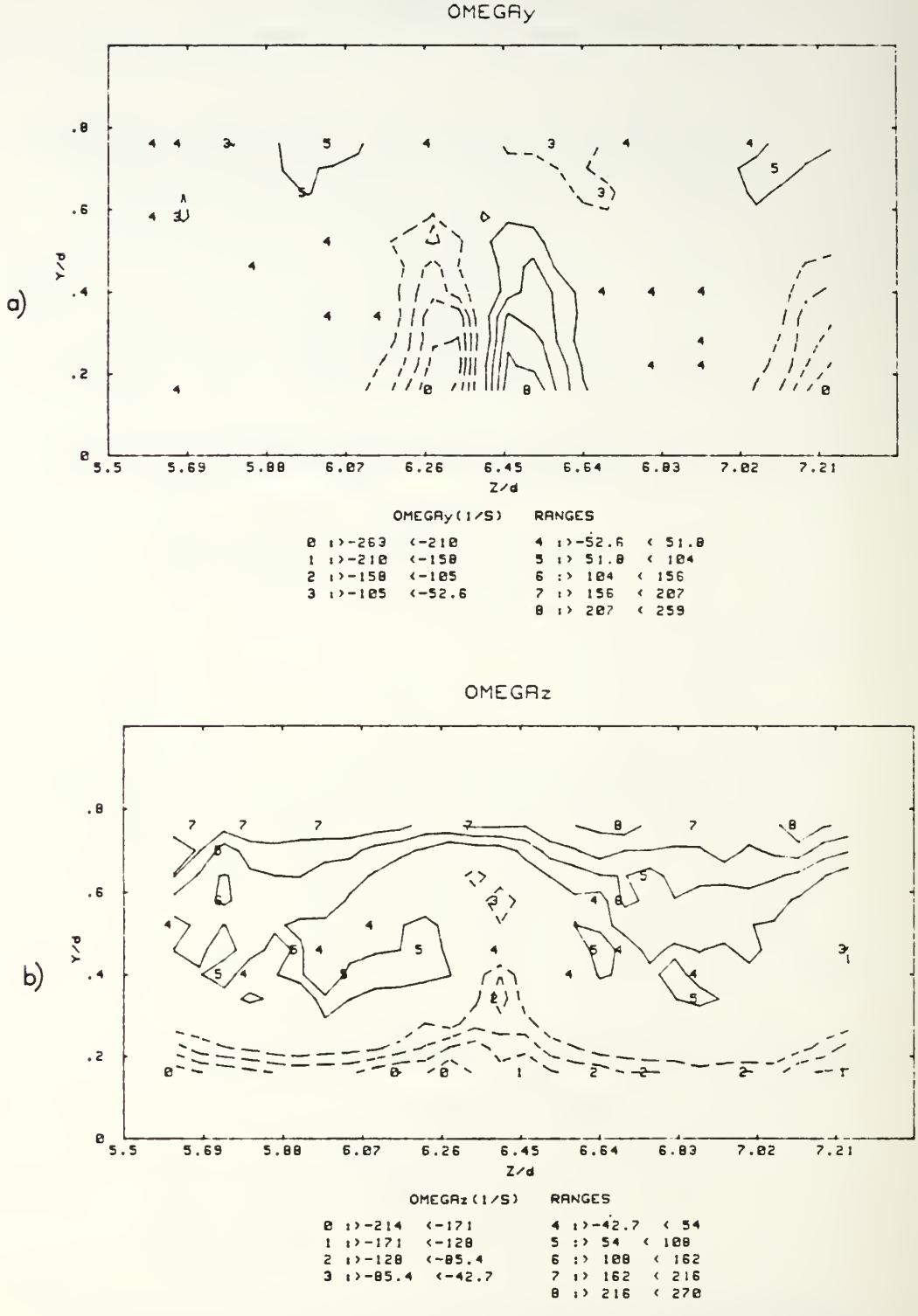

Figure 68. De=102.2, a) Radial Vorticity Contours
b) Spanwise Vorticity Contours

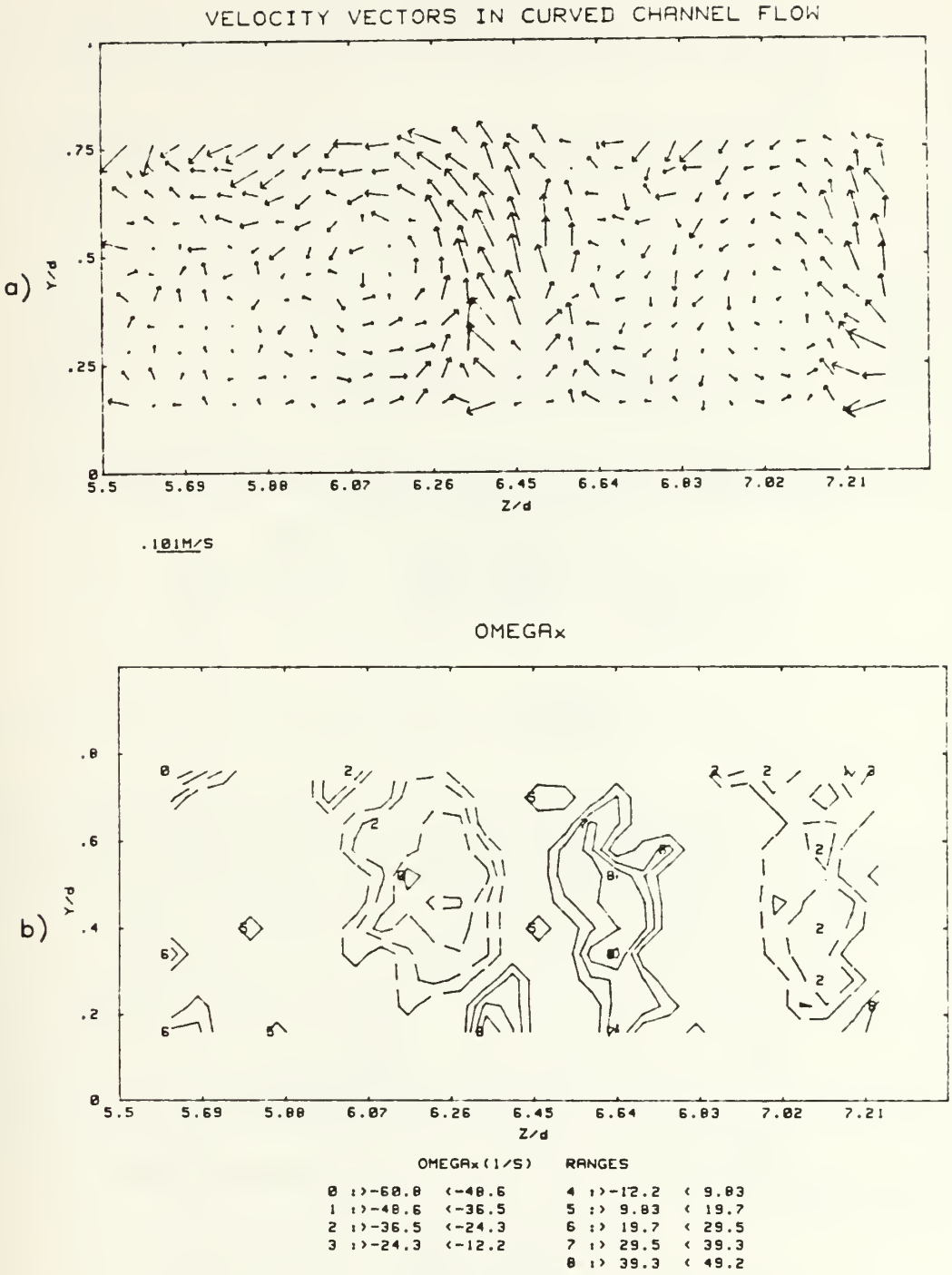

Figure 69. De=119.0, a) Secondary Flow Vectors
b) Spanwise Vorticity Contours

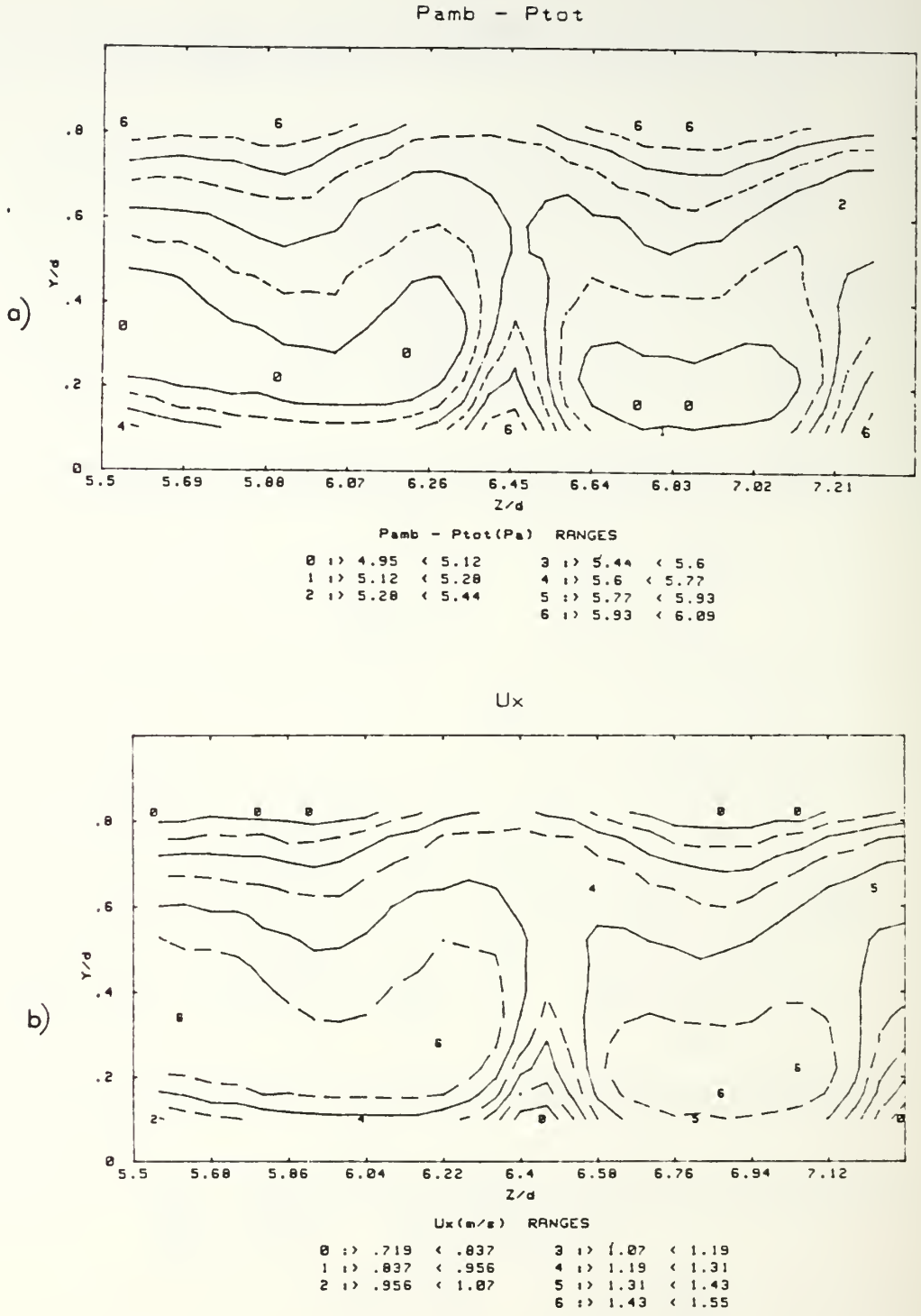

Figure 70. De=119.0, a) Total Pressure Contours
b) Streamwise Velocity Contours

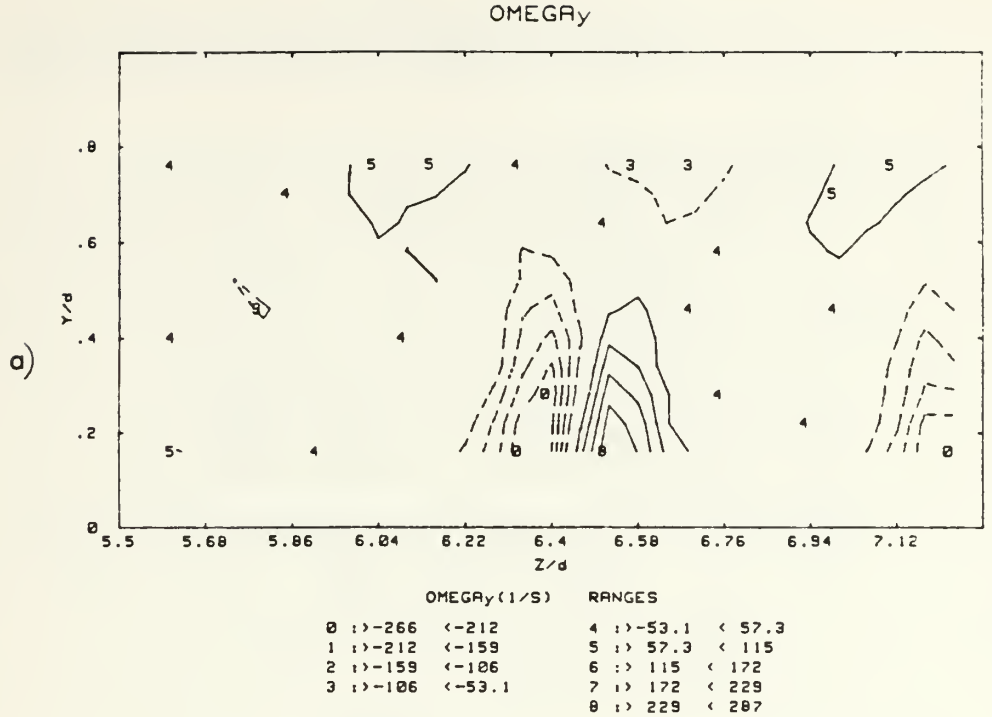

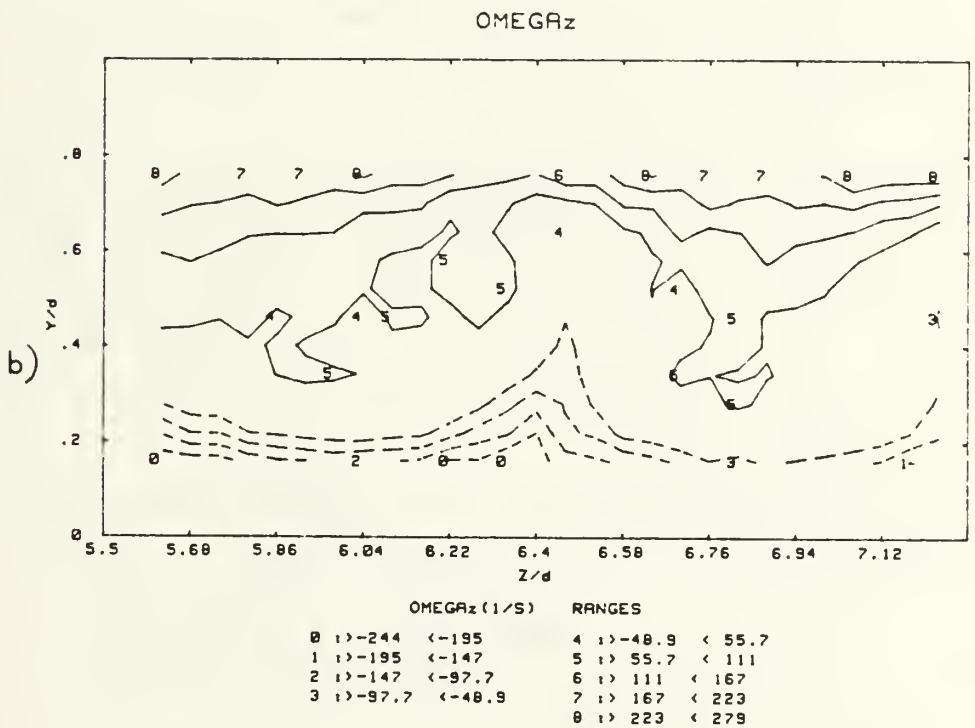

Figure 71. De=119.0, a) Radial Vorticity Contours
b) Spanwise Vorticity Contours

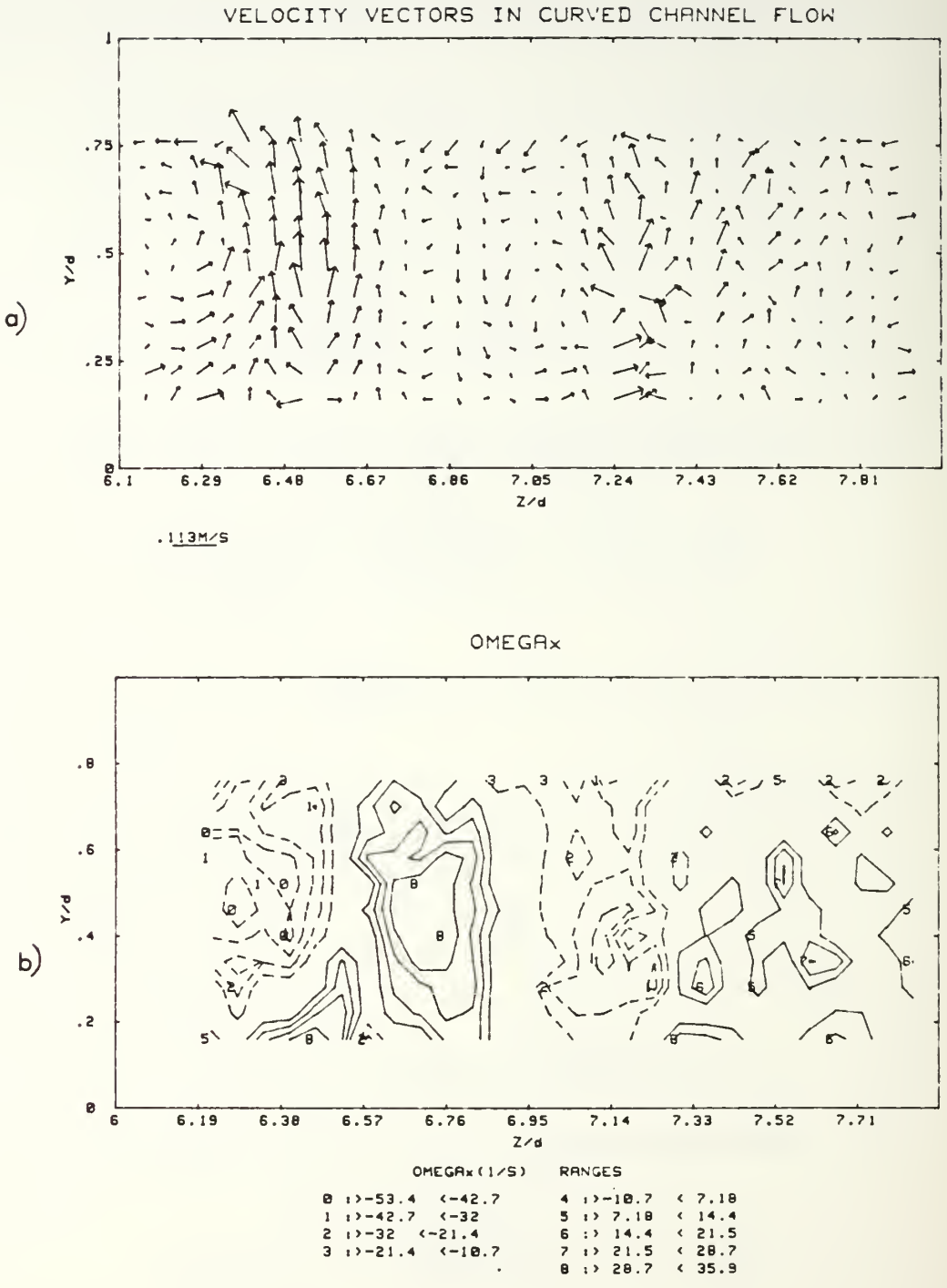

Figure 72. De=131.6, a) Secondary Flow Vectors
b) Streamwise Vorticity Contours

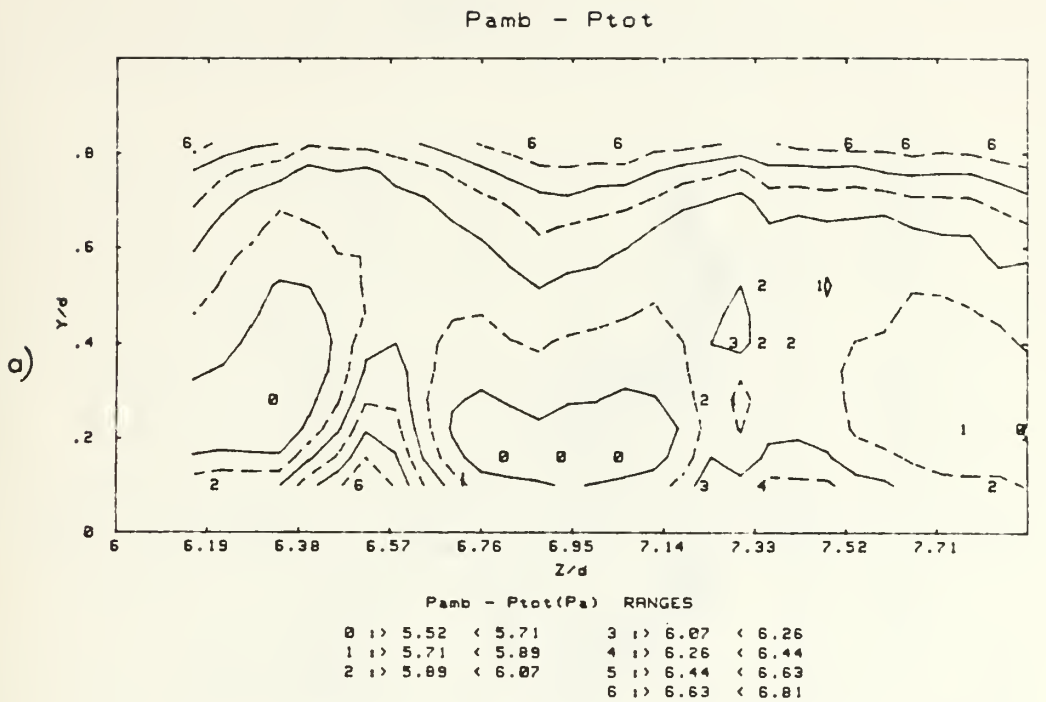

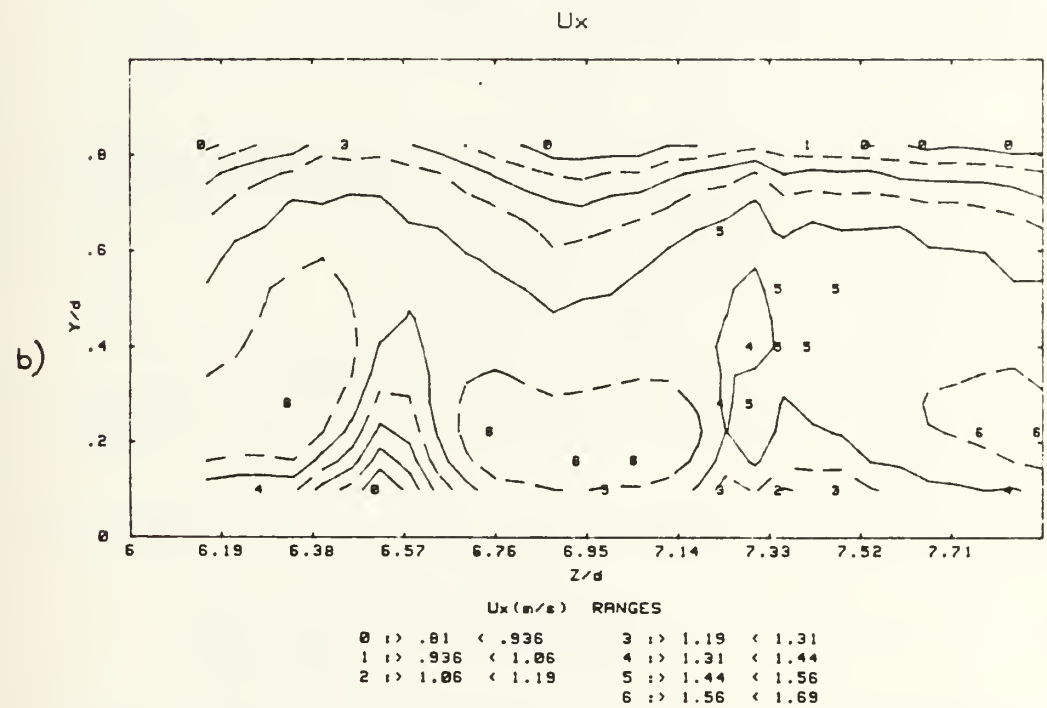

Figure 73. De=131.6, a) Total Pressure Contours
b) Streamwise Velocity Contours

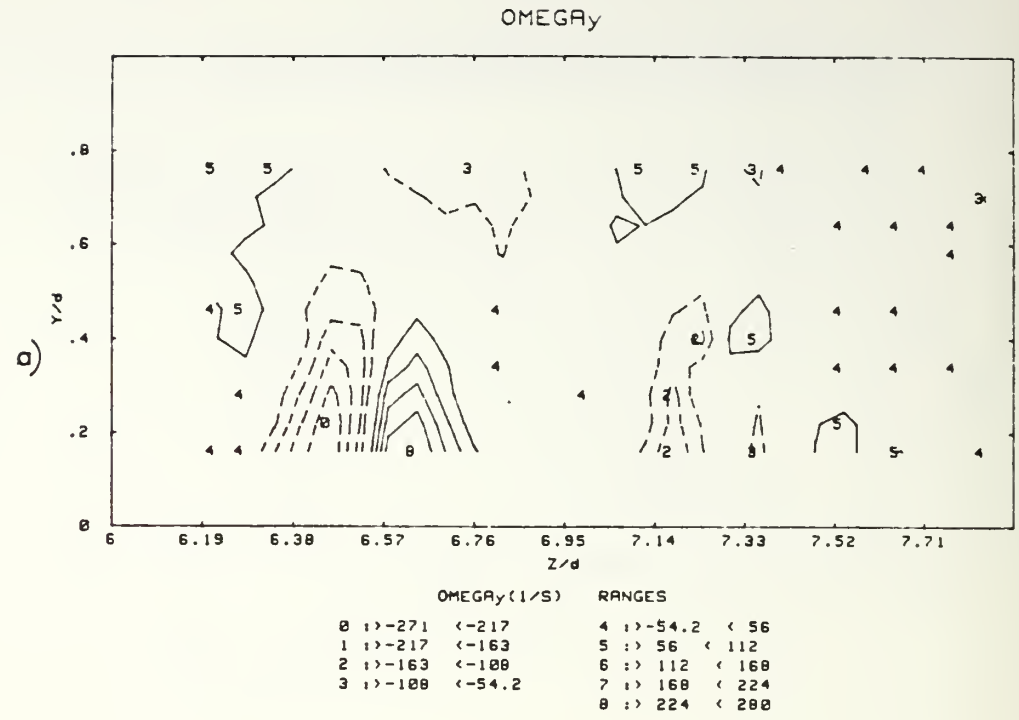

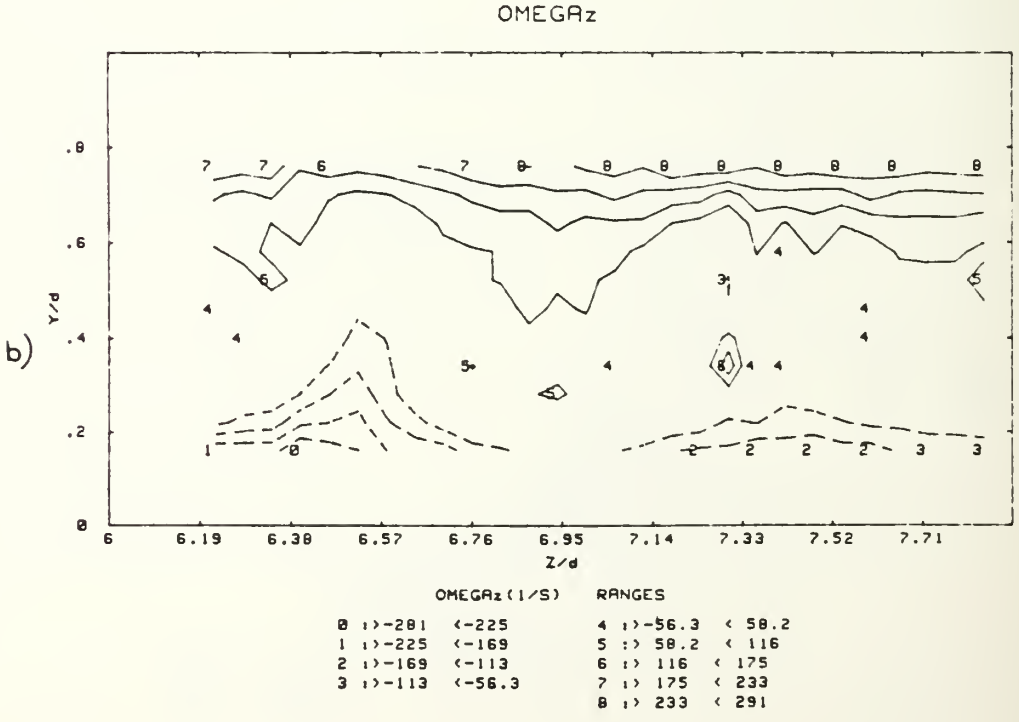

Figure 74. De=131.6, a) Radial Vorticity Contours
b) Spanwise Vorticity Contours

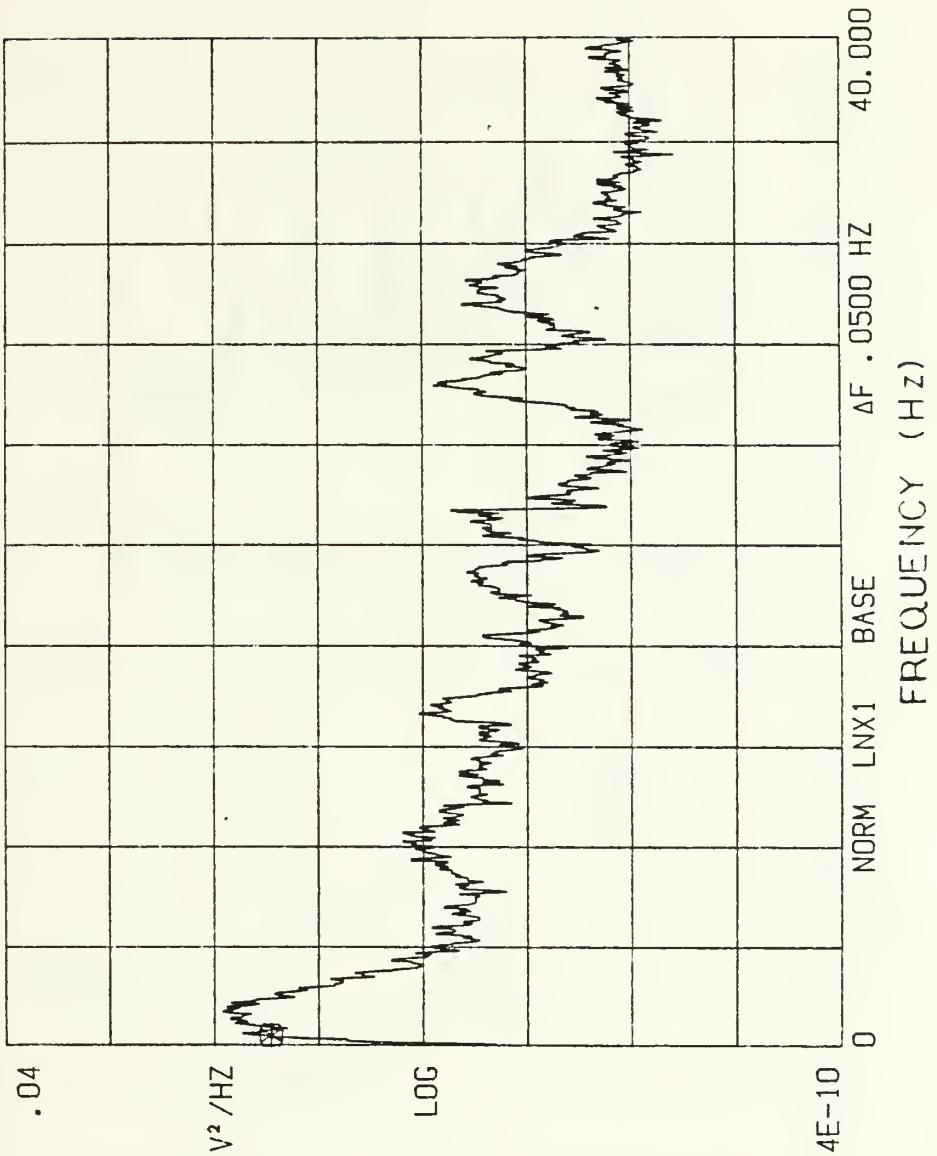

Figure 75. De=40, Subminiature Hot-wire Spectra, Real Time Analysis

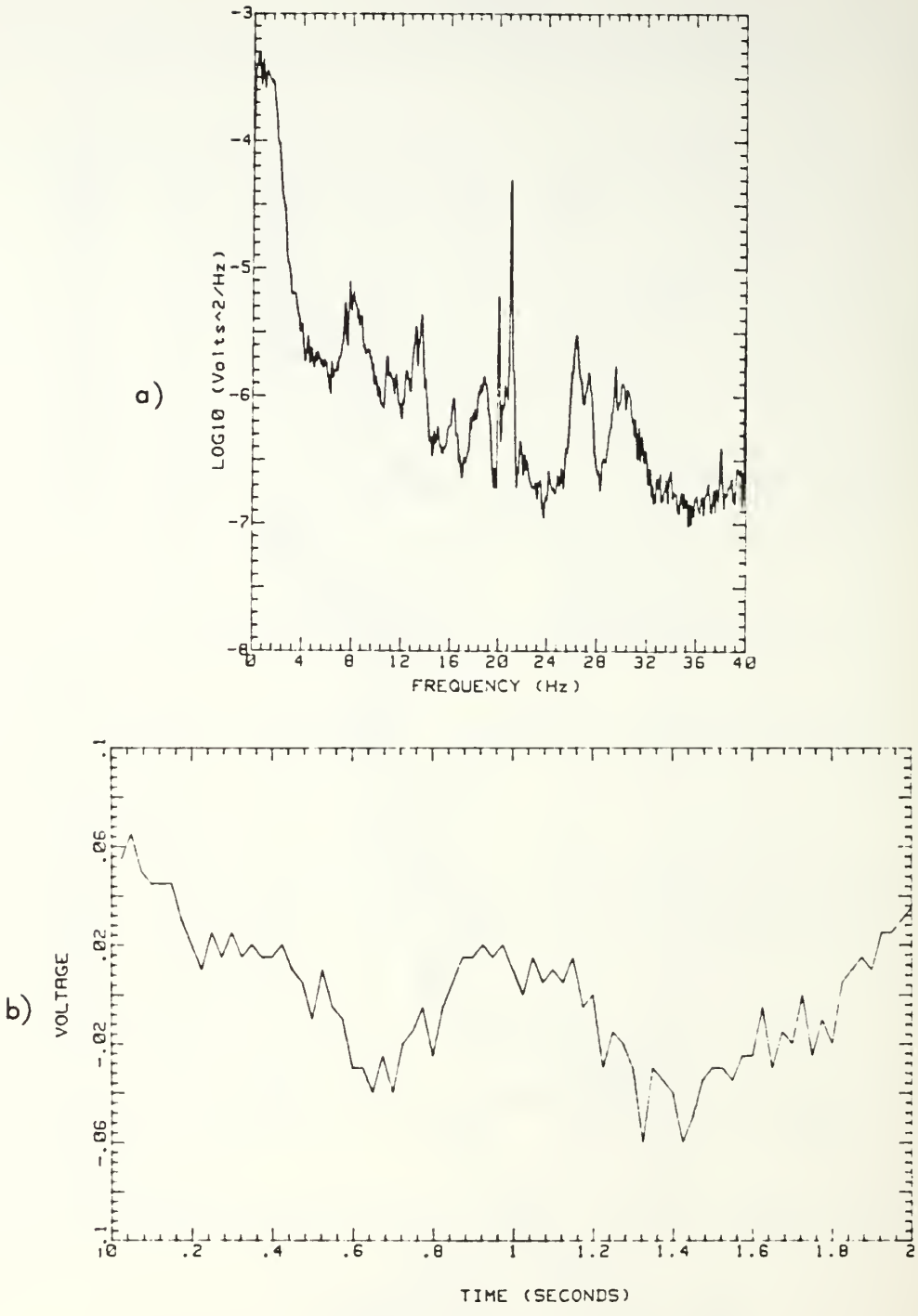

Figure 76. De=40, a) Subminiature Hot-wire Spectra, Digital Analysis
b) Sample Time Trace

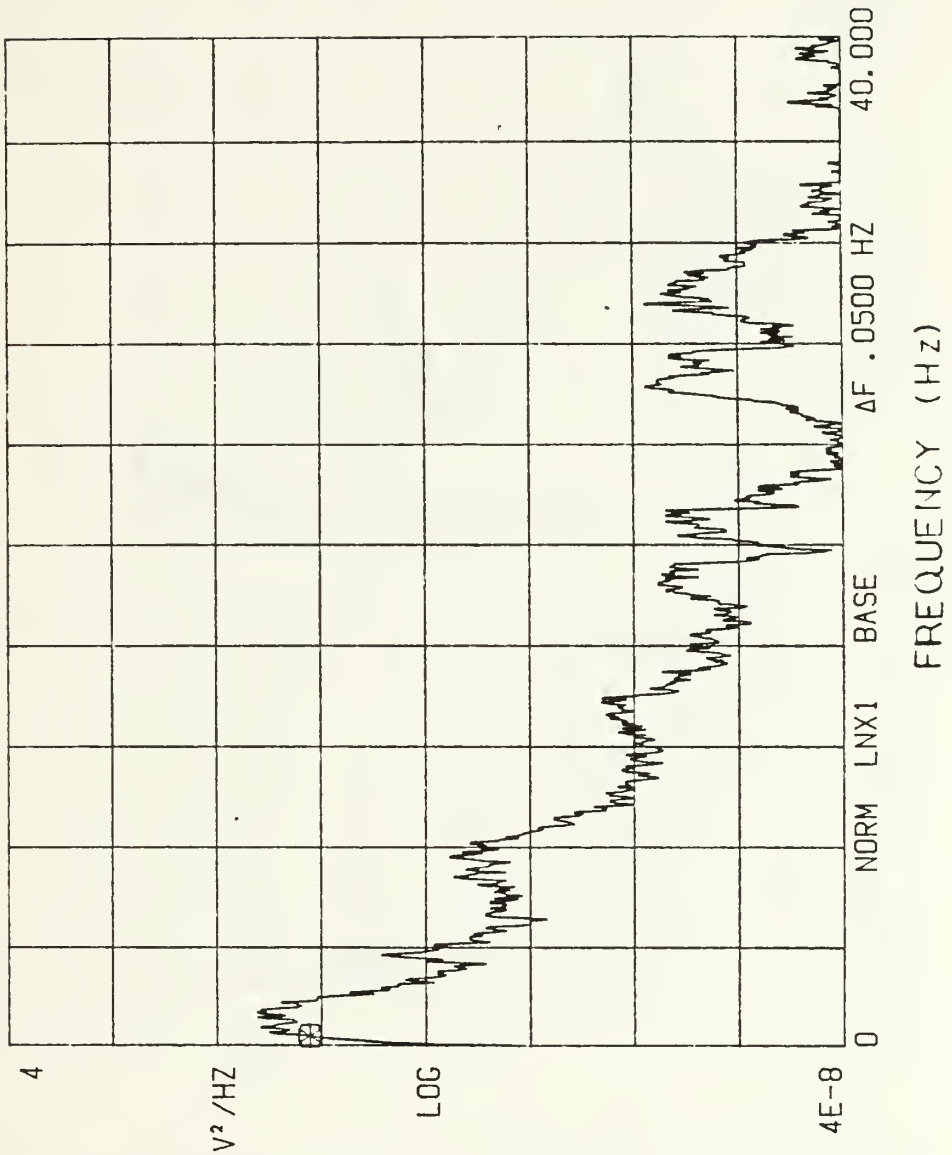

Figure 77. De= 60, Subminiature Hot-wire Spectra Real Time Analysis

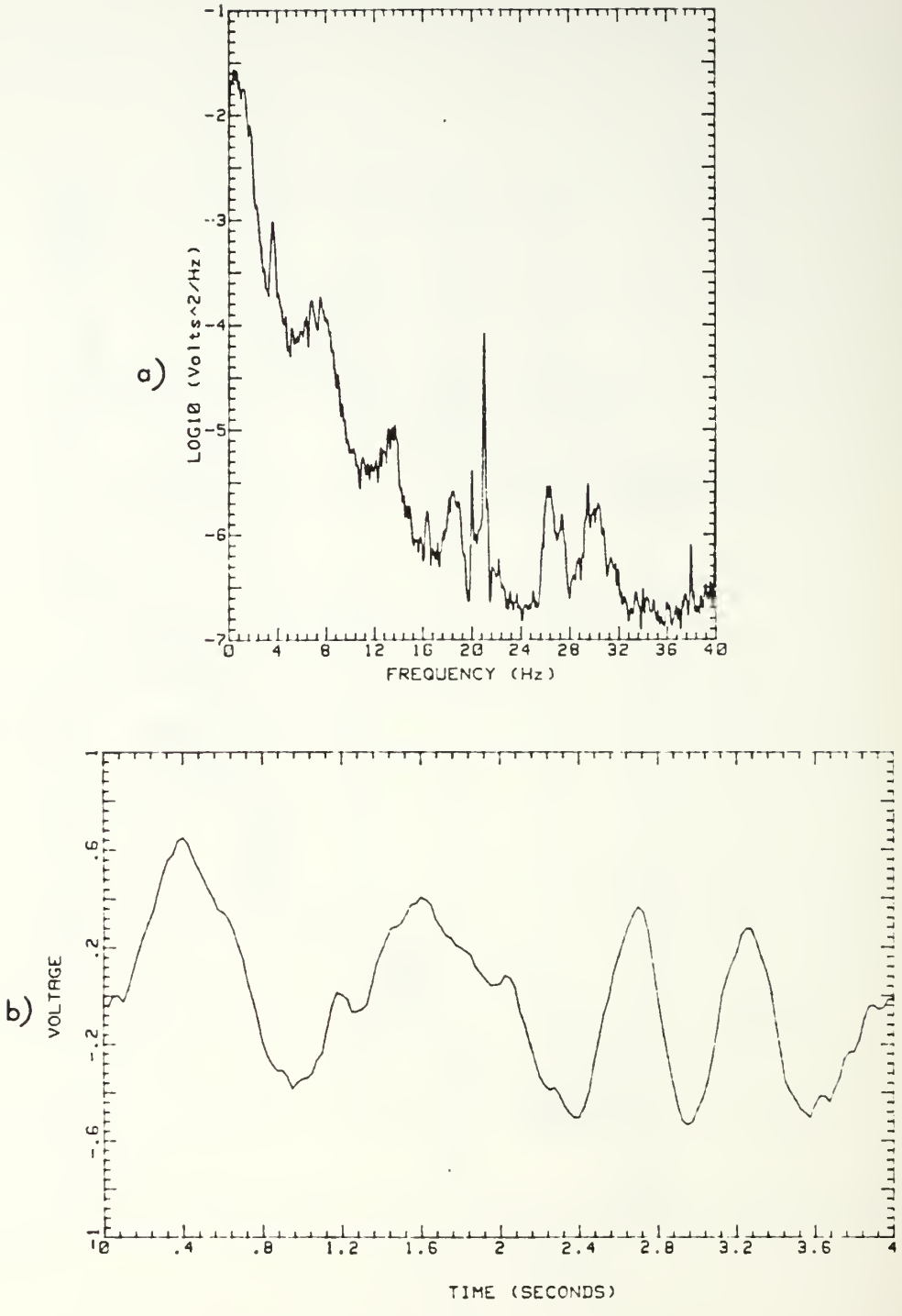

Figure 78. De=60, a) Subminiature Hot-wire Spectra, Digital Analysis
b) Sample Time Trace

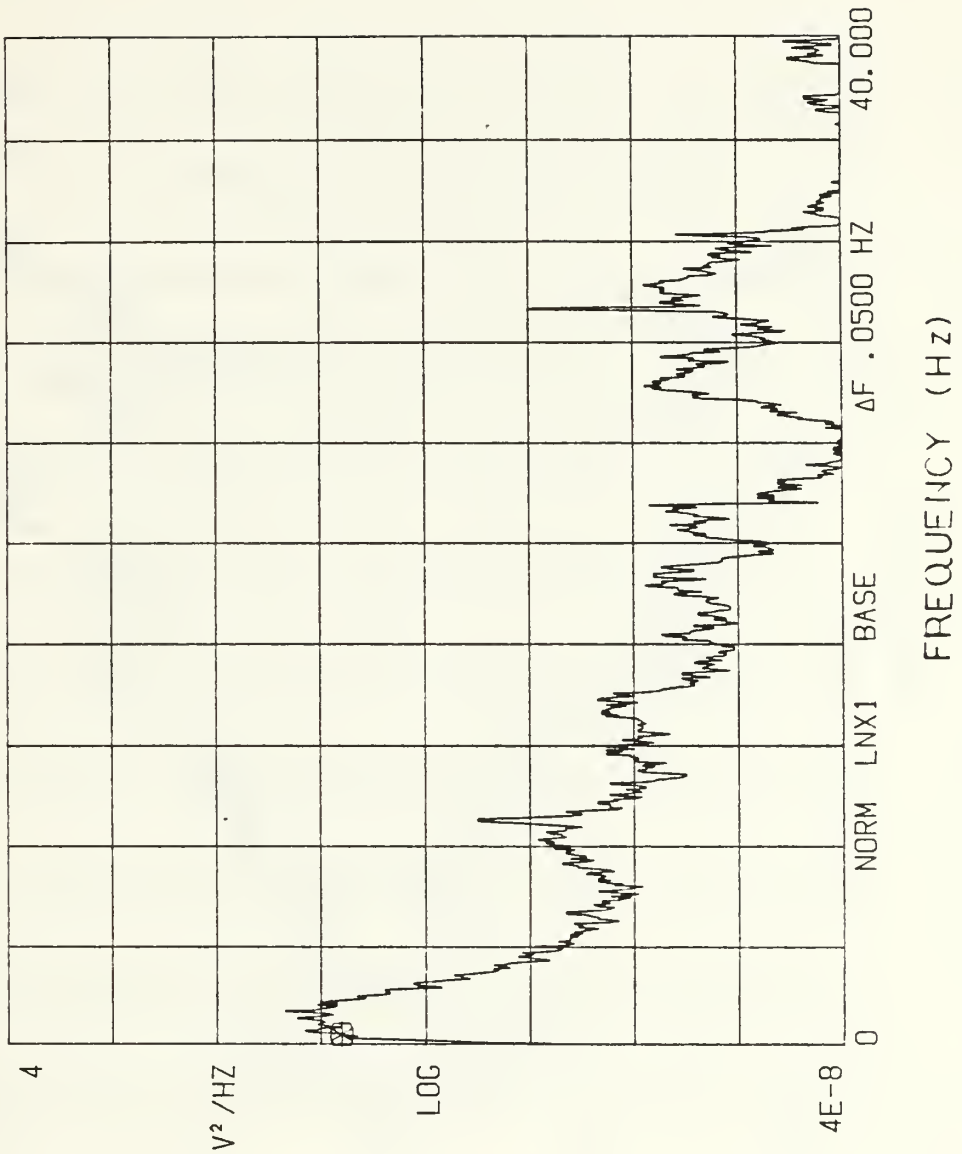

Figure 79. De= 69, Subminiature Hot-wire Spectra, Real Time Analysis

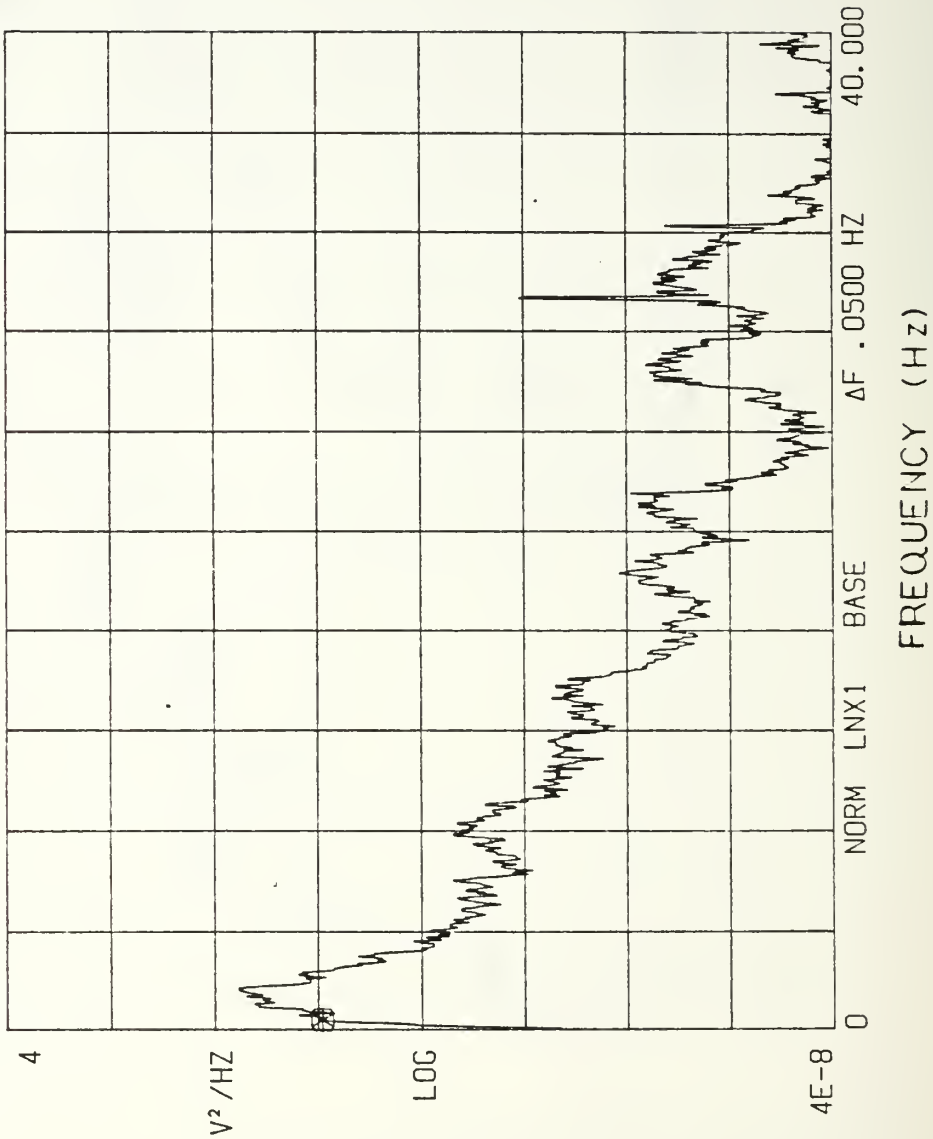

Figure 80. De=78, Subminiature Hot-wire Spectra, Real Time Analysis

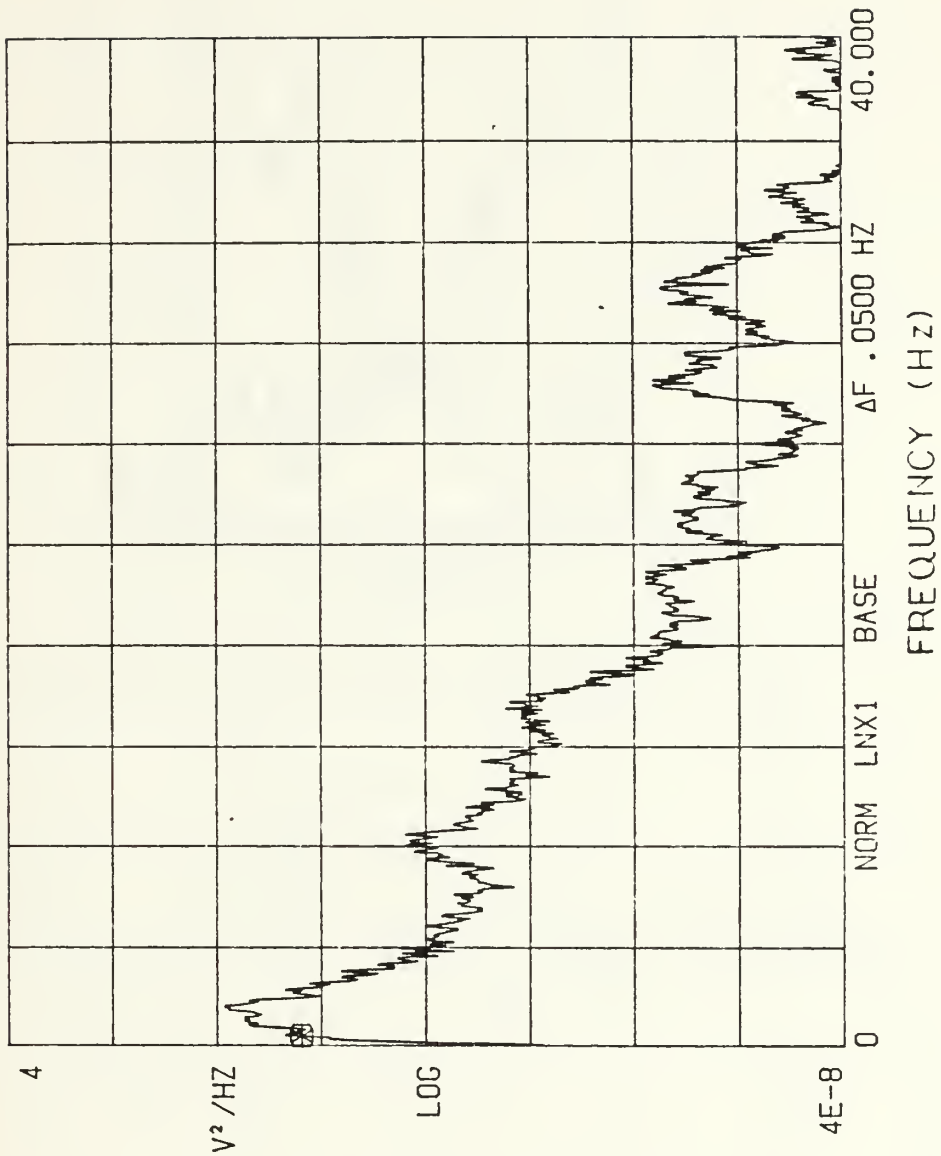

Figure 81. De=80, Subminiature Hot-wire Spectra, Real Time Analysis

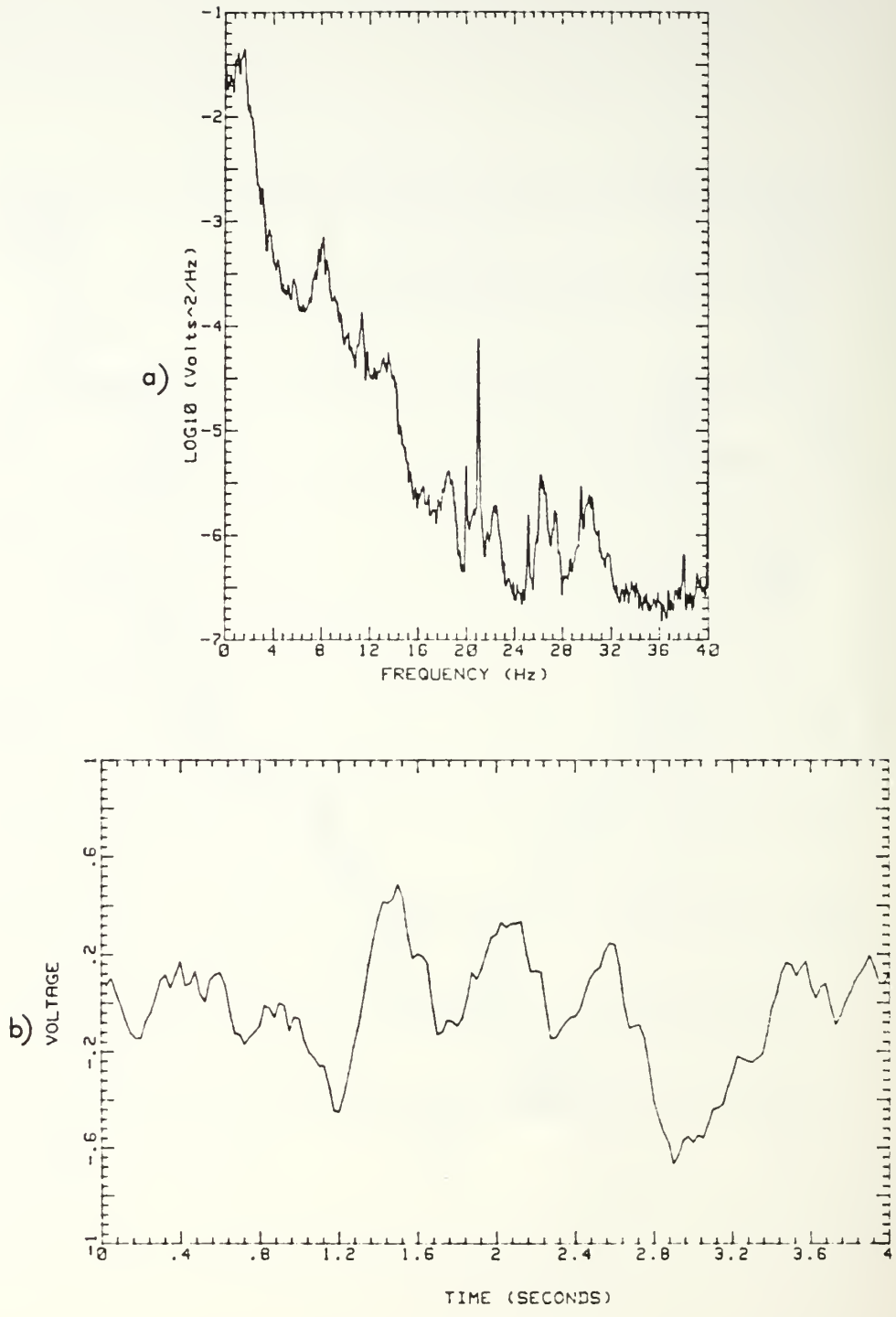

Figure 82. De=80, a) Subminiature Hot-wire Spectra, Digital Analysis
b) Sample Time Trace

Figure 83. De=90, a) Subminiature Hot-wire Spectra, Digital Analysis
b) Sample Time Trace

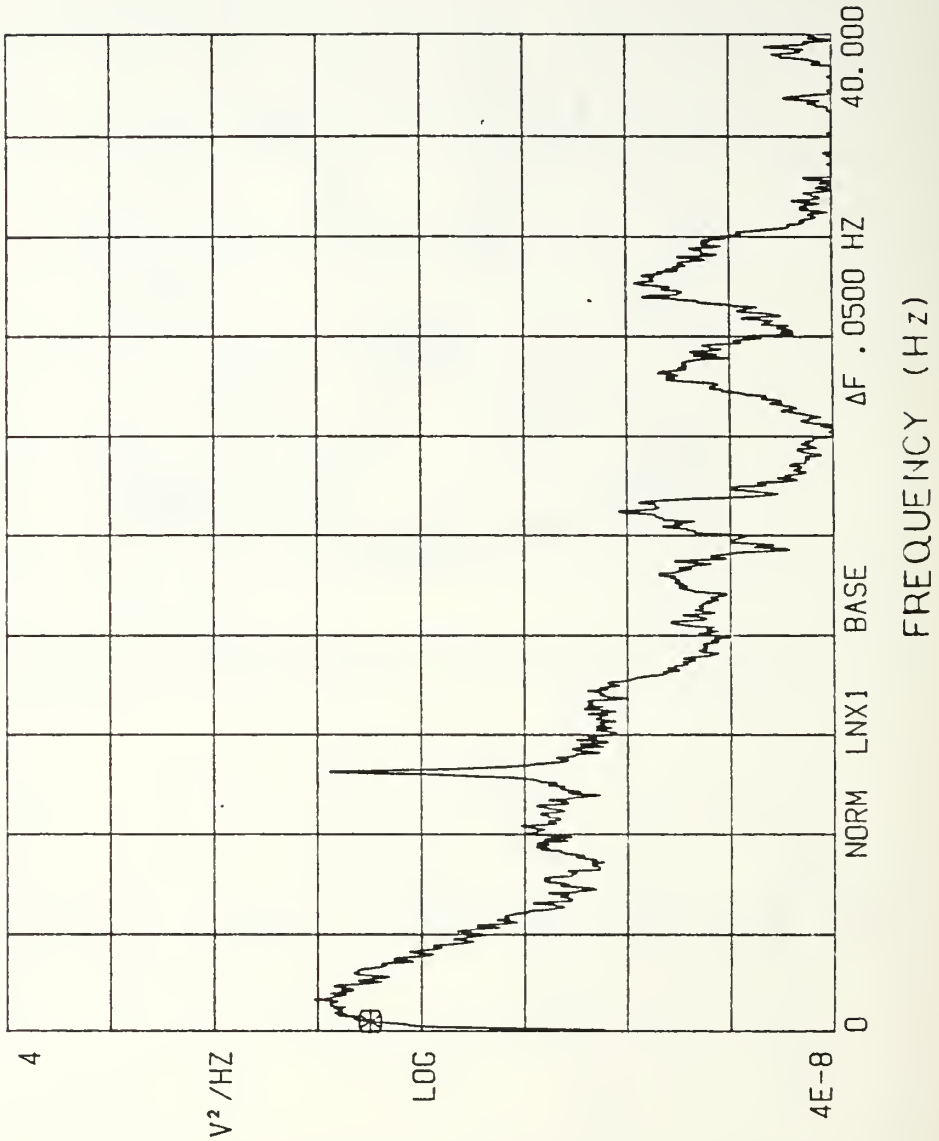

Figure 84. De=95, Subminiature Hot-wire Spectra, Real Time Analysis

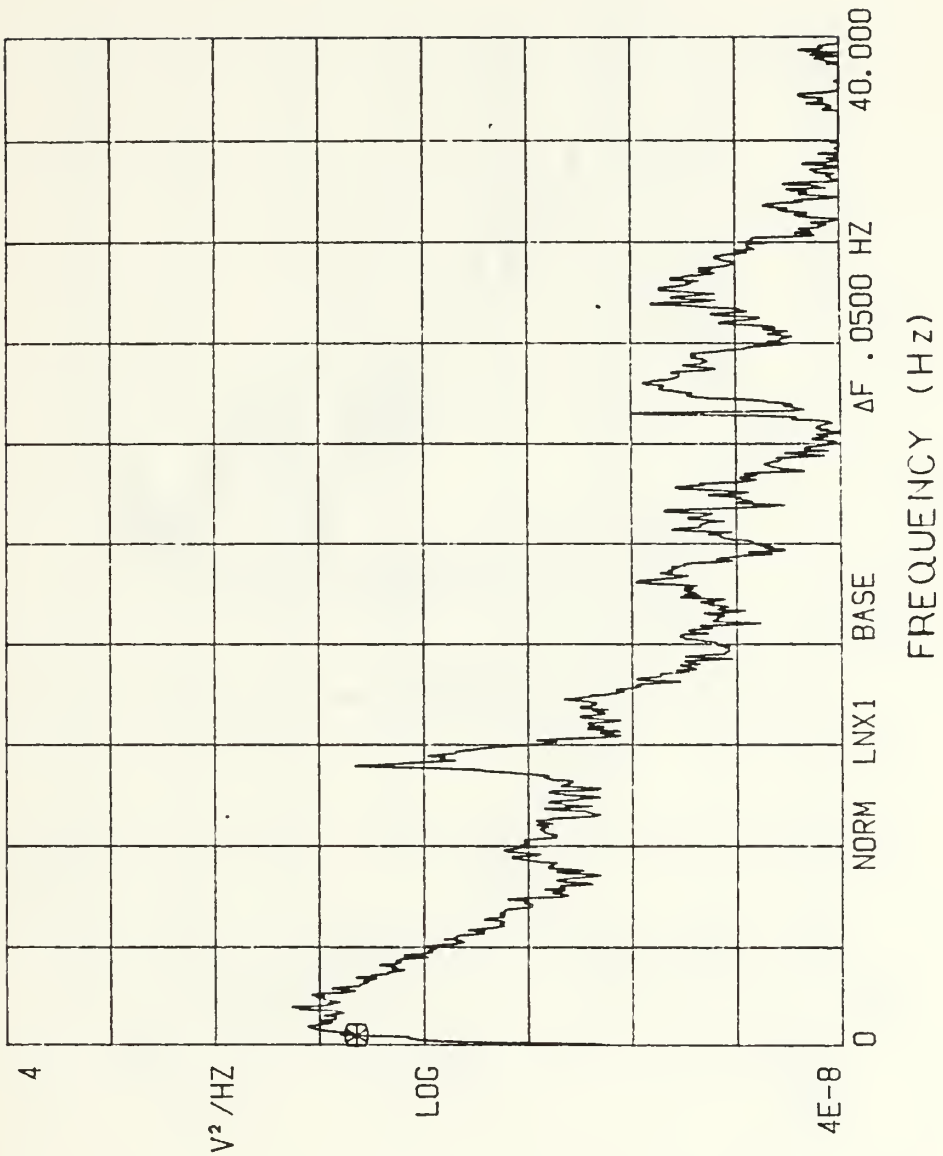

Figure 85. De=100, Subminiature Hot-wire Spectra, Real Time Analysis

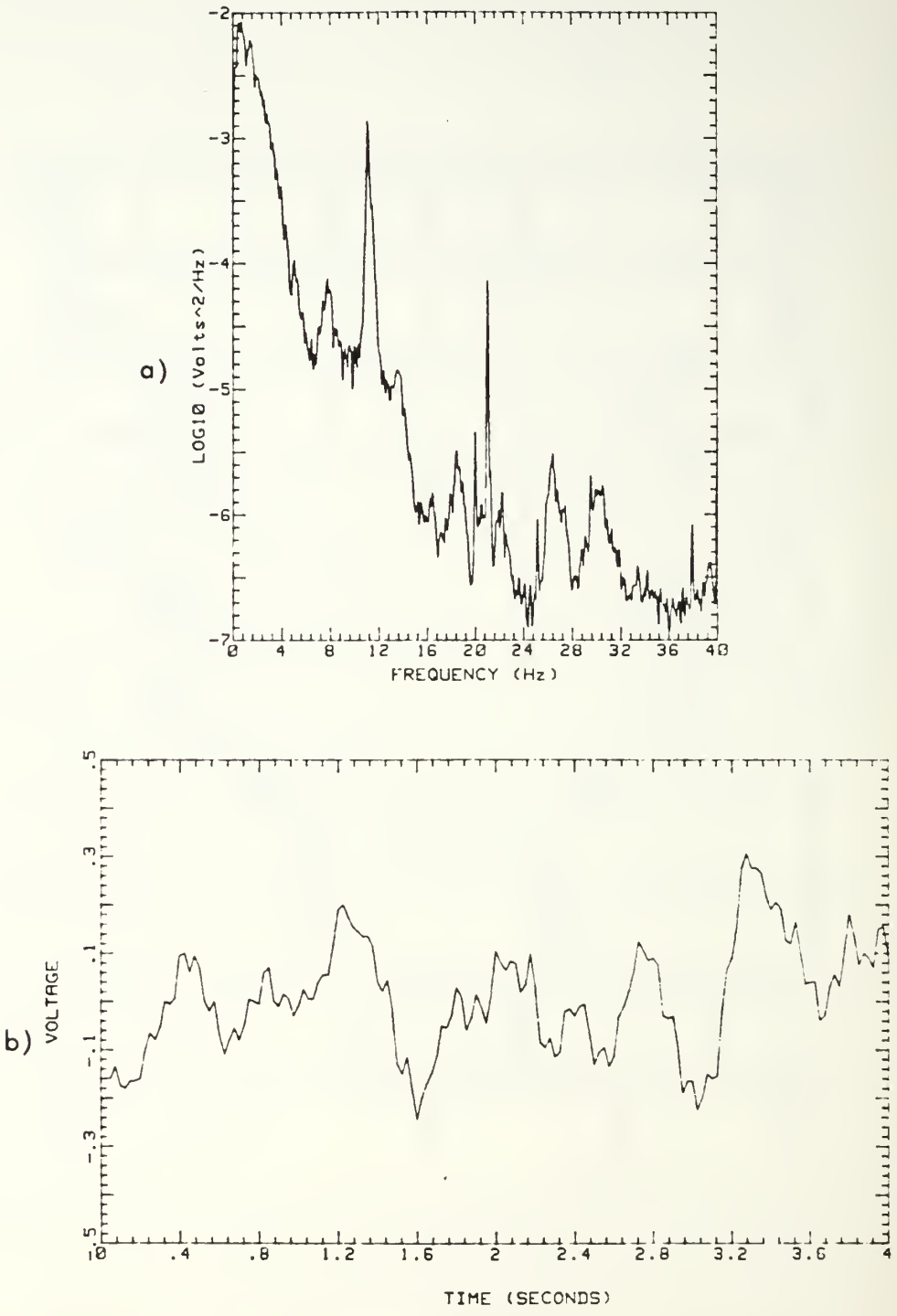

Figure 86. De=100, a) Subminiature Hot-wire Spectra, Digital Analysis
b) Sample Time Trace

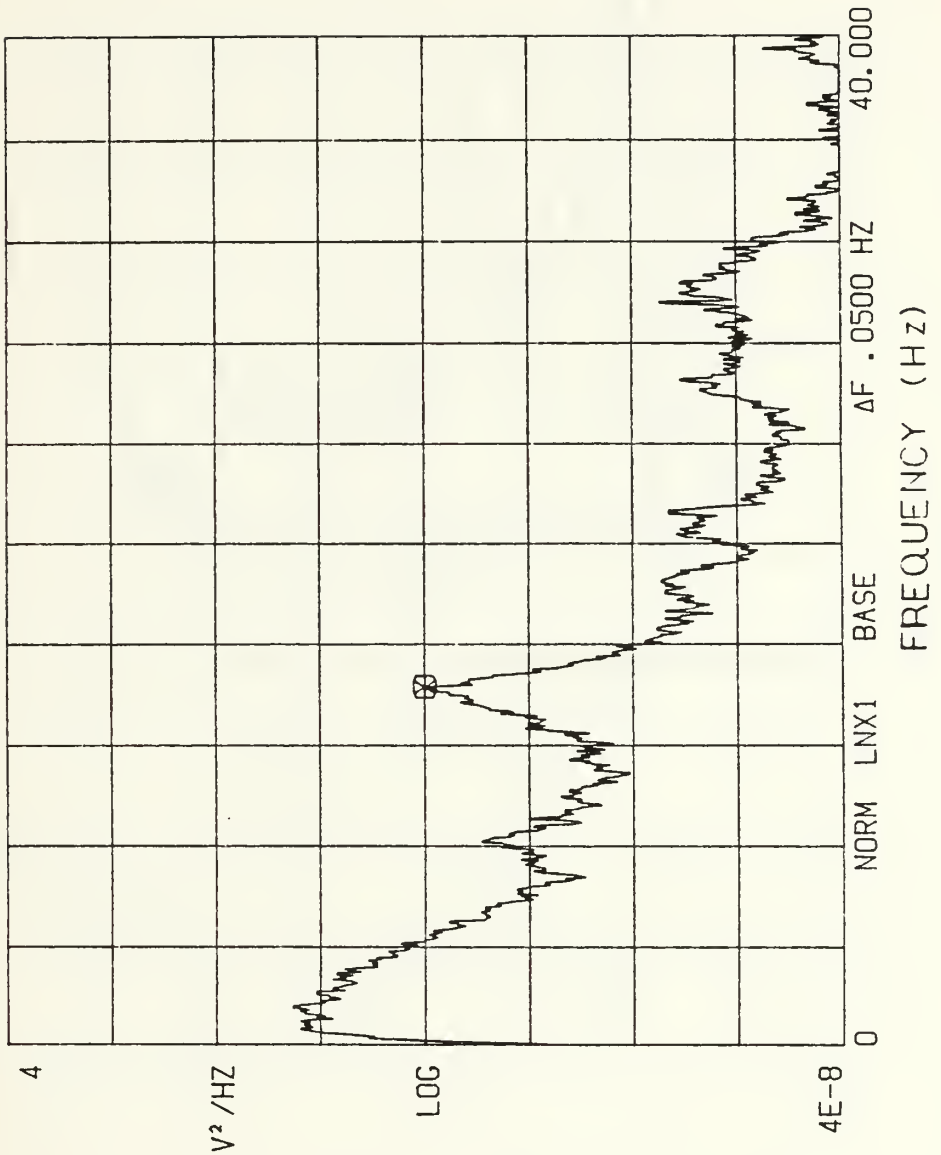

Figure 87. De=110, Subminiature Hot-wire Spectra, Real Time Analysis

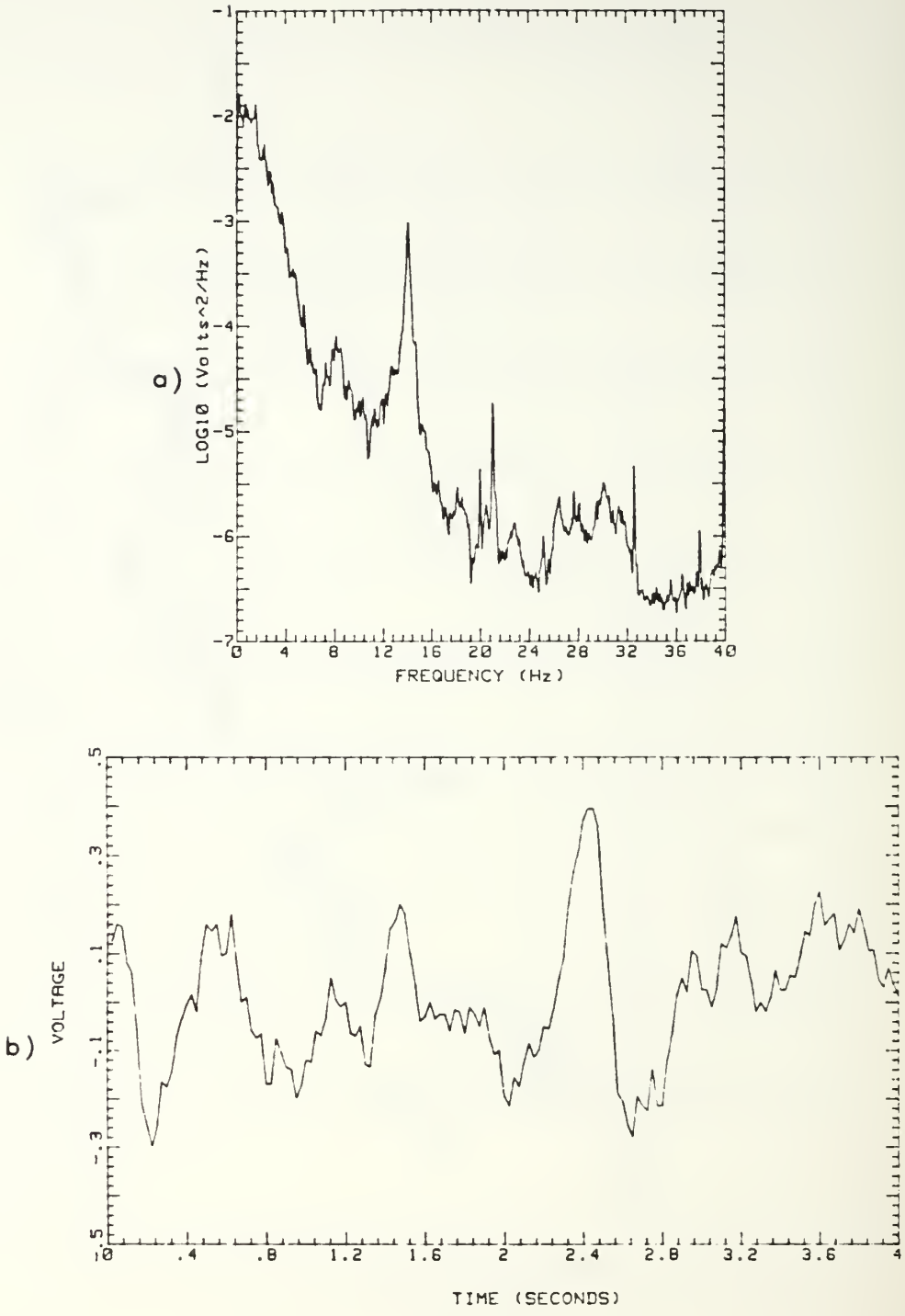

Figure 88. De=110, a) Subminiature Hot-wire Spectra, Digital Analysis
b) Sample Time Trace

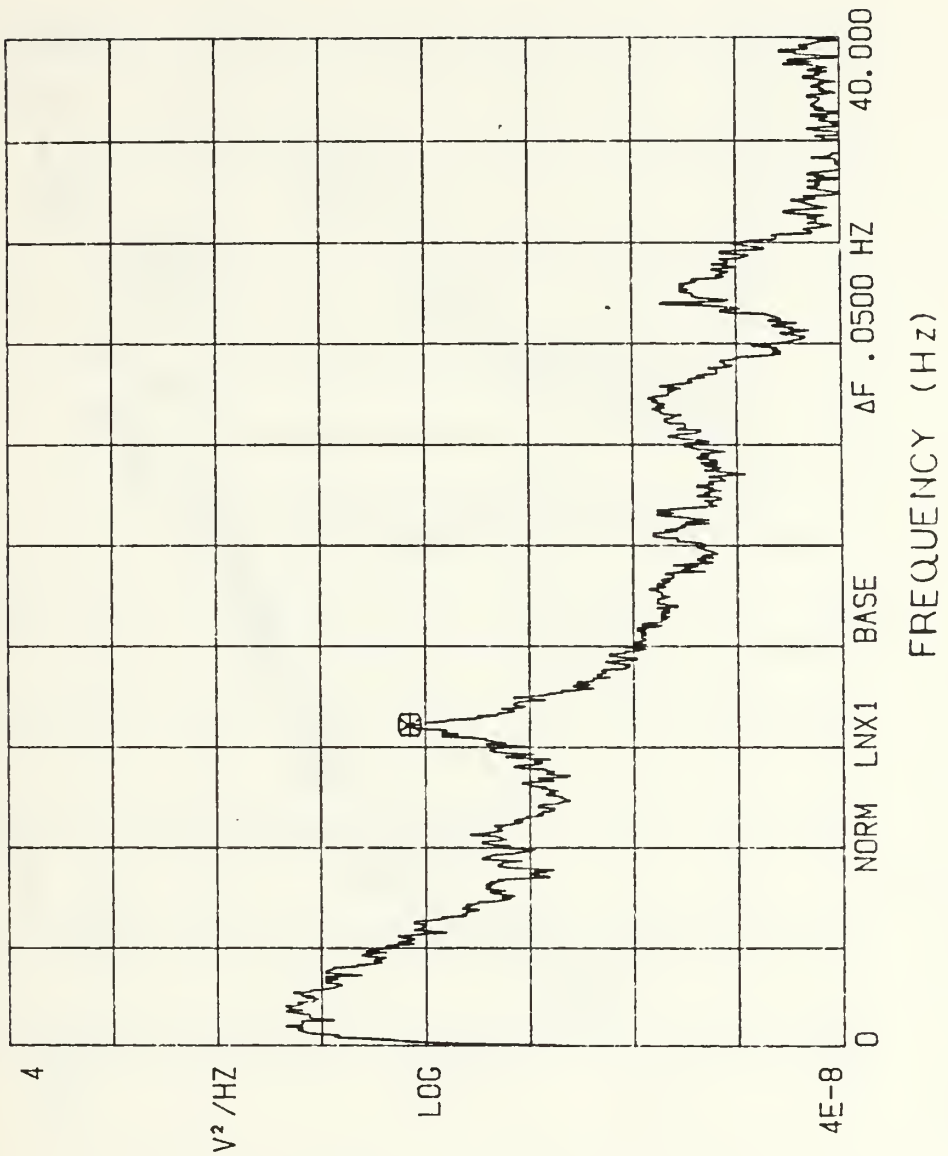

Figure 89. De=114, Subminiature Hot-wire Spectra Real Time Analysis

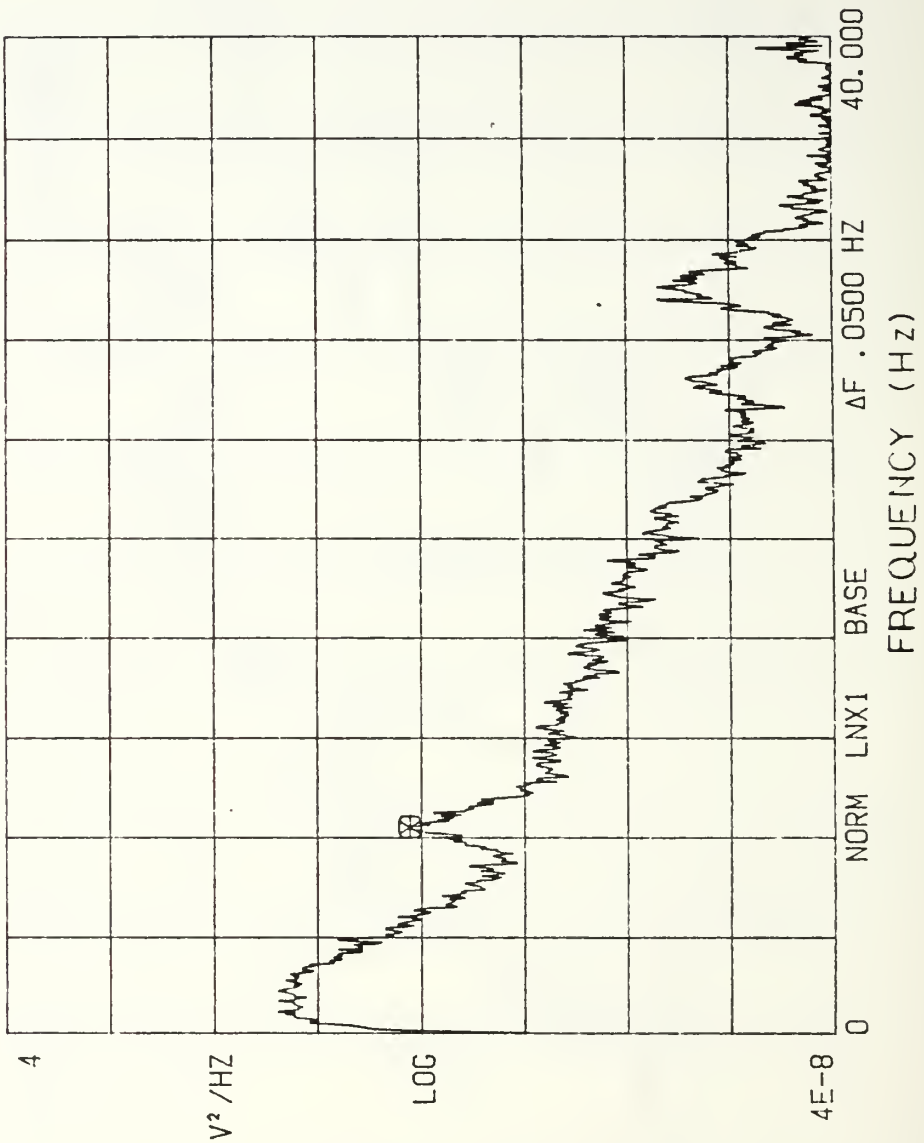

Figure 90. De=120, Subminiature Hot-wire Spectra, Real Time Analysis

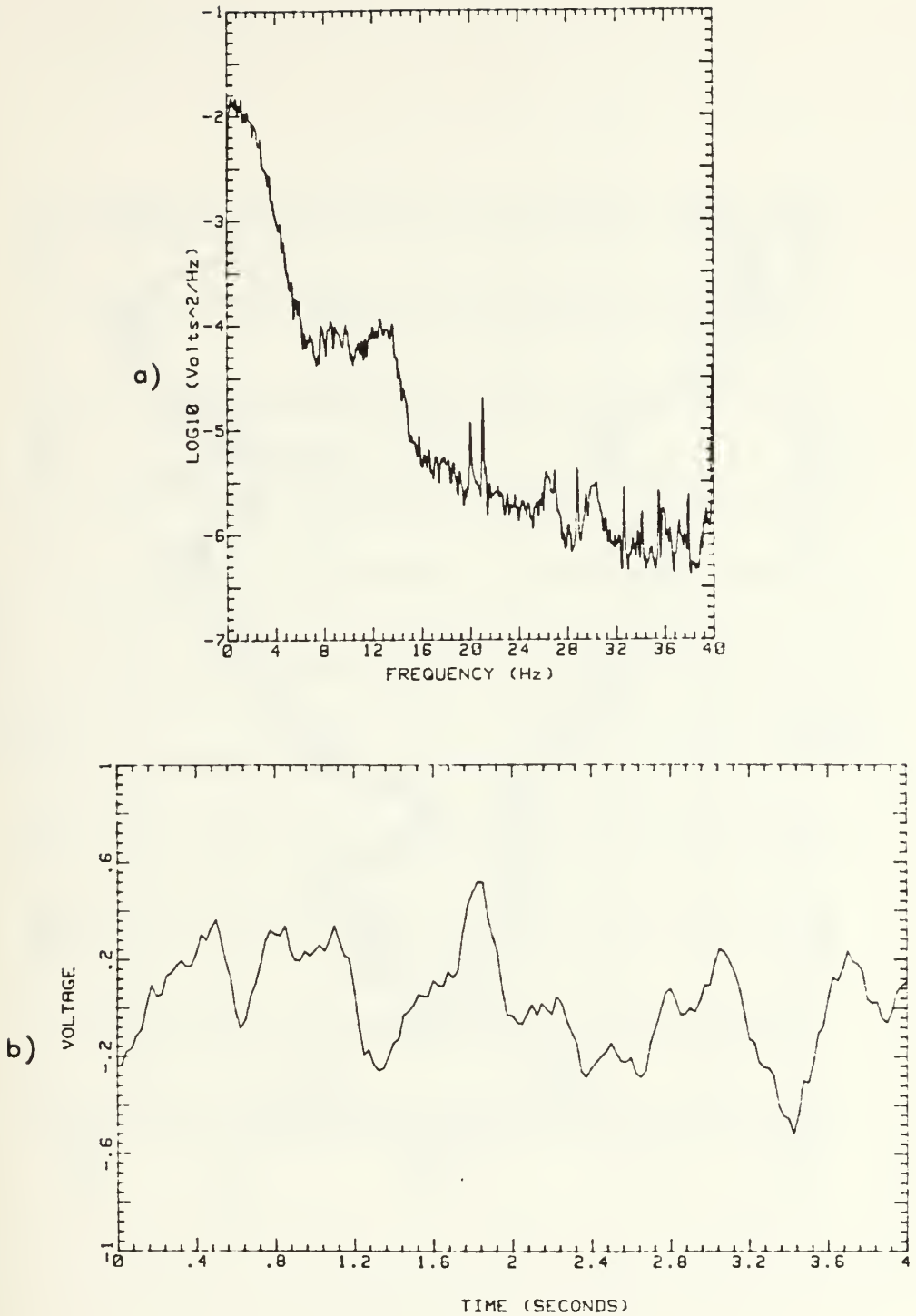

Figure 91. De=120, a) Subminiature Hot-wire Spectra, Digital Analysis
b) Sample Time Trace

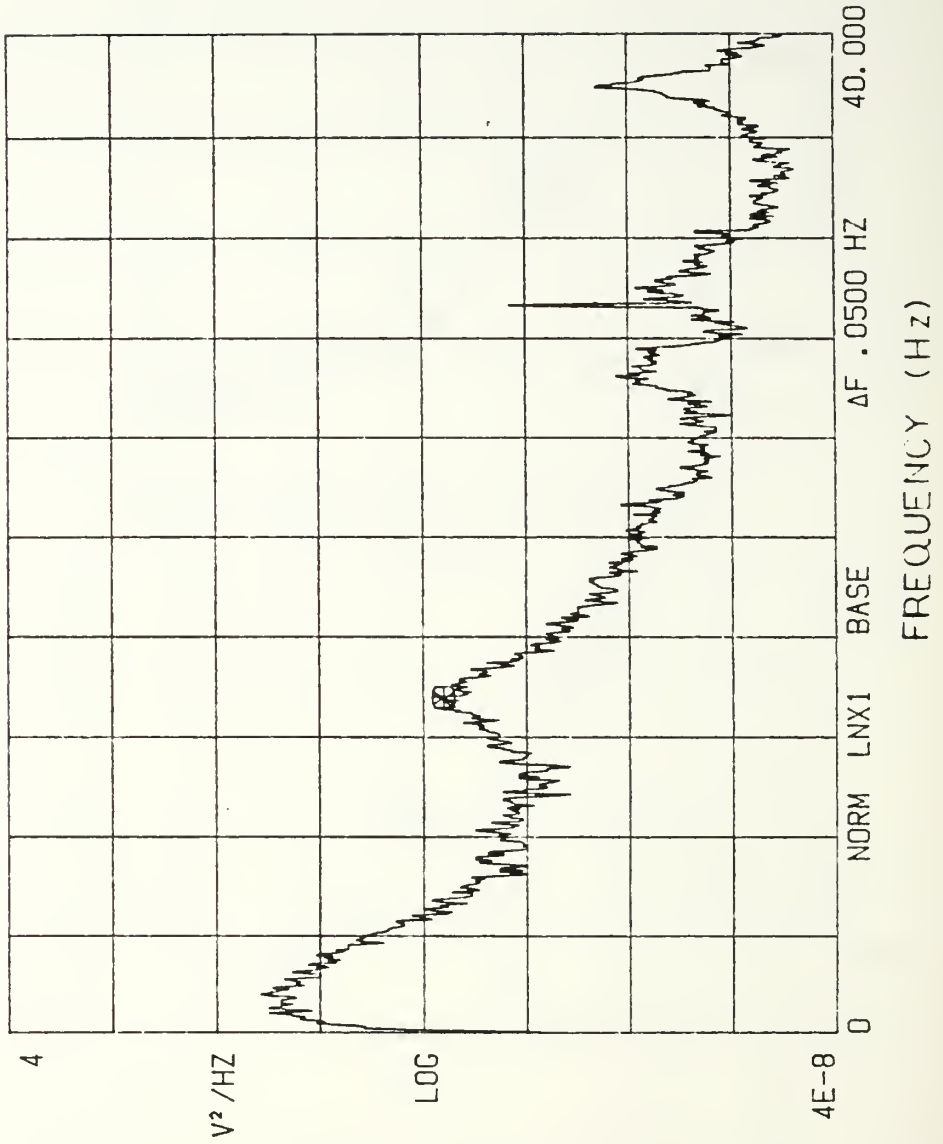

Figure 92. De=126, Subminiature Hot-wire Spectra Real Time Analysis

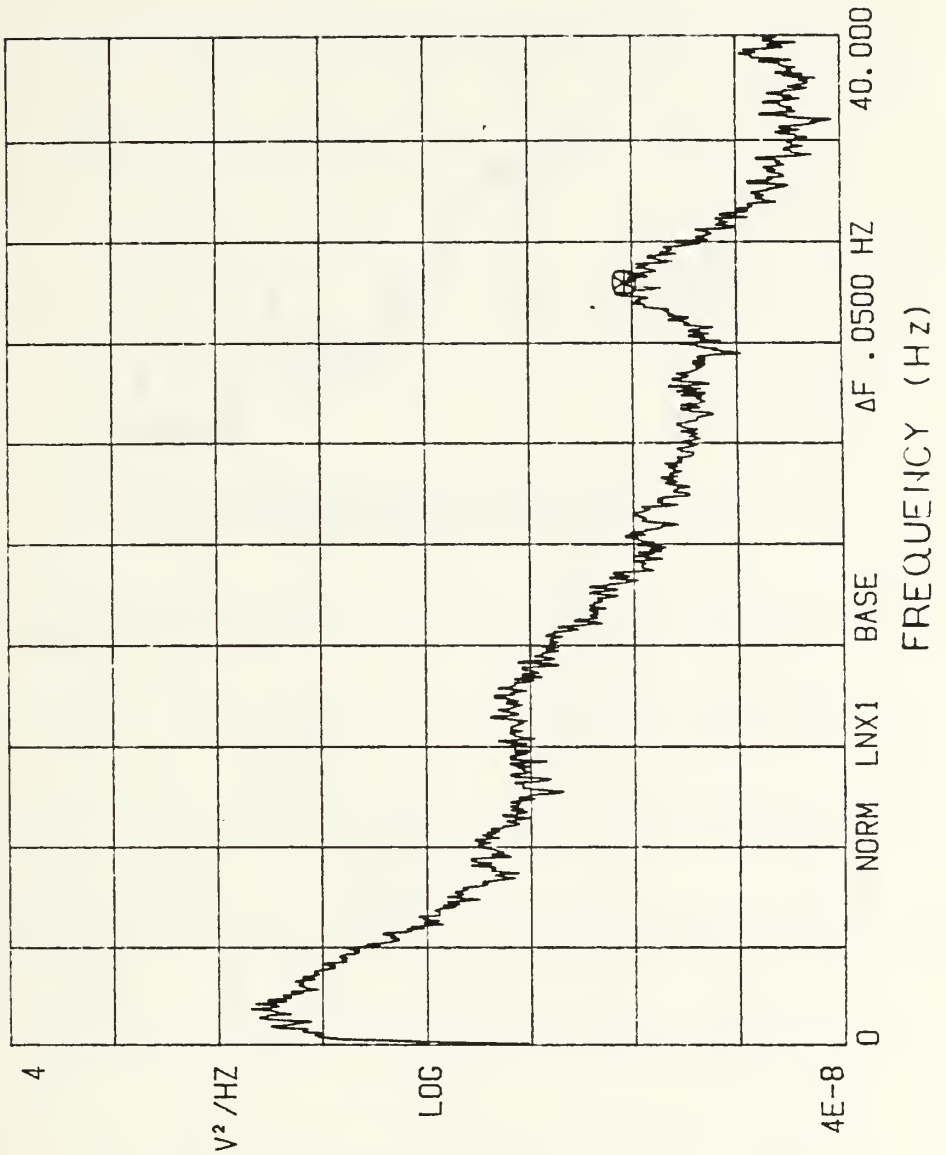

Figure 93. De=130, Subminiature Hot-wire Spectra, Real Time Analysis

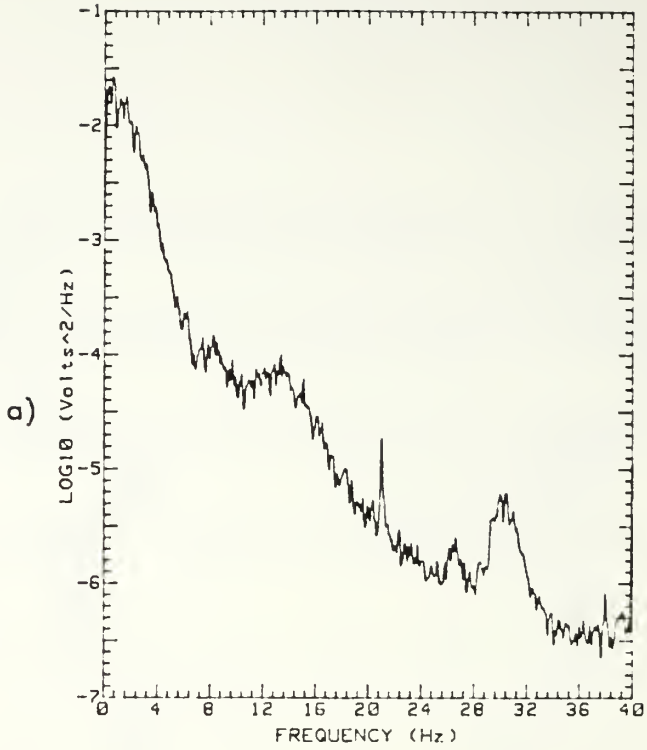

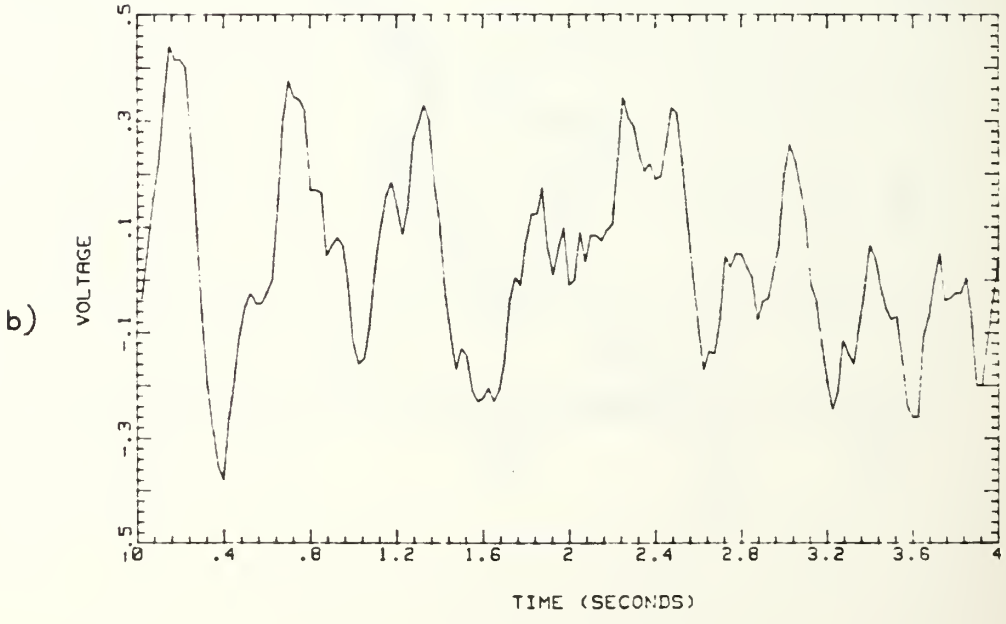

Figure 94. De=130, a) Subminiature Hot-wire Spectra, Digital Analysis
b) Sample Time Trace

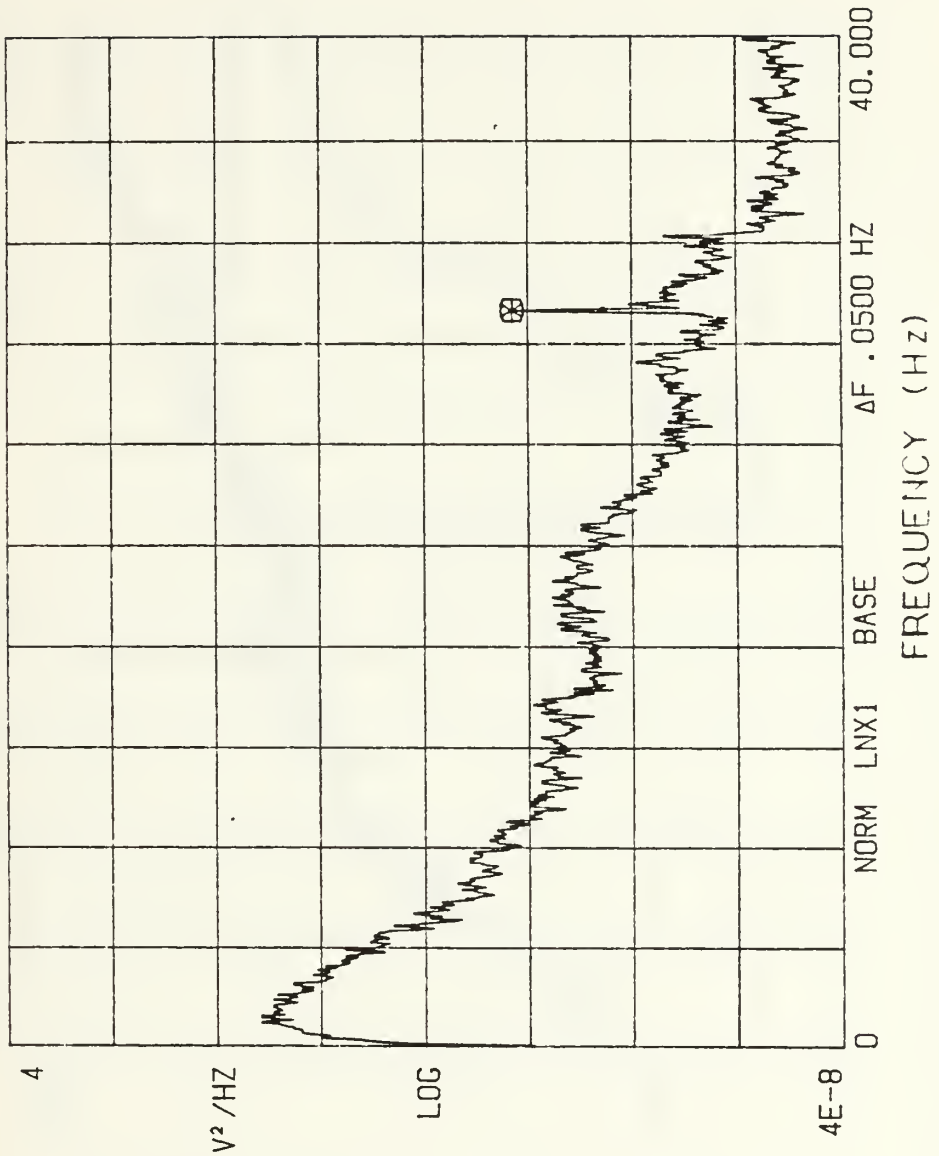

Figure 95. De=134, Subminiature Hot-wire Spectra, Real Time Analysis

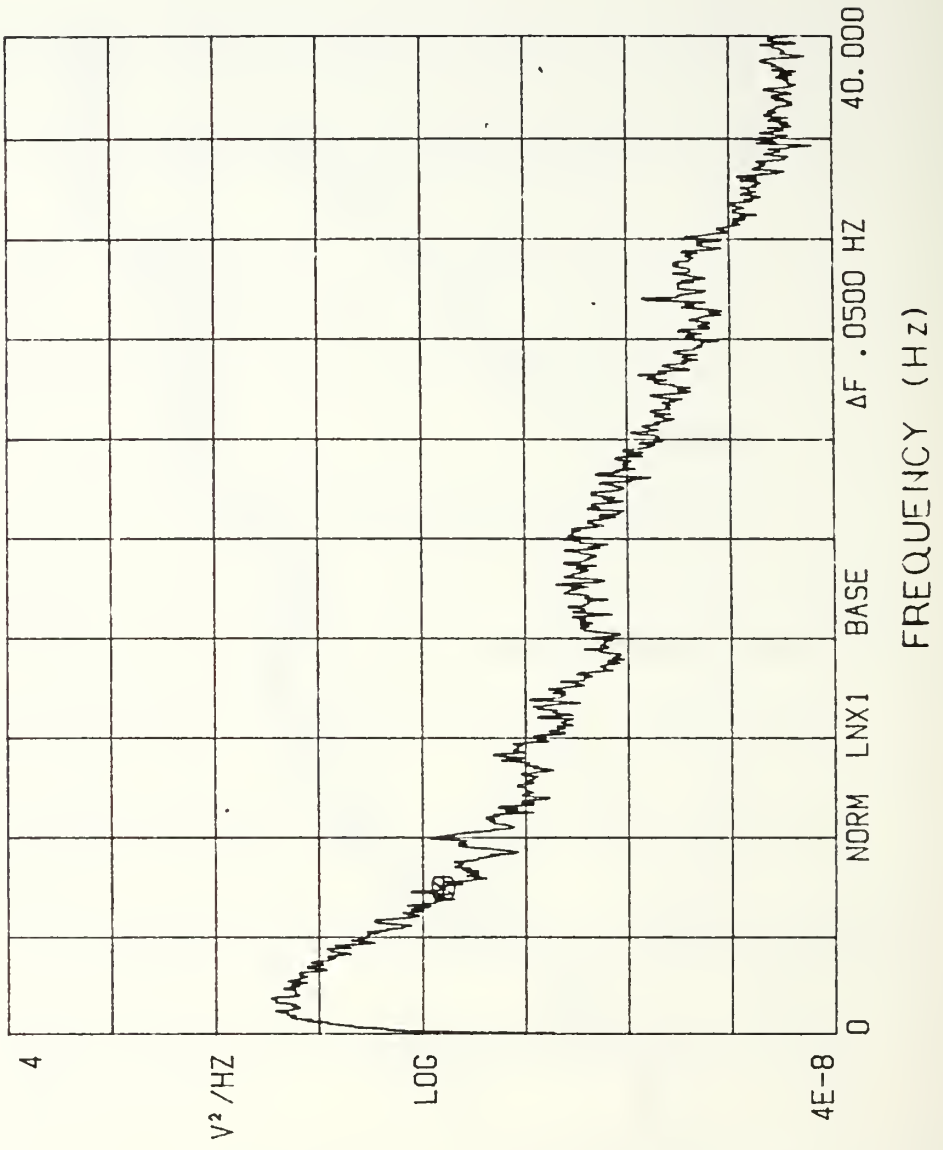

Figure 96. De=140, Subminiature Hot-wire Spectra, Real Time Analysis

Figure 97. De=140, a) Subminiature Hot-wire Spectra, Digital Analysis
b) Sample Time Trace

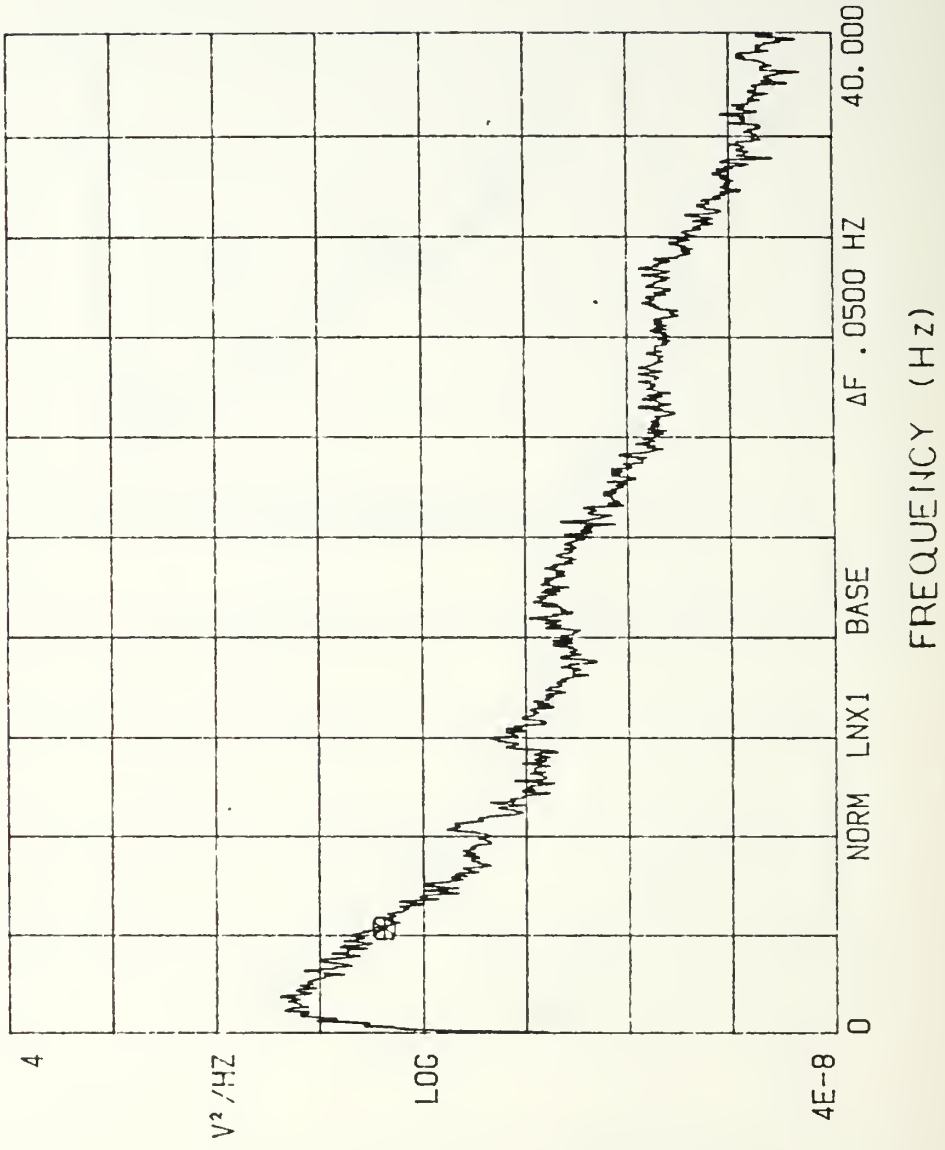

Figure 98. De=150, Subminiature Hot-wire Spectra, Real Time Analysis

Figure 99. De=150, a) Subminiature Hot-wire Spectra, Digital Analysis
b) Sample Time Trace

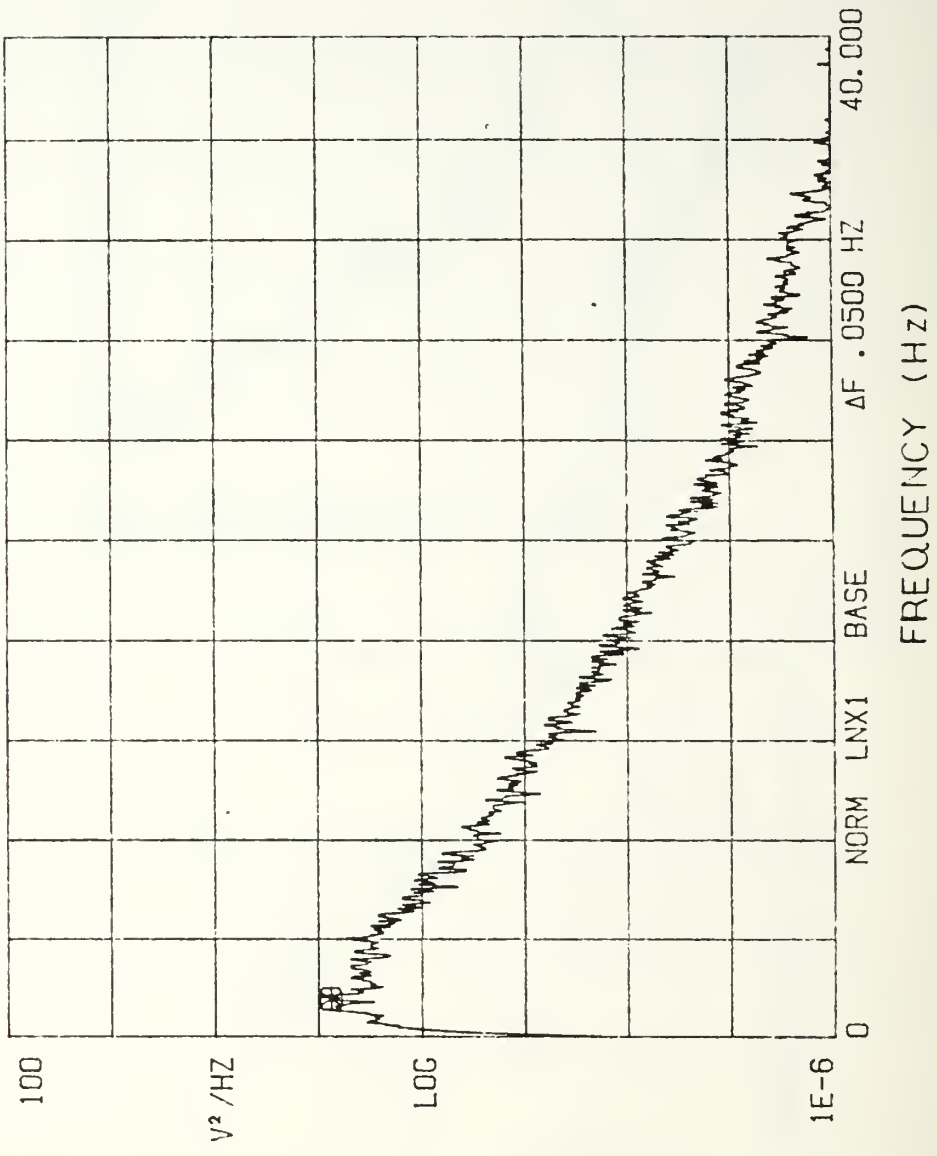

Figure 100. De=150, Subminiature Hot-wire Spectra, Real Time Analysis

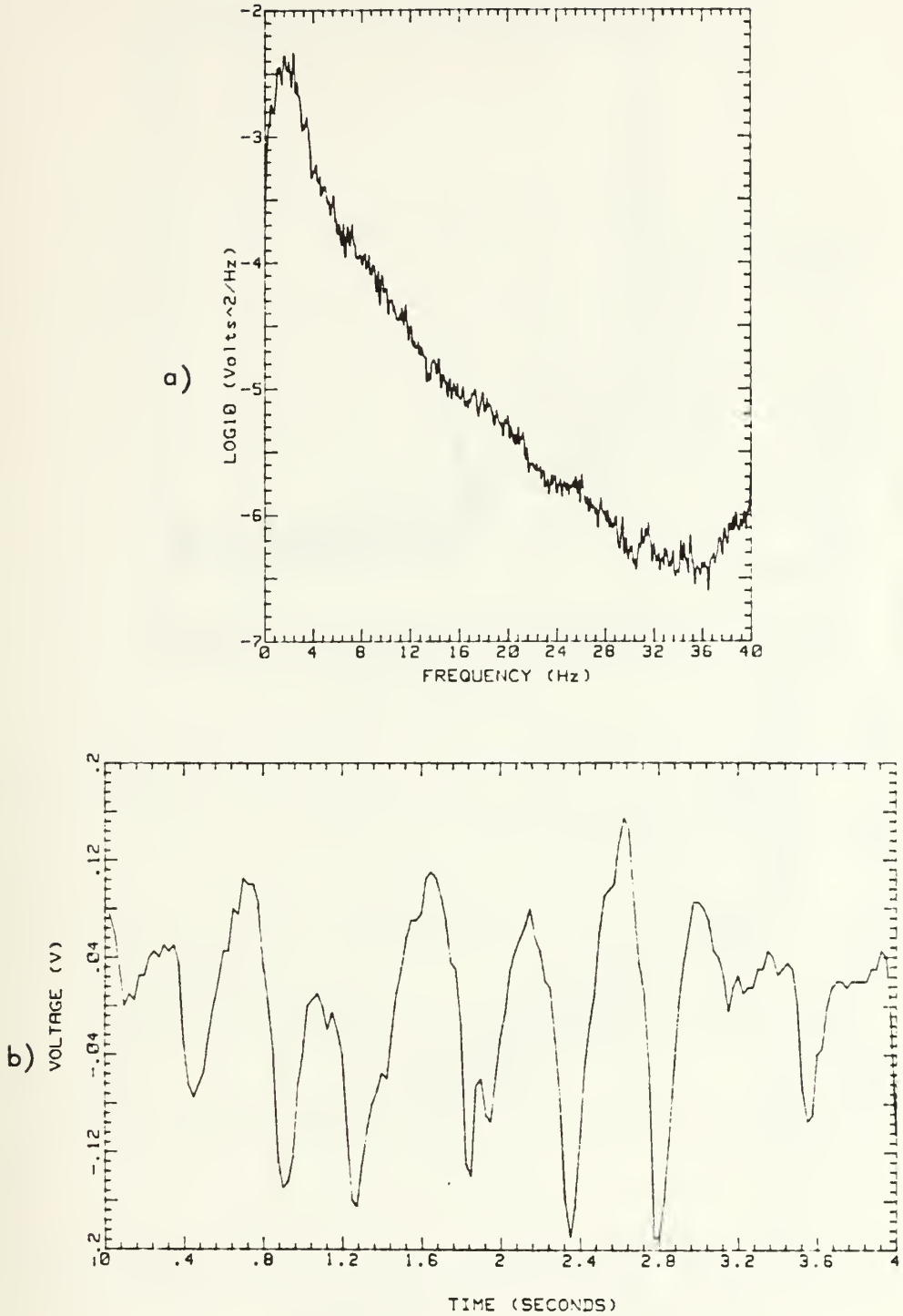

Figure 101. De=160, a) Subminiature Hot-wire Spectra, Digital Analysis
b) Sample Time Trace

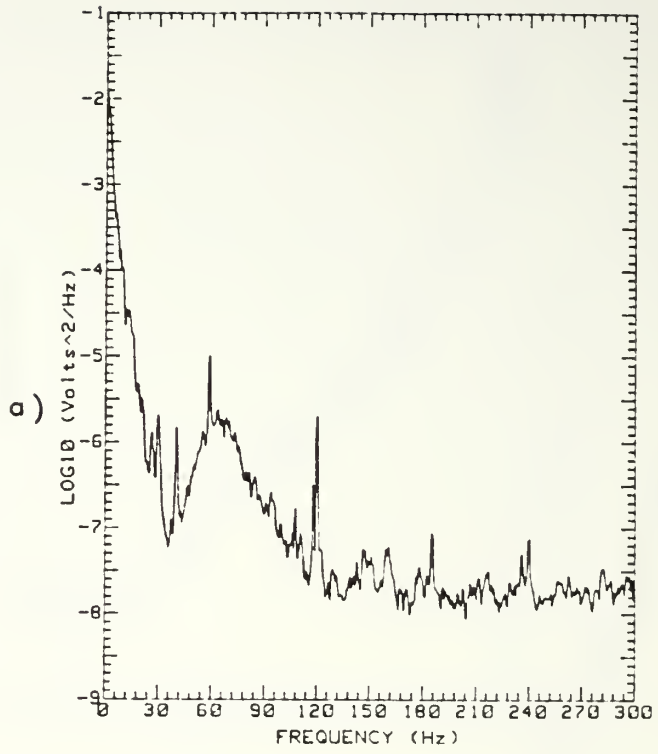

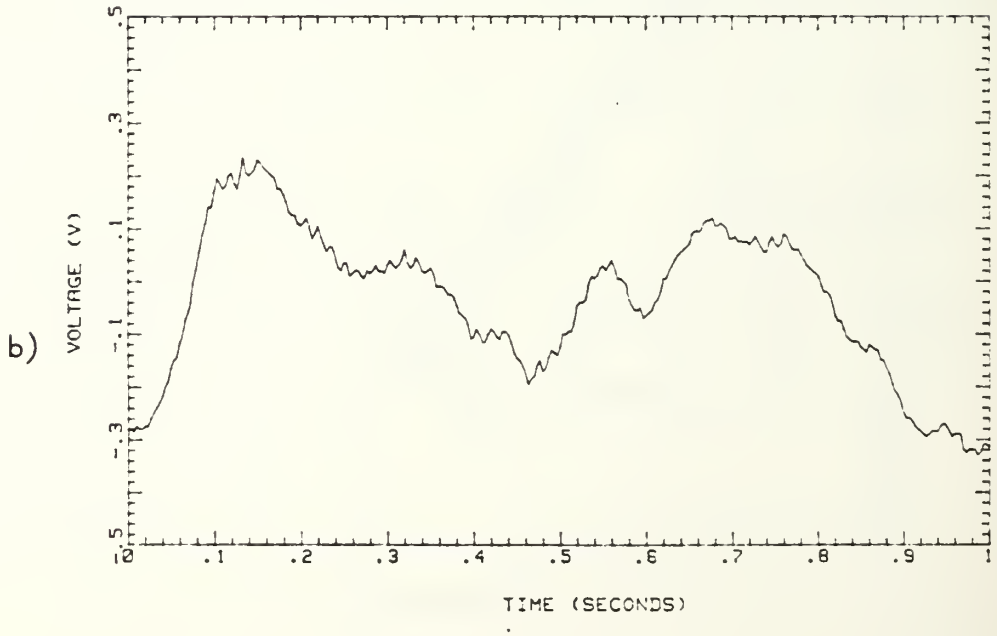

Figure 102. De=132, a) Conventional Hot-wire Spectra, Digital Analysis
b) Sample Time Trace

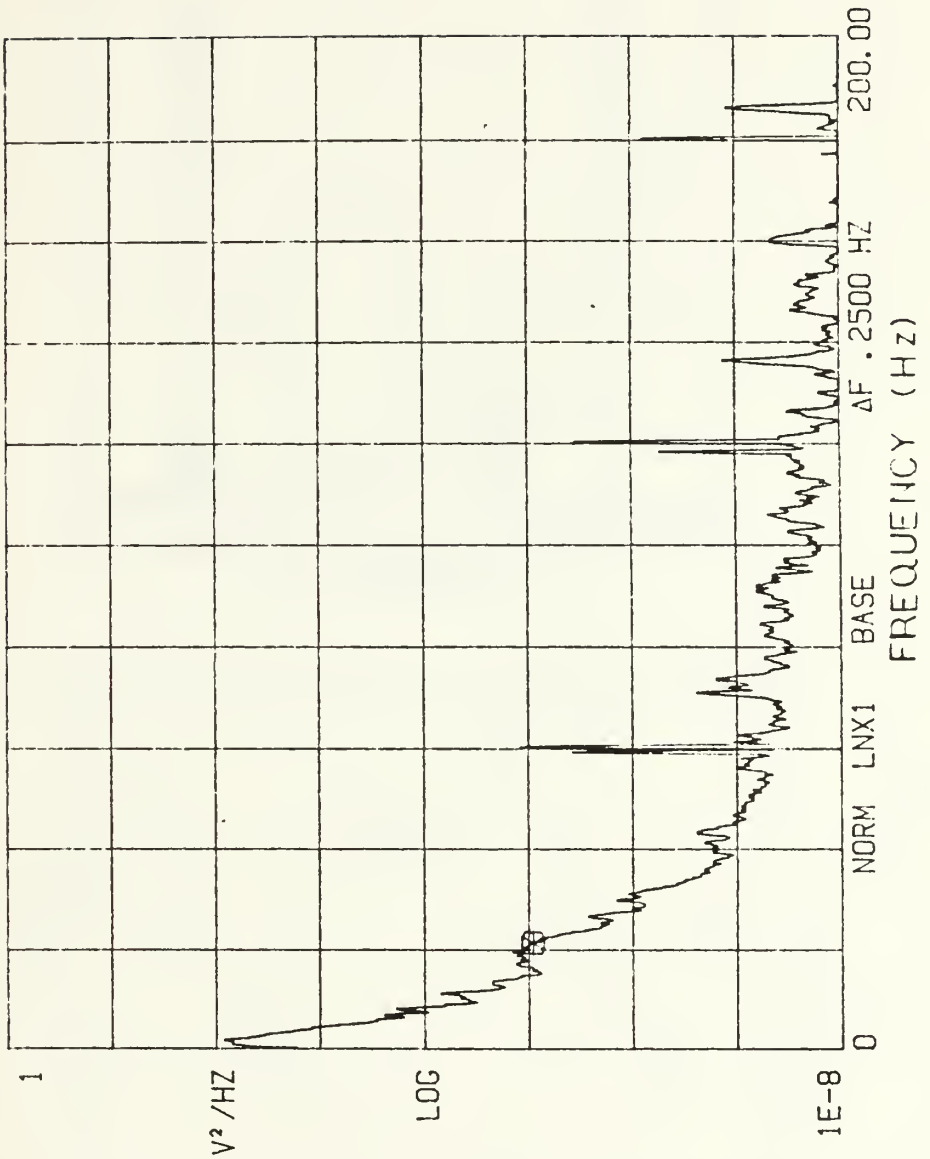

Figure 103. De=140, Subminiature Hot-wire Spectra, Real Time Analysis

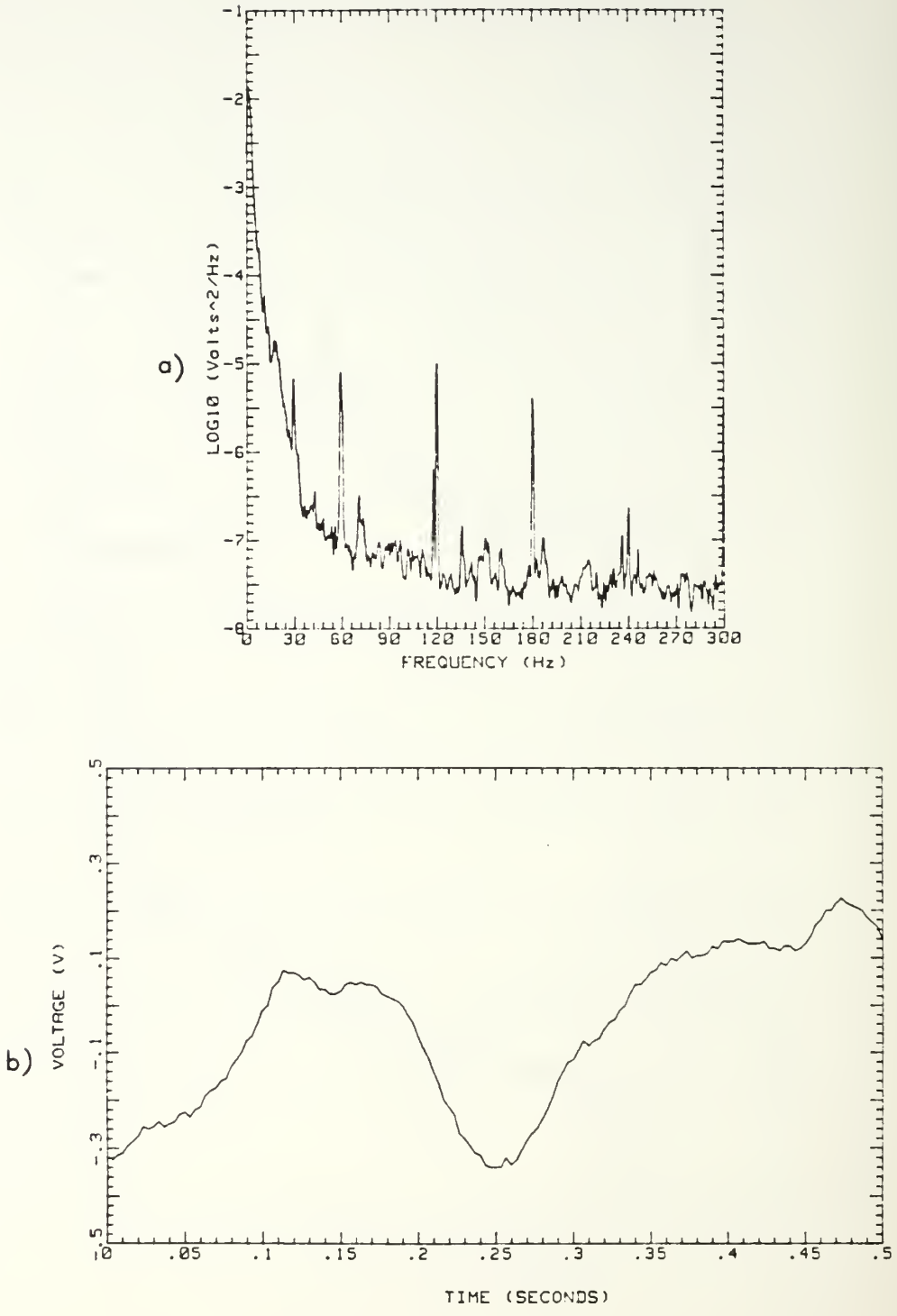

Figure 104. De=140, a) Subminiature Hot-wire Spectra, Digital Analysis
b) Sample Time Trace

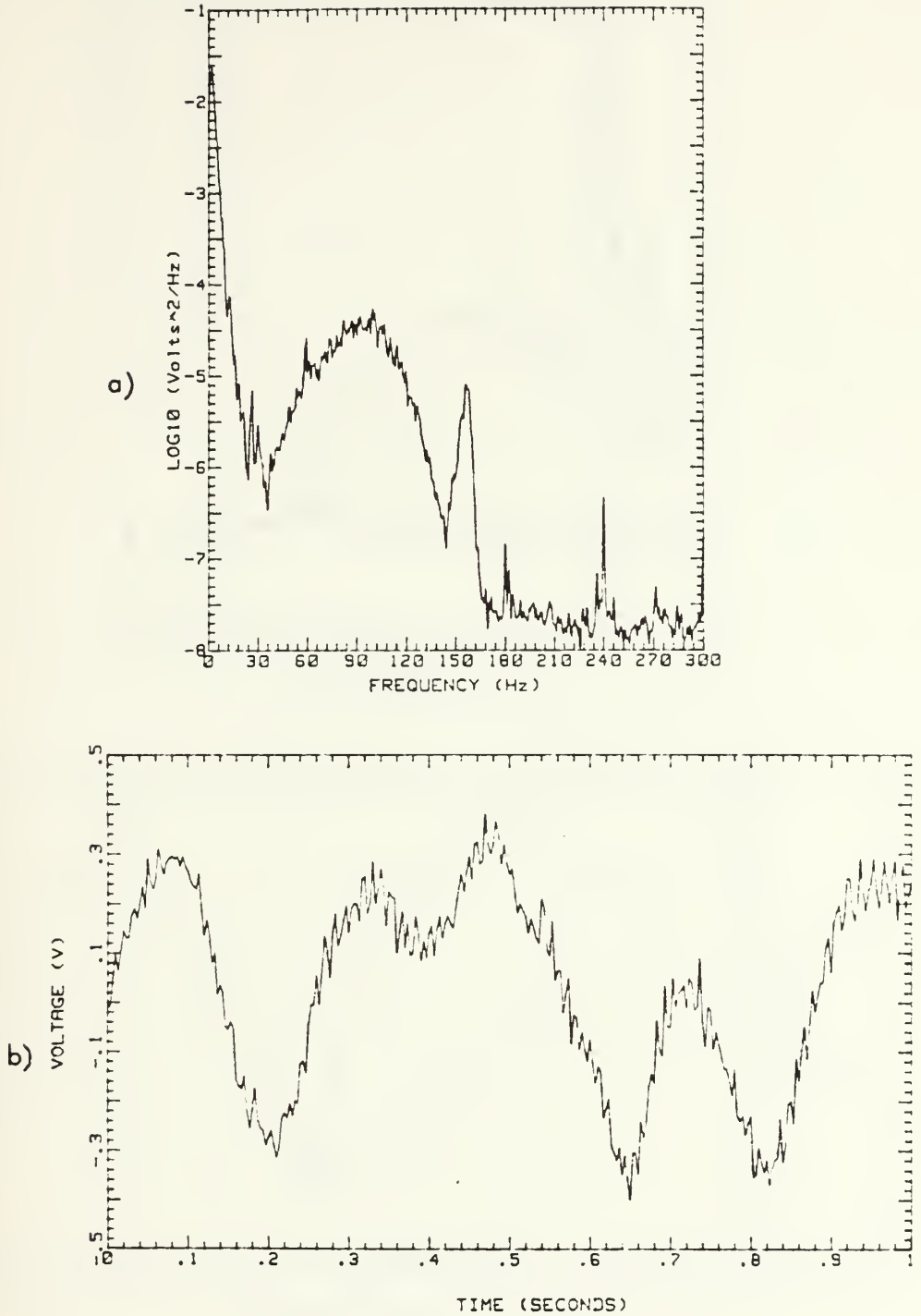

Figure 105. De=140, a) Conventional Hot-wire Spectra, Digital Analysis
b) Sample Time Trace

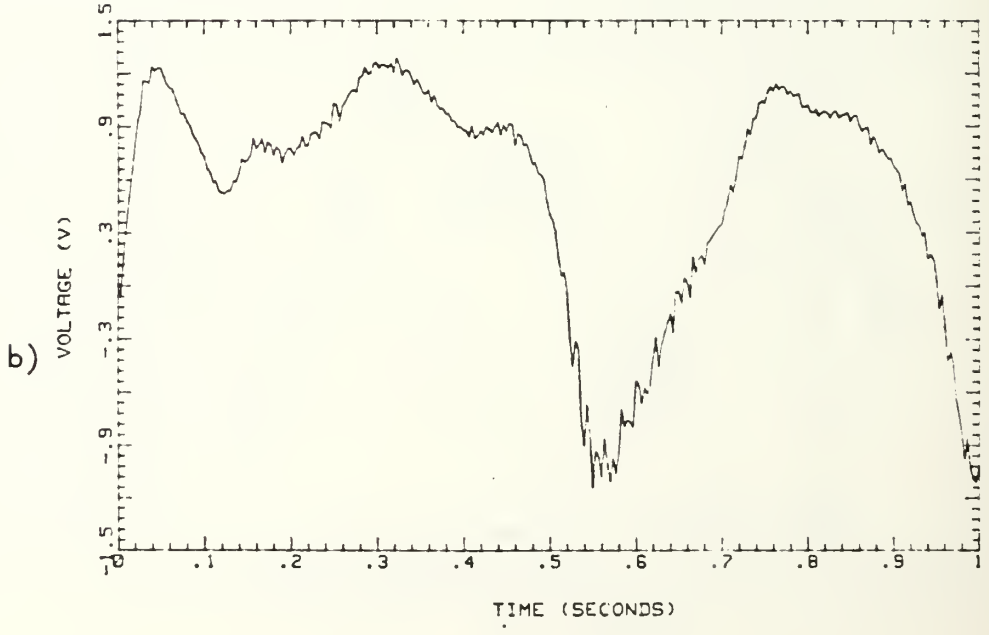

Figure 106. De=152, a) Conventional Hot-wire Spectra, Digital Analysis
b) Sample Time Trace

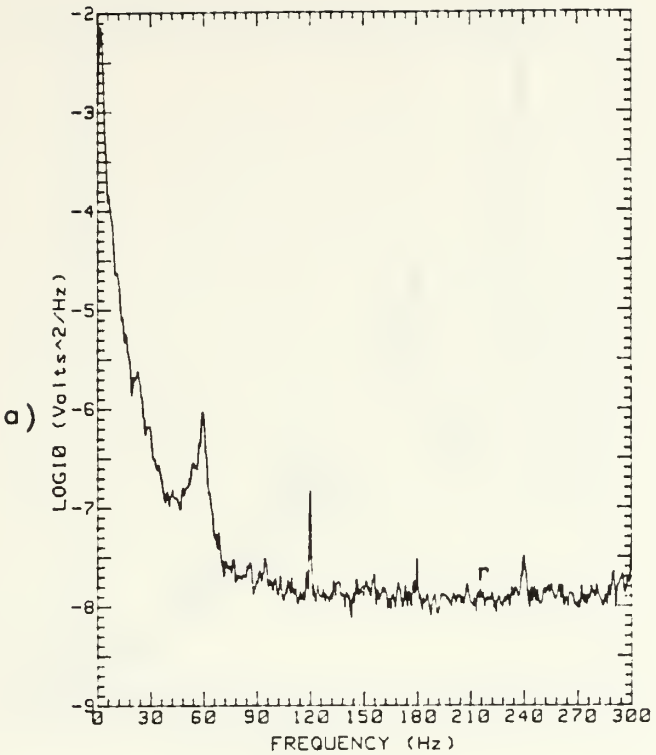

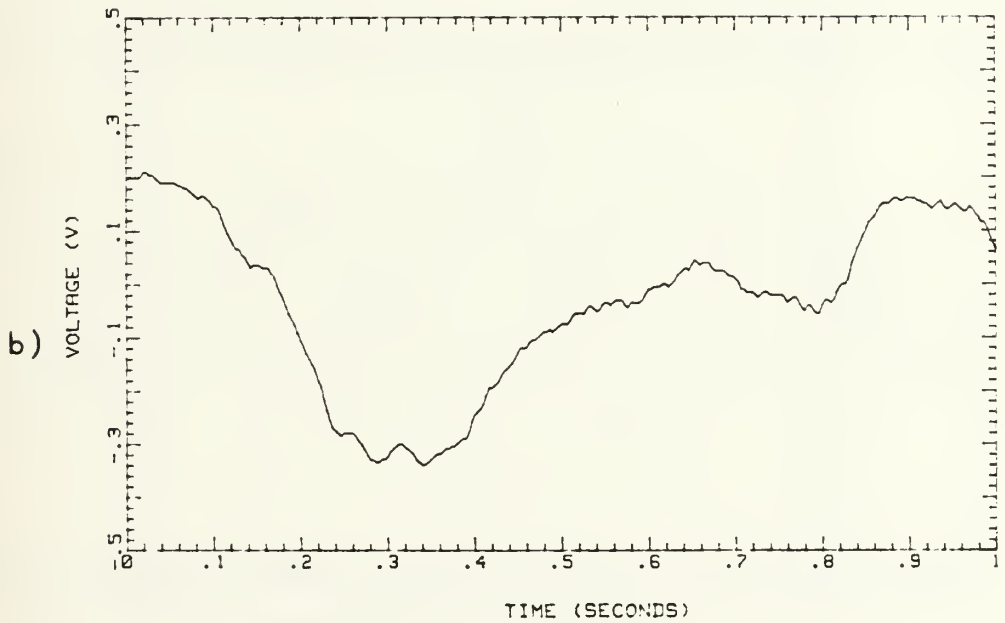

Figure 107. De=153, a) Subminiature Hot-wire Spectra, Digital Analysis
b) Sample Time Trace

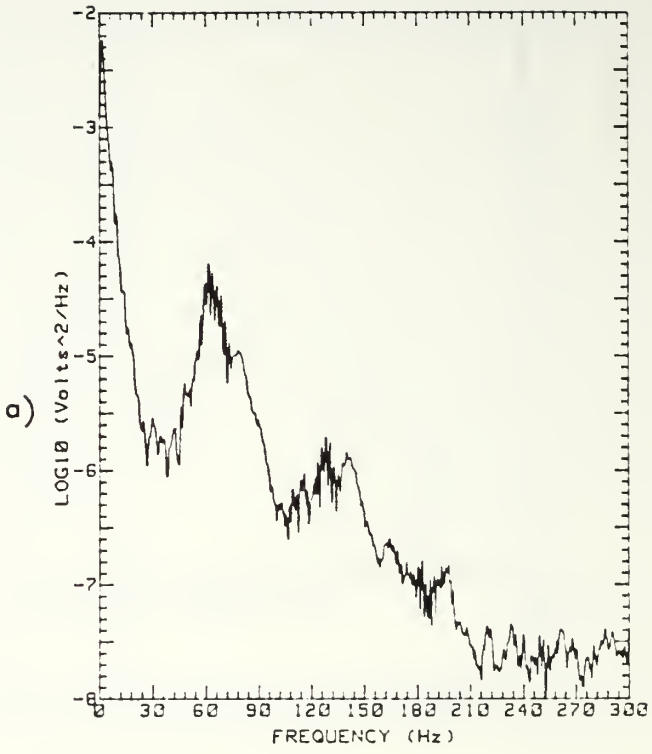

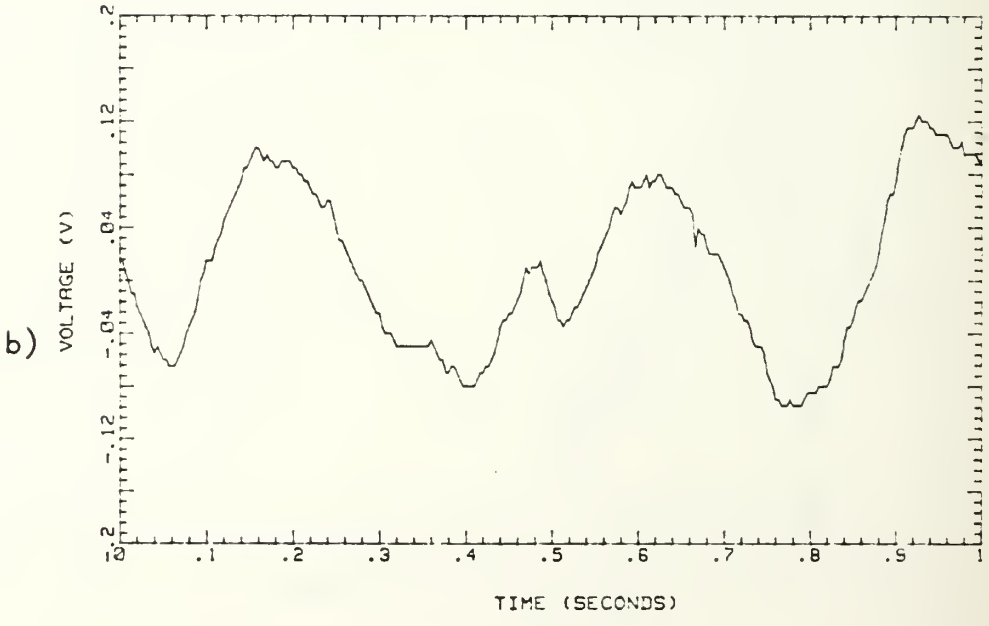

Figure 108. De=157, a) Subminiature Hot-wire Spectra, Digital Analysis
b) Sample Time Trace

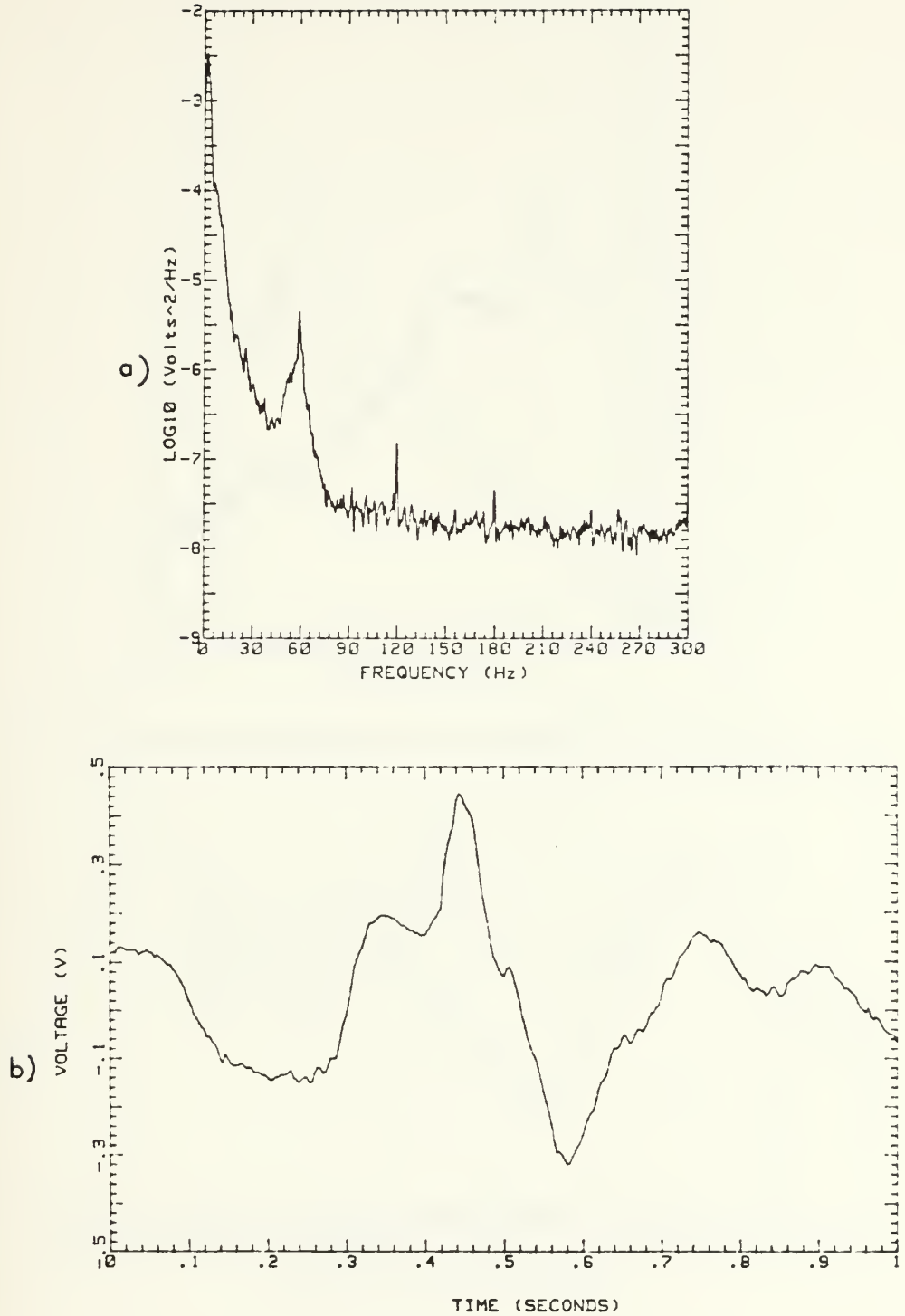

Figure 109. De=160, a) Subminiature Hot-wire Spectra, Digital Analysis
b) Sample Time Trace

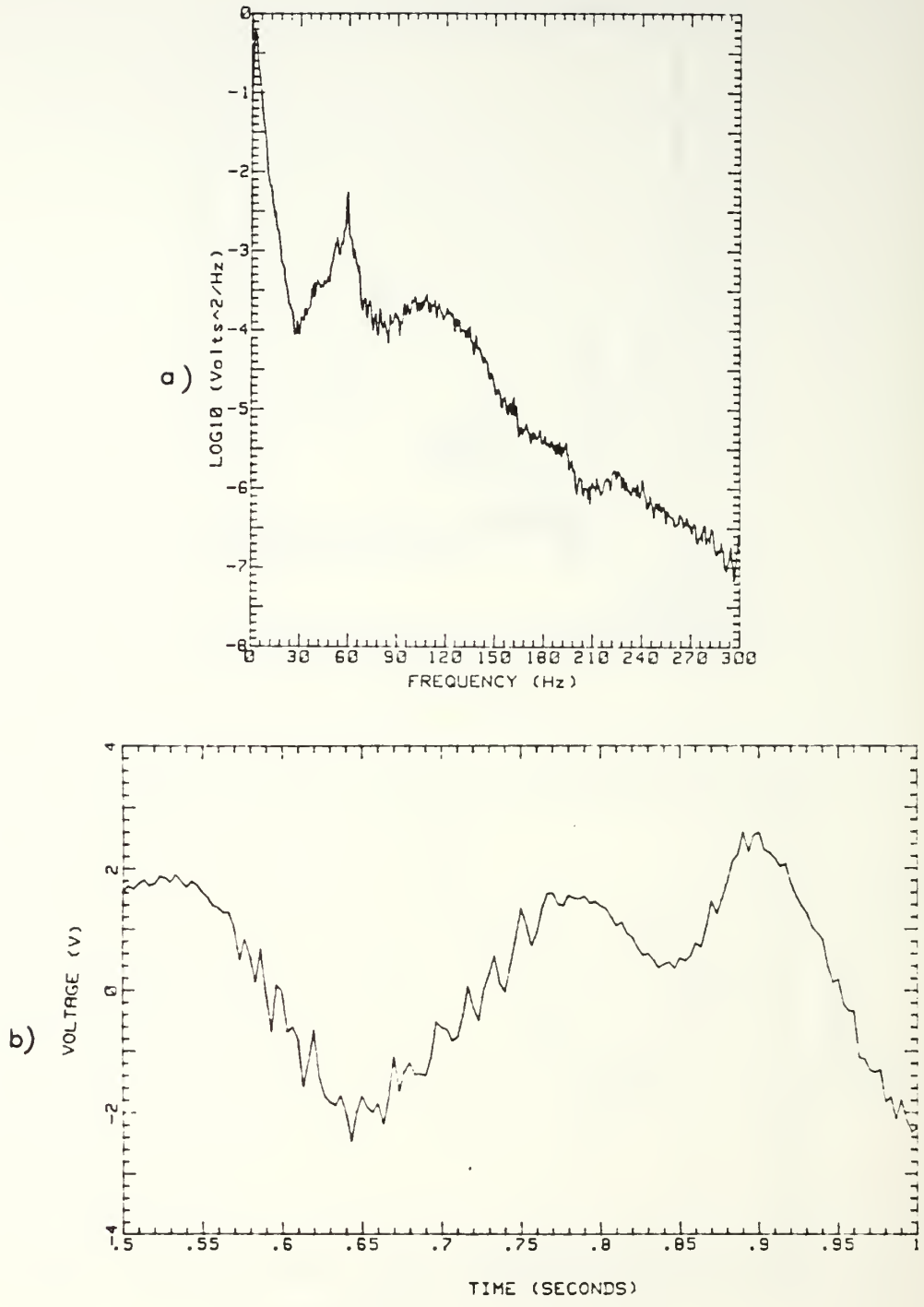

Figure 110. De=165, a) Conventional Hot-wire Spectra, Digital Analysis
b) Sample Time Trace

Figure 111. De=168, a) Conventional Hot-wire Spectra, Digital Analysis
b) Sample Time Trace

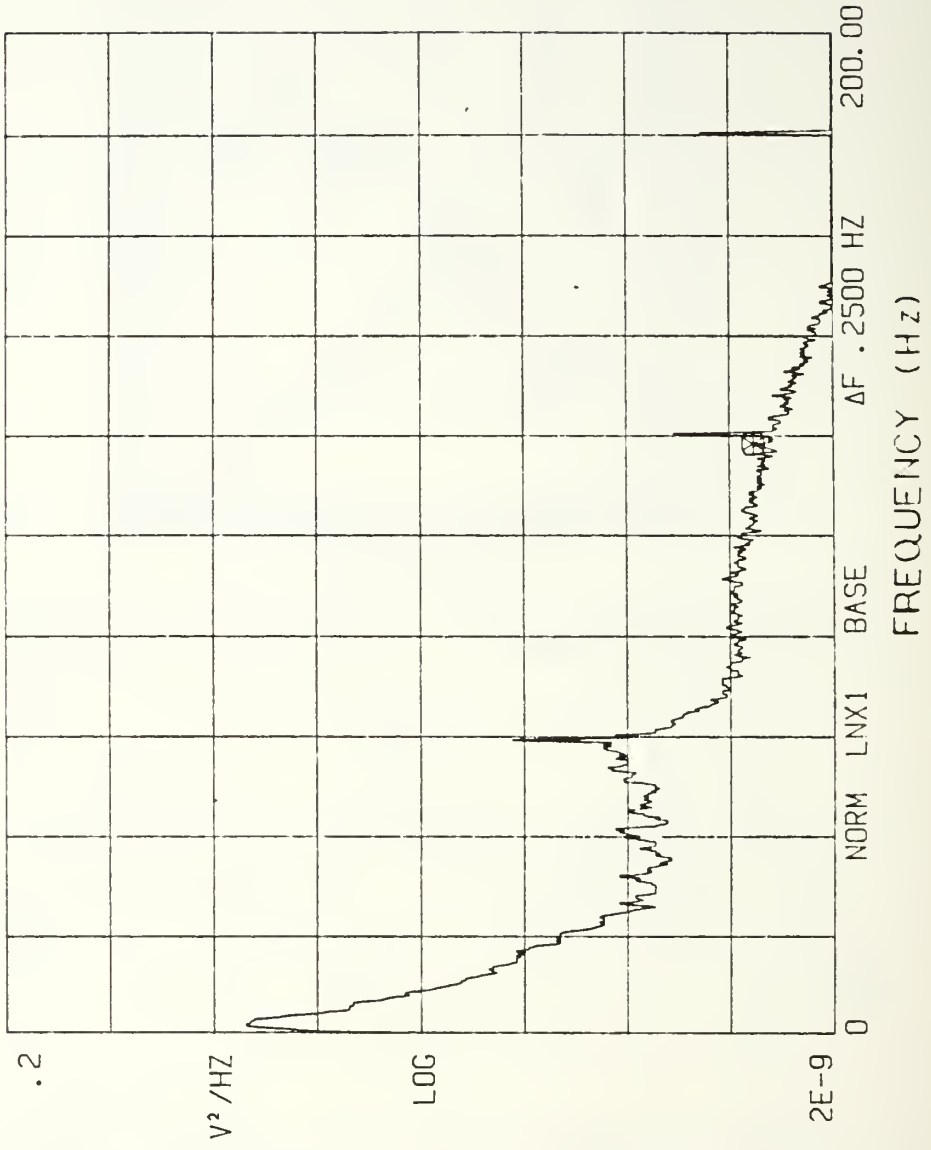

Figure 112. De=170, Subminiature Hot-wire Spectra, Real Time Analysis

Figure 113. De=175, a) Conventional Hot-wire Spectra, Digital Analysis
b) Sample Time Trace

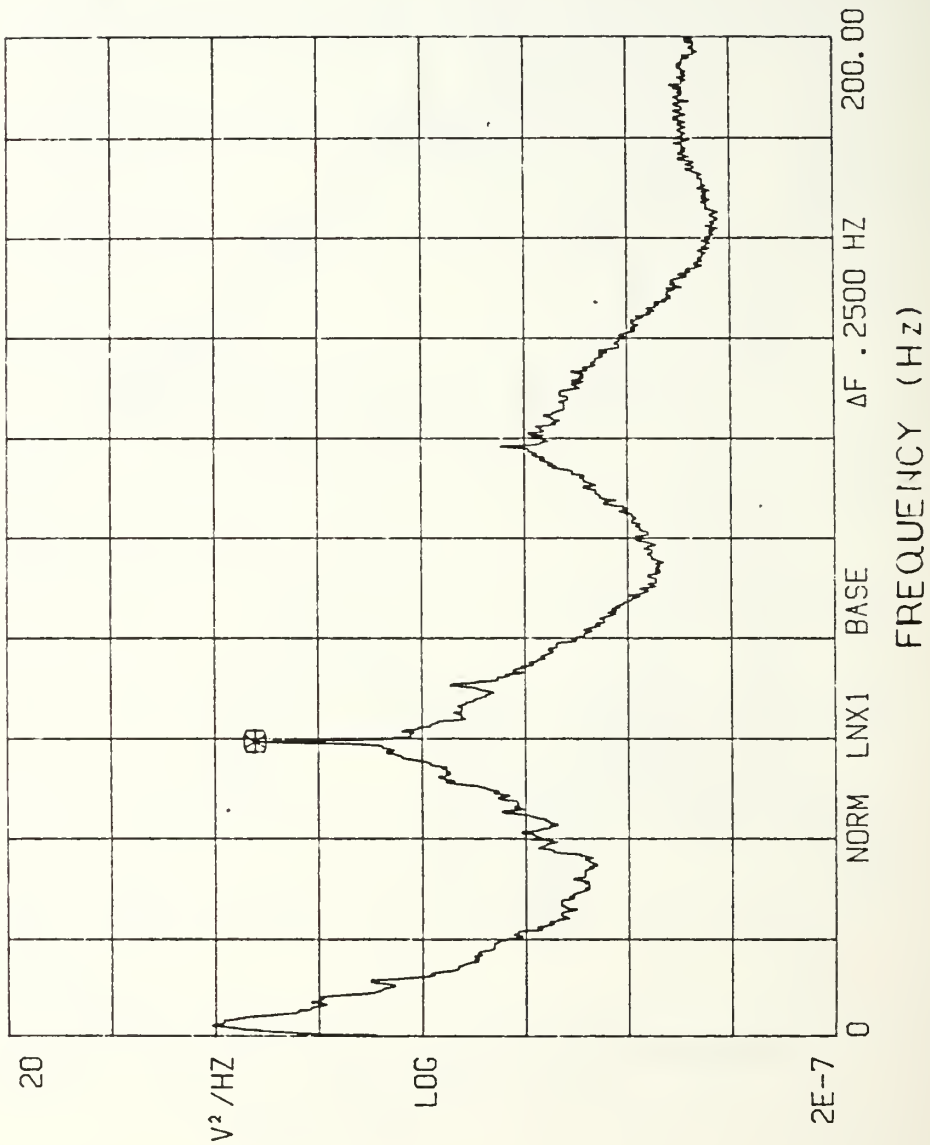

Figure 114. De=180, Conventional Hot-wire Spectra Real Time Analysis

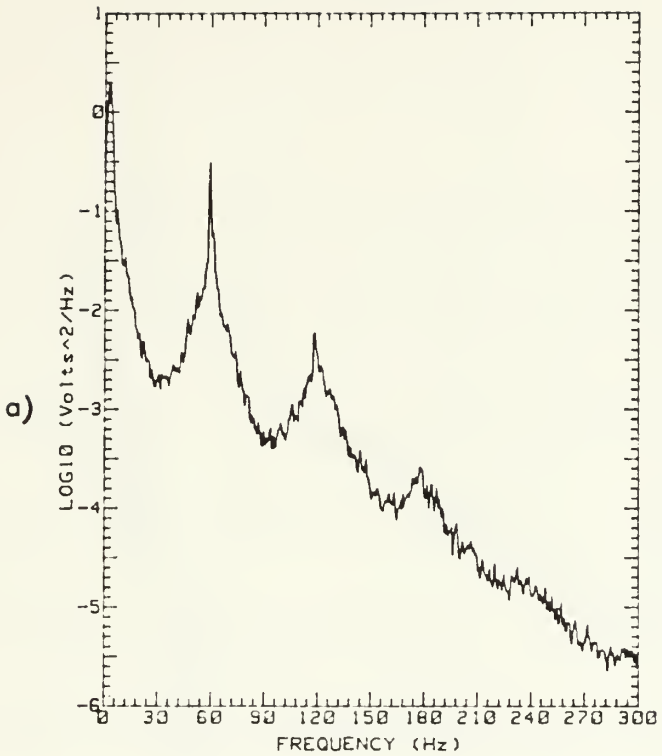

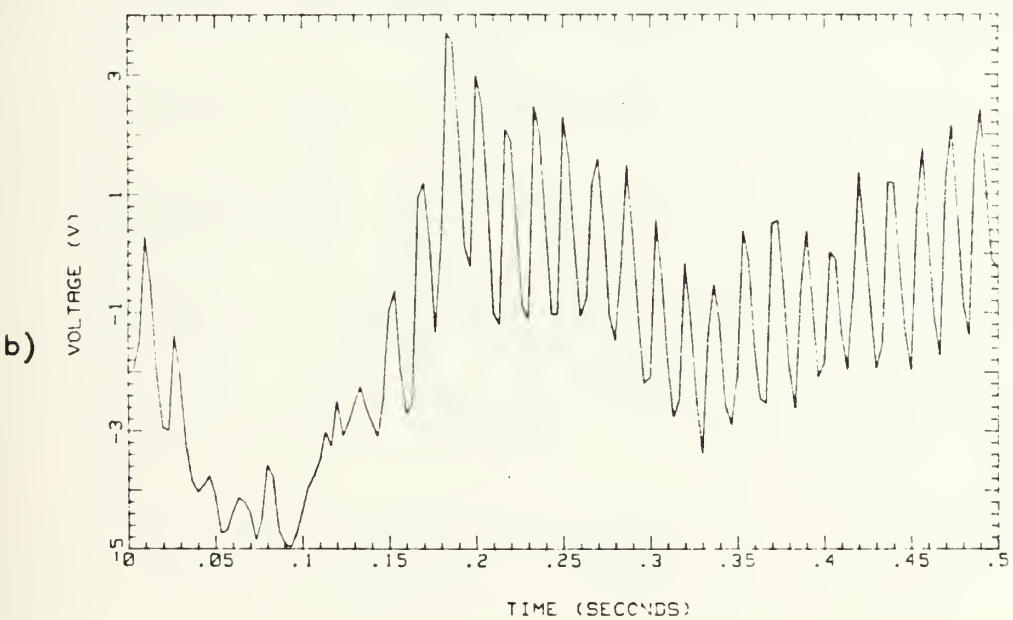

Figure 115. De=180, a) Conventional Hot-wire Spectra, Digital Analysis
b) Sample Time Trace

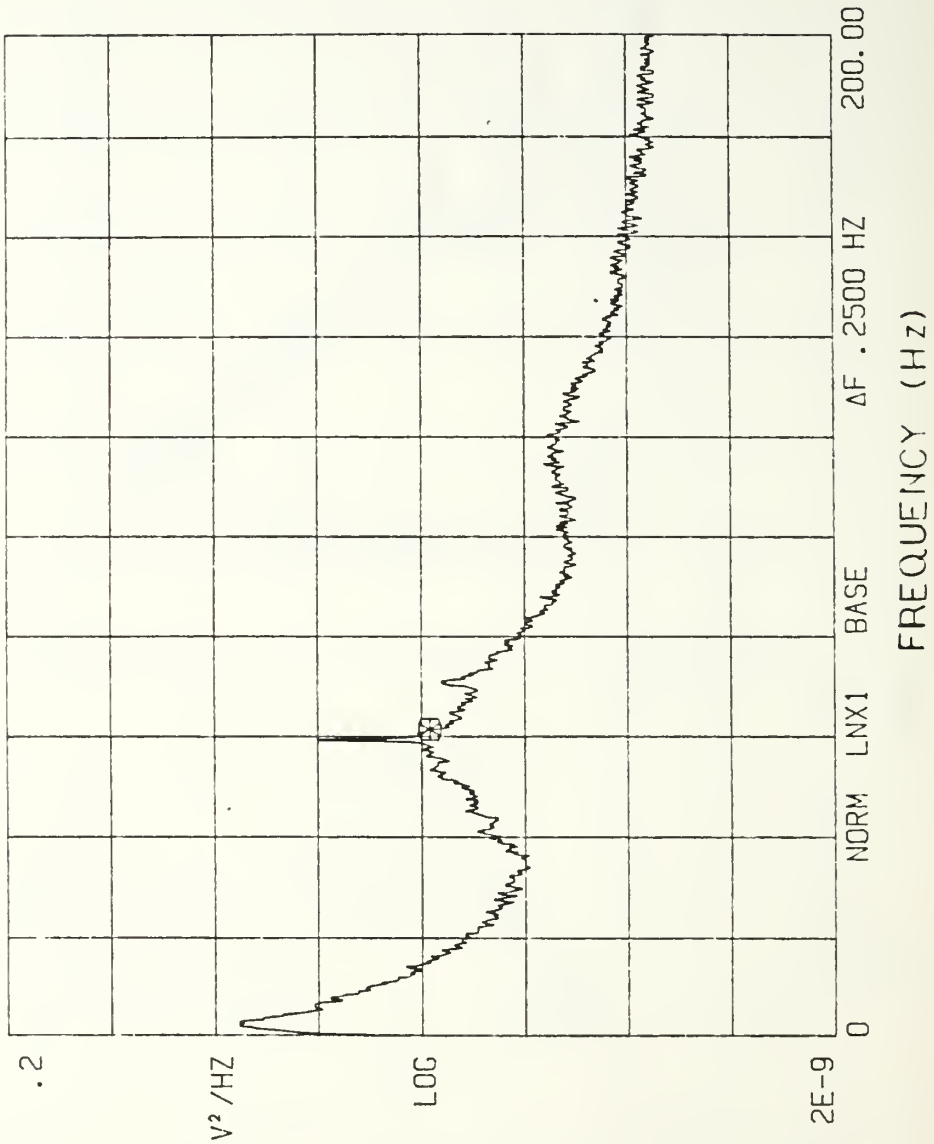

Figure 116. De=184, Subminiature Hot-wire Spectra, Real Time Analysis

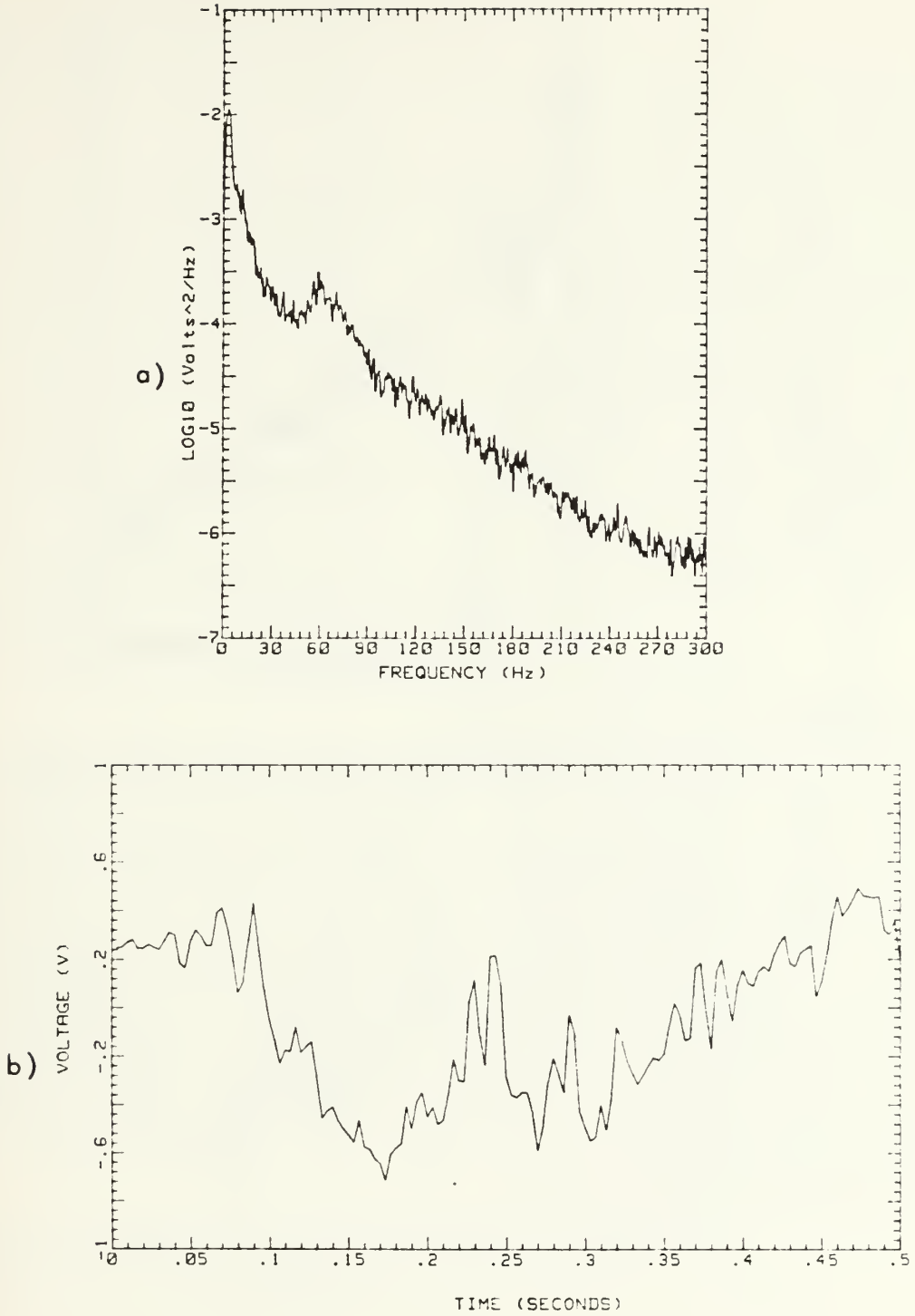

Figure 117. De=190, a) Subminiature Hot-wire Spectra, Digital Analysis
b) Sample Time Trace

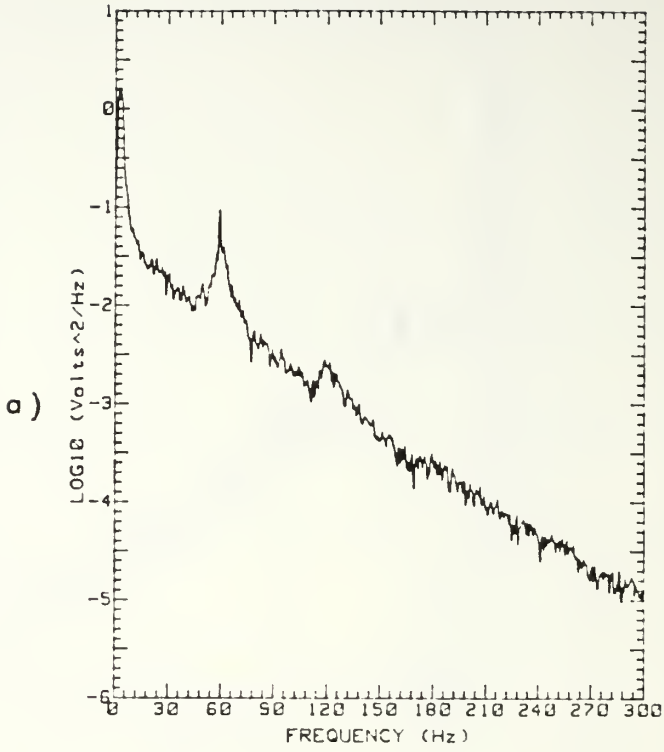

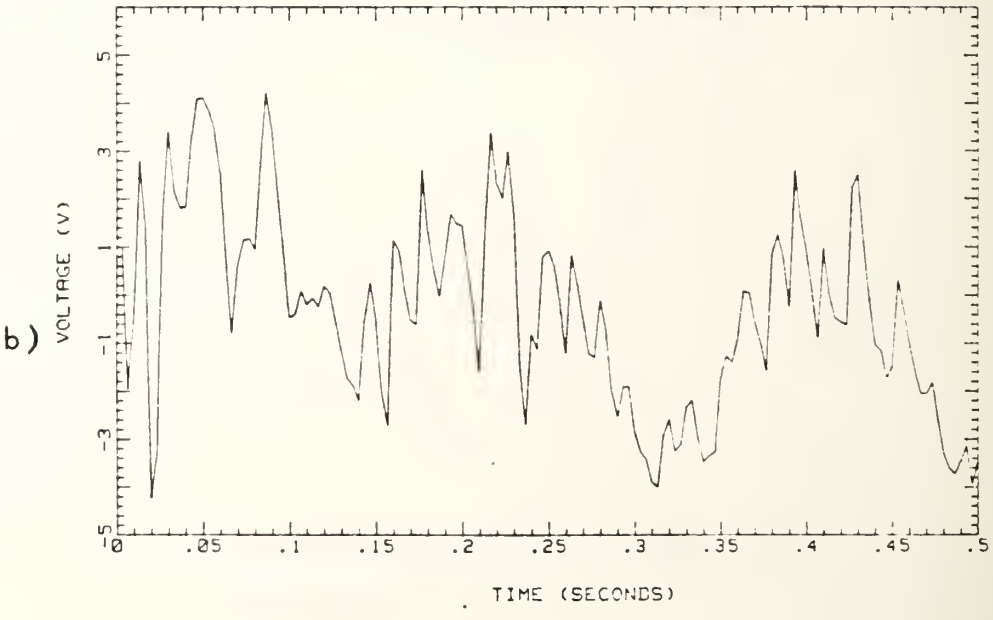

Figure 118. De=190, a) Conventional Hot-wire Spectra, Digital Analysis
b) Sample Time Trace

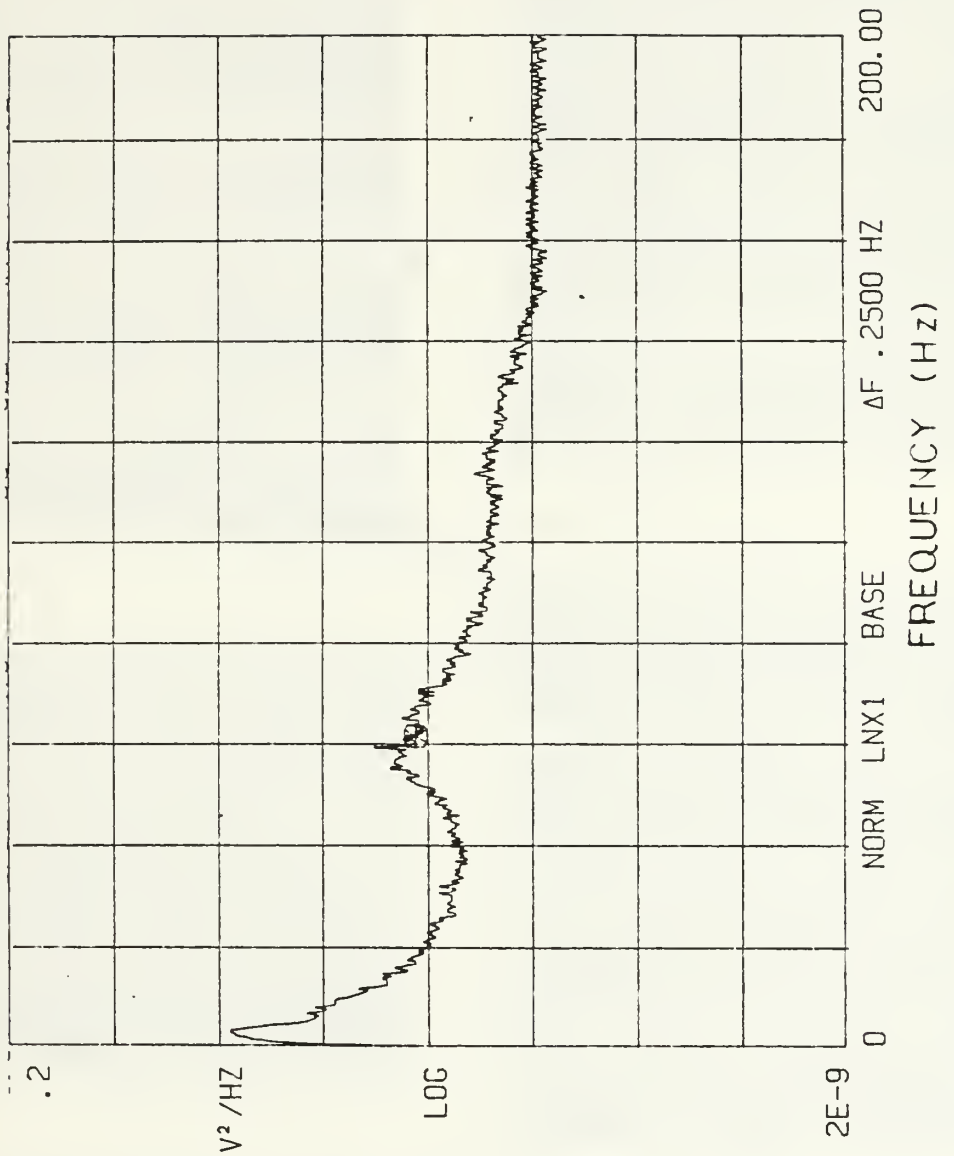

Figure 119. De=190, Subminiature Hot-wire Spectra, Real Time Analysis

Figure 120. De=200, a) Conventional Hot-wire Spectra Digital Analysis
b) Sample Time Trace

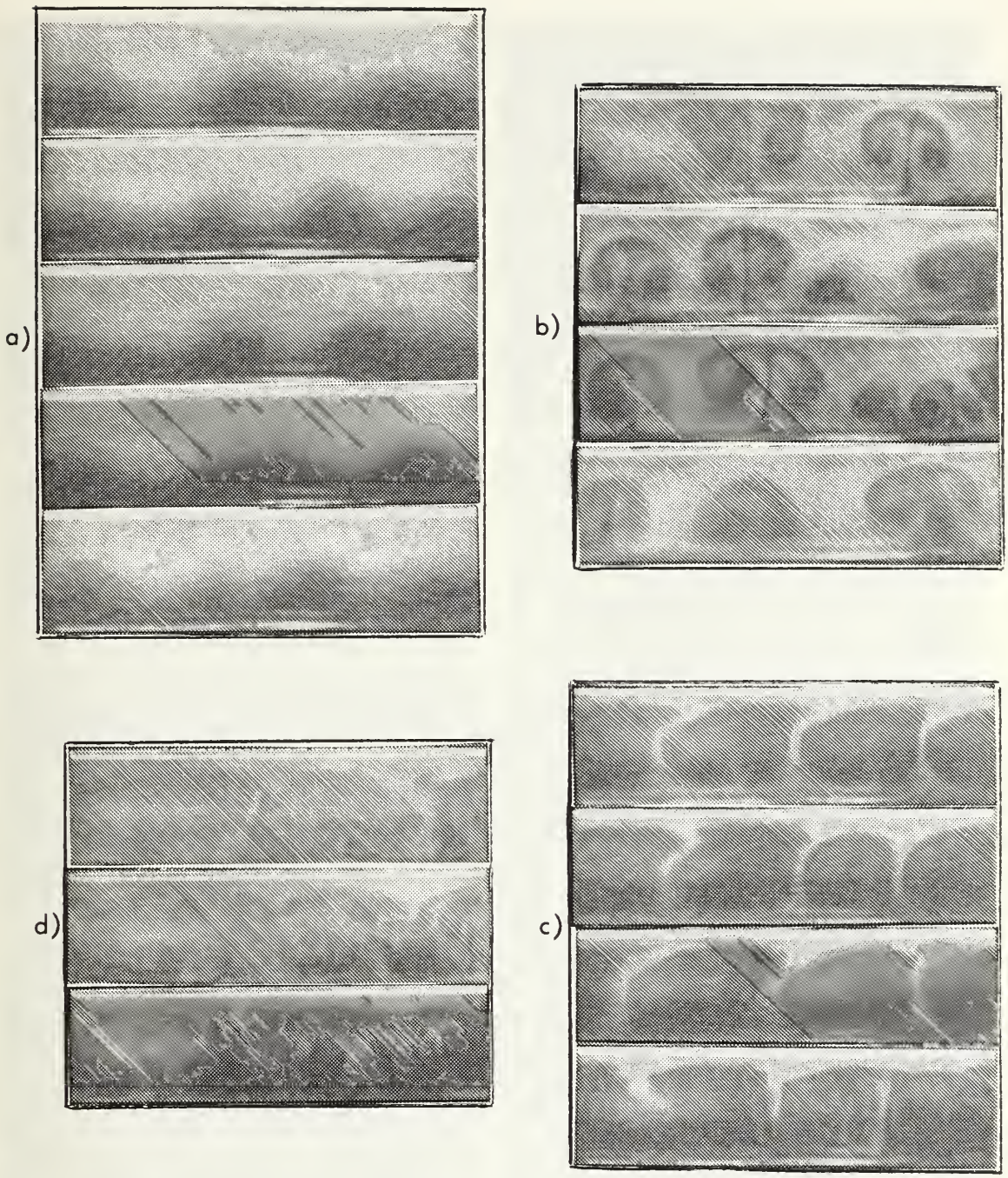

Figure 121. Radial-Spanwise Plane Flow Visualization
a) De=51.9, b) De=64.4, c) De=95.4 d) De=107.7

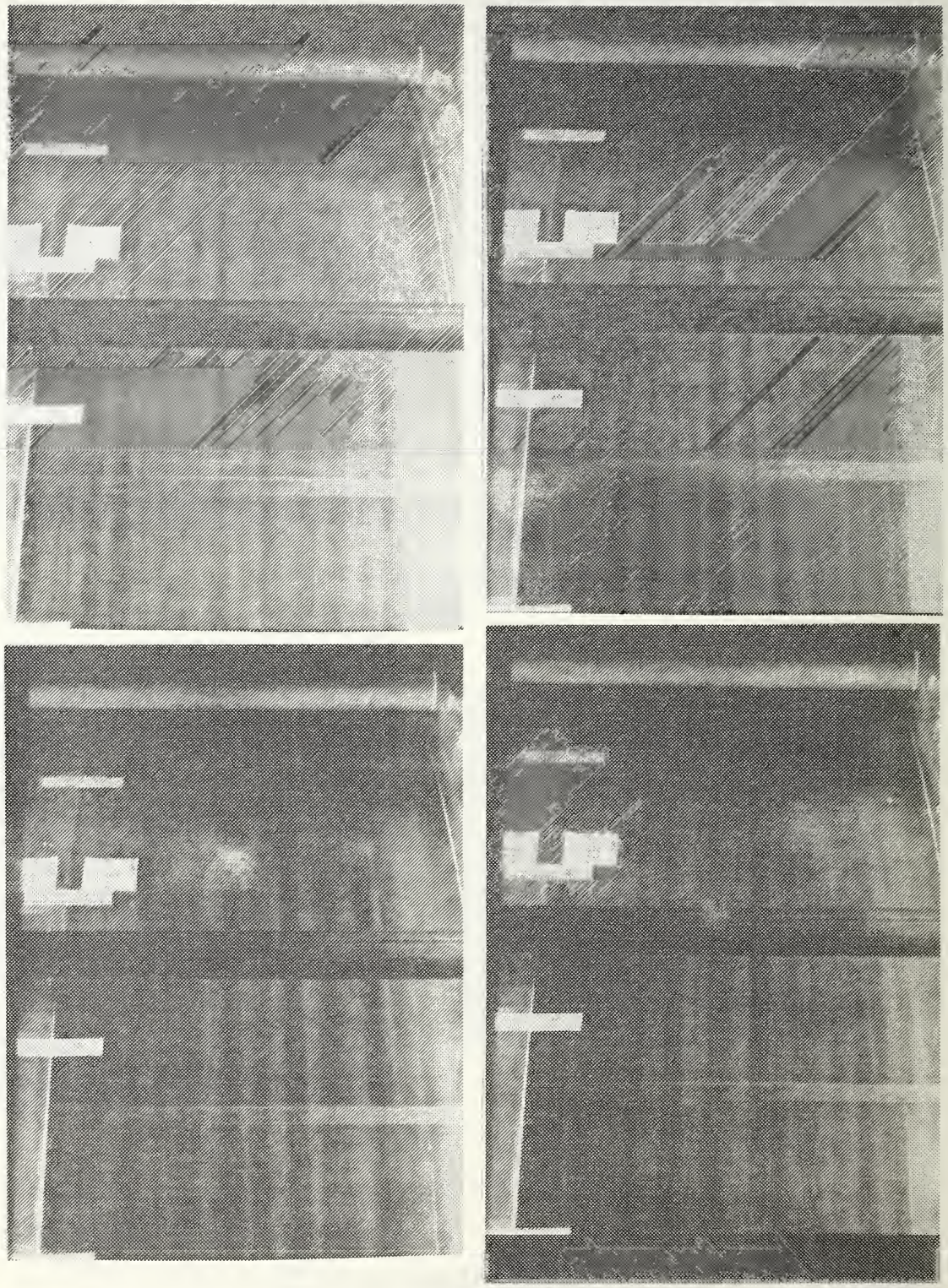

Figure 122. Concave Surface Flow Visualization, De=88.5, 50°-80°

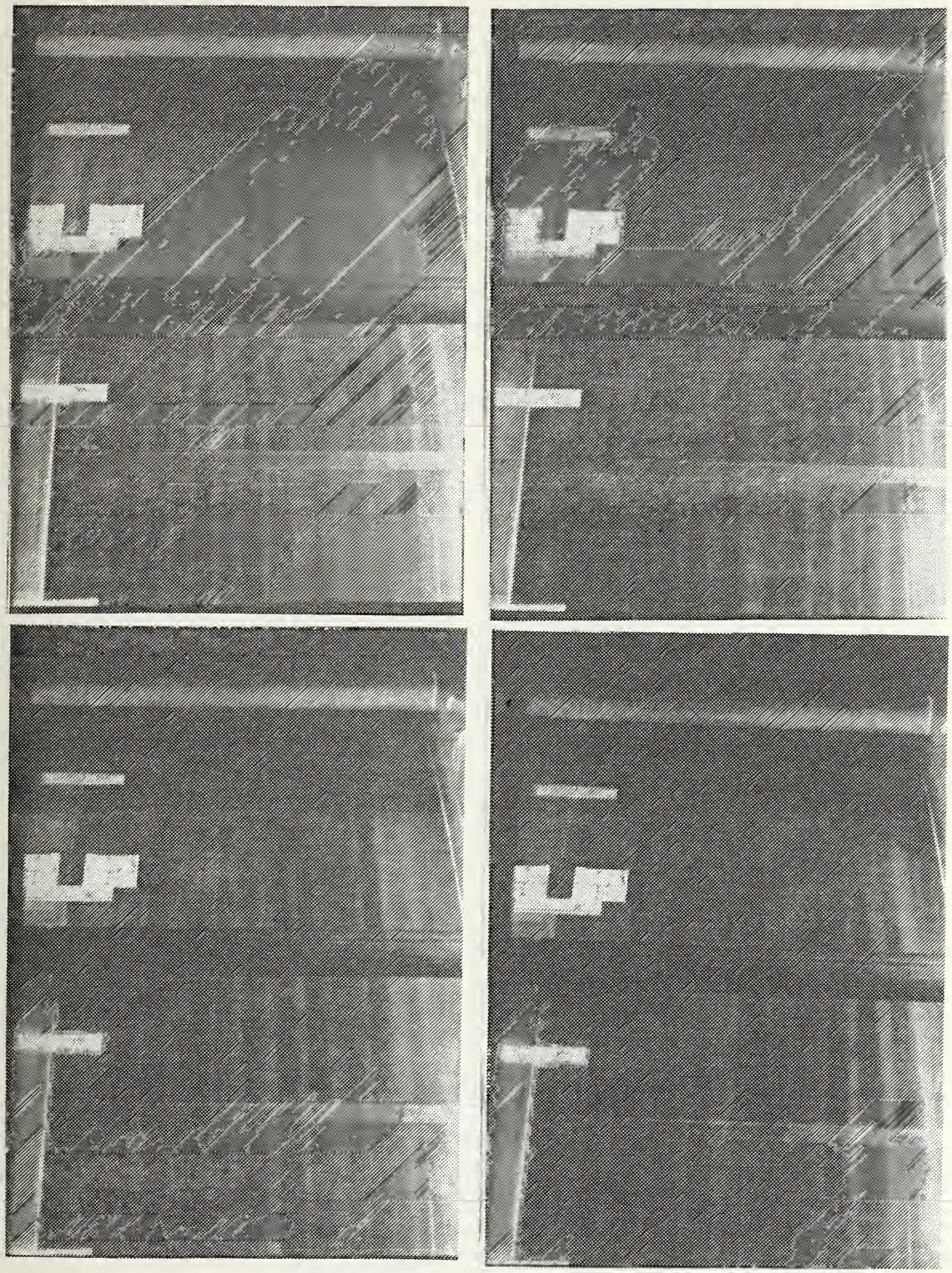

Figure 123. Concave Surface Flow Visualization, De=97.0, 50°-80°

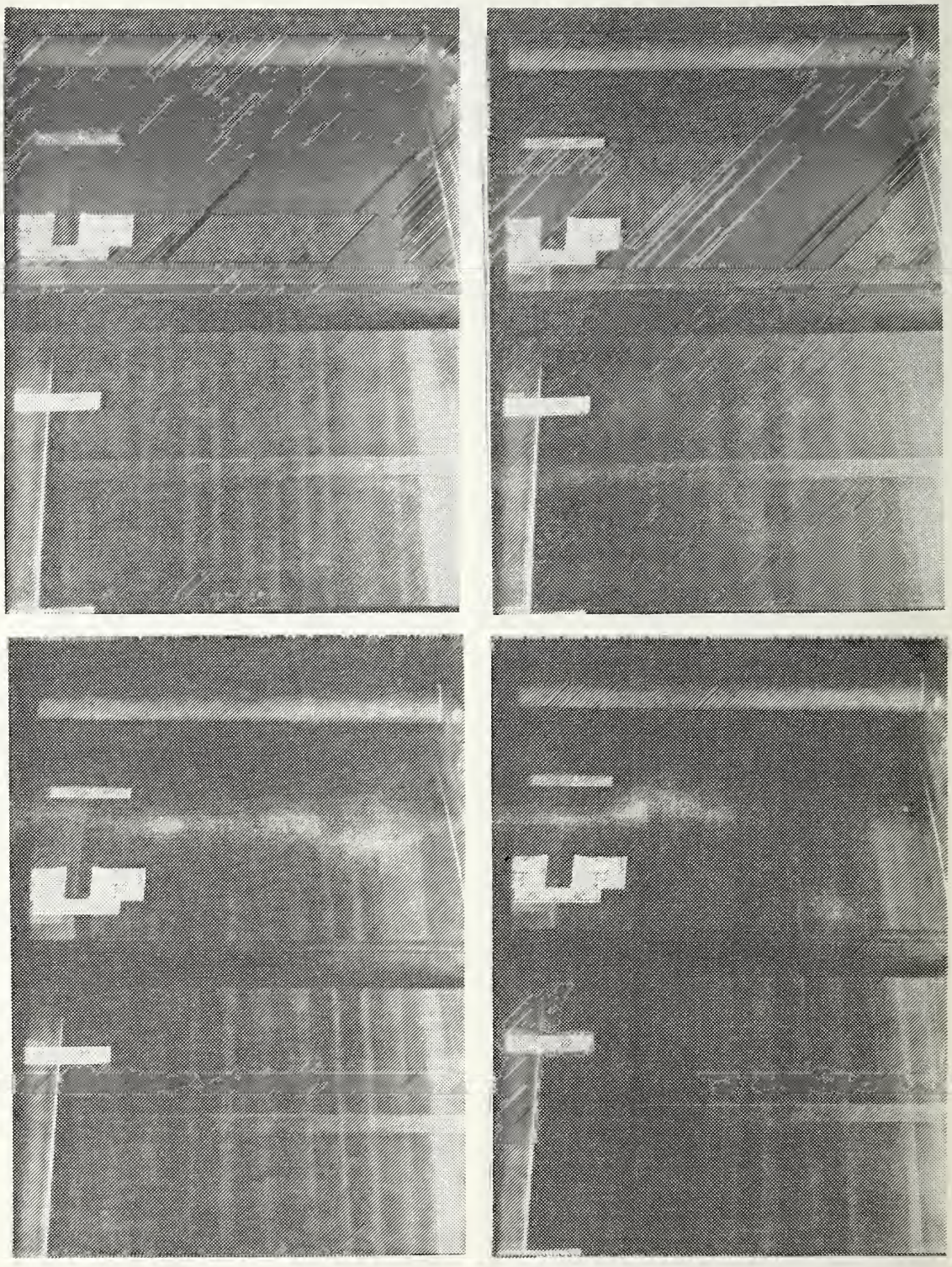

Figure 124. Concave Surface Flow Visualization, De=106.6, 50°-80°

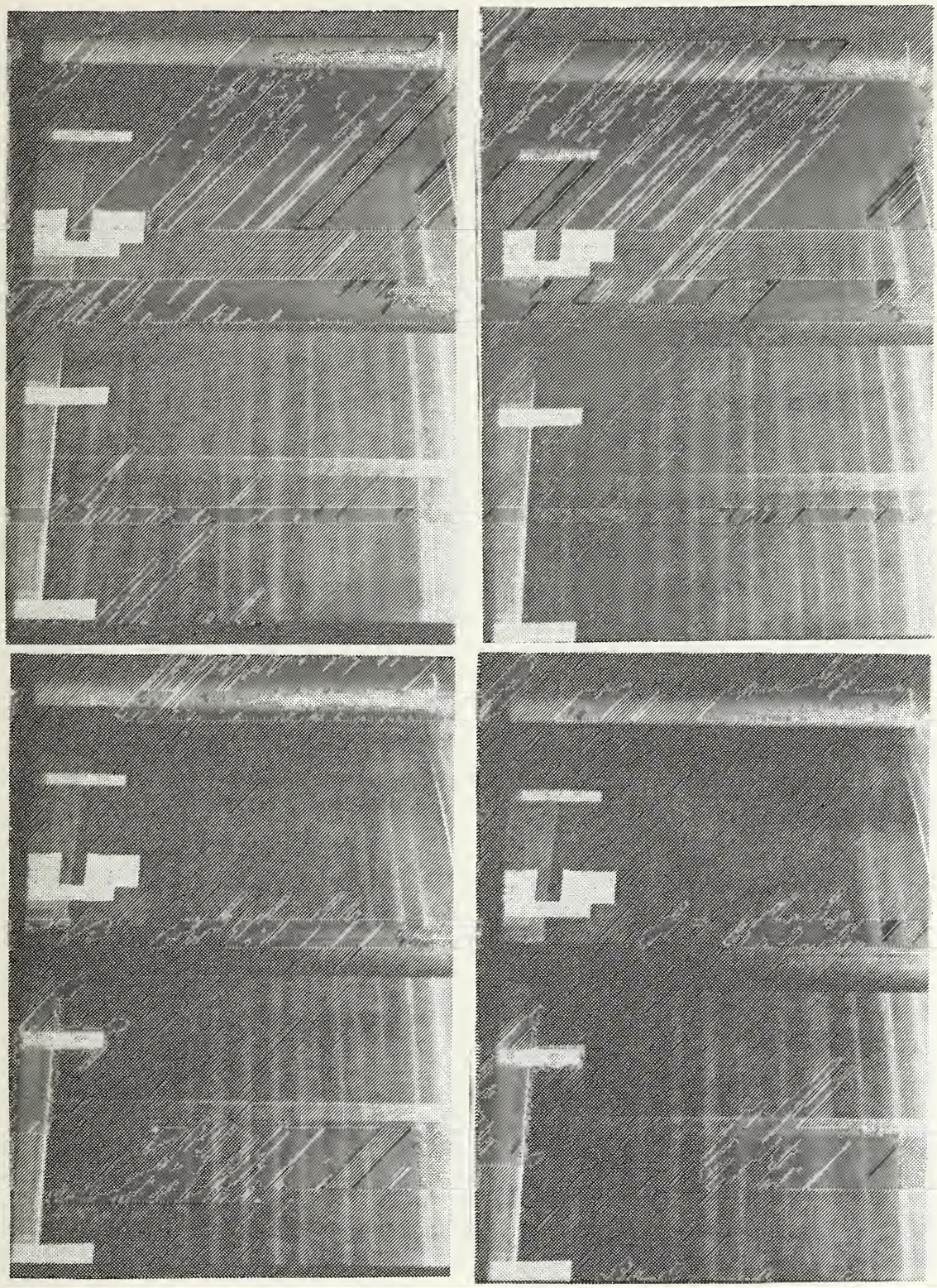

Figure 125. Concave Surface Flow Visualization, De=125.4, 50°-80°

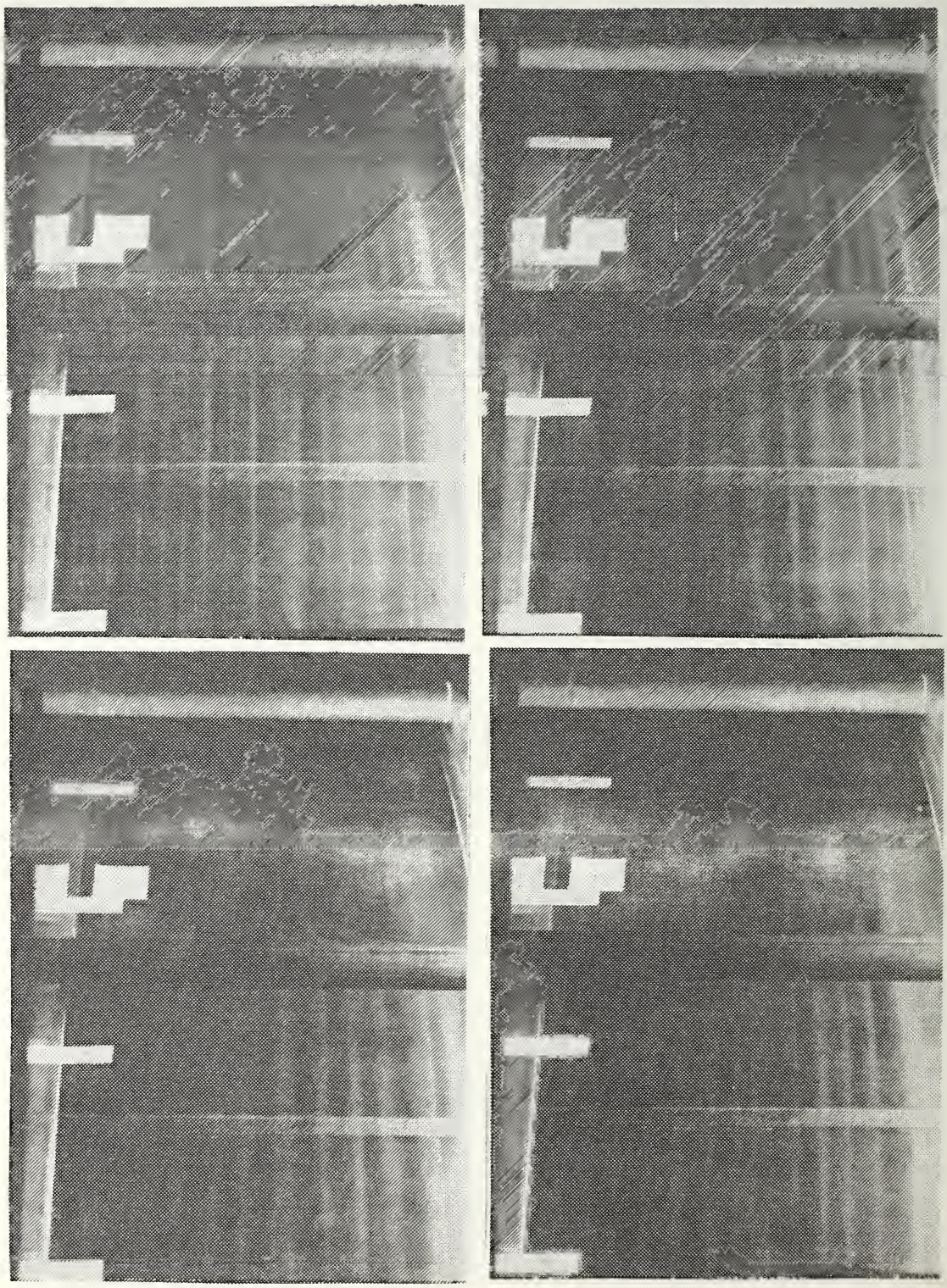

Figure 126. Concave Surface Flow Visualization, De=145.2, 50°-80°

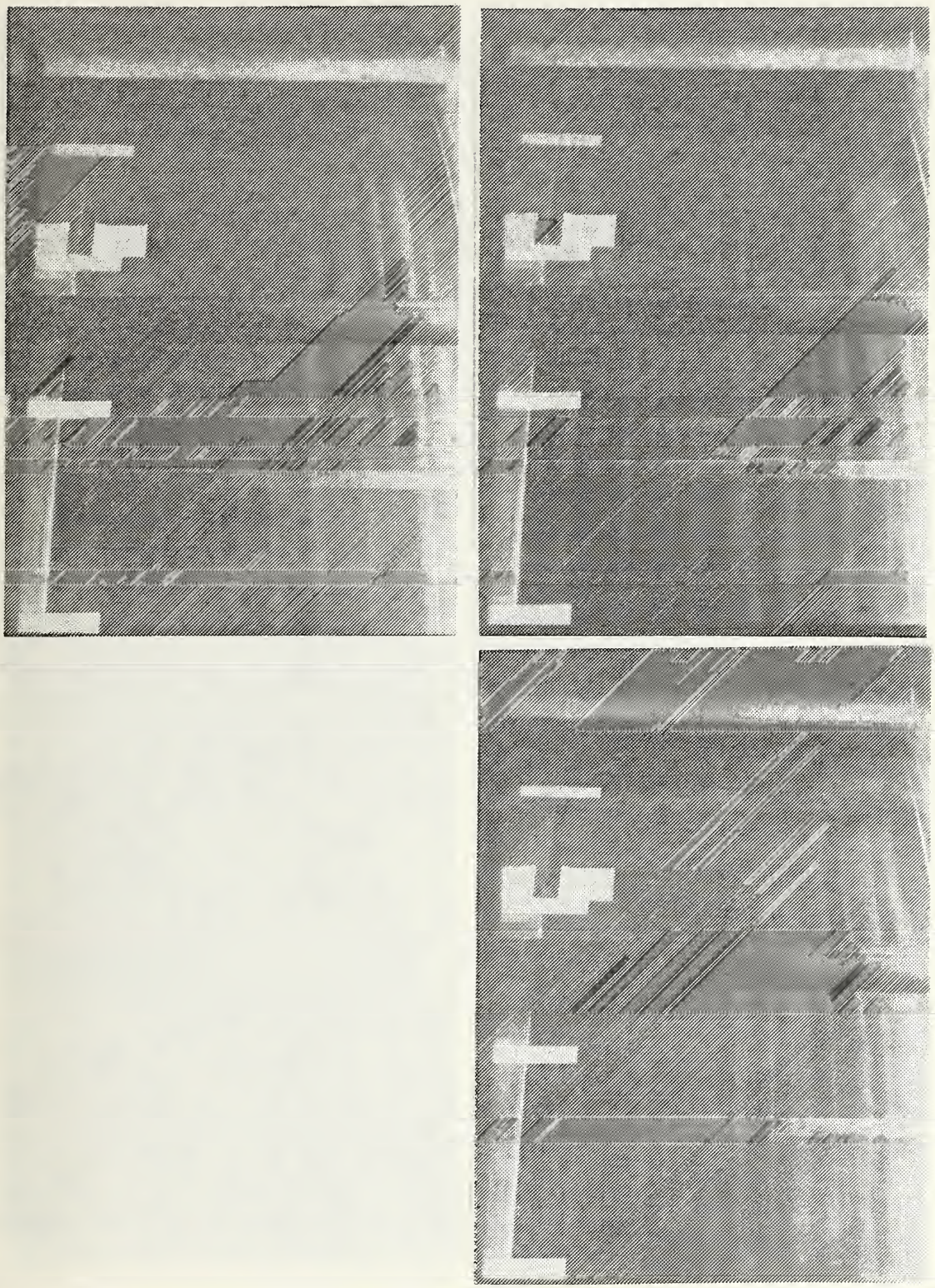

Figure 127. Concave Surface Flow Visualization, De=165.6, 50°-80°

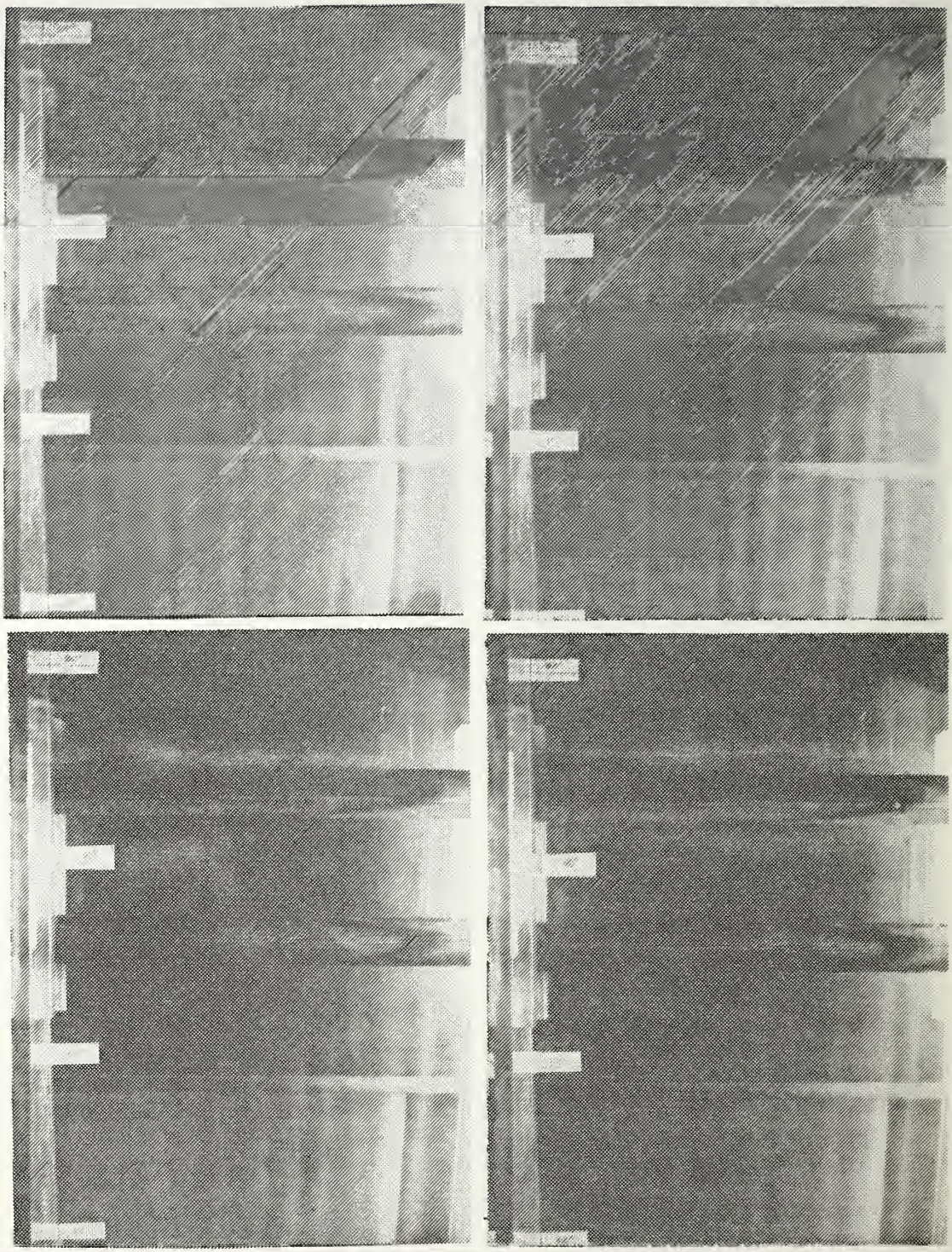

Figure 128. Concave Surface Flow Visualization, De=54.2, 80°-110°

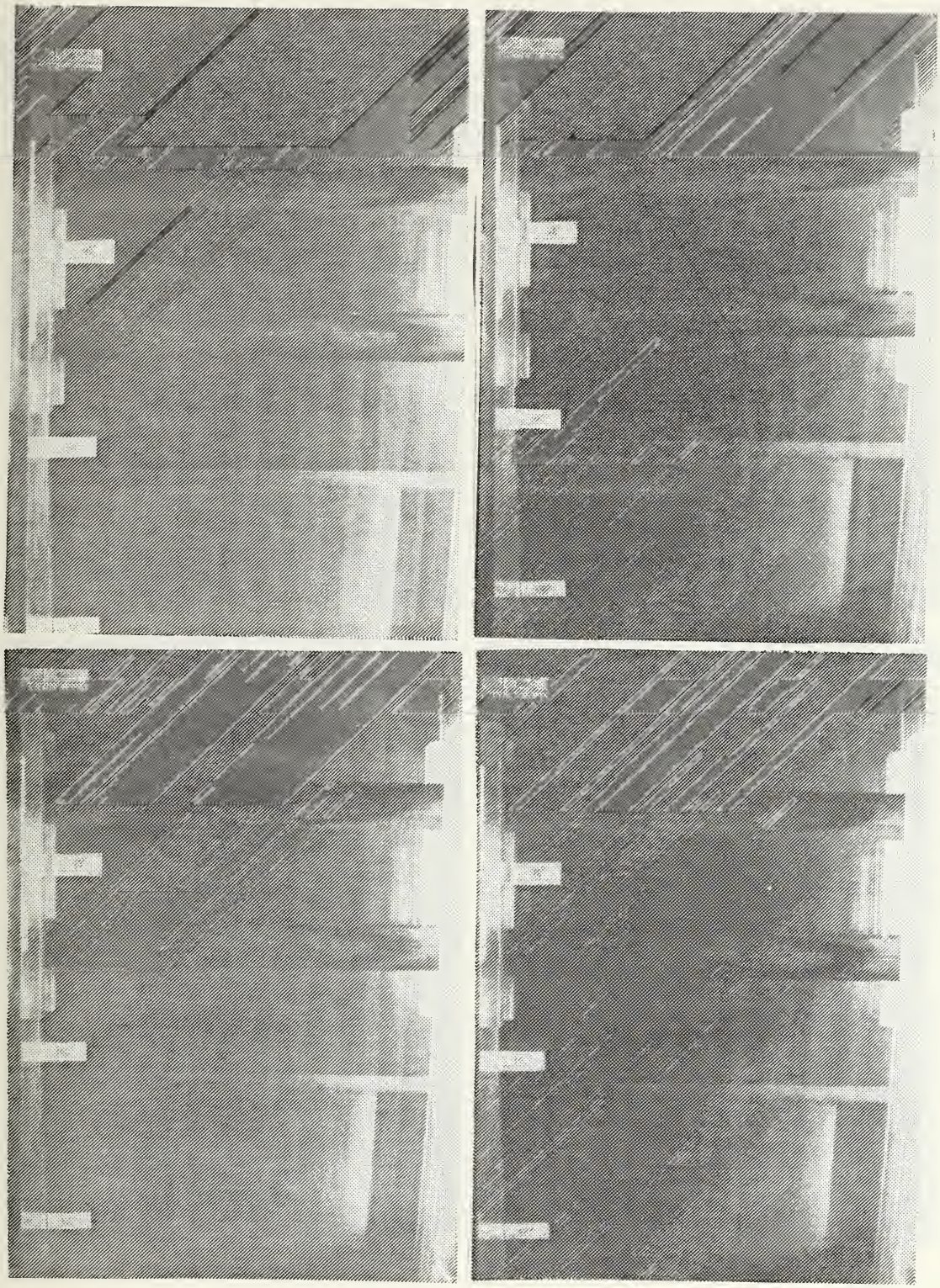

Figure 129. Concave Surface Flow Visualization, De=64.5, 80°-110°

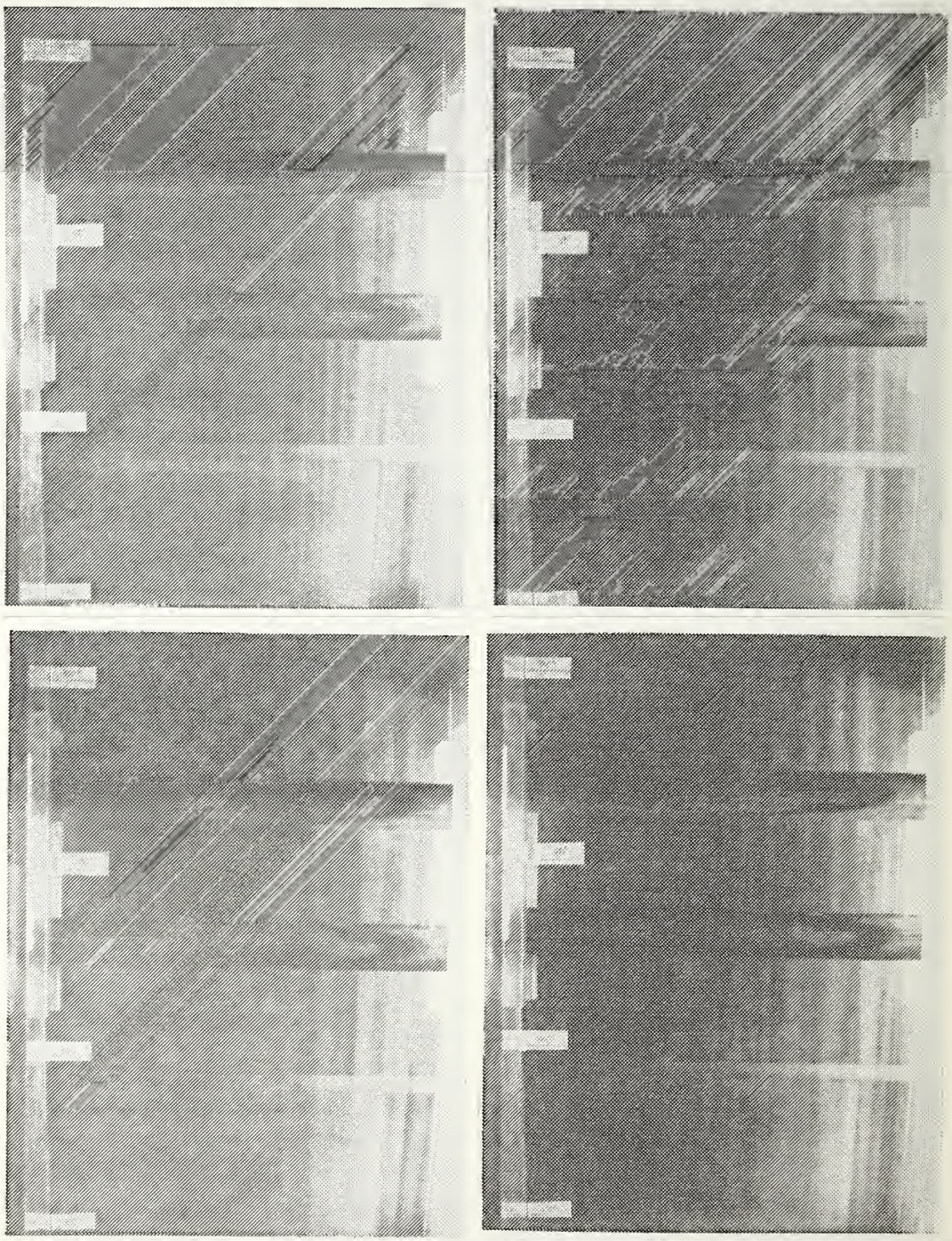

Figure 130. Concave Surface Flow Visualization, De=74.8, 80°-110°

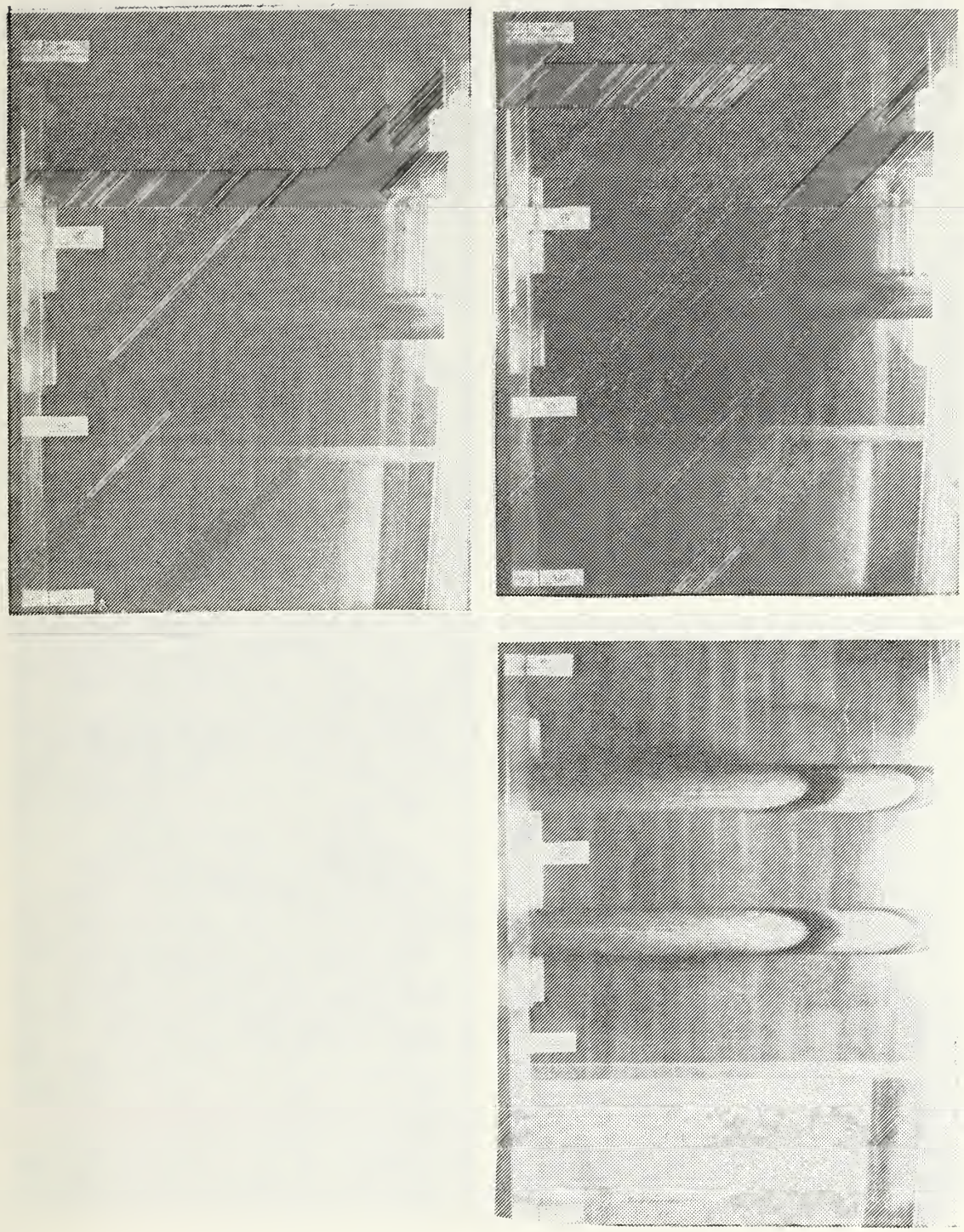

Figure 131. Concave Surface Flow Visualization, De=86.1, 80°-110°

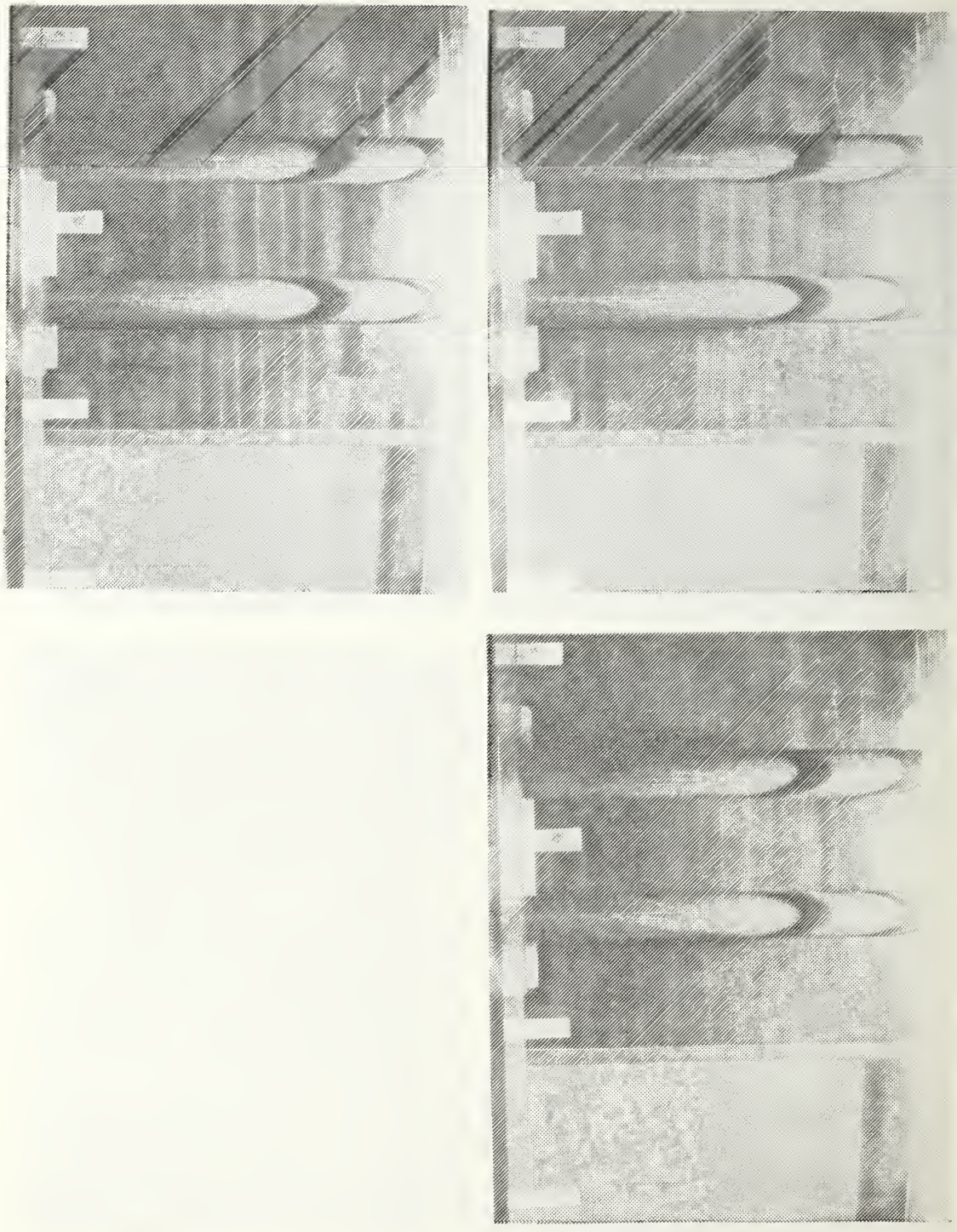

Figure 132. Concave Surface Flow Visualization, De=94.5, 80°-110°

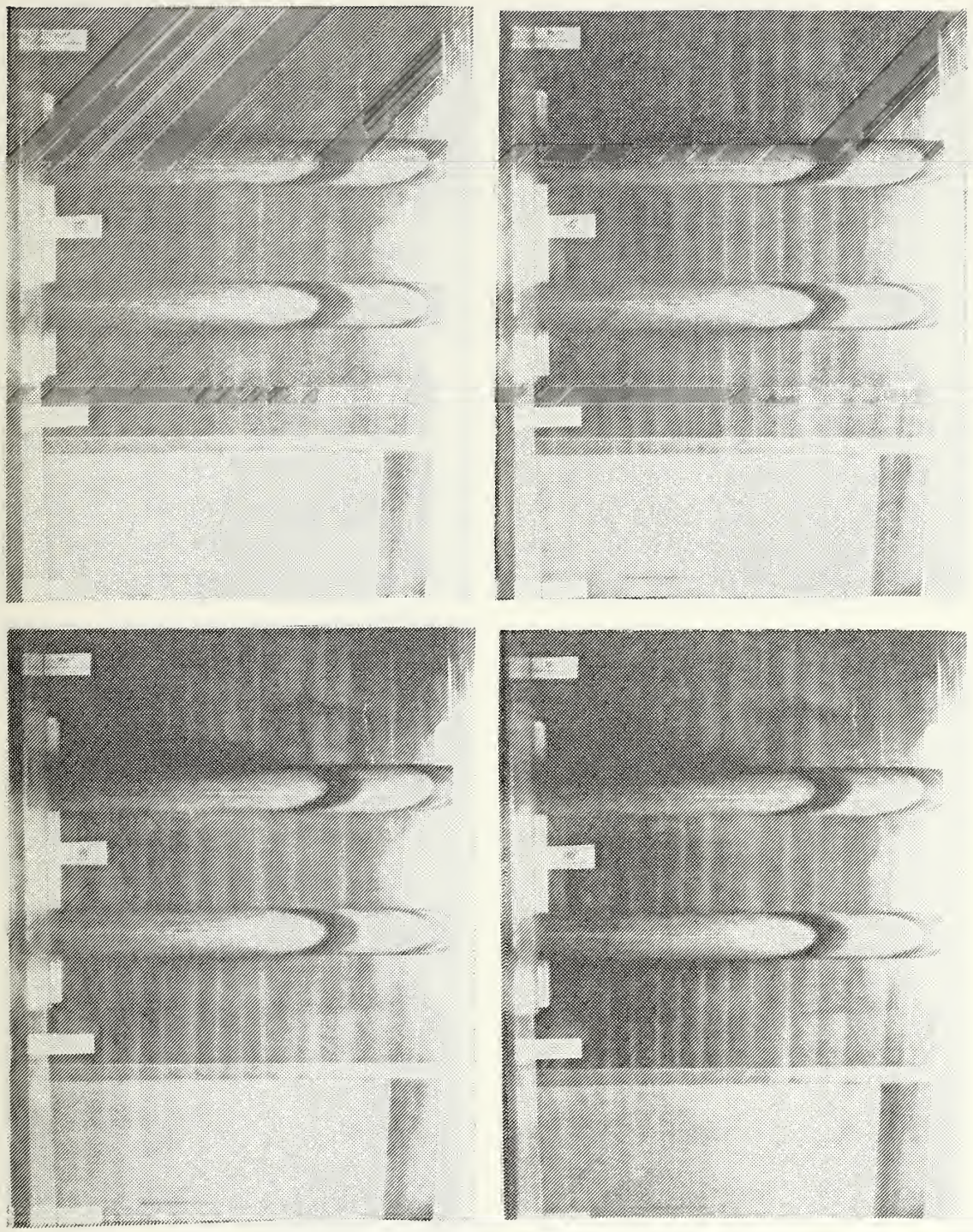

Figure 133. Concave Surface Flow Visualization, De=104.8, 80°-110°

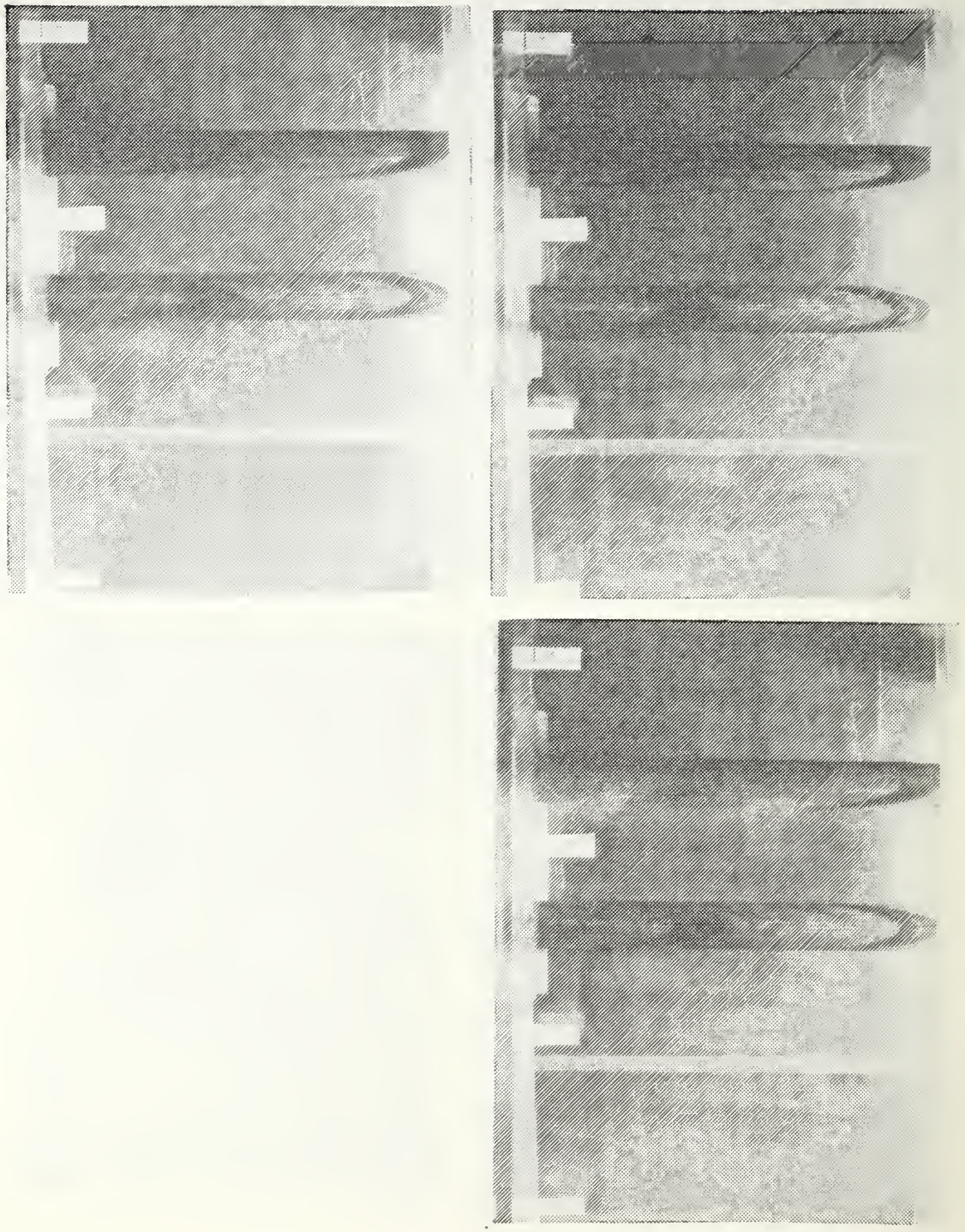

Figure 134. Concave Surface Flow Visualization, De=142.8, 80°-110°

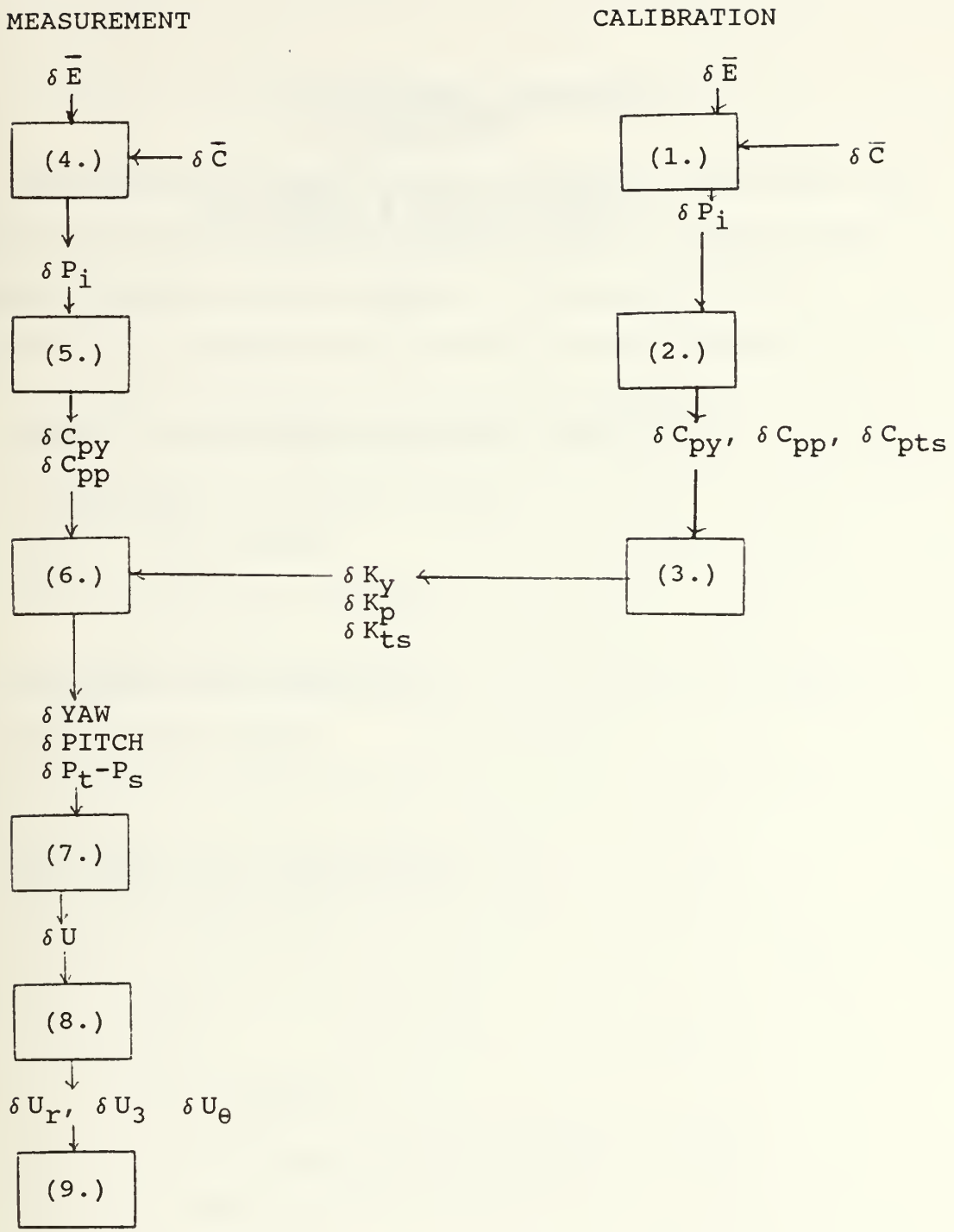

Figure 135. Uncertainty Analysis Flow Chart

APPENDIX B

UNCERTAINTY ANALYSIS

I. DEAN NUMBER UNCERTAINTY

Uncertainty in Dean number calculation is derived from the uncertainty in the measurement of the pressure drop across an ASME standard orifice. A sample set of uncertainty quantities for De=150 is listed below;

A. CELESCO TRANSDUCER CALIBRATION UNCERTAINTY

$\delta P_{manometer} = \pm .002$ in. H_2O

$\delta \bar{E} = \pm .0007$ Volts

$\delta \bar{C} = \pm .0012$ in. H_2O/Volt

B. PRESSURE DROP UNCERTAINTY

$\delta \bar{E} = \pm .047$ Volts

$\delta \Delta P_{or} = \pm .005$ in. H_2O

C. MASS FLOW RATE UNCERTAINTY

$\delta A_{or} = \pm .012$ in.^{2}

$\delta K = \pm .001$

$\delta Y = \pm .02$

$\delta \rho = \pm .002$ lbm/ft^3

$\delta \dot{m} = \pm .0004$ lbm/sec (95% confidence level)

$\delta Ach = \pm .0052$ in.^{2}

$\delta De = \pm 4.4$ (95% confidence level)

II. FIVE HOLE PROBE VELOCITY MEASUREMENT UNCERTAINTY

Uncertainty in five hole probe velocity components is derived from the uncertainty in actual pressure measurements as well as the inherent uncertainty in the probe calibration. The flow chart used in determining the uncertainty of velocity components is shown in Figure 135. A sample set of uncertainty quantities for De=100.3, Y/d=.5, Z/d=6.0 is listed below. Numbers refer to the position in the flow chart.

A. TRANSDUCER CALIBRATION COEFFICIENT UNCERTAINTY, VALYDINE TRANSDUCERS

$\delta P_{manometer} = \pm$ .001 in. H_2O

$\delta \bar{E} = \pm$ .0007 Volts

$\delta \bar{C} = \pm$ .000072 in. H2O/Volt (bias error is disregarded since it will cancel out when pressure differentials are calculated).

B. **PROBE CALIBRATION UNCERTAINTY, PITCH = 0° , YAW = -10°**

1)

$$\delta \bar{E} = \pm .0004 \text{ Volts}$$
$$\delta P_1 = \pm .0006 \text{ in. } H_2O$$
$$\delta P_2 = \pm .0001 \text{ in. } H_2O$$
$$\delta P_3 = \pm .0005 \text{ in. } H_2O$$
$$\delta P_4 = \pm .0002 \text{ in. } H_2O$$
$$\delta P_5 = \pm .0003 \text{ in. } H_2O$$
$$\delta P_s = \pm .00004 \text{ in. } H_2O$$
$$\delta P_t = \pm .0007 \text{ in. } H_2O$$
$$\delta P = \pm .00015 \text{ in. } H_2O$$

2)

$$\delta C_{py} = \pm .025$$
$$\delta C_{pp} = \pm .011$$
$$\delta C_{pts} = \pm .045$$

3)

$$\delta K_y = \pm .004 \text{ degrees}^{-1}$$
$$\delta K_p = \pm .004 \text{ degrees}^{-1}$$
$$\delta K_{ts} = \pm .003 \text{ degrees}^{-1}$$

C. CURVED CHANNEL MEASUREMENT UNCERTAINTY

4)
$$\left[\begin{array}{l} \delta\bar{E},\ \delta\bar{C} \text{ as before} \\ \delta P_1 = \pm\ .0002 \text{ in. } H_2O \\ \delta P_2 = \pm\ .0002 \text{ in. } H_2O \\ \delta P_3 = \pm\ .0002 \text{ in. } H_2O \\ \delta P_4 = \pm\ .0002 \text{ in. } H_2O \\ \delta P_5 = \pm\ .0002 \text{ in. } H_2O \\ \delta\bar{P} = \pm\ .0001 \text{ in. } H_2O \end{array}\right.$$

5)
$$\left[\begin{array}{l} \delta C_{py} = \pm\ .134 \\ \delta C_{pp} = \pm\ .141 \end{array}\right.$$

6)
$$\left[\begin{array}{l} \delta \text{Yaw} = \pm\ 1.33 \text{ degrees} \\ \delta \text{Pitch} = \pm\ 1.4 \text{ degrees} \end{array}\right.$$

7) $\delta (P_{total} - P_{static}) = \pm\ .0004 \text{ in. } H_2O$

8) $\delta U = \pm\ .063 \text{ m/s}$

9)
$$\left[\begin{array}{l} \delta U_\theta = \pm\ .062 \text{ m/s} \\ \delta U_r = \pm\ .062 \text{ m/s} \\ \delta U_z = \pm\ .030 \text{ m/s} \end{array}\right.$$

APPENDIX C

SOFTWARE DIRECTORY

This Appendix gives a listing of the various programs used in the thesis. Each program listing contains a summary of how the program is used, user inputs, program outputs and additional features, if any. Programs are listed by type; five hole, pressure probe, hot-wire spectra or plotting routines. All programs were written in BASIC 4.0 for use on the HP9836S computer.

I. FIVE HOLE PRESSURE PROBE PROGRAMS

A. ORIENT:

Program to orient five hole probe in the calibration wind tunnel before calibration begins.

user inputs: coefficients of transducers calibration

program output: P1, P2, P3, P4, P5, $\bar{P}$, C_{py}, C_{pp}

additional features: allows user to continue through the program and adjust the probe calibration sled until satisfactory C_{py} and C_{pp} are attained ($C_{py} \simeq 0.$, $C_{pp} \simeq -.15$).

B. PROCAL:

Program used for calibration of the five hole pressure probe in the calibration wind tunnel.

user inputs: a) number of yaw points.

b) number of pitch points.

c) pitch and yaw resolution.

d) pressure offset corrections due to pitching of transducers.

program outputs: a) data file of calibration coefficients; pitch, yaw, C_{py}, C_{pp}, C_{pt}, C_{ps}, C_{pts}.

b) data file of pressures; pitch, yaw, P_1, P_2, P_3, P_4, P_5, P_{static}, P_{total}.

additional features: a) allows user to calibrate transducers or input calibration coefficients.

b) allows to vary yaw at constant pitch or vary pitch at constant yaw.

c) can accommodate five, six or seven transducers.

d) allows for simultaneous printout of data if desired.

C. ALIGN:

Program to align the five hole pressure probe in the curved channel at zero pitch and zero yaw angles. Interfaces with MITAS controller to position probe at a desired location, repositions probe to original position upon completion of the program.

user input: a) original position of the probe.

b) desired position of the probe.

program output: total velocity, C_{pp}, C_{py}, P_1, P_2, P_3, P_4, P_5.

additional features: allows user to re-align the probe between measurement sequences.

D. FIVE HOLE:

Program for control of five hole probe positioning and data acquisition in the curved channel. Interfaces with MITAS controller to control the probe position.

user inputs: a) initial position of pressure probe.

b) number of x and y points to take data at.

c) resolution of data.

d) ambient pressure.

e) delay time to start the experiment.

program outputs: a) data file of raw pressures;

X, Y, P_1, P_2, P_3, P_4, P_5, $\bar{P}$, Dean no.

b) data file of uncorrected pressure coefficients; X, Y, C_{py}, C_{pp}

additional features: a) reads temperature and calculates ambient density and Dean number for each group of pressure measurements.

b) averages Dean number at end of experiment.

c) allows user to calibrate transducers or input calibration coefficients.

E. PADJUST:

Program to implement spatial resolution correction as described in Chapter IV.

user inputs: a) distance between port 1 and center of other pressure ports (YLEN, ZLEN), .016 in. for miniature five hole pressure probe.

b) data file and name for raw pressure data, same raw pressure data as is output from FIVE HOLE.

program output: corrected file of pressure coefficients.

F. VELOCITY:

Program to calculate pitch and yaw angles for curved channel flow measurements. From this data the three mean velocity components at each measurement location are determined.

user inputs: a) data file of calibration coefficients and pressure data as output from program PROCAL. Program reads in this data for linear/bilinear interpolation.

b) values of Δ (DELY, DELZ) for y and z direction downwash velocity correction (Chapter IV). Typically a value of 0.1 was used for Δ.

c) data file of pressure coefficients as output by program PADJUST.

program output: data file of pressures and velocities for each measured location as follows;

$Y, Z, P_{total}, U, U_{\theta}, U_r, U_z$.

G. CCPF:

Program to calculate Curved Channel Poiseuille Flow at a given Dean number. The value of CCPF at each radial location is subtracted from actual streamwise velocity values at each measured location.

user input: data file of velocities as output by program velocity.

program output: U_x - UCCPF values as follows;

$Y,Z,UCCPF,U_x$-UCCPF

H. VORTICITY:

Program to calculate the three mean components of vorticity at each measured location. Methods used for calculating vorticity are presented in Chapter VIII.

user input: data file of velocities as output by program VELOCITY.

program output: data file vorticities as follows;

$$Y \quad Z \quad \omega \quad \omega_r \quad \omega_3$$

I. CIRC:

Program to calculate peak vorticity levels and circulation values from a particular set of vorticity data.

user input: a) data file of vorticities as output by program VORTICITY.

b) threshold limits, as a percentage, for omitting data points when circulation is calculated. For example, a 20% threshold will cause the program to omit all vorticity values less than 20% of peak vorticity.

c) limits of Y and Z to "look at" when calculating circulation or peak vorticities. This allows the user to calculate circulation for a particular pair of vortices as "seen" from previous data plots.

program output: hard copy and/or binary data file of Y and Z limits, peak vorticities and circulation for a particular vortex pair.

J. DEAN:

Program to sample orifice pressure drop and calculate Dean number (see Chapter II).

user input: a) ambient pressure

b) transducer calibration coefficient, or allows user to calibrate transducer.

program output: a) mass flow rate

b) orifice pressure drop

c) Dean number

additional features: allows user to adjust throttle valve (flow rate) and then calculates another Dean number.

K. GET-DATA:

Program to access various data files and printout applicable data.

user input: a) type of data file (Pressures, Pressure coefficients, Velocity).

b) Y and Z location to sample.

program output: list of data for sample point.

II. HOT-WIRE VOLTAGE SIGNAL, DATA ACQUISITION AND PROCESSING

A. HOT-WIRE:

Program to interface with HP67755A high speed data acquisition system and collect a sample set of hot-wire voltage signals.

user input: a) Dean number

b) Sampling frequency

program output: data file of voltage values.

B. CONTOUR:

General contour plotting routine has been adapted for specific plotting purposes. Plots contour lines between predetermined levels.

user inputs: a) type of data file to plot (pressure, velocity, vorticity, etc.).

b) bytes of data to skip over.

c) number of data files to average (maximum is 20).

d) option to plot average values, average of deviations from mean value, or average of standard deviations from mean value.

e) number of contour levels to plot.

f) allows for user to define levels or will equispace levels.

program output: contour plot and table of levels, labels local extrema.

C. QPLOT:

General X-Y plotting routine.

user inputs: a) number of columns in data to be read.

b) column of independent variable (x).

c) column of dependent variable (y).

d) arrangement of data file.

e) titles, subtitles, etc.

program output: an x-y plot of data as input can include up to five curves per plot.

D. O-SCOPE:

Adaptation of QPLOT to plot hot-wire voltage signal vs. time.

user inputs: a) time to begin plotting (point number)

b) total time range to plot (determined from frequency of data acquisition).

program output: hot-wire voltage vs. time plot.

E. SAMPLTCHAN:

Program to sample data from up to seven channels from HP3497A data acquisition system. Used for plotting pressure signal vs. time.

user inputs: a) number of channels to sample.

b) number of samples to take per channel.

c) time between samples.

program output: signal vs. time plots for up to seven channels.

F. VECTOR:

Program to plot secondary flow vectors in a flow field, largest vector is labeled (5% of subplot width).

user inputs: velocity data file (output from program VELOCITY.

program outputs: secondary velocity vectors.

G. PLTRAV:

Program to plot traverses of pressure probe measurements will plot up to ten radial traverses, for different spanwise locations in a "three-dimensional" format.

user inputs: a) velocity data file (output form program VELOCITY).

b) Spanwise positions to plot.

program outputs: radial traverse plots.

H. 3DPLOT:

Program to plot seven radial-spanwise contour plots from curved channel measurements (See Figure 33).

user inputs: a) type of plot desired, vorticity, total pressure, streamwise velocity or U_x-UCCPF.

b) Appropriate data files.

program output: Contour plots.

REFERENCES

1. Thermosciences Division, Department of Mechanical Engineering, Stanford University Report TF-30, Instability and Transition in Curved Channel Flow, by W.H. Finlay, J.B. Keller and J.H. Ferziger, Stanford, California, May 1987.

2. Dean, W.R., "Fluid Motion in a Curved Channel," Proceedings of the Royal Society of London, Series A, V. 121, pp. 402-420, 1928.

3. Reid, W.H., "On the Stability of Viscous Flow in a Curved Channel," Proceedings of the Royal Society of London, Series A, V. 244, pp. 186-198, 1958.

4. Hammerlin, G., "Die Stabilitat der Stromung in Einem Gekrummten Kanal," Archive for Rational Mechanics and Analysis, V. 1, pp. 212-224, 1958.

5. Kelleher, M.D., Flentie, D.L., and McKee, R.J., "An Experimental Study of the Secondary Flow in a Curved Rectangular Channel," ASME Journal of Fluids Engineering, V. 102, pp. 92-96, 1980.

6. Siedband, M.A., A Flow Visualization Study of Laminar/Turbulent Transition in a Curved Channel, Master's Thesis, Naval Postgraduate School, Monterey, California, March 1987.

7. Niver, R.D., Structural Characteristics of Dean Vortices in a Curved Channel, Master's Thesis, Naval Postgraduate School, Monterey, California, June 1987.

8. Finlay, W.H., Keller, J.B., and Ferziger, J.H., "Finite Amplitude Vortices in Curved Channel Flow," submitted to Journal of Fluid Mechanics, 1988.

9. Ligrani, P.M. and Niver, R.D., "Flow Visualization of Dean Vortices in a Curved Channel with 40 to 1 Aspect Ratio," to appear in Physics of Fluids, 1988.

10. Ligrani, P.M., Singer, B.A., and Baun, L.R., "Miniature Five Hole Pressure Probe for Measurement of Three Mean Velocity Components in Low Speed Flows," submitted to Journal of Physics E - Scientific Instruments, 1988.

11. Holman, J.P. and Gajda, W.J., Jr., Experimental Methods for Engineers, 4th Edition, pp. 238-247, McGraw-Hill, 1984.

12. ASME Power Test Committee, ASME Power Test Codes, (Supplement on Instruments and Apparatus), part 5, Chapter 4, p. 25, American Society of Mechanical Engineers, 1959.

13. Treaster, A.L. and Yocum, A.M., "The Calibration and Application of Five Hole Probes," ISA Transactions, V. 18, No. 3, pp. 23-34, 1979.

14. Treaster, A.L. and Houtz, H.E., "Fabricating and Calibrating Five Hole Probes," Proceedings from the Fluid Measurements and Instrumentation Forum, V. 34, 1986.

15. Welz, J.P., "An Algorithm for Using the Five Hole Probe in the Non-nulled Mode," Proceedings from the Fluid Measurements and Instrumentation Forum, V.34, 1986.

16. Ligrani, P.M., Singer, B.A., and Baun, L.R., "Spatial Resolution and Downwash Velocity Corrections for Multiple-Hole Pressure Probes in Complex Flows," to appear in Experiments in Fluids, 1988.

17. Young, A.D. and Maas, J.M., "The Behavior of a Pitot Tube in a Transverse Total Pressure Gradient," British Research and Memoranda, V. 1770, 1936.

18. Livesey, J.L., "The Behavior of Transverse Cylindrical and Forward Facing Total Pressure Probes in Transverse Total Pressure Gradients," Journal of Aeronautical Sciences, V. 23, pp. 949-955, 1956.

19. Lighthill, M.J., "Contribution to the Theory of the Pitot-Tube Displacement Effect," Journal of Fluid Mechanics, V. 2, pp. 493-512, 1957.

20. National Aeronautics and Space Administration, Technical Memorandum 100052, Development of Subminiature Multi-Sensor Hot-wire Probes, by Westphal, R.V., Ligrani, P.M., and Lemos, F.R., March 1988.

21. Ligrani, P.M. and Bradshaw, P., "Subminiature Hot-wire Sensors: Development and Use," Journal of Physics E - Scientific Instruments, V. 20, pp. 323-332, 1987.

22. Schlichting, H., Boundary Layer Theory, Sixth Edition, pp. 28-32, McGraw-Hill, 1968.

23. Brigham, E.O., The Fast-Fourier Transform, Prentice-Hall, 1974.

INITIAL DISTRIBUTION LIST

		No. Copies
1.	Defense Technical Information Center Cameron Station Alexandria, Virginia 22304-6145	2
2.	Library, Code 0142 Naval Postgraduate School Monterey, California 93943-5002	2
3.	Professor P.M. Ligrani, Code 69Li Department of Mechanical Engineering Naval Postgraduate School Monterey, California 93943-5000	12
4.	Department Chairman, Code 69 Department of Mechanical Engineering Naval Postgraduate School Monterey, California 93943-5000	1
5.	Dr. K. Civinskas Propulsion Directorate U.S. Army Aviation Research and Technology Activity AVSCOM NASA-Lewis Research Center Cleveland, Ohio 45433	10
6.	LT Lawrence R. Baun 6918 Espey Lane McLean, Virginia 22101	2

Thesis
B242933 Baun
c.1 The development and structural characteristics of Dean vortices in a curved rectangular channel.

Thesis
B242933 Baun
c.1 The development and structural characteristics of Dean vortices in a curved rectangular channel.

DEMCO

AMERICAN BINDERY
TOPEKA KANSAS

thesB242933
The development and structural character
3 2768 000 84640 6
DUDLEY KNOX LIBRARY